APPLIED COMPUTATIONAL ELECTROMAGNETICS SOCIETY JOURNAL

June 2025
Vol. 40 No. 6
ISSN 1054-4887

The ACES Journal is abstracted in INSPEC, in Engineering Index, DTIC, Science Citation Index Expanded, the Research Alert, and to Current Contents/Engineering, Computing & Technology.

The illustrations on the front cover have been obtained from the ARC research group at the Department of Electrical Engineering, Colorado School of Mines

Published, sold and distributed by: River Publishers, Alsbjergvej 10, 9260 Gistrup, Denmark

JUNE 2025 REVIEWERS

Kiran Ajetrao
Guillaume Andrieu
Sami Barmada
Mohammad Sajjad Bayati
Abdelfattah Darwish
Junbing Duan
Biswajit Dwivedy
Nunzia Fontana
Nasr H. Gad
Taha Imeci
Yuchen Ma
Durga Prasad Mishra
Beulah Jabeseeli N.
Michel M. Ney
Mahdi Oliaei
Antonio Orlandi
Ananya Parameswaran
S. Peddakrishna
Andrew Peterson
Winner Pulakhandam
Ehsan Akbari Sekehravani
Partha Shome
Somchat Sonasang
Praneeth Suri
Mario Versaci
Salah I. Yahya
Yaqdhan
Yongliang Zhang

THE APPLIED COMPUTATIONAL ELECTROMAGNETICS SOCIETY JOURNAL

Vol. 40 No. 6 June 2025

TABLE OF CONTENTS

Novel Strategies for Efficient Computational Electromagnetic (CEM) Simulation of Microstrip Circuits, Antennas, Arrays, and Metamaterials Part-II: Characteristic Basis Function Method, Perfectly Matched Layer, GPU Acceleration

Raj Mittra[1], Tomislav Marinovic[2], Ozlem Ozgun[3], Shuo Liu[4], and Ravi K. Arya[5]

[1]Department of Electrical & Computer Science, University of Central Florida
Orlando, FL, USA
rajmittra@ieee.org

[2]Computational Electromagnetics Department, Multiverse Engineering
Zagreb, Croatia
tommarinovich@gmail.com

[3]Electrical & Electronics Engineering Department, Hacettepe University
Ankara, Turkey
ozgunozlem@gmail.com

[4]Amedac, Shanghai, China
liushuo_hit@outlook.com

[5]Zhongshan Institute of Changchun University of Science and Technology
Zhongshan, Guangdong, China
raviarya@cust.edu.cn

Abstract – As mentioned in Part-I [1], rapid prototyping plays a critical role in the design of antennas and related planar circuits for wireless communications, especially as we embrace the 5G/6G protocols going forward into the future. Existing commercial software modules are often inadequate for this task in the millimeter-wave range since the memory requirements and runtimes are often too high for them to be acceptable as design tools. Using approximate equivalent circuit models for various components comprising the antenna and the feed system is not the answer either, because these models are not sufficiently accurate. Consequently, it becomes necessary to resort to the use of more sophisticated simulation techniques based on full-wave solvers that are numerically rigorous, albeit computer-intensive. Furthermore, optimizing the dimensions of antennas and circuits to enhance the performance of the system is frequently desired, and this often exacerbates the problem since the simulation must be run a large number of times to achieve the performance goal, namely an optimized design. Consequently, as pointed out earlier, it is highly desirable to develop accurate yet efficient techniques, both in terms of memory requirements and runtimes, to expedite the design process as much as possible.

In the first part of this paper [1], we presented three strategies to address these issues, mostly related to Green's Functions of layered media. We have shown that the proposed techniques are not only useful for antennas and printed circuits on layered media but also for antennas embellished with metamaterials for the purpose of their performance enhancement.

In this sequel to Part-I, we present several other Efficient Computational Electromagnetic (CEM) simulation strategies for expediting the runtime and improving the capability of handling large problems that are highly memory-intensive. These include a domain decomposition technique, which utilizes the Characteristic Basis Function Method (CBFM); the T-matrix approach which is also useful for hybridizing Finite Methods (FEM or FDTD) with the Method of Moments (MoM); Mesh truncation in Finite Method by using a conformal Perfectly Matched Layer (PML); and Graphics Processing Unit (GPU) acceleration of MoM and FDTD codes.

Index Terms – 5G/6G Communication, Antenna Design, Computational Electromagnetics (CEM), Electromagnetic Scattering, Finite-Difference Time-Domain (FDTD), Finite Element Method (FEM), GPU acceleration, Method of Moments (MoM), Microwave

Submitted On: November 1, 2024
Accepted On: April 24, 2025

https://doi.org/10.13052/2025.ACES.J.400601

Circuits, Millimeter waves, Perfectly Matched Layer (PML).

I. INTRODUCTION

In Part-I [1] of this paper, we presented three different strategies for enhancing the performance of efficient Computational Electromagnetic (CEM) techniques to enable them to handle the simulation of antennas, circuits as well as metamaterials at millimeter wavelengths. In this sequel to Part-I, we describe three additional strategies that complement those presented in Part-I. The topics covered in this sequel include: High-Level basis functions called the Characteristic Basis Functions (CBFs); conformal PML (Perfectly Matched Layer) for mesh truncation; and GPU acceleration of MoM codes and those based on Finite Methods. The details are presented in the sections that follow (sections II through V).

II. CHARACTERISTIC BASIS FUNCTION METHOD (CBFM) FOR EFFICIENT ANALYSIS OF ARRAY ANTENNAS

This section focuses on the characteristic basis function method (CBFM), a reduced-order technique for efficient electromagnetic (EM) analysis of large-scale radiation and scattering problems, by revisiting its theoretical framework (section II part A), outlining its key application areas and its placement within the broader CEM context (section II part B); and introducing a novel two-level formulation of this algorithm with a single CBF per subdomain at its top level (section II part C). While our previous research on this topic, presented in conference publications [2–4], has demonstrated the potential of this CBFM formulation for enabling efficient EM analysis of both periodic and aperiodic antenna arrays in radiating mode, its efficacy has not been extensively analyzed in the existing literature, which primarily relates to the conventional CBFM formulations that employ multiple subdomain CBFs. Thus, section II part C aims to provide a unified and detailed analysis of the CBFM algorithm with a single high-level subdomain basis function, building upon the foundational concepts introduced in our previous conference publications [2–4]. This analysis establishes the proposed CBFM formulation as an effective tool for EM analysis in the context of rapid prototyping of disconnected array antennas used in radio astronomical research, 5G/6G communication systems that utilize MIMO antenna arrays, and other applications. Furthermore, section II part D outlines our ongoing research efforts aimed at integrating the proposed CBFM approach with existing CEM solution techniques to extend its applicability to connected antenna arrays and circuits printed on multilayered dielectric substrates for 5G/6G communication systems.

A conventional approach for conducting the EM analysis of finite antenna arrays is by using full-wave solution methods such as the finite-difference time-domain (FDTD) method, the finite element method (FEM), or the Method of Moments (MoM) [5]. For arrays composed of metallic antenna elements in homogeneous space, which are in the focus of the analysis in this paper, the surface formulation of MoM maximizes the numerical efficiency of the solution process by discretizing only the conductive surfaces, whereas the FDTD and FEM methods require meshing the entire computational volume, as noted in [6, Chapter 5.11]. This formulation is based upon the transformation of discretized surface integral equations into a linear matrix system:

$$\boldsymbol{Z}^{\mathrm{RWG}}\boldsymbol{I}^{\mathrm{RWG}} = \boldsymbol{V}^{\mathrm{RWG}}. \tag{1}$$

Here, $\boldsymbol{V}^{\mathrm{RWG}}$ and $\boldsymbol{I}^{\mathrm{RWG}}$ are the excitation or right-hand side (r.h.s.) vector and the solution vector, respectively, with a size of N^{RWG}. The term $\boldsymbol{Z}^{\mathrm{RWG}}$ denotes the moment matrix of the antenna array with a size of $N^{\mathrm{RWG}} \times N^{\mathrm{RWG}}$. The dimensions of this matrix are determined by the overall number of Rao-Wilton-Glisson (RWG) basis functions, which are used to model the surface current distribution on triangulated surfaces [5]. This, in turn, determines the number of degrees of freedom (DoFs) for the solution in the MoM-based matrix equation (1).

A. CBFM algorithm

In many antenna array problems characterized by a high number of array elements, large electrical sizes, or dense discretization of the antenna geometry, the MoM-based matrix system can become too large to solve on standard desktop computers. To overcome this challenge, the dimension of the original MoM-based matrix system (1) for these array problems can be reduced. This reduction can be achieved by decomposing the entire problem domain into several subdomains, and by grouping the low-level RWG basis functions within each subdomain to create a smaller set of high-level characteristic basis functions (CBFs) specific to that subdomain. This strategy forms the basis for the CBFM, which was originally introduced in [7] for efficient modeling of large-scale EM scattering problems.

In the CBFM, the solution vector for the RWG basis functions associated with the ith subdomain can be expanded in terms of the CBFs generated on that subdomain as follows:

$$\boldsymbol{I}_i^{\mathrm{RWG}} \approx \sum_{k=1}^{N_i^{\mathrm{CBF}}} \iota_{i,k}^{\mathrm{CBF}} \boldsymbol{f}_{i,k}^{\mathrm{CBF}}. \tag{2}$$

Here, the term $\boldsymbol{f}_{i,k}^{\mathrm{CBF}}$ represents the kth CBF vector corresponding to subdomain i, with a size of N_i^{RWG}, containing the expansion coefficients for the N_i^{RWG} low-level RWG subdomain basis functions associated with

this CBF. Additionally, the term $\iota_{i,k}^{\mathrm{CBF}}$ is the expansion coefficient for the corresponding CBF. Note that, following the domain decomposition step of the problem geometry, the defined subdomains may partially overlap, and consequently, some RWG basis functions may be associated with more than one subdomain [8, Chapter 4.3.1].

The initial set of subdomain CBFs is typically selected to capture the underlying physics of the actual current (i.e., the solution, yet to be determined) on that subdomain. For instance, in radiating mode, this can be achieved by generating primary CBFs that correspond to the solutions of uncoupled subdomains, and secondary or higher-order CBFs that account for mutual coupling (MC) effects between subdomains. In scattering mode, where the expected number of incident angles for incoming plane waves can be relatively large, this can be accomplished by collecting the responses of the subdomain geometry when illuminated by a set of incident plane waves. Alternatively, subdomain CBFs can be generated from various numerical basis sets used to expand the solution on that subdomain. These basis sets can be derived from previous subdomain solutions in an iterative method, characteristic modes, or physical optics-based currents associated with the subdomain, to list a few examples.

However, note that the initial set of subdomain CBFs is often redundant from a linear algebraic perspective. This means that some CBFs within this set can be expressed as linear combinations of other CBFs from the same set. To ensure that the CBFs are linearly independent and that each CBF contributes unique information to the solution, the singular value decomposition (SVD) algorithm or a similar matrix-decomposition algorithm can be applied to orthogonalize the initial set of CBFs. Moreover, a thresholding process can be applied to the orthogonalized subdomain CBFs to eliminate those below the specified threshold, retaining only the most significant subset. Consequently, the number of generated subdomain CBFs, $N_i^{\mathrm{CBF}}\,(i=1,\ldots,M)$, may vary across subdomains, where M corresponds to the total number of subdomains. By applying the thresholding procedure, the overall number of DoFs in the reduced-order system is reduced, improving the computational efficiency of the solution process. In addition, enforcing mutual orthogonality among the CBFs typically leads to a well-conditioned reduced-order matrix. This not only minimizes the loss of numerical accuracy due to suboptimal matrix conditioning in both direct and iterative solution approaches but also allows iterative methods to be performed without the need for applying advanced matrix preconditioning schemes, which is typically required to enhance the convergence of these methods when applied to MoM-based matrices with relatively high condition numbers.

After decomposing the entire problem domain into subdomains and generating the subdomain CBFs, a CBFM-based reduced-order matrix equation can be formulated as follows:

$$\boldsymbol{Z}^{\mathrm{CBF}}\boldsymbol{\iota}^{\mathrm{CBF}}=\boldsymbol{V}^{\mathrm{CBF}}. \tag{3}$$

Here, $\boldsymbol{V}^{\mathrm{CBF}}$ and $\boldsymbol{\iota}^{\mathrm{CBF}}$ represent the reduced-order excitation vector and CBF coefficients vector, respectively, both with a size of N^{CBF}, where N^{CBF} is the total number of CBFs across all subdomains. Additionally, the term $\boldsymbol{Z}^{\mathrm{CBF}}$ represents the reduced-order antenna array coupling matrix, with a size of $N^{\mathrm{CBF}}\times N^{\mathrm{CBF}}$. By applying a domain decomposition scheme to subdivide the entire problem domain into subdomains, the MoM-based matrix for this problem can be structured as a block matrix. The diagonal blocks (submatrices of the full matrix) contain the self and MC interactions between the RWG basis functions within each subdomain, while the off-diagonal blocks (submatrices) represent the MC interactions between the RWG basis functions across different subdomains. Consequently, the CBFM-based reduced-order matrix can be constructed in a block-based manner by modeling intra- or inter-block coupling interactions between the CBFs associated with the blocks p and q through the corresponding submatrix of the original MoM matrix, as follows:

$$\boldsymbol{Z}_{pq}^{\mathrm{CBF}}=\left(\boldsymbol{f}_p^{\mathrm{CBF}}\right)^{\dagger}\boldsymbol{Z}_{pq}^{\mathrm{RWG}}\boldsymbol{f}_q^{\mathrm{CBF}}\quad\left(\{p,q\}=1,\ldots,M\right), \tag{4}$$

where

$$\boldsymbol{f}_i^{\mathrm{CBF}}=\left[\boldsymbol{f}_{i,1}^{\mathrm{CBF}}|\ldots|\boldsymbol{f}_{i,N_i^{\mathrm{CBF}}}^{\mathrm{CBF}}\right]\quad\left(i=1,\ldots,M\right), \tag{5}$$

is a column-augmented CBF matrix of size $N_i^{\mathrm{RWG}}\times N_i^{\mathrm{CBF}}$, with $i=p$ for the CBF matrix containing N_p^{CBF} test (observation) CBFs on the pth subdomain, and $i=q$ for the CBF matrix containing N_q^{CBF} source CBFs on the qth subdomain [8, Chapter 4.3.1]. The symbol $\{\cdot\}^{\dagger}$ denotes the conjugate transpose operator. In addition, $\boldsymbol{Z}_{pq}^{\mathrm{RWG}}$, with a size of $N_p^{\mathrm{RWG}}\times N_q^{\mathrm{RWG}}$, is the submatrix extracted from the MoM-based matrix $\boldsymbol{Z}^{\mathrm{RWG}}$, which contains the coupling interactions between subdomains p and q. Consequently, the size of each matrix term $\boldsymbol{Z}_{pq}^{\mathrm{CBF}}$ is $N_p^{\mathrm{CBF}}\times N_q^{\mathrm{CBF}}$, and this matrix is incorporated as a submatrix into the reduced-order matrix $\boldsymbol{Z}^{\mathrm{CBF}}$. When an array is composed of identical antenna elements, $N_p^{\mathrm{RWG}}=N_q^{\mathrm{RWG}}=N_{\mathrm{s}}^{\mathrm{RWG}}$.

Similarly, the CBFM-based reduced-order excitation vector can be constructed in a block-based manner as follows:

$$\boldsymbol{V}_p^{\mathrm{CBF}}=\left(\boldsymbol{f}_p^{\mathrm{CBF}}\right)^{\dagger}\boldsymbol{V}_p^{\mathrm{RWG}}\quad\left(p=1,\ldots,M\right), \tag{6}$$

where $\boldsymbol{V}_p^{\mathrm{RWG}}$ is the pth subdomain excitation vector of size N_p^{RWG}, extracted from the MoM-based excitation vector $\boldsymbol{V}^{\mathrm{RWG}}$. Consequently, the size of each vector term

$\boldsymbol{V}_p^{\mathrm{CBF}}$ is N_p^{CBF}, and this vector is incorporated as a subvector into the reduced-order excitation vector $\boldsymbol{V}^{\mathrm{CBF}}$. Note that, instead of using (4) and (6) to calculate the blocks of the reduced-order matrix and excitation vector by processing the available MoM-based matrix and excitation vector data, these blocks can be calculated directly by evaluating the reaction integrals between the radiated (scattered) field from the source CBF and the observation (test) CBF, as described in [8, Chapter 4.3.1].

The runtime costs of the CBFM algorithm include the initial cost of generating the MoM matrix, the cost of generating subdomain CBFs, and the costs associated with setting up and solving the reduced-order matrix. Here, the runtime for generating the moment matrix scales as $\mathcal{O}\left(\left(N^{\mathrm{RWG}}\right)^2\right)$. In the CBFM algorithm applied to large antenna (array) problems, the cost of generating subdomain CBFs is typically less significant compared to the costs of setting up and solving the reduced-order matrix. The cost of constructing the reduced-order matrix $\boldsymbol{Z}^{\mathrm{CBF}}$ via (4) can be estimated as $\mathcal{O}\left(\left(N^{\mathrm{RWG}}\right)^2 \times \overline{N}_{\mathrm{s}}^{\mathrm{CBF}}\right)$, under the assumption that the average number of subdomain CBFs, $\overline{N}_{\mathrm{s}}^{\mathrm{CBF}}$, is considerably smaller than the number of RWG basis functions per subdomain $\left(\text{i.e., } \overline{N}_{\mathrm{s}}^{\mathrm{CBF}} \ll N_{\mathrm{s}}^{\mathrm{RWG}}\right)$, as detailed in [9]. Finally, solving the CBFM-based reduced-order matrix system (3) to extract the CBF coefficients vector, $\boldsymbol{\imath}^{\mathrm{CBF}}$, scales as $\mathcal{O}\left(\left(N^{\mathrm{CBF}}\right)^3\right)$ when using a direct solver, or $\mathcal{O}\left(K_{\mathrm{it.}} \times \left(N^{\mathrm{CBF}}\right)^2\right)$ when using an iterative method, where $K_{\mathrm{it.}}$ is the number of iterations required to reach convergence. Direct solution methods are generally preferred in applications that require handling a large number of excitation vectors, such as in radar cross-section (RCS) analysis. This is mainly because a direct solver requires solving the reduced-order matrix only once, after which generating solutions for the desired excitation vectors is reduced to performing efficient matrix-vector multiplications. However, in many applications, the dimension of the reduced-order matrix may still be large due to factors such as the large electrical size of the problem or a high number of array elements, potentially with a relatively large average number of generated CBFs per element. In such cases, or more generally in applications where the desired number of excitation vectors is relatively small, iterative methods can offer greater computational efficiency in comparison to direct solution approaches. Note that for both direct and iterative solution methods, the CBFM typically significantly reduces the overall solution times of MoM-based algorithms, while maintaining reliable solution accuracy. This is achieved by rigorously accounting for EM coupling effects within and between subdomains during the construction of the reduced-order matrix through (4). As a result, the CBFM enables accurate and systematic analysis of arbitrary large-scale 2D and 3D antenna array and scattering problems in a computationally efficient manner [7].

B. CBFM: Applications and related methods in computational electromagnetics

Since its inception, the CBFM has been extensively used for efficient analysis of various EM scattering problems [7, 10–33]. In addition, this algorithm has been effectively adapted for the analysis of a range of microwave structures [34–40], as well as array antennas in free space [41–45], or antennas printed on top of layered media [20, 46–48]. The numerical advantages of using the CBFM for analyzing printed antennas have been demonstrated, for instance, in [36] and [48], showing significant improvements in both runtime and memory requirements compared to the MoM, often by orders of magnitude. In addition, the CBFM has been successfully utilized in the context of analysis based on the FEM [49–54], as well as in analyses of scattering from rough surfaces [55] and forest scattering [56]. Moreover, it has recently been shown that the CBFM, which was originally developed to reduce the matrix size by using high-level basis functions that made it feasible to use a direct solver even for relatively large size problems, can also be implemented into various classical iterative schemes to improve their convergence significantly [9, 45, 57–62]. Recently, the CBFM has been implemented within the novel deep integration paradigm for efficient multiscale analysis of integrated active antenna arrays [40, Chapter 6]. These developments highlight the versatility and robustness of the CBFM algorithm in handling a wide range of real-world EM problems, as well as its potential for integration with existing CEM codes and algorithms, enhancing their numerical efficiency and accuracy and expanding their range of applicability. Finally, it is worth mentioning that, as of 2023, the CBFM solver has been integrated in the commercially available EM simulation software tool FEKO [63], further highlighting the significance of this algorithm in modern antenna analysis and design. For further insights into the application of the CBFM in antenna design, interested readers may consult [64, Chapter 2].

However, it is important to note that the concepts of domain decomposition and the use of high-level subdomain basis functions are not unique to the CBFM. In this context, the CBFM should be seen as part of a broader family of CEM solution techniques that utilize high-level subdomain basis functions. Notable examples of these techniques include the combined expansion scheme [65], the expansion wave concept [66], the diakoptics-based

approach [67], the subdomain multilevel approach [68], the eigencurrent approach [69–71], the synthetic functions approach [72], the domain decomposition procedure [73], the macrobasis function approach [58, 74, 75] and the accurate subentire-domain (ASED) basis function method [76–86]. Interested readers are encouraged to refer to the references listed above to explore the conceptual differences in domain decomposition, high-level basis function aggregation, reduced-order matrix construction, and numerical acceleration techniques integrated within these methods. In addition, it is worth noting that the CBFM differs conceptually from the higher-order MoM (see [87] and the citing references), another widely adopted, numerically efficient CEM solution strategy. The strategy behind higher-order MoM is to reduce the number of basis functions—and consequently the size of the resulting MoM matrix—by defining a smaller set of basis functions over larger subdomains, typically on the order of a wavelength or more, while increasing their order to capture complex variations in the current distribution. In contrast, the CBFM algorithm models the actual current distribution by aggregating low-order subdomain basis functions across smaller subdomains, compared to those used in the high-order MoM, to generate a reduced set of high-level basis functions on these subdomains.

C. CBFM algorithm using single high-level CBF per subdomain

In this subsection, we provide a unified and extended account of the efficient CBFM formulation, which employs a single CBF per subdomain, as introduced in our previous conference publications [2–4]. As part of this analysis, we introduce a novel two-level CBFM formulation that utilizes a single CBF per subdomain at its top level, greatly improving the numerical efficiency of the algorithm presented in [4].

1. Background and concept

The CBFM formulation using single CBF per subdomain is proposed as an efficient alternative for the analysis and design of large-scale antenna arrays, a process that typically requires several iterations—each involving EM analysis of the array being designed or, alternatively, a multiphysics analysis that also considers circuit-theoretic, mechanical, or thermal factors to ensure that the design meets targeted goals. In such applications, it is often preferable to split the design process into two stages: initially using computationally efficient methods, such as the CBFM, in the early design phases, and reserving full-wave solvers for later stages to refine or validate the design. During the early design stages, the solution only needs to provide a reasonably accurate approximation of the actual physical current (or the resulting scattered field) to guide the design toward its objectives. This enables the reformulation of the conventional CBFM algorithm, which typically employs multiple subdomain CBFs, into a more compact and computationally efficient form that utilizes only a single subdomain CBF. Consequently, extracting the subdomain solution generally involves two steps: (a) generating a single CBF for each subdomain; and (b) weighting the generated CBF by its corresponding CBF coefficient, obtained by solving the CBFM-based reduced-order matrix equation (3). Thus, the effect of array MC on the subdomain solution vector is captured through these two steps: first, by approximating and fixing the complex profile (shape) of the solution current during the generation of the subdomain CBF, and then by adjusting its magnitude using the corresponding CBFM-based coefficient, which accounts for all interelement coupling interactions within the array.

2. Context and contributions

In our previous work [2], we introduced the concept of the CBFM algorithm using a single subdomain CBF, demonstrating that in truncated-periodic array configurations, CBFs can be assumed identical across all array elements and approximated as the solution of a unit cell in a virtually infinite, doubly periodic array environment [2]. This is simulated by applying periodic boundary conditions (PBCs) to the unit cell [2]. To account for deviations in current distributions on edge and corner elements due to finite-array truncation effects, we proposed a modified CBF generation approach in [3]. In this method, localized MoM-based subarray problems, comprising 4 or 6 elements, are defined and solved to generate CBFs for these elements, while the infinite-array solution is retained as the CBF for interior array elements [3]. In addition, in [4], we demonstrated that the subarray-based approach to CBF generation can be extended to aperiodic array configurations, where each element's CBF is synthesized by solving a localized MoM-based subarray problem associated with that element, defined by the element's radius of influence (RoI). This strategy is particularly effective in arrays with relatively large average interelement spacing, where perturbations in the elements' current profiles are primarily determined by the effects of MC with neighboring elements within their sphere of influence; while the effects of MC with elements outside this sphere can be effectively incorporated through the CBFM-based weighting coefficient.

While the proposed CBFM algorithm, which employs a single subarray-based subdomain CBF, significantly reduces the computational cost of a MoM solver applied directly to the array problem as in (1), solving a set of subarray problems using the MoM can still be computationally expensive; particularly when the

subarrays comprise electrically large and geometrically complex elements represented by a large number of low-level basis functions. To enhance the efficiency of the subarray-based CBF generation process, this paper introduces a novel two-level CBFM strategy. In this strategy, the CBFM is first applied locally to a subarray problem defined for each array element, extracting the solution for that element at the bottom level of the CBFM algorithm. This solution is then utilized as a single CBF at its top level, where the algorithm is applied to the entire array problem. Consequently, this method completely eliminates the need for a low-level direct solution approach for array or subarray problems at any stage of the solution process, significantly reducing computational cost.

The proposed algorithm differs from the conceptually similar multilevel CBFM approaches presented in [14–16, 44], which rely on recursive formulations where the reduced-order system variables at each level are calculated based on those from the previous level, generally retaining multiple CBFs per subdomain. However, these formulations can suffer from accuracy degradation when only one CBF per subdomain is used at the top level, as observed in [44]. In contrast, our strategy preserves solution accuracy by directly constructing the reduced-order system at both levels of the CBFM algorithm using the low-level matrix system data as in (1), while minimizing the computational cost by employing a single CBF per subdomain at the top level of this algorithm. A similar two-level CBFM approach was reported in [20]; however, this approach retains multiple CBFs per subdomain and is tailored for truncated-periodic arrays, limiting its applicability to more general antenna configurations, while our proposed strategy extends to both truncated-periodic and aperiodic arrays.

Compared to existing subarray-based macrobasis function solution frameworks for aperiodic antenna arrays [45, 75, 88–90], our proposed approach leverages the CBFM to efficiently solve localized subarray problems without relying on computationally expensive low-level lower–upper (LU) decomposition techniques or the explicit construction of active impedance matrices for subarray elements. In particular, eliminating low-level LU decomposition significantly enhances the scalability of the proposed solution method when dealing with large (sub)array problems. Moreover, while [45] employs the CBFM to solve localized subarray problems, this CBFM implementation generates multiple CBFs per subdomain, leading to increased computational overhead compared to our approach. Finally, similar to our proposed CBFM algorithm, various formulations of the ASED basis function solution method [76–80, 84, 86] utilize either a single or multiple subarray-based high-level basis functions per subdomain. However, these algorithms were primarily developed for periodic antenna arrays in scattering mode. While [86] extends the ASED basis function method to radiating mode, it remains restricted to periodic arrays, whereas our approach applies to both periodic and aperiodic configurations.

3. Implementation

In this paper, the proposed two-level CBFM algorithm is used to analyze various arrays of M identical, disconnected antenna elements, such as the bowtie antenna array shown in Fig. 1. In the analysis, each array element is treated as a subdomain within the CBFM framework. Algorithmically, both levels of the CBFM algorithm follow the same development sequence, as described by equations (3) to (6). The key distinction between the two levels is in the number of CBFs assigned per element: at the top level, a single CBF is used to represent each array element, whereas at the bottom level, multiple CBFs are generated for each subarray element.

The CBFs for the top-level CBFM algorithm are assigned as follows. For truncated-periodic array problems, the infinite-array solution is either uniformly assigned as a CBF to all array elements or only to interior elements. In the latter case, the CBFs for edge and corner elements are extracted from the solution vectors of localized subarray problems associated with these elements, with subarray sizes of up to $3(2) \times 2(3)$, as illustrated in Fig. 1 [3]. Similarly, for aperiodic array problems, the CBF for each array element $p = 1, \ldots, M$ is extracted from the solution vector of its corresponding localized subarray problem. The size of the pth subarray, $M_{\mathrm{sa},p}$, accounts for the pth element itself along with $M_{\mathrm{sa},p} - 1$ neighboring elements within its sphere of influence. To efficiently calculate the solution vector for a given subarray problem, we use the conventional CBFM formulation that utilizes primary and secondary CBFs. In this formulation, the CBFs for each element m of the subarray p, denoted as $m(p) = 1, \ldots, M_{\mathrm{sa},p}$, are obtained by initially defining a single primary CBF, representing the isolated element solution, and a set of $N^{\mathrm{S}}_{\mathrm{sa},p} = M_{\mathrm{sa},p} - 1$ secondary CBFs, representing the scattered currents induced at this element by other elements within the subarray, as detailed in [46]. The primary and secondary CBFs are denoted by "P" and "S", respectively. For $N^{\mathrm{S}}_{\mathrm{sa},p} \geq 1$, the combined CBF representation for the element $m(p)$ can be expressed as:

$$\boldsymbol{f}^{\mathrm{CBF}}_{\mathrm{sa},m(p)} = \Phi\left(\left[\boldsymbol{I}^{\mathrm{P}}_{\mathrm{sa},m(p)} \,|\, \boldsymbol{I}^{\mathrm{S}1}_{\mathrm{sa},m(p)} \,|\, \ldots \,|\, \boldsymbol{I}^{\mathrm{S}_{N^{\mathrm{S}}_{\mathrm{sa},p}}}_{\mathrm{sa},m(p)} \right] \right), \quad (7)$$

where $\Phi(\cdot)$ represents the orthogonalization process based on the SVD algorithm, which renders the initial set of CBFs mutually orthogonal. Note that, if no neighboring elements are captured within the sphere of influence of the pth element, the CBF assigned to that element in the top-level CBFM algorithm defaults to its primary CBF. Given the relatively small subarray sizes

in the implementation of this algorithm in this paper, all CBFs are retained after orthogonalization. For larger subarrays, redundant CBFs could be discarded to reduce the sizes of CBFM-based subarray problems, accelerating their analysis without compromising accuracy. Furthermore, the relatively small sizes of the reduced-order systems associated with these subarrays allow for the use of a direct solution method without incurring significant computational overhead.

By assigning only a single CBF per element in the top-level CBFM algorithm, the dimension of the reduced-order matrix system is reduced to the number of array elements, i.e., $N^{\mathrm{CBF}} = M$, leading to a major reduction in the original MoM-based matrix size, N^{RWG}, by a factor of $N_{\mathrm{s}}^{\mathrm{RWG}}$ [2–4]. The benefits of this reduction are particularly evident when analyzing arrays composed of electrically large and geometrically complex antenna elements, which require a large number of low-level basis functions per element, $N_{\mathrm{s}}^{\mathrm{RWG}}$. In such cases, the original matrix size can be reduced by several orders of magnitude, enabling efficient analysis of large-scale antenna array problems even on standard desktop machines with limited CPU and RAM resources when employing the proposed CBFM method [2–4].

4. Simulation setup and validation strategy

The efficacy of the proposed CBFM algorithm employing a single CBF per array element for analyzing periodic antenna arrays, is numerically evaluated using an 8×8 array of bow-tie antenna elements shown in Fig. 1. In addition, to evaluate the efficacy of the proposed approach for analyzing aperiodic arrays comprising electrically large and geometrically complex antenna elements, we consider a 10-element irregular sparse array (ISA) of log-periodic antenna elements shown in Fig. 2. The former element type is commonly used in antenna arrays for various communication system applications, while the latter type is primarily utilized in radio astronomy. For the analysis, the base bow-tie element (see [9, Fig. 1]) is discretized in FEKO using a $\lambda/20$ triangular mesh resolution, with regard to the excitation frequency of $f = 28$ GHz, resulting in $N_{\mathrm{s}}^{\mathrm{RWG}} = 80$ RWG basis functions per element, where λ is the free-space wavelength. Similarly, the base log-periodic element (see [9, Fig. 7]) is discretized in FEKO using a $\lambda/15$ resolution at the excitation frequency of $f = 1$ GHz, resulting in $N_{\mathrm{s}}^{\mathrm{RWG}} = 4260$ RWG basis functions per element.

In the next step, FEKO is used to generate the moment matrices and excitation vectors for the bow-tie and log-periodic array problems, as well as the infinite-array solution for the bow-tie element unit-cell problem with a specified squint angle of $\theta_{\mathrm{s}} = \phi_{\mathrm{s}} = 0^{\circ}$. Both arrays are uniformly excited using a gap voltage source model in FEKO with unit-magnitude and zero-phase excitation settings. However, note that the proposed CBFM algorithm also supports alternative internal excitation configurations, including scanned excitations, as well as external excitation via incoming plane waves, which are not considered in the analysis in this paper. The array matrices and excitation vectors generated in FEKO are then used to construct the CBFM-based reduced-order system through (4) to (6), as well as to define localized subarray problems for extracting subarray-based CBFs for both array problems, as detailed in section II part C.3. The subarray problems associated with the edge and corner elements of the bow-tie antenna array are solved using the MoM due to their relatively small sizes in terms of the number of DoFs. In contrast, the subarray problems associated with the elements of the log-periodic array are solved using localized CBFM formulations to demonstrate the runtime advantages of the proposed two-level CBFM approach.

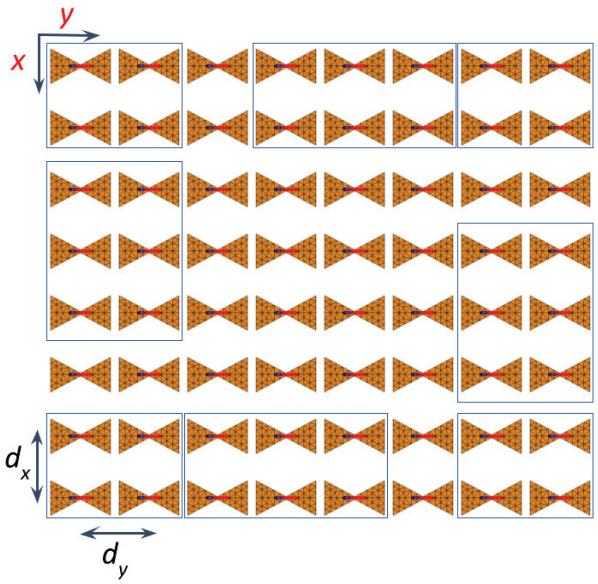

Fig. 1. Periodic 8×8 array of bow-tie antenna elements (see [9, Fig. 1]) with a spacing of $d_x = d_y = 0.5\lambda$ at the excitation frequency of $f = 28$ GHz. The subarray problems used to calculate the CBFs for the highlighted edge and corner elements are enclosed within rectangles.

The efficacy of the proposed CBFM algorithm is evaluated numerically by assessing its accuracy and computational cost in comparison to FEKO's MoM solver and the domain Green's Function method (DGFM) [91], as presented in section II part C.5. The DGFM is selected for this comparison as a reduced-order solution technique with a (computational) cost-to-performance ratio similar to that of the CBFM, as detailed in [91]. Moreover, its commercial availability

within FEKO has led to its extensive use in the analysis of large-scale antenna arrays across various applications, making it a suitable reference for comparison. To assess the accuracy of our algorithm, we focus on the prediction of both far-field and near-field characteristics, which are typically of interest to array designers, while also evaluating the accuracy of surface current distributions, which provide additional theoretical insights. To quantify the error in the approximation of the solution current for the ith subdomain relative to FEKO's reference MoM-based solution of (1), we define the norm-based relative error percentage for the ith subdomain as follows:

$$\varepsilon_i = \frac{|\tilde{\boldsymbol{I}}_i^{\mathrm{RWG}} - \boldsymbol{I}_i^{\mathrm{RWG}}|_2}{|\boldsymbol{I}_i^{\mathrm{RWG}}|_2} \cdot 100\%, \tag{8}$$

where $\tilde{\boldsymbol{I}}_i^{\mathrm{RWG}}$ and $\boldsymbol{I}_i^{\mathrm{RWG}}$ represent the approximation of the solution and FEKO's reference MoM-based solution vector for the ith subdomain, respectively. Additionally, $\{\cdot\}_2$ denotes the L_2-norm. In the CBFM algorithm, the subdomain solution $\tilde{\boldsymbol{I}}_i^{\mathrm{RWG}}$ is approximated through the CBF expansion in (2).

To ensure an unbiased comparison, both the CBFM and DGFM algorithms were implemented in Julia, a high-performance programming language optimized for scientific computing [92]. The latter algorithm is implemented according to [91]. Additionally, to eliminate any potential impact of differing parallelization paradigms used in FEKO's MoM solver and our Julia-based algorithmic implementations on the runtime of the studied solution methods, all algorithms were executed in a strictly serial manner. Furthermore, all simulations were conducted on an Intel i7-9700K processor running at 3.6 GHz with 32 GB of RAM.

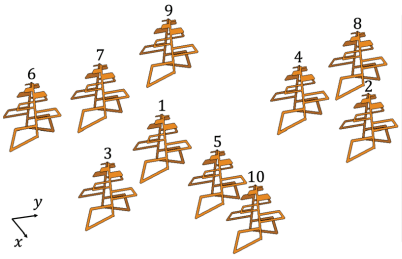

Element	x [m]	y [m]
1	1.229	0.779
2	1.400	1.791
3	1.677	0.282
4	0.932	1.644
5	1.757	0.826
6	0.545	0.291
7	0.506	0.787
8	0.645	2.085
9	0.115	1.332
10	2.247	0.799

Fig. 2. The irregular sparse array of 10 log-periodic antenna elements (see [9, Fig. 7]), excited at the frequency of $f = 1$ GHz, with annotated indices and positions.

5. Numerical results

Before evaluating the accuracy of the CBFM algorithm, we first investigate the efficacy of the solution of a unit-cell element in an infinite, doubly periodic array environment. This infinite-array solution approximation is often used for the rapid estimation of the characteristics of large, truncated-periodic antenna arrays. While the accuracy of this approximation generally improves with increasing array size, its overall reliability remains inherently limited, as it does not rigorously account for MC and truncation effects within a finite array. This is demonstrated in Table 1, which shows the norm-based relative error percentage of the infinite-array solution approximation, calculated for each element of the bow-tie array problem shown in Fig. 1. As expected, the infinite-array solution approach predicts the solution for interior elements with reasonable accuracy; however, its performance progressively degrades toward the edges and corners of the array. At this stage, the CBFM algorithm is introduced, where the infinite-array solution is uniformly assigned as the CBF to each array element. These CBFs are then weighted with their corresponding coefficients obtained by solving the CBFM-based reduced-order matrix equation (3), which significantly improves the accuracy of the infinite-array solution approximation, as demonstrated in Table 2. This improvement can be attributed to the rigorous inclusion of the array MC effects during the construction of the reduced-order matrix system through (4).

Table 1: Norm-based relative error percentage (8), considering the infinite-array solution approximation and MoM-based solution vectors for the elements of the bow-tie antenna array shown in Fig. 1

17.7	22.9	22.4	20.5	20.5	22.4	22.9	17.7
16.7	7.9	5.3	5.6	5.6	5.3	7.9	16.7
14.6	6.9	3.4	2.8	2.8	3.4	6.9	14.7
15.7	7	4	2.3	2.3	4	7	15.7
15.7	7	4	2.3	2.3	4	7	15.7
14.6	6.9	3.4	2.8	2.8	3.4	6.9	14.7
16.7	7.9	5.3	5.6	5.6	5.3	7.9	16.7
17.7	22.9	22.4	20.5	20.5	22.4	22.9	17.7

Nevertheless, in spite of this overall improvement, the error in the final solution remains higher for edge and corner elements in comparison to the interior elements. Note that, when using a single CBF per element, the spatial distributions (profiles) of the element's CBF and its associated final solution are essentially identical, with the difference arising from the applied scaling by a complex weighting coefficient calculated in the presence of array MC effects. Therefore, the inclusion of MC effects via the weighting coefficient only partially counterbalances the error introduced by finite array truncation effects—which cause the largest perturbation in the solution from the assumed infinite-array solution approximation, and consequently the largest error—for edge and corner elements. To improve the solution accuracy

while maintaining a single CBF per element, we employ a hybrid CBF generation strategy, in which the CBFs for edge and corner elements are extracted from the solutions of their respective subarray problems, while the interior elements retain the infinite-array solution as their CBF, as detailed in section II part C.3. The improvement in accuracy in the final CBFM-based solution for edge and corner elements is evident from the error results presented in Table 3. To enable visual comparison of the errors presented in Tables 1 through 3, an identical color scheme has been applied across these tables, mapping the range between the minimum and maximum error values to their corresponding color codes.

Table 2: Norm-based relative error percentage (8), considering the CBFM-based and MoM-based solution vectors for the elements of the bow-tie antenna array shown in Fig. 1. In the CBFM algorithm, each array element is assigned an identical CBF corresponding to the infinite-array solution approximation

7.8	9.4	8.4	8.6	8.6	8.4	9.4	7.9
5.1	3.9	3.8	3.1	3.1	3.8	3.9	5
4.9	4.5	2.9	2.5	2.5	2.9	4.5	4.8
4.6	3.5	3.1	2	2	3.1	3.6	4.6
4.6	3.5	3.1	2	2	3.1	3.6	4.6
4.9	4.5	2.9	2.5	2.5	2.9	4.5	4.8
5.1	3.9	3.8	3.1	3.1	3.8	3.9	5
7.8	9.4	8.4	8.6	8.6	8.4	9.4	7.9

Table 3: Norm-based relative error percentage (8), considering the CBFM-based and MoM-based solution vectors for the elements of the bow-tie antenna array shown in Fig. 1. In the CBFM algorithm, an identical CBF corresponding to the infinite-array solution approximation is assigned to the interior elements, while the CBFs for the edge and corner elements are calculated by solving localized MoM-based subarray problems specific to these elements

2.4	3.6	4	3.5	3.5	4	3.6	2.4
2.9	3.3	3.9	3.2	3.2	3.9	3.3	2.9
2.7	3.6	2.5	2.5	2.5	2.5	3.6	2.7
2.6	2.5	2.8	1.9	1.9	2.8	2.5	2.6
2.6	2.5	2.8	1.9	1.9	2.8	2.5	2.6
2.7	3.6	2.5	2.5	2.5	2.5	3.6	2.7
2.9	3.3	3.9	3.2	3.2	3.9	3.3	2.9
2.4	3.6	4	3.5	3.5	4	3.6	2.4

To assess the performance of the CBFM algorithm with a single CBF per element in relation to the applied CBF generation scheme for the truncated-periodic bow-tie antenna array problem, we compare its near-field and far-field results against FEKO's reference MoM-based solutions. Specifically, we compare the electric near-field results in the observation plane of interest, as shown in Fig. 3, and the far-field (directivity) results in the elevation plane at $\theta = 30^\circ$, as shown in Fig. 4. These results suggest that although the CBFs for edge and corner elements more accurately represent the actual current distribution when a modified CBF generation scheme is used for these elements, the overall impact of this improvement on the accuracy of near- or far-field calculations may be limited in various practical scenarios [3]. Moreover, in many practical applications where the primary focus is on efficiently characterizing antenna array far-field patterns, both versions of the CBFM algorithm might produce similar design outcomes [3]. Nevertheless, the improved solution accuracy for the edge and corner elements, as shown in Table 3, suggests that for observation points closer to the antenna surface, the salutary effects of this improvement will be more noticeable. Finally, the limited accuracy of far-field results based on the infinite-array solution approximation, as displayed in Fig. 4, highlights the importance of integrating the CBFM into the solution algorithm to improve the accuracy in both near- and far-field predictions [3], leading to well-informed design decisions.

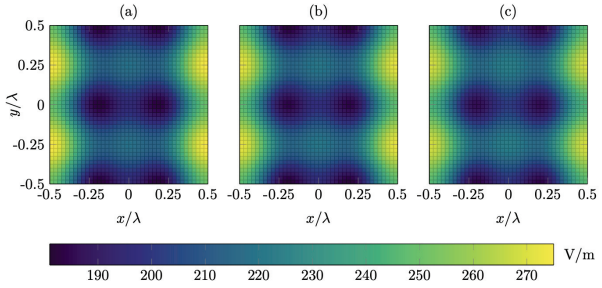

Fig. 3. Surface plots illustrating the E_y-component of the electric near field in the observation plane at $z = 0.25\lambda$, radiated by the uniformly excited bow-tie antenna array shown in Fig. 1, and calculated using: (a) the CBFM solver with an identical CBF corresponding to the infinite-array solution approximation for all array elements [2]; (b) the CBFM solver with an identical CBF for the interior elements and region-specific CBFs for the edge and corner elements [3]; and (c) FEKO's MoM solver.

For the analysis of the ISA of log-periodic antenna elements shown in Fig. 2, the RoI is set to 2.5λ relative to the excitation frequency. Consequently, each subarray defined by this RoI contains between 2 and 4 elements, as summarized in Table 4. In addition, Table 4 compares the norm-based relative error percentage for the CBFs

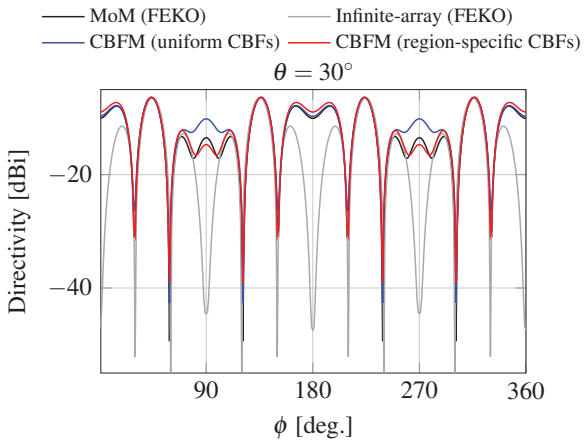

Fig. 4. Directivity plots for the antenna array shown in Fig. 1.

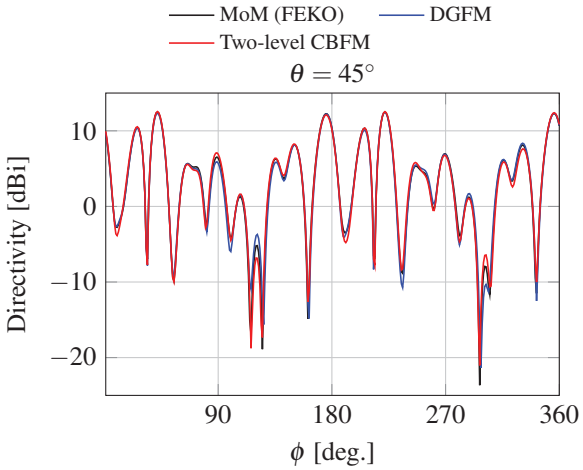

Fig. 5. Directivity plots for the antenna array shown in Fig. 2.

Table 4: Norm-based relative error percentage (8), considering the top-level CBF and final solution vectors of the two-level CBFM algorithm and MoM-based reference solution vectors for the elements of the irregular sparse array of log-periodic antenna elements shown in Fig. 2. The third column shows the error associated with the pth element's CBF, calculated from its corresponding subarray problem of size $M_{\text{sa},p}$ (second column), given the RoI of 2.5λ corresponding to the excitation frequency of $f = 1\,\text{GHz}$, while the last column presents the error associated with the final solution of this algorithm

Element p	$M_{\text{sa},p}$	**CBF Error** (%)	**CBFM Solution Error** (%)
1	4	6.1	6.6
2	2	8.5	7.4
3	3	3.1	3.3
4	3	6.9	5.1
5	4	5.9	6.7
6	2	7.5	5.2
7	4	6.3	5.0
8	2	8.0	6.1
9	2	2.9	2.5
10	2	4.0	2.9

derived from localized subarray-based CBFM formulations and the corresponding final solutions of the two-level CBFM algorithm, demonstrating relatively good accuracy of both representations when compared to the reference MoM-based solution. These results support the hypothesis that, in the two-level CBFM solution process, the shape of the solution for each element can be well approximated during the CBF generation step at the bottom level of this algorithm by considering only the MC interactions within the localized subarray problem associated with that element; while the contributions of elements outside the subarray are effectively accounted for by refining the generated CBFs at the top level using CBFM-based weighting coefficients. The effectiveness of the CBFM algorithm in modeling surface currents translates directly to accurate far-field characterization, as shown in Fig. 5, which compares the directivity results in the $\theta = 45^\circ$ cut plane obtained using our method with the reference results from the DGFM and FEKO's MoM-based solver. The CBFM-based result successfully reproduces the reference complex oscillatory directivity pattern, despite the approximations used in this algorithm [4].

Table 5 presents the computational costs and solution accuracy of the proposed two-level CBFM approach in comparison to DGFM-based and MoM-based reference solutions considering the studied ISA of log-periodic antenna elements. In addition, Table 6 provides an overview of runtime complexities of these solution methods at different stages of the solution process. The computational complexities listed in Table 6 were approximated by considering the total number of scalar multiplications of the most computationally intensive process in each step of the solution process, as detailed in [9].

Several observations can be made based on the results displayed in Table 5: (a) the proposed two-level CBFM approach, leveraging local CBFM formulations, greatly outperforms FEKO's MoM-based reference solver in both runtime and peak memory consumption, achieving an order-of-magnitude improvement in

Table 5: Computational costs and solution accuracy relative to FEKO's MoM-based reference for different solver implementations, considering the 10-element ISA of log-periodic antenna elements shown in Fig. 2 with the RoI 2.5λ relative to the excitation frequency. The second column lists all unique DoFs encountered throughout the solution process, corresponding to the size of the matrix (or matrices) solved using a direct solution method (LU decomposition). For the two-level CBFM with local CBFM formulations, the listed DoFs correspond to: the size of the isolated element matrix, which is decomposed once and then reused to generate the primary and secondary CBFs at the bottom level; the maximum size of the reduced-order matrix across all subarray problems; and the size of the top-level reduced-order matrix, respectively. Runtime values in parentheses indicate the breakdown of the total runtime into the bottom-level CBF generation and the top-level CBFM solution processes. The peak memory requirement is calculated by assuming a double-precision storage scheme, with each complex matrix element stored using 16 bytes of memory

	# DoFs	**Runtime (s)**	**Peak Memory Usage (GB)**	**Error (%)**
CBFM (local MoM)	17040 | 10	838 (825+13)	4.33	5
CBFM (local CBFM)	4260 | 16 | 10	96 (83+13)	0.27	5.21
DGFM	4260	65	0.27	6.33
MoM (FEKO)	42600	2719	27.04	n/a

both metrics while maintaining comparable accuracy in the solution current; (b) replacing CBFM-based local formulations with their MoM-based counterparts significantly increases the overall runtime, without providing substantial improvements in solution accuracy. However, the latter approach still considerably outperforms FEKO's MoM solver in both the runtime and memory usage; (c) compared to the DGFM, our proposed approach achieves slightly improved accuracy, albeit with a slightly larger but competitive runtime. This overhead is likely due to the fact that neither algorithm is fully numerically optimized in Julia. However, the DGFM follows a more straightforward algorithmic implementation routine, potentially leading to faster execution times in the unoptimized implementations of these algorithms. More importantly, the runtime comparison does not fully reflect the theoretical advantages of our CBFM method in terms of numerical efficiency for many practical antenna array problems, as evidenced in Table 6. A key disadvantage of the DGFM in this context is its reliance on solving the active impedance matrix for each element independently using a direct

Table 6: Overview of approximated runtime complexities for different solver implementations. Here, the symbol "#" denotes the number of instances of different processes, while $\mathcal{O}(\cdot)$ represents their corresponding computational complexity. The variables are defined as follows: M is the number of subdomains; $\overline{M}_{\text{sa}}$ is the average subarray size; $N_{\text{s}}^{\text{RWG}}$ and N^{RWG} represent the sizes of the MoM-based subdomain and array matrices, respectively. In the bottom-level CBFM algorithm, we assign a single primary CBF and a set of secondary CBFs to each subarray element, while retaining all CBFs following their orthogonalization via the SVD algorithm. Consequently, the total average number of CBFs per subarray element corresponds to the average subarray size $\overline{M}_{\text{sa}}$. In deriving the runtime of generating the secondary CBFs, we use the following approximation: $\overline{M}_{\text{sa}} \cdot (\overline{M}_{\text{sa}} - 1) \approx \overline{M}_{\text{sa}}^2$. Furthermore, assuming that $N_{\text{s}}^{\text{RWG}} \gg \overline{M}_{\text{sa}}$, as is typically the case for geometrically large and complex antenna elements, the runtime complexity of the classical Golub-Reinsch SVD algorithm applied to the CBFs of each subarray element can be approximated as $\mathcal{O}((2N_{\text{s}}^{\text{RWG}})^2 \cdot \overline{M}_{\text{sa}})$ (see [94, Fig. 8.6.1]). In addition, note that for arrays composed of identical antenna elements, the generation of primary CBFs in the proposed CBFM algorithm requires only a single instance, as the base element matrix needs to be solved only once

	MoM	**DGFM** [91]		**Proposed Two-Level CBFM Algorithm**	
		#	$\mathcal{O}(\cdot)$	#	$\mathcal{O}(\cdot)$
MoM Matrix Generation	$\left(N^{\text{RWG}}\right)^2$	1	$\left(N^{\text{RWG}}\right)^2$	1	$\left(N^{\text{RWG}}\right)^2$
Generation of Primary CBFs	n/a	n/a	n/a	1	$\left(N_{\text{s}}^{\text{RWG}}\right)^3$
Generation of Secondary CBFs	n/a	n/a	n/a	M	$\left(N_{\text{s}}^{\text{RWG}} \cdot \overline{M}_{\text{sa}}\right)^2$
SVD Ortho-gonalization	n/a	n/a	n/a	M	$\left(2 \cdot N_{\text{s}}^{\text{RWG}} \cdot \overline{M}_{\text{sa}}\right)^2$
Bottom-Level CBFM Systems Setup	n/a	n/a	n/a	M	$\left(N_{\text{s}}^{\text{RWG}} \cdot \overline{M}_{\text{sa}}\right)^2 \cdot \overline{M}_{\text{sa}}$
Bottom-Level CBFM Systems Solution	n/a	n/a	n/a	M	$\left(\overline{M}_{\text{sa}} \cdot \overline{M}_{\text{sa}}\right)^3$
Top-Level CBFM System Setup	n/a	n/a	n/a	1	$\left(N^{\text{RWG}}\right)^2$
Top-Level CBFM System Solution	n/a	n/a	n/a	1	M^3
DGFM Solution	n/a	M	$\left(N_{\text{s}}^{\text{RWG}}\right)^3$	n/a	n/a
MoM Matrix Solution	$\left(N^{\text{RWG}}\right)^3$	n/a	n/a	n/a	n/a

solution method. The cumulative computational cost of this process is typically higher than that of dealing with the reduced-order systems at both levels of our CBFM algorithm. Note that in our method, the runtime is typically dominated by the construction of the reduced-order systems, while the additional solution overhead is often negligible for many practical array problems, as is evident from Table 5. In addition, a key advantage of our approach over the DGFM is its ability to systematically enhance solution accuracy. This can be achieved by increasing the RoI to define larger subarray problems or by incorporating higher-order CBFs at the bottom level to more effectively capture interelement coupling effects, leading to improved solution fidelity, whereas the standard DGFM formulation lacks this flexibility.

Note that the size of the studied array example is not constrained by the computational complexity of our method, which significantly improves upon those of MoM- and DGFM-based solvers, as demonstrated in Tables 5 and 6. Instead, the maximal array size is limited by the use of FEKO's full-rank array matrix, which exceeds the RAM capacity of standard desktop machines even for moderately sized log-periodic antenna arrays. Meanwhile, the numerical efficiency of our proposed two-level CBFM algorithm suggests that significantly larger arrays can be analyzed using our method, even on standard machines, such as the ISA composed of 2048 log-periodic antenna elements shown in [45, Fig. 5]. However, achieving this would require applying a matrix compression scheme, such as the adaptive cross approximation (ACA) algorithm [93], to significantly reduce the effective size of the moment matrix. This could be implemented in two ways: first, by precalculating and storing the compressed moment matrix for the entire antenna array at the initial step of the two-level CBFM algorithm, allowing its submatrices to be reused throughout different stages of this algorithm; or alternatively, by dynamically recalculating the intra- or interelement coupling submatrices on demand, rather than storing them in advance. This represents a trade-off between runtime and memory consumption, where the first approach minimizes runtime by avoiding repeated calculations of the coupling submatrices at the cost of increased memory consumption. In contrast, the second approach reduces the memory usage by storing only small-sized compressed submatrices instead of the full array matrix, enabling the simulation of larger arrays on machines with fixed RAM capacity, albeit at the expense of increased runtime due to repeated calculations of the same submatrices. Nevertheless, when using the first approach and excluding matrix generation times from the analysis—since this matrix is required for all methods considered—the complexities listed in Table 6 suggest that for elements with a larger number of DoFs per element and larger array sizes, the runtime advantages of our method become more pronounced due to its favorable scaling. Finally, the proposed two-level CBFM approach is fully parallelizable, allowing for its numerically efficient implementation on multi-threaded CPUs and GPUs.

6. Future work and concluding remarks

As part of the future work, in addition to applying the matrix compression scheme to further reduce the computational requirements of the proposed two-level CBFM formulation, we will extend the analysis of this method to antenna arrays above an infinite ground plane. Since the impact of the ground plane is embedded into the calculation of the full or compressed array moment matrix, the proposed method can be applied in its present form. In addition, we will investigate the potential integration of the overlapping subarray strategy detailed in [75] into our algorithm to efficiently account for the coupling effects from array elements just outside the specified RoI. This would enhance the accuracy of the single-CBF representation for each element in the CBFM algorithm. The use of an overlapping subarray strategy to generate subarray CBFs with improved accuracy—or alternatively, a different approach, such as employing higher-order CBFs beyond secondary—may be particularly important when analyzing array problems with connected subdomains, where the current CBF generation scheme may not effectively capture strong MC effects between subdomains. Furthermore, to extend the applicability of this method to printed antenna array problems on multilayered substrates, we will investigate its integration with the equivalent medium approach (EMA), as detailed in section II part D, or alternatively, by embedding substrate effects directly during the construction of the MoM matrix. The former approach seamlessly integrates into our method with negligible computational overhead but may not fully capture exact field interactions across layers, surface wave modes, or material inhomogeneities, particularly in antenna arrays with relatively thick substrates. Conversely, the explicit use of a multilayered Green's Function generally improves accuracy; however, this improvement comes at the expense of significantly increased computational cost, an effect that becomes particularly pronounced at millimeter-wave frequencies, such as in 5G/6G system applications, as detailed in section II part D. Moreover, an iterative formulation of this algorithm, inspired by [9], will be explored to improve solution accuracy in applications with high-precision requirements.

In this section, we presented a novel two-level formulation of the CBFM algorithm for efficient analysis

of large-scale antenna arrays. In this approach, local CBFM formulations generate a single CBF per element at the top level. Our results demonstrate that this method achieves over an order-of-magnitude improvement in both memory efficiency and runtime compared to MoM. Furthermore, it ensures reliable accuracy not only in the antenna far field—typically the primary concern for array designers—but also in the near field, establishing the proposed two-level CBFM algorithm as a powerful and highly efficient alternative for analyzing large, complex antenna arrays.

D. Toward a numerically efficient CBFM implementation for mm-wave problems

While the previous section focused on the CBFM with a single basis per element and outlined future research directions within that framework, a broader paradigm shift is necessary to enhance the effectiveness of the general CBFM framework in addressing the challenges of modern antenna analysis and design. One of the primary challenges today is the growing demand for efficient electromagnetic simulations at millimeter-wave (mm-wave) frequencies and beyond, particularly in the context of 5G/6G communication systems, as discussed in section II of [1]. The shift to higher operating frequencies, coupled with fixed space constraints in electronic devices, has significantly increased the electrical sizes of antennas and circuit modules, introducing new challenges for their effective EM simulation in the mm-wave region. A major challenge in this context concerns the numerically efficient calculation of Green's Functions, which are essential for MoM-based analysis of antennas and circuits printed on layered media [95]. Herein, the Sommerfeld integrals used in the calculation of Green's functions can become highly oscillatory and slowly decaying, reducing solution accuracy while increasing the runtime [95].

In section II of [1], an efficient numerical strategy for evaluating the Sommerfeld integrals in layered media problems is discussed, as recently proposed in [95]. This approach employs a strategic interpolation and extrapolation scheme to minimize the number of sample points needed to accurately represent the integrand, enabling analytical integration which in turn significantly accelerates the calculation of Green's functions [95]. In contrast, section III of [1] presents a novel strategy for the numerical modeling of planar circuits and antennas printed on layered media, which completely eliminates the need for constructing the layered-medium Green's Function in the MoM. This strategy utilizes the EMA to replace the original layered geometries with equivalent geometries embedded in an infinite homogeneous medium, characterized by the corresponding effective dielectric constant. By replacing the original geometry with the equivalent one, the problem that originally required using a volumetric MoM formulation can instead be effectively addressed using a surface formulation based on Green's Function in a homogeneous medium, significantly improving the computational efficiency of the solution process.

In addition to its integration with the EMA, we highlight a promising research direction for improving the numerical efficiency of the CBFM algorithm by formulating it based on quadrilateral surface discretization (see [96, Fig. 3]) with piecewise sinusoidal (PS) basis functions between pairs of quadrilateral elements, as in [28], instead of using conventional triangular meshing with RWG basis functions. The three key benefits of using quadrilateral discretization with PS basis functions are: (a) the reduced number of basis functions compared to the number of RWG basis functions for identical patch and mesh sizes, combined with the more favorable scaling with domain size, as demonstrated in Fig. 6; (b) the ability to efficiently generate matrix elements by testing observation basis functions against the scattered fields from sinusoidal current filaments or sheets corresponding to source basis functions, which are available in closed form (see [28] and references therein). This eliminates the need for evaluating computationally intensive numerical integrals when generating these elements in conventional MoM algorithms that use triangular discretization with RWG basis functions; and (c) the ability to reuse previously calculated matrix elements for equivalent pairs of basis functions, leveraging the inherent geometric regularity and repeatability of the structured mesh. Note that quadrilateral and triangular meshes can be hybridized to model arbitrary planar geometries, such as the bow-tie antenna array shown in Fig. 1, with the former used in interior regions and the latter conforming to the geometry's edges.

To fully leverage the computational advantages of quadrilateral mesh discretization with PS basis functions, the EMA, and the CBFM, a hybrid approach is being developed in our group that integrates these methods. This approach utilizes the EMA to eliminate the direct computation of Green's Functions for antenna arrays printed on layered media, the quadrilateral MoM with PS basis functions to efficiently generate the array moment matrix, and the CBFM to accelerate the solution process. Initial results from this study will be presented in future work.

III. LCPML-LOG: A PARAMETER-FREE PERFECTLY MATCHED LAYER METHOD FOR FINITE METHODS

In this section, we introduce the LCPML-log method, an advanced Locally-Conformal Perfectly Matched Layer (LCPML) technique optimized for addressing mesh truncation challenges in solving

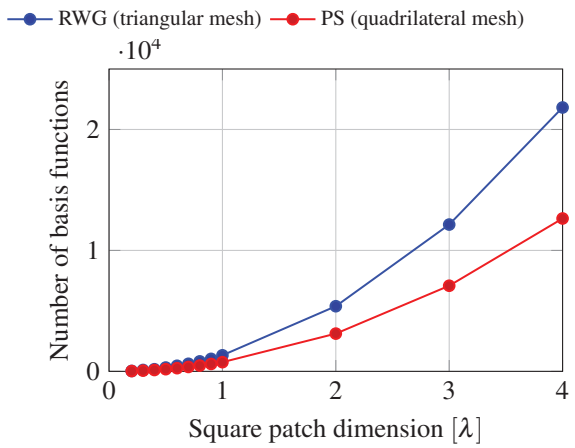

Fig. 6. Comparison of the number of RWG basis functions for triangular discretization in FEKO versus the number of PS basis functions for quadrilateral discretization of a square patch with varying dimensions, using a $\lambda/20$ mesh size.

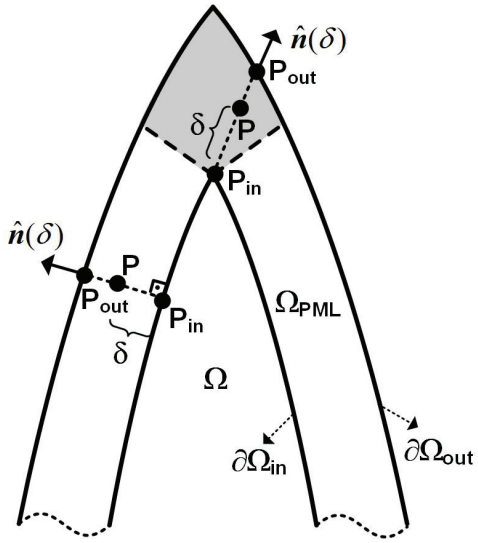

Fig. 7. Illustration of the LCPML-log method.

electromagnetic radiation and scattering problems using the FEM. LCPML-log is distinguished by (a) achieving optimal PML performance without requiring parameter tuning and (b) yielding superior results even with a minimal, single-layer PML configuration. This approach represents a significant advancement in both cost-effectiveness and robustness in PML technology.

In computational electromagnetics, the PML is essential for simulating open-region electromagnetic wave problems, providing an artificial boundary that absorbs outgoing waves with minimal reflection. Traditional PML approaches, developed in the 1990s, laid the foundation for this technology but often struggle with arbitrary geometries and require complex parameter adjustments [97–102]. The Locally-Conformal PML, introduced by Ozgun and Kuzuoglu in 2007 [103], [104], revolutionized the field by offering a more flexible, geometry-agnostic solution.

Recently, Ozgun and Kuzuoglu have developed a variant of the LCPML method, named LCPML-log, which utilizes a logarithmic decay function in its coordinate transformation [105, 106]. Unlike its predecessor, LCPML-log modifies the matrix formation phase of the FEM, embedding the logarithmic function directly into the core of the computational process, rather than simply substituting real coordinates with complex ones. While this method may require a more intricate implementation, it offers clear benefits: enhanced performance without the need for prior parameter adjustments and increased accuracy with a single PML layer. This efficiency leads to a significant reduction in computational resources, making LCPML-log a breakthrough for large-scale simulations.

Initially developed for 2D electromagnetic problems governed by the scalar Helmholtz equation [105], LCPML-log was subsequently extended to address 3D problems involving the vector wave equation [106]. This section provides a brief overview of the LCPML-log method, supplemented with examples that demonstrate its effectiveness and practicality.

A. Mathematical formulation

The LCPML-log method constructs a PML region Ω_{PML} that conforms to an arbitrary region (Ω), designed to enclose the sources or objects of interest within the smallest possible convex set. As shown in Fig. 7, the PML region is defined by its inner and outer boundaries ($\partial\Omega_{\text{in}}$ and $\partial\Omega_{\text{out}}$). Each point $\mathbf{r} \in \Re^3$ in the PML region is mapped to a complex coordinate $\tilde{\mathbf{r}} \in \mathbb{C}^3$ through the following transformation, assuming time-harmonic fields of the form $\exp(j\omega t)$:

$$\tilde{\mathbf{r}} = \mathbf{r} + (jk)^{-1} f(\delta)\,\hat{\mathbf{n}}(\delta), \tag{9}$$

where $f(\delta)$ is the decay or attenuation function, which is a monotonically increasing function of the decay parameter $\delta = \|\mathbf{r}-\mathbf{r}_{\text{in}}\|/\|\mathbf{r}_{\text{out}}-\mathbf{r}_{\text{in}}\|$ confined within $(0,1)$. The unit vector $\hat{\mathbf{n}}(\delta) = (\mathbf{r}-\mathbf{r}_{\text{in}})/\|\mathbf{r}-\mathbf{r}_{\text{in}}\|$ indicates the direction of decrease within the PML region. The position vectors $\mathbf{r}$, $\mathbf{r}_{\text{in}}$, and $\mathbf{r}_{\text{out}}$ correspond to points within Ω_{PML}, $\partial\Omega_{\text{in}}$, and $\partial\Omega_{\text{out}}$, respectively, while k denotes the wavenumber, and the Euclidean norm is used for magnitude calculations. The most critical component in this transformation is the decay function $f(\delta)$, which drives the transformation and is defined as follows:

$$f(\delta) = -\log(1-\delta), \tag{10}$$

In developing the FEM formulation, we start by deriving the weak variational form of the wave equation via the weighted residual method. The computa-

tional domain is then discretized into a mesh of elements—triangular in 2D and tetrahedral in 3D—over which the weak form is solved. The integration necessary for the weak form is simplified by mapping the original domain to a master element (ξ,η,ζ), using isoparametric mapping. The coordinates within this master element are expressed using the same shape functions as those for the unknown field variables, facilitated by a Jacobian matrix.

LCPML-log's uniqueness lies in its handling of the Jacobian matrix. The process involves two successive transformations: $(\xi,\eta,\zeta) \rightarrow (x,y,z) \rightarrow (\tilde{x},\tilde{y},\tilde{z})$. The complex coordinates, now composite functions, are mapped through these stages, i.e., $\tilde{x}(x,y,z) = \tilde{x}\Big(x(\xi,\eta,\zeta), y(\xi,\eta,\zeta), z(\xi,\eta,\zeta)\Big)$. Here, for example, $x(\xi,\eta,\zeta)$ is expressed as a combination of the shape functions and real coordinates: $x(\xi,\eta,\zeta) = \sum_{j=1}^{n^e} N_j(\xi,\eta,\zeta)x_j$, where x_j is the real coordinate of the j-th node, N_j is the j-th shape function, and n^e is the number of nodes in an element. Here, $\mathbf{J} = \mathbf{J}_m\mathbf{J}_c$ represents the Jacobian matrix, where $\mathbf{J}_m = \partial(x,y,z)/\partial(\xi,\eta,\zeta)$ pertains to the standard FEM transformation and $\mathbf{J}_c = \partial(\tilde{x},\tilde{y},\tilde{z})/\partial(x,y,z)$ captures the logarithmic transformation unique to LCPML-log.

The entries of $\mathbf{J}_c$ are given in (11), where α, β, and γ represent the directional components of the unit vector $\hat{\mathbf{n}}$. Partial derivatives such as $f_x = \partial f/\partial x$ are computed analytically, when possible, or numerically by using the functional dependence of boundary points. For numerical computation, central differencing formulas can be applied. The boundary points on the PML boundaries are determined by employing the Lagrange multiplier method, as detailed in [105] and [106].

$$\mathbf{J}_c = \begin{bmatrix} (jk)^{-1}(\alpha f_x + f\alpha_x)+1 & (jk)^{-1}(\beta f_x + f\beta_x) & (jk)^{-1}(\gamma f_x + f\gamma_x) \\ (jk)^{-1}(\alpha f_y + f\alpha_y) & (jk)^{-1}(\beta f_y + f\beta_y)+1 & (jk)^{-1}(\gamma f_y + f\gamma_y) \\ (jk)^{-1}(\alpha f_z + f\alpha_z) & (jk)^{-1}(\beta f_z + f\beta_z) & (jk)^{-1}(\gamma f_z + f\gamma_z)+1 \end{bmatrix}. \tag{11}$$

B. Numerical results

To demonstrate the performance of the LCPML-log method, we first consider the problem of constructing the free-space Green's Function for the Helmholtz equation within a given domain. Specifically, we examine a scenario where a line source located at (0.2 m, 0) radiates within a circular region of radius $a = 1$ m, as depicted in Fig. 8. The mean-square error (MSE), which compares the computed and analytical field values, is plotted as a function of the number of PML layers for different wavelength (λ) values. We observe that the LCPML-log method outperforms the original LCPML method, particularly when using a single PML layer. As evident from the vertical axis (MSE values), even with a single layer, the LCPML-log method achieves significantly low error levels across different frequencies and mesh resolutions. This indicates that increasing the number of PML layers beyond a certain point does not necessarily provide a substantial accuracy improvement, as the error is already minimized at very low levels. Moreover, many applications require broadband frequency sweeps using the same mesh, which poses challenges in both computational cost and accuracy. The LCPML-log method, as demonstrated by the almost flat nature of the error curves, remains robust and nearly independent of frequency even with a relatively coarse mesh. This stability further supports the argument that a large number of PML layers is not essential, as the method maintains low error levels across a wide frequency range with minimal computational effort.

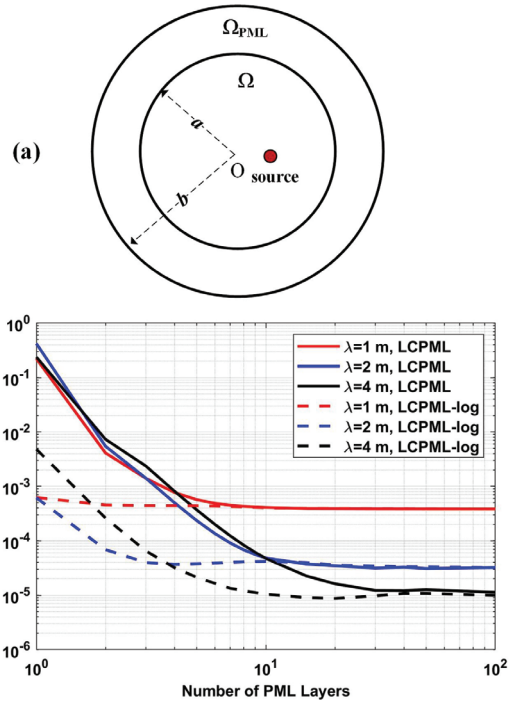

Fig. 8. A line source radiating in a circular PML region. (a) Geometry, (b) plot of mean-square error (MSE) vs. number of PML layers. (*Axes are logarithmic.*)

Next, we examine a scattering problem involving a conducting 'golden' ellipsoid, where the ratio of the semi-major axis to the semi-minor axis is approximately

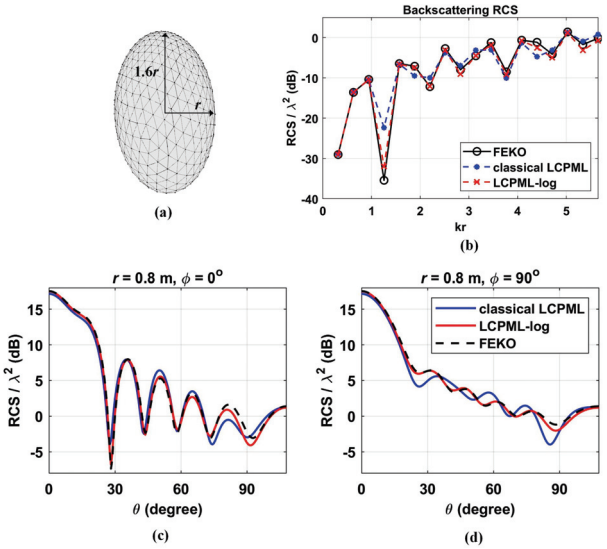

Fig. 9. Golden ellipsoidal PML. (a) Geometry, (b) backscattering RCS, (c) bistatic RCS profile at $\phi = 0^\circ$ plane, (d) bistatic RCS profile at $\phi = 90^\circ$ plane.

the golden ratio (i.e., 1.6) (see Fig. 9). The object is illuminated by an x-polarized plane wave propagating along the z-axis, with a conformal PML applied around its spherical boundary. The wavenumber k is 2π, corresponding to a wavelength λ of 1 m. The computational setup includes a cell size of $\lambda/20$ and a separation of $\lambda/2$ between the inner PML boundary and the object. A single PML layer with a thickness of $\lambda/20$ is employed. The radar cross-section (RCS) values obtained using the LCPML method, optimized for best performance, are compared in Fig. 9 with those from the LCPML-log method, which requires no parameter tuning. The results are also compared with those obtained using the commercial electromagnetic solver FEKO. The results clearly demonstrate that LCPML-log performs well even with a single PML layer and without the need for parameter adjustments.

IV. GPU ACCELERATION OF MOM AND FDTD

In this section, we briefly discuss the GPU acceleration of MoM and, separately, the FDTD algorithm. GPU Acceleration of CEM codes [107] is currently a very popular topic, and we have included brief writeups in this work for the sake of completeness. For additional details, the reader is encouraged to refer to select publications on this topic that have been cited herein.

The Graphics Processing Unit (GPU) is a highly parallelized stream processor, originally designed for image processing, where it executes parallel operations on all pixels simultaneously. Consequently, GPUs are optimized for handling large-scale data that is uniform in type and exhibits minimal interdependency. Due to differing design objectives, the architecture of GPUs significantly contrasts with that of Central Processing Units (CPUs). As illustrated in Fig. 10, the CPU architecture comprises key components such as a controller (which orchestrates the operation of various units), an arithmetic logic unit (which performs data processing), registers, cache, and data/control/status buses. The CPU's functions include program control (regulating the order of instruction execution), operation control (managing the execution of instructions), timing control (coordinating the timing of operations), and data processing (performing arithmetic and logical calculations). In essence, the CPU manages the temporal and spatial control of instruction and data flow. It is particularly adept at handling complex operations like distributed tasks and coordinated control, making it highly versatile.

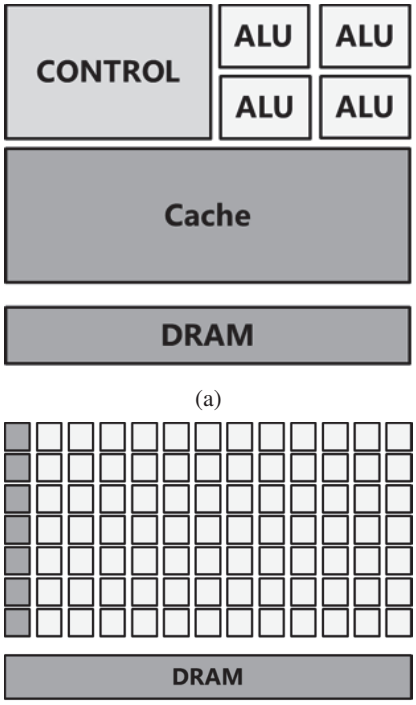

Fig. 10. Comparison between GPU and CPU architectures

In contrast, GPUs consist of numerous processing units and feature long pipelines, but the design of their logical units is relatively simple. The number of cores in a GPU far exceeds that of a CPU, allowing the same instruction to be dispatched to multiple cores to process different data simultaneously. This architecture makes GPUs particularly well-suited for tackling computationally intensive tasks.

General-purpose computing on GPUs (GPGPU) refers to using graphics cards for general-purpose computations beyond rendering graphics. In recent years, the computational speed of GPU units has increased dramatically and, in some applications, GPUs have significantly outperformed CPUs. This has led to the emergence of a new research field: GPGPU, which focuses on utilizing GPUs for a broader range of computational tasks beyond traditional graphics processing.

A. GPU acceleration of MoM

Operation of 5G mobile devices at millimeter-wave frequencies (e.g., 30 GHz) introduces substantial complexity, leading to significantly increased problem sizes compared to sub-5 GHz operation. This imposes a significant computational burden, since it demands extensive CPU time and memory resources for electromagnetic analysis. To effectively mitigate these challenges, we propose and implement several acceleration techniques: geometry simplification, numerical reduction of degrees of freedom, and GPU-based parallel processing. Primary memory reduction is achieved via the CBFM, an efficient iteration-free technique for compressing basis functions [7]. CBFM has been extensively applied and investigated, including for the analysis of structures embedded in multilayered media [108].

These acceleration techniques are illustrated by using the geometry of a mobile device, comprising a metallic frame and an antenna mounted on a layered substrate (see Figs. 11 and 12). The initial step involves geometrical simplification without compromising the device's electrical characteristics. This measure yields a significant reduction in the number of degrees of freedom, from 99738 down to 1892 unknowns at 30 GHz. Subsequently, the CBFM formulation, originally developed for scattering analysis, is adapted for layered media antenna applications by employing two distinct types of excitations—Edge Port(EP) and Dipole Moment (DM)—to generate the CBFs for the antenna structure [109]. Compared to conventional MoM, CBFM inherently reduces the dimension of the system matrix. This reduction is achieved irrespective of the excitation type, and our study indicates that the performance of the EP excitation is superior. This is because EP and DM excitations incorporate near-field components, including content related to the 'invisible' spectrum (evanescent waves) that are typically absent in traditional plane wave excitations, and this, in turn, enhances the accuracy of the representation. The impedance matrix, $\mathbf{Z}$, computed via MoM, is utilized to construct the CBFs. GPU acceleration significantly expedites this process by parallelizing the computationally intensive filling of the MoM matrix. The MoM mesh and geometrical data are initially transferred to GPU global memory. The rows of the MoM impedance matrix are then computed in serial batches. Within each batch, the matrix elements are calculated in parallel on the GPU, with each element computation assigned to a dedicated GPU thread. Upon completion of a batch computation, the elements are copied back from the GPU global memory to CPU host memory for subsequent use in solving the MoM linear system. To mitigate the overhead associated with GPU-CPU data transfer initialization, a large GPU batch size is selected to maximize the utilization of the global memory. Numerical results confirm that leveraging GPU parallel processing substantially reduces fill time of the MoM matrix.

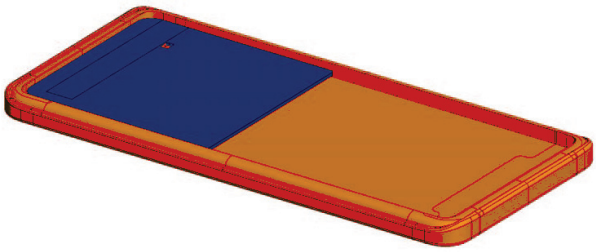

Fig. 11. Cellphone model.

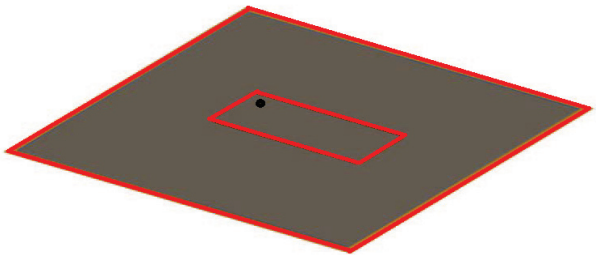

Fig. 12. Simplified full-size cellphone.

Future development of the GPU-accelerated CBFM scheme will involve defining GPU batches based on the MoM interactions required for generating a set of CBFs, rather than simply grouping a fixed number of MoM matrix rows. Following GPU processing of a batch, the MoM elements relevant to CBF construction will be copied back to the CPU host, where the SVD for forming the CBFs will be performed.

1. CBFM for microwave circuit and antenna problems

Based on the mixed-potential integral equation (MPIE), CBFs are constructed by using a set of low-level basis functions, specifically the Rao-Wilton-Glisson (RWG) functions. For each CBF level l, the corresponding reduced matrix equation is formulated as:

$$[Z^l]_{\sum_i^{B_l} K_{l,i} \times \sum_i^{B_l} K_{l,i}} [I^l(\theta,\phi)]_{\sum_i^{B_l} K_{l,i} \times 1} = [V^l(\theta,\phi)]_{\sum_i^{B_l} K_{l,i} \times 1}, \quad (12)$$

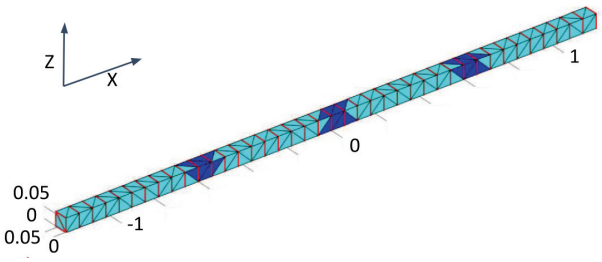

Fig. 13. Edge ports on a dipole.

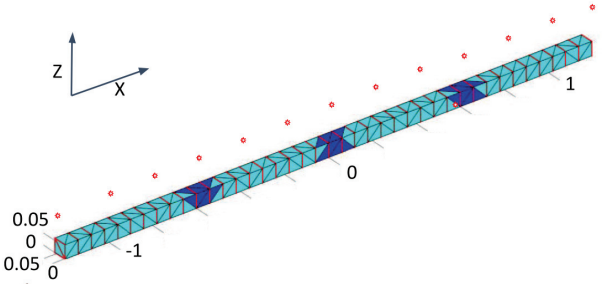

Fig. 14. Dipole moments above a dipole.

where Z^l, I^l, and V^l represent the l-level reduced impedance matrix, the vector of current distribution coefficients, and the excitation vector, respectively. It is noteworthy that for $l = 0$, this formulation reduces to the original MoM system matrix equation.

To effectively adapt CBFM for millimeter-wave circuit and antenna problems, we utilize EPs defined on the surface of the analyzed structure (see Fig. 13). This approach is the natural choice for constructing the excitation vector in antenna problems, providing a direct interface to circuit ports, in contrast to plane wave excitations used in scattering analysis. As an illustrative example, the dipole geometry is partitioned into four blocks; the dark blue faces in the figure delineate the extended region used in the CBFM construction, while the red lines indicate the EPs oriented along the x-axis. Furthermore, in an antenna application employing a single delta-gap source for excitation, this source—implemented as an EP—must be included as one of the contributions to the excitation vector.

An alternative excitation strategy employs sources that are neither solely far-field (e.g., a plane wave) nor located exclusively on the object's body (e.g., an EP, as illustrated in Fig. 14). In this method, equivalent dipole moments positioned in the vicinity of the object are selected as sources to generate the excitation matrix. This inherently ensures the inclusion of both near-field (evanescent) and far-field (propagating) information, which is crucial for accurate CBF construction.

2. Numerical results

We now present some numerical results demonstrating the accuracy and efficiency of applying CBFM to antenna problems, along with the effectiveness of GPU acceleration. The first example analyzes a Perfect Electric Conductor (PEC) dipole in free space (see Fig. 15). For the CBFM implementation, the dipole geometry is partitioned into four blocks along its longitudinal axis, and a delta gap port is utilized for excitation at the center. The analysis is performed across a frequency range from 300 MHz to 700 MHz, with a step size of 50 MHz. The antenna structure is discretized by using 324 triangular elements, with element lengths approximately 0.1 wavelengths at 500 MHz. For constructing the CBFs, an extension region equivalent to 0.1 wavelengths at 500 MHz is employed. The computed input impedance (Z_{11}) is plotted in Fig. 16, using results obtained from the conventional MoM as a reference for validation. Table 7 summarizes the SVD down-selection thresholds, as well as the number of samples and unknowns characterizing the reduced matrices for different excitation types: EP denotes edge-port, PW denotes plane-wave, and DM denotes dipole-moment excitation.

Our second numerical example analyzes a Perfect Electric Conductor (PEC) cross situated on the interface of a layered medium (see Fig. 17). This case is specifically employed to illustrate the computational acceleration achieved using GPU processing. The cross

Fig. 15. PEC dipole.

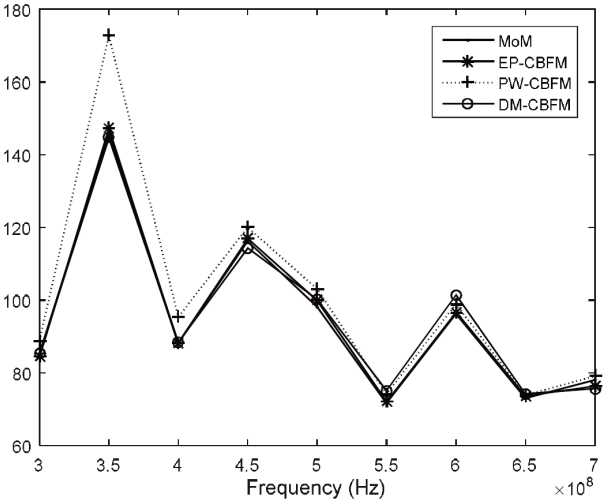

Fig. 16. Z11 of example 11 obtained by using CBFM.

Table 7: Parameters and results of example 11

Method	Threshold	Samples	Unknowns	
			Min.	Max.
EP-CBFM	0	96	96	96
PW-CBFM	1e-3	400	110	184
DM-CBFM	0	120	120	120
MoM	0	0	486	486

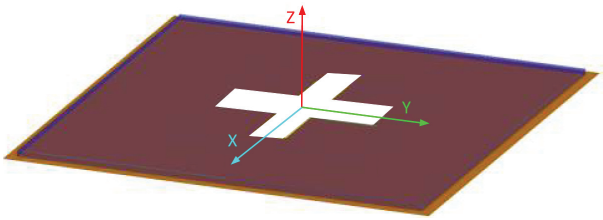

Fig. 17. PEC cross embedded in layered medium.

consists of arms measuring 10 wavelengths in length and 2 wavelengths in width. The layered medium is backed by a PEC plane. The analysis is conducted at 30 GHz, involving a total of 12085 unknowns. Table 8 presents the matrix fill-time, which clearly demonstrates significant computational acceleration when utilizing the GPU. The hardware platform used for this comparison included an Nvidia GTX860M GPU and an Intel I7-4710HQ CPU. The system was equipped with 8 GB of host memory. For comparative purposes, the CPU-based numerical results were obtained using commercial electromagnetic simulation software.

Specifically, the GPU acceleration process [110, 111] is organized as follows:

- All geometrical and material data required for MoM computations are first transferred to GPU global memory.
- The impedance matrix is computed in batches of rows. Each batch is processed serially, while the elements within a batch are computed in parallel on the GPU. Each thread handles one matrix element (i.e., a source-observer pair).
- After completing each batch, the results are copied back from GPU global memory to CPU memory. This approach is designed to balance GPU memory usage and data transfer overhead. To reduce the latency of memory transfers, the batch size is chosen to maximize the occupancy of GPU global memory.
- The MoM impedance matrix computed in this way is subsequently used to form the reduced-order system in the CBFM framework.

Table 8: Time used for matrix filling on different platforms

Platform	Matrix filling time (minutes)
GPU	0.7
1 CPU-Core	26.6
2 CPU-Core	20.0
4 CPU-Core	24.0
6 CPU-Core	26.4
8 CPU-Core	26.5

- In our current workflow, SVD is performed on the CPU after GPU-based computation of the MoM matrix elements.

Additional detail on GPU acceleration may be found in [112–116].

B. GPU acceleration of FDTD

Since its inception, the FDTD method has developed into a mature and comprehensive numerical computation technique. Its straightforward and intuitive implementation, combined with its applicability to various computational models, has led to its widespread use and recognition as one of the fundamental methods in computational electromagnetics. However, due to the effects of numerical dispersion and stability, as well as the limitations of CPU floating-point performance, single-CPU implementations of the FDTD method can only handle the simulation and analysis of electrically small problems. These simulations may take several hours or even days to complete, and the simulation of electrically large targets presents even greater challenges. When applied to large-scale electromagnetic simulations, the FDTD method requires extensive memory and computing time.

To address these limitations, researchers have extensively explored several approaches, including higher-order FDTD methods, time-domain multiresolution analysis, and parallel FDTD algorithms. Among these, parallel FDTD, combining the computational power of parallel processing with the simplicity and clarity of the FDTD method, has gained prominence, particularly with the rapid advancement of GPGPU [117–120].

The workflow of the GPU-accelerated parallel FDTD algorithm is shown in Fig. 18. In this approach, the GPU acts as a coprocessor, working in tandem with the CPU. The program flow is divided into two parts: the host (CPU) part and the device (GPU) part, as depicted in Fig. 18. The right side of Fig. 18 represents the device section, which is executed by the GPU, while the left side shows the host section, managed by the CPU. The CPU primarily handles tasks such as memory allocation, field initialization, and time advancement of the simulation. The GPU is responsible for computationally intensive

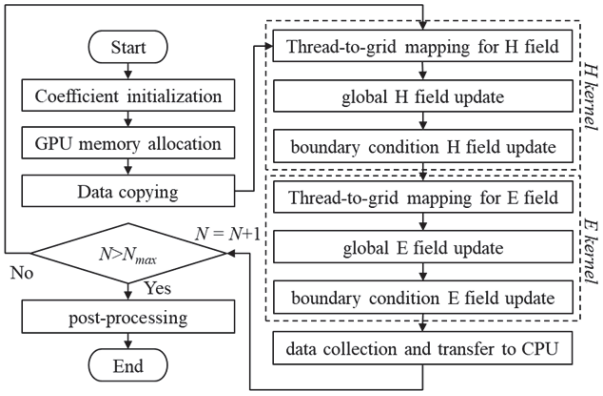

Fig. 18. Flowchart of the GPU-based parallel FDTD algorithm.

operations, performing field value calculations at each time step and updating the electric and magnetic fields in a recursive manner.

Using the E_x component as an example, at each time step, the GPU reads the previous E_x values, along with the H_y and H_z values, computational coefficients, and auxiliary variables related to boundary conditions from global memory. The GPU first executes the FDTD standard update equation kernel in parallel to compute the E_x field values across the entire domain. After that, it runs a boundary condition kernel in parallel to update the field components located at the boundaries. Once this is complete, the new E_x values and the associated auxiliary variables for the boundary conditions are written back to global memory for use in the field updates during the next time step.

The calculation process for other field components follows a similar procedure. After all field components for a given time step are computed, the CPU advances the simulation to the next time step, allowing the GPU to begin the next round of field calculations. The reason for using the CPU to handle time advancement is that Compute Unified Device Architecture (CUDA) lacks global thread synchronization capabilities, which is essential for FDTD's time-domain iterations. The algorithm requires that all E (or H) field components be fully computed at a given time step before advancing to the H (or E) field components. To address this, the device-side computation is split into two kernel functions: one for computing the E fields and another for computing the H fields, which are executed sequentially. The CPU ensures global synchronization between these two steps, preventing computation errors that would result from improper synchronization.

In this work, parallel computation is implemented by assigning one thread to handle each Yee cell. For example, in the case of calculating the Ex component, within an FDTD computational domain of dimensions $N_x \times N_y \times N_z$, the number of E_x components to be updated is typically $N_x \times (N_y+1) \times (N_z+1)$. Both the grid and block structures used in this paper are one-dimensional, with each block consisting of nT threads. The CUDA thread index corresponding to the E_x component at position (i, j, k) in the FDTD domain can be calculated by:

$$blockx = [(i-1+j\cdot N_x + k\cdot N_x \cdot N_y)/N_T], \quad (13)$$

$$threadIdx = (i-1+j\cdot N_x + k\cdot N_x\cdot(N_y+1))\%N_T, \quad (14)$$

where $[\cdot]$ represents the floor operation, and % denotes the modulo operation. It is important to note that N_T must be a multiple of the GPU's warp size, which is typically 32. This thread allocation strategy ensures that the memory assigned to each block is contiguous in the x-direction, which satisfies global memory alignment requirements. This allows for continuous memory access, thereby improving the effective memory bandwidth.

The authors are currently pursuing further research in the area of GPU/FDTD acceleration and plan to report the results in a future publication [121].

In summary, GPUs have become indispensable for accelerating computational electromagnetics simulations. In FEM, GPUs enhance the solution of large sparse matrix systems through parallelized iterative solvers and efficient handling of element-wise computations. For MoM, which involves dense matrix operations for surface integral equations, GPUs leverage their high memory bandwidth and parallel processing capabilities to accelerate matrix filling and matrix-vector products, significantly reducing solution times. In FDTD, GPUs excel by parallelizing the explicit time-stepping updates across the computational grid, enabling real-time or large-scale simulations of wave propagation and scattering problems. By exploiting massive parallelism, GPUs deliver orders-of-magnitude speedups over CPUs, making them essential for high-performance electromagnetic analysis in research and industry. Future advancements in exascale computing, AI-driven numerics, and heterogeneous architectures will further push the limits of GPU-accelerated EM simulation.

V. CONCLUDING REMARKS

In this work, we have presented several innovative CEM techniques for numerical modeling of microwave circuits, antennas, and array configurations, with special emphasis on techniques for efficient simulation at millimeter-waves, and beyond, where the conventional simulation techniques become both memory-intensive and time-consuming. We have focused on solving a variety of practical design and analysis problems and have presented a wide array of example geometries that are useful for 5G/6G applications. Looking into the future,

the authors are currently developing an AI-based antenna design software [122] which will integrate some of the simulation algorithms presented in this work to speed up the design process.

ACKNOWLEDGMENT

The authors acknowledge their team members and research collaborators, including Chao Li, Donia Ouesleti, Koushik Dutta, Yang Su, and others for their contributions and helpful discussions. We thank Dr. Danie Ludick for pointing us to the "cemagg/SUN-EM" GitHub library, which was used to parse FEKO's MoM-based data into MATLAB. We also acknowledge the responsible use of ChatGPT, developed by OpenAI, for assistance in text editing during the preparation of this manuscript. The tool was used solely to improve clarity and language, without contributing to the scientific content of the paper.

REFERENCES

[1] R. Mittra, O. Ozgun, V. Kaim, A. Nasri, P. Chaudhary, and R. K. Arya, "Novel strategies for efficient computational electromagnetic (CEM) simulation of microstrip circuits, antennas, arrays and metamaterials Part-I: Introduction, layered medium Green's Function, equivalent medium approach," *Applied Computational Electromagnetics Society (ACES) Journal*, pp. 000-000, 2025.

[2] T. Marinović and R. Mittra, "Efficient analysis of large periodic array antennas using the characteristic basis function method," in *2022 IEEE Int. Symp. Antennas Propag. USNC-URSI Radio Sci. Meeting*, pp. 417-418, Denver, CO, USA, July 2022.

[3] T. Marinović and R. Mittra, "Characteristic basis function method using single high-level basis function per subdomain for efficient analysis of large periodic array antennas," in *2023 IEEE Int. Symp. Antennas Propag. USNC-URSI Radio Sci. Meeting*, pp. 807-808, Portland, OR, USA, July 2023.

[4] T. Marinović and R. Mittra, "Characteristic basis function method using single high-level subdomain basis function for efficient analysis of irregular sparse array antennas," in *2024 IEEE Int. Symp. Antennas Propag. INC/USNC-URSI Radio Sci. Meeting*, pp. 229-230, Florence, Italy, July 2024.

[5] S. Rao, D. Wilton, and A. Glisson, "Electromagnetic scattering by surfaces of arbitrary shape," *IEEE Trans. Antennas Propag.*, vol. 30, no. 3, pp. 409-418, 1982.

[6] F. Gustrau and D. Manteuffel, *EM Modeling of Antennas and RF Components for Wireless Communication Systems*. Berlin and Heidelberg: Springer-Verlag, 2006.

[7] V. V. S. Prakash and R. Mittra, "Characteristic basis function method: A new technique for efficient solution of method of moments matrix equations," *Microw. Opt. Technol. Lett.*, vol. 36, no. 2, pp. 95-100, Jan. 2003.

[8] R. Maaskant, *Analysis of large antenna systems*, Ph.D. thesis, Eindhoven University of Technology, Eindhoven, 2010.

[9] T. Marinović, R. Maaskant, R. Mittra, and G. A. E. Vandenbosch, "Comparison of CBFM-enhanced iterative methods for MoM-based finite antenna array analysis," *IEEE Trans. Antennas Propag.*, vol. 70, no. 5, pp. 3538-3548, May 2022.

[10] E. Lucente, G. Tiberi, A. Monorchio, G. Manara, and R. Mittra, "The characteristic basis function method (CBFM): A numerically efficient strategy for solving large electromagnetic scattering problems," *Turkish J. Electr. Eng.*, vol. 16, no. 1, pp. 41-56, 2008.

[11] E. Lucente, A. Monorchio, and R. Mittra, "An iteration-free MoM approach based on excitation independent characteristic basis functions for solving large multiscale electromagnetic scattering problems," *IEEE Trans. Antennas Propag.*, vol. 56, no. 4, pp. 999-1007, Apr. 2008.

[12] C. Delgado, R. Mittra, and F. Cátedra, "Accurate representation of the edge behavior of current when using PO-derived characteristic basis functions," *IEEE Antennas Wireless Propag. Lett.*, vol. 7, pp. 43-45, 2008.

[13] C. Delgado, M. F. Cátedra, and R. Mittra, "Application of the characteristic basis function method utilizing a class of basis and testing functions defined on NURBS patches," *IEEE Trans. Antennas Propag.*, vol. 56, no. 3, pp. 784-791, 2008.

[14] C. Delgado, M. F. Cátedra, and R. Mittra, "Efficient multilevel approach for the generation of characteristic basis functions for large scatters," *IEEE Trans. Antennas Propag.*, vol. 56, no. 7, pp. 2134-2137, 2008.

[15] C. Delgado, E. García, F. Cátedra, and R. Mittra, "Generation of characteristic basis functions defined over large surfaces by using a multilevel approach," *IEEE Trans. Antennas Propag.*, vol. 57, no. 4, pp. 1299-1301, 2009.

[16] J. Laviada, F. Las-Heras, M. R. Pino, and R. Mittra, "Solution of electrically large problems with multilevel characteristic basis functions," *IEEE Trans. Antennas Propag.*, vol. 57, no. 10, pp. 3189-3198, Oct. 2009.

[17] J. Laviada, J. Gutierrez-Meana, M. Pino, and F. Las-Heras, "Analysis of partial modifications

on electrically large bodies via characteristic basis functions," *IEEE Antennas Wireless Propag. Lett.*, vol. 9, pp. 834-837, 2010.

[18] L. Hu, L.-W. Li, and R. Mittra, "Electromagnetic scattering by finite periodic arrays using the characteristic basis function and adaptive integral methods," *IEEE Trans. Antennas Propag.*, vol. 58, no. 9, pp. 3086-3090, 2010.

[19] J. Laviada, M. R. Pino, and F. Las-Heras, "Generation of excitation-independent characteristic basis functions for three-dimensional homogeneous dielectric bodies," *IEEE Trans. Antennas Propag.*, vol. 59, no. 9, pp. 3318-3327, Sep. 2011.

[20] J. Hu, W. Lu, H. Shao, and Z. Nie, "Electromagnetic analysis of large scale periodic arrays using a two-level CBFs method accelerated with FMM-FFT," *IEEE Trans. Antennas Propag.*, vol. 60, no. 12, pp. 5709-5716, Dec. 2012.

[21] K. Konno, Q. Chen, K. Sawaya, and T. Sezai, "Optimization of block size for CBFM in MoM," *IEEE Trans. Antennas Propag.*, vol. 60, no. 10, pp. 4719-4724, Oct. 2012.

[22] H. Shao, J. Hu, W. Lu, H. Guo, and Z. Nie, "Analyzing large-scale arrays using tangential equivalence principle algorithm with characteristic basis functions," *Proc. IEEE*, vol. 101, no. 2, pp. 414-422, Feb. 2013.

[23] X. Wang, D. H. Werner, and J. P. Turpin, "Investigation of scattering properties of large-scale aperiodic tilings using a combination of the characteristic basis function and adaptive integral methods," *IEEE Trans. Antennas Propag.*, vol. 61, no. 6, pp. 3149-3160, June 2013.

[24] C. S. Park, Y. R. Jeong, I. P. Hong, and J. G. Yook, "Block size optimization of CBFM for scattering problems," *IEEE Trans. Antennas Propag.*, vol. 66, no. 10, pp. 5370-5377, Oct. 2018.

[25] C. Delgado and M. F. Cátedra, "Dynamic threshold selection based on radiation pattern characteristics for the generation of macro basis functions," *IEEE Antennas Wireless Propag. Lett.*, vol. 17, no. 10, pp. 1812-1816, 2018.

[26] C. Delgado and M. F. Cátedra, "Sparse approximate inverse preconditioner with parametric sparsity pattern applied to the macrobasis function methods," *IEEE Antennas Wireless Propag. Lett.*, vol. 17, no. 5, pp. 849-852, 2018.

[27] F. Huang and Y. Sun, "Efficient solution of electromagnetic scattering from dielectric objects via characteristic basis function method based on large-size blocks with multilevel subdivision," *IEEE Access*, vol. 7, pp. 71741-71748, May 2019.

[28] C. Li, M. S. Sharawi, and R. Mittra, "Fast computation of electromagnetic scattering from dielectric objects using quadrilateral piecewise sinusoidal basis and characteristic basis function method," *IEEE Trans. Antennas Propag.*, vol. 70, no. 7, pp. 5683-5692, 2022.

[29] H. Shao, K. Fu, Z. Fu, X. Ying, and J. Hu, "A fast model order reduction method for electromagnetic scattering of large periodic arrays with connected elements," *IEEE Trans. Antennas Propag.*, vol. 71, no. 11, pp. 9142-9147, Nov. 2023.

[30] C. Li, M. S. Sharawi, and R. Mittra, "Enhancing CBFM with adaptive frequency sampling for wideband scattering from objects buried in layered media," *IEEE Trans. Antennas Propag.*, vol. 71, no. 8, pp. 7006-7011, Aug. 2023.

[31] X. Wang, L. Chen, C. Liu, Y. Liu, Y. Zeng, Z. Xu, and W. Lin, "An efficient hybrid method of CBFM/AIM and equivalent dipole-moment for computation of electromagnetic scattering problems," *IEEE Trans. Antennas Propag.*, vol. 72, no. 10, pp. 8103-8108, 2024.

[32] E. García, C. Delgado, and F. Cátedra, "A computationally efficient technique using characteristic basis functions and large block sizes," *IEEE Antennas Wireless Propag. Lett.*, vol. 23, no. 4, pp. 1341-1345, 2024.

[33] Z. Dong, X. Chen, F. Gao, C. Gu, Z. Li, W. Yang, and W. Lu, "Efficient iterative solution of combined source integral equation using characteristic basis function method with initial guess," *IEEE J. Multiscale Multiphys. Comput. Tech.*, vol. 9, pp. 142-148, 2024.

[34] S. J. Kwon, K. Du, and R. Mittra, "Characteristic basis function method: A numerically efficient technique for analyzing microwave and RF circuits," *Microw. Opt. Technol. Lett.*, vol. 38, pp. 444-448, 9 2003.

[35] G. Bianconi, C. Pelletti, R. Mittra, K. Du, and A. Monorchio, "An efficient technique for the evaluation of the reduced matrix in the context of the CBFM for layered media," *IEEE Antennas Wireless Propag. Lett.*, vol. 10, pp. 674-677, 2011.

[36] G. Bianconi and R. Mittra, "Efficient analysis of microwave circuits/printed antennas and scattering problems via the characteristic basis function method (CBFM)," *FERMAT J.*, vol. 2, 2014.

[37] R. Maaskant, *Fast Analysis of Periodic Antennas and Metamaterial-based Waveguides*, pp. 75–109, New York, NY: Springer, 2014.

[38] W. R. Dommisse, J. T. Du Plessis, P. I. Cilliers, M. M. Botha, and T. Rylander, "Macro basis functions for efficient analysis of thick wires in the

MoM," *IEEE Trans. Antennas Propag.*, vol. 72, no. 7, pp. 5865-5876, 2024.

[39] I. Kim, H.-R. Im, I.-P. Hong, H. Lee, and J.-G. Yook, "An accelerated method of a generalized transition matrix model using characteristic basis functions for large-scale open-ended cavities," *IEEE Trans. Antennas Propag.*, vol. 72, no. 8, pp. 6813-6818, Aug. 2024.

[40] R. Mittra, *Developments in Antenna Analysis and Design: Volume 2. London:* The Institution of Engineering and Technology, 2018.

[41] R. Maaskant, R. Mittra, and A. Tijhuis, "Fast analysis of large antenna arrays using the characteristic basis function method and the adaptive cross approximation algorithm," *IEEE Trans. Antennas Propag.*, vol. 56, no. 11, pp. 3440-3451, Nov. 2008.

[42] R. Maaskant, R. Mittra, and A. Tijhuis, "Fast solution of multi-scale antenna problems for the square kilometre array (SKA) radio telescope using the characteristic basis function method (CBFM)," *Applied Computational Electromagnetics Society (ACES) Journal*, vol. 24, pp. 174-188, 2009.

[43] G. Öğücü, R. Mittra, and K. Du, "An interpolation algorithm to reduce the reduced matrix fill-time in CBFM," *IEEE Antennas Wireless Propag. Lett.*, vol. 8, pp. 457-460, Apr. 2009.

[44] R. Maaskant, R. Mittra, and A. Tijhuis, "Multilevel characteristic basis function method (MLCBFM) for the analysis of large antenna arrays," *URSI Radio Sci. Bulletin*, vol. 2011, no. 336, pp. 23-34, Mar. 2011.

[45] K. Sewraj and M. M. Botha, "Macro basis function methods with multilevel DCA acceleration for antenna array analysis," *IEEE Trans. Antennas Propag.*, vol. 72, no. 11, pp. 8621-8634, 2024.

[46] J. Yeo, V. V. S. Prakash, and R. Mittra, "Efficient analysis of a class of microstrip antennas using the characteristic basis function method (CBFM)," *Microw. Opt. Technol. Lett.*, vol. 39, no. 6, pp. 456-464, Dec. 2003.

[47] S. G. Hay, D. O. John, and R. Mittra, "Connected patch array analysis using the characteristic basis function method," *IEEE Trans. Antennas Propag.*, vol. 59, no. 6, pp. 1828-1837, June 2011.

[48] K. Konno, Q. Chen, and R. J. Burkholder, "Numerical analysis of large-scale finite periodic arrays using a macro block-characteristic basis function method," *IEEE Trans. Antennas Propag.*, vol. 65, no. 10, pp. 5348-5355, Oct. 2017.

[49] O. Ozgun, R. Mittra, and M. Kuzuoglu, "Multilevel characteristic basis finite-element method (ML-CBFEM)—An efficient version of a domain decomposition algorithm for large-scale electromagnetic problems," *IEEE Trans. Antennas Propag.*, vol. 57, no. 10, pp. 3381-3387, 2009.

[50] O. Ozgun, R. Mittra, and M. Kuzuoglu, "Parallelized characteristic basis finite element method (CBFEM-MPI)—A non-iterative domain decomposition algorithm for electromagnetic scattering problems," *J. Comput. Phys.*, vol. 228, no. 6, pp. 2225-2238, 2009.

[51] O. Ozgun, R. Mittra, and M. Kuzuoglu, "CBFEM-MPI: A parallelized version of characteristic basis finite element method for extraction of 3-D interconnect capacitances," *IEEE Trans. Adv. Packag.*, vol. 32, no. 1, pp. 164-174, 2009.

[52] O. Ozgun, R. Mittra, and M. Kuzuoglu, "General-purpose characteristic basis finite element method for multi-scale electrostatic and electromagnetic problems," *Electromagn.*, vol. 30, no. 1-2, pp. 205-221, 2010.

[53] O. Ozgun, R. Mittra, and M. Kuzuoglu, "PO-based characteristic basis finite element method (CBFEM-PO)—A parallel, iteration-free domain decomposition algorithm using perfectly matched layers for large-scale electromagnetic scattering problems," *Microw. Opt. Technol. Lett.*, vol. 52, no. 5, pp. 1053-1060, 2010.

[54] O. Ozgun and M. Kuzuoglu, "Monte Carlo-based characteristic basis finite-element method (MC-CBFEM) for numerical analysis of scattering from objects on/above rough sea surfaces," *IEEE Trans. Geosci. Remote Sens.*, vol. 50, no. 3, pp. 769-783, 2012.

[55] C. Bourlier, Y. A. Noa, G. Kubické, and S. Bellez, "Two domain decomposition methods, SDIM and CBFM, for scattering from a two-dimensional perfectly conducting rough surface: comparison and parametric study," *J. Opt. Soc. Am. A*, vol. 37, no. 9, pp. 1512-1525, Sep. 2020.

[56] I. Fenni, H. Roussel, M. Darces, and R. Mittra, "Fast analysis of large 3-D dielectric scattering problems arising in remote sensing of forest areas using the CBFM," *IEEE Trans. Antennas Propag.*, vol. 62, no. 8, pp. 4282-4291, Aug. 2014.

[57] N. A. Ozdemir, D. González-Ovejero, and C. Craeye, "On the relationship between multiple-scattering macro basis functions and Krylov subspace iterative methods," *IEEE Trans. Antennas Propag.*, vol. 61, no. 4, pp. 2088-2098, Apr. 2013.

[58] C. Craeye, J. Laviada, R. Maaskant, and R. Mittra, "Macro basis function framework for solving Maxwell's equations in surface integral equation form," *FERMAT J.*, vol. 3, pp. 1-16, 2014.

[59] O. A. Iupikov, C. Craeye, R. Maaskant, and M. V. Ivashina, "Domain-decomposition approach to Krylov subspace iteration," *IEEE Antennas Wireless Propag. Lett.*, vol. 15, pp. 1414-1417, 2016.

[60] D. J. Ludick, M. M. Botha, R. Maaskant, and D. B. Davidson, "The CBFM-enhanced Jacobi method for efficient finite antenna array analysis," *IEEE Antennas Wireless Propag. Lett.*, vol. 16, pp. 2700-2703, 2017.

[61] T. Marinović, *Study of mutual coupling in finite antenna arrays for massive MIMO applications*, Licentiate thesis, Chalmers University of Technology, Gothenburg, Nov. 2020.

[62] T. Marinović, *Efficient modeling of mutually coupled array antennas for massive MIMO applications*, Ph.D. thesis, KU Leuven and Chalmers University of Technology, Leuven and Gothenburg, 2021.

[63] Altair Engineering Inc. (2024). *FEKO* [Online]. Available: https://altair.com/feko/

[64] R. Mittra, *Developments in Antenna Analysis and Design: Volume 1*. The Institution of Engineering and Technology, 2018.

[65] G. A. E. Vandenbosch and A. R. Van de Capelle, "Use of a combined expansion scheme to analyze microstrip antennas with the Method of Moments," *Radio Sci.*, vol. 27, no. 6, pp. 911-916, 1992.

[66] G. A. E. Vandenbosch and F. J. Demuynck, "The expansion wave concept—Part II: A new way to model mutual coupling in microstrip arrays," *IEEE Trans. Antennas Propag.*, vol. 46, no. 3, pp. 407-413, Mar. 1998.

[67] S. Ooms and D. De Zutter, "A new iterative diakoptics-based multilevel moments method for planar circuits," *IEEE Trans. Microw. Theory Tech.*, vol. 46, no. 3, pp. 280-291, Mar. 1998.

[68] E. Suter and J. Mosig, "A subdomain multilevel approach for the efficient MoM analysis of large planar antennas," *Microw. Opt. Technol. Lett.*, vol. 26, no. 4, pp. 270-277, Aug. 2000.

[69] D. J. Bekers, S. J. L. van Eijndhoven, A. A. F. van de Ven, P.-P. Borsboom, and A. G. Tijhuis, "Eigencurrent analysis of resonant behavior in finite antenna arrays," *IEEE Trans. Microw. Theory Tech.*, vol. 54, no. 6, pp. 2821-2829, June 2006.

[70] D. J. Bekers, S. J. L. van Eijndhoven, and A. G. Tijhuis, "An eigencurrent approach for the analysis of finite antenna arrays," *IEEE Trans. Antennas Propag.*, vol. 57, no. 12, pp. 3772-3782, Dec. 2009.

[71] V. Lancellotti, B. P. D. Hon, and A. G. Tijhuis, "An eigencurrent approach to the analysis of electrically large 3-D structures using linear embedding via green's operators," *IEEE Trans. Antennas Propag.*, vol. 57, no. 11, pp. 3575-3585, Nov. 2009.

[72] L. Matekovits, V. A. Laza, and G. Vecchi, "Analysis of large complex structures with the synthetic-functions approach," *IEEE Trans. Antennas Propag.*, vol. 55, no. 9, pp. 2509-2521, Sep. 2007.

[73] S. M. Rao, "A true domain decomposition procedure based on method of moments to handle electrically large bodies," *IEEE Trans. Antennas Propag.*, vol. 60, no. 9, pp. 4233-4238, Sep. 2012.

[74] C. Craeye, "A fast impedance and pattern computation scheme for finite antenna arrays," *IEEE Trans. Antennas Propag.*, vol. 54, no. 10, pp. 3030-3034, 2006.

[75] H. Bui-Van, J. Abraham, M. Arts, Q. Gueuning, C. Raucy, D. González-Ovejero, E. de Lera Acedo, and C. Craeye, "Fast and accurate simulation technique for large irregular arrays," *IEEE Trans. Antennas Propag.*, vol. 66, no. 4, pp. 1805-1817, Apr. 2018.

[76] W. B. Lu, T. J. Cui, Z. G. Qian, X. X. Yin, and W. Hong, "Accurate analysis of large-scale periodic structures using an efficient sub-entire-domain basis function method," *IEEE Trans. Antennas Propag.*, vol. 52, no. 11, pp. 3078-3085, 2004.

[77] W. B. Lu, T. J. Cui, X. X. Yin, Z. G. Qian, and W. Hong, "Fast algorithms for large-scale periodic structures using subentire domain basis functions," *IEEE Trans. Antennas Propag.*, vol. 53, no. 3, pp. 1154-1162, 2005.

[78] W. B. Lu, T. J. Cui, and H. Zhao, "Acceleration of fast multipole method for large-scale periodic structures with finite sizes using sub-entire-domain basis functions," *IEEE Trans. Antennas Propag.*, vol. 55, no. 2, pp. 414-421, 2007.

[79] X. Wang, D. H. Werner, and J. P. Turpin, "A fast analysis of scattering from large-scale finite periodic microstrip patch arrays arranged on a non-orthogonal lattice using sub-entire domain basis functions," *IEEE Trans. Antennas Propag.*, vol. 62, no. 5, pp. 2543-2552, May 2014.

[80] P. Du, G. Zheng, C. Wang, and W. J. Fu, "Efficient wideband computation of electromagnetic scattering by finite periodic structures combining ASED basis function with frequency-independent reaction," *IEEE Antennas Wireless Propag. Lett.*, vol. 17, no. 2, pp. 234-237, Feb. 2018.

[81] W. Xiang, T. Xiong, W.-B. Lu, W. Yang, and Z.-G. Liu, "New accurate subentire-domain basis functions method for the analysis of large-scale finite

periodic structures with electrically connected cells," *IEEE Trans. Antennas Propag.*, vol. 67, no. 3, pp. 2017-2022, Mar. 2019.

[82] P. Du, G. Zheng, W.-B. Lu, and W. Xiang, "Wideband solution of electrically connected finite periodic arrays using modified accurate subentire-domain basis function method and improved frequency-independent reaction," *IEEE Antennas Wireless Propag. Lett.*, vol. 20, no. 9, pp. 1775-1778, Sep. 2021.

[83] P. Du, W. Xiang, and S.-S. Zhu, "A comparison of MB-CBFM and modified ASED basis function method to analyze interconnected finite periodic arrays," *IEEE Antennas Wireless Propag. Lett.*, vol. 21, no. 9, pp. 1822-1826, Sep. 2022.

[84] W. Xiang, Z. Zhang, W. Zheng, J. Li, W. Yang, and W. Lu, "Rapid subentire-domain basis functions method based on adaptive artificial neural networks," *IEEE Trans. Antennas Propag.*, vol. 70, no. 7, pp. 5156-5164, July 2022.

[85] T. Guo and P. Du, "Scattering analysis of finite periodic array in the vicinity of arbitrary object using hybrid macro basis function method," *IEEE Antennas Wireless Propag. Lett.*, vol. 22, no. 3, pp. 626-630, Mar. 2023.

[86] W. Xiang, W. Yang, and W. Lu, "Fast subentire-domain basis functions method for analysis of composite finite periodic structures with dielectric-conductor cells," *IEEE Antennas Wireless Propag. Lett.*, vol. 22, no. 2, pp. 233-237, Feb. 2023.

[87] M. Djordjevic and B. Notaros, "Double higher order method of moments for surface integral equation modeling of metallic and dielectric antennas and scatterers," *IEEE Trans. Antennas Propag.*, vol. 52, no. 8, pp. 2118-2129, Aug. 2004.

[88] M. Chose, A. S. Conradie, P. I. Cilliers, and M. M. Botha, "Physics-based iterative scheme for computing antenna array embedded element patterns," *Microw. Opt. Technol. Lett.*, vol. 65, no. 8, pp. 2359-2365, 2023.

[89] A. S. Conradie, M. Chose, P. I. Cilliers, and M. M. Botha, "Antenna array analysis by iterative DGFM-based local solutions," *IEEE Trans. Antennas Propag.*, vol. 71, no. 6, pp. 5199-5211, 2023.

[90] A. S. Conradie and M. M. Botha, "Preconditioned localized-solution iterative solver with nested cross approximation for large arrays," *IEEE Trans. Antennas Propag.*, vol. 72, no. 8, pp. 6584-6598, 2024.

[91] D. J. Ludick, R. Maaskant, D. B. Davidson, U. Jakobus, R. Mittra, and D. de Villiers, "Efficient analysis of large aperiodic antenna arrays using the domain Green's Function method," *IEEE Trans. Antennas Propag.*, vol. 62, no. 4, pp. 1579-1588, Apr. 2014.

[92] J. Bezanson, A. Edelman, S. Karpinski, and V. B. Shah, "Julia: A fresh approach to numerical computing," *SIAM Rev.*, vol. 59, no. 1, pp. 65-98, 2017.

[93] K. Zhao, M. N. Vouvakis, and J.-F. Lee, "The adaptive cross approximation algorithm for accelerated method of moments computations of EMC problems," *IEEE Trans. Electromagn. Compat.*, vol. 47, no. 4, pp. 763-773, Nov. 2005.

[94] G. H. Golub and C. F. Van Loan, *Matrix Computations*, 4th ed. Philadelphia, PA: Johns Hopkins University Press, 2013.

[95] O. Ozgun, R. Mittra, and M. Kuzuoglu, "An efficient numerical approach for evaluating Sommerfeld integrals arising in the construction of Green's functions for layered media," *IEEE J. Multiscale Multiphys. Comput. Tech.*, vol. 7, pp. 328-335, 2022.

[96] R. Mittra, P. Chaudhary, T. Marinovic, and A. Nasri, "New strategies for CEM simulation of microstrip circuits and antennas," in *2023 IEEE Int. Symp. Antennas Propag. USNC-URSI Radio Sci. Meeting*, pp. 1615-1616, 2023.

[97] J.-P. Berenger, "A perfectly matched layer for the absorption of electromagnetic waves," *J. Comput. Phys.*, vol. 114, no. 2, pp. 185-200, 1994.

[98] Z. Sacks, D. Kingsland, R. Lee, and J.-F. Lee, "A perfectly matched anisotropic absorber for use as an absorbing boundary condition," *IEEE Trans. Antennas Propag.*, vol. 43, no. 12, pp. 1460-1463, 1995.

[99] S. Gedney, "An anisotropic perfectly matched layer-absorbing medium for the truncation of FDTD lattices," *IEEE Trans. Antennas Propag.*, vol. 44, no. 12, pp. 1630-1639, 1996.

[100] M. Kuzuoglu and R. Mittra, "Mesh truncation by perfectly matched anisotropic absorbers in the finite-element method," *Microw. Opt. Technol. Lett.*, vol. 12, no. 3, pp. 136-140, 1996.

[101] M. Kuzuoglu and R. Mittra, "Investigation of nonplanar perfectly matched absorbers for finite-element mesh truncation," *IEEE Trans. Antennas Propag.*, vol. 45, no. 3, pp. 474-486, 1997.

[102] F. Teixeira and W. Chew, "Systematic derivation of anisotropic PML absorbing media in cylindrical and spherical coordinates," *IEEE Microw. Guided Wave Lett*, vol. 7, no. 11, pp. 371-373, 1997.

[103] O. Ozgun and M. Kuzuoglu, "Non-Maxwellian locally-conformal PML absorbers for finite

element mesh truncation," *IEEE Trans. Antennas Propag.*, vol. 55, no. 3, pp. 931-937, 2007.

[104] O. Ozgun and M. Kuzuoglu, "Near-field performance analysis of locally-conformal perfectly matched absorbers via Monte Carlo simulations," *J. Comput. Phys.*, vol. 227, no. 2, pp. 1225-1245, 2007.

[105] O. Ozgun, M. Kuzuoglu, H. Beriot, and R. Mittra, "Parametrization-free locally-conformal perfectly matched layer method for finite element solution of Helmholtz equation," *J. Comput. Phys.*, vol. 288, no. 108741, 2023.

[106] O. Ozgun, M. Kuzuoglu, and R. Mittra, "Self-tuning locally conformal PML mesh truncation for 3-D vector finite element method," *IEEE Trans. Antennas Propag.*, vol. 72, no. 2, pp. 2036-2040, 2024.

[107] I. Will, "Electromagnetic modeling with GPUs," *CiteseerX*, 2010.

[108] Y. Su, C. Li, R. Mittra, and W. Sheng, "Multi-level characteristic basis function method for analysis of scattering from objects embedded in multilayered media," *Journal of Electromagnetic Waves and Applications*, vol. 31, no. 1, pp. 47-56, 2017.

[109] Y. Su and R. Mittra, "Numerically efficient methods for electromagnetic modeling of antenna radiation and scattering problems," in *Developments in Antenna Analysis and Design: Volume 2*, R. Mittra, Ed. London: The Institution of Engineering and Technology, pp. 213–258, 2018.

[110] B. M. Kolundzija and D. P. Zoric, "Efficient evaluation of MoM matrix elements using CPU and/or GPU," in *2012 6th European Conference on Antennas and Propagation (EuCAP)*, pp. 702-706, IEEE, 2012.

[111] E. Lezar and D. B. Davidson, "GPU-accelerated method of moments by example: Monostatic scattering," *IEEE Antennas and Propagation Magazine*, vol. 52, no. 6, pp. 120-135, 2010.

[112] J. I. Pérez, E. García, J. A. de Frutos, and F. Cátedra, "Application of the characteristic basis function method using CUDA," *International Journal of Antennas and Propagation*, vol. 2014, no. 1, p. 721580, 2014.

[113] M. J. Inman, A. Z. Elsherbeni, and C. Reddy, "CUDA based GPU solver for method of moments simulations," in *26th Annual Review of Progress in Applied Computational Elctromagnetics-ACES2010*, Tampere, Finland, pp. 59-60, 2010.

[114] S. Li, R. Chang, A. Boag, and V. Lomakin, "Fast electromagnetic integral-equation solvers on graphics processing units," *IEEE Antennas and Propagation Magazine*, vol. 54, no. 5, pp. 71-87, 2012.

[115] M. T. Zhu, H. Z. Lu, and M. S. Tong, "An efficient GPU acceleration scheme for solving electromagnetic problems with moderate scales," in *2024 International Conference on Electromagnetics in Advanced Applications (ICEAA)*, pp. 548-550, IEEE, 2024.

[116] J. Guan, S. Yan, and J.-M. Jin, "An accurate and efficient finite element-boundary integral method with GPU acceleration for 3-D electromagnetic analysis," *IEEE Trans. Antennas Propag.*, vol. 62, no. 12, pp. 6325-6336, 2014.

[117] D. De Donno, A. Esposito, L. Tarricone, and L. Catarinucci, "Introduction to GPU computing and CUDA programming: A case study on FDTD [EM programmer's notebook]," *IEEE Antennas and Propagation Magazine*, vol. 52, no. 3, pp. 116-122, 2010.

[118] K.-H. Kim and Q.-H. Park, "Overlapping computation and communication of three-dimensional FDTD on a GPU cluster," *Computer Physics Communications*, vol. 183, no. 11, pp. 2364-2369, 2012.

[119] P. D. Cannon and F. Honary, "A GPU-accelerated finite-difference time-domain scheme for electromagnetic wave interaction with plasma," *IEEE Trans. Antennas Propag.*, vol. 63, no. 7, pp. 3042-3054, 2015.

[120] P. Sypek, A. Dziekonski, and M. Mrozowski, "How to render FDTD computations more effective using a graphics accelerator," *IEEE Transactions on Magnetics*, vol. 45, no. 3, pp. 1324-1327, 2009.

[121] S. Huang, Y. Cheng, R. Mittra, X. Zhang, and X. Zhang, "Accelerating GPU-based parallel FDTD with advanced operator fusion," *IEEE Antennas and Wireless Propagation Letters*, (under review).

[122] R. Mittra, R. K. Arya, P. Chaudhary, and A. Nasri, "A novel AI-based antenna design software," in *2024 IEEE INC-USNC-URSI Radio Science Meeting (Joint with AP-S Symposium)*, pp. 213-214, IEEE, 2024.

Raj Mittra is a Professor in the Department of Electrical and Computer Engineering of the University of Central Florida in Orlando, FL., where he is the Director of the Electromagnetic Communication Laboratory. Before joining the University of Central Florida, he worked at Penn State as a Professor in the Electrical and Computer Engineering from 1996 through June 2015. He was a Professor in the Electrical and Computer Engineering at the University of Illinois in Urbana-Champaign from 1957 through 1996, when he moved to Penn State University. Currently, he also holds the position of Hi-Ci Professor at King Abdulaziz University in Saudi Arabia and a Visiting Distinguished Professor in Zhongshan Institute of CUST, China. He is a Life Fellow of the IEEE, a Past-President of AP-S, and has served as the Editor of the Transactions of the Antennas and Propagation Society. He won the Guggenheim Fellowship Award in 1965, the IEEE Centennial Medal in 1984, and the IEEE Millennium Medal in 2000. Other honors include the IEEE/AP-S Distinguished Achievement Award in 2002, the Chen-To Tai Education Award in 2004 and the IEEE Electromagnetics Award in 2006, and the IEEE James H. Mulligan Award in 2011. He has also been recognized by the IEEE with an Alexander Graham Bell award from the IEEE Foundation.

Tomislav Marinovic received the M.Sc. degree in information and communication technology (summa cum laude) from the University of Zagreb, Zagreb, Croatia, in 2016; the Licentiate of Engineering degree from the Chalmers University of Technology, Gothenburg, Sweden, in 2020; and the double Ph.D. degree from KU Leuven, Leuven, Belgium, and the Chalmers University of Technology, in 2021. During his Ph.D., he participated in the Marie Skłodowska-Curie Innovative Training Network (ITN) "SILIKA" project funded by the European Union's Horizon 2020 Research and Innovation Programme. In this period, he was a Visiting Researcher with NXP Semiconductors, Eindhoven, The Netherlands; Eindhoven University of Technology, Eindhoven; TNO, The Hague, The Netherlands; Ericsson Research, Gothenburg; and Stellenbosch University, Stellenbosch, South Africa. He is currently a researcher at Multiverse Engineering, Croatia, focusing on the development of cost-effective Computational Electromagnetics simulation tools for antenna systems applications.

Ozlem Ozgun is currently a full professor in the Department of Electrical and Electronics Engineering at Hacettepe University, Ankara, Turkey. She received her B.Sc. and M.Sc. degrees from Bilkent University and her Ph.D. from Middle East Technical University (METU), all in Electrical and Electronics Engineering. She was a postdoctoral researcher at Penn State University, USA. Her research focuses on computational electromagnetics and radiowave propagation, including numerical methods, domain decomposition, transformation electromagnetics, and stochastic electromagnetic problems. Dr. Ozgun is a Senior Member of IEEE and URSI and a past chair of the URSI Turkey steering committee. She has been selected as a Distinguished Lecturer (DL) by the IEEE Antennas and Propagation Society (AP-S) for the period of 2025-2027. Her awards include the METU Best Ph.D. Thesis Award (2007), the Felsen Fund Excellence in Electromagnetics Award (2009), and the IEEE AP-S Outstanding Reviewer Award (2023-2024). She was recognized among the world's top 2% most influential scientists (Stanford University & Elsevier, 2023–2024) and received the Hacettepe University 2024 Science Award.

Shuo Liu is a Senior R&D Engineer at Amedac, Shanghai, China, holding a Ph.D. in Electronic Information Engineering. His doctoral research specialized in computational electromagnetics, covering electromagnetic wave propagation, antenna design, and numerical modeling of complex fields. Recognized for his contributions, he received the IEEE APS Fellowship (2022), the Chinese National Scholarship for Ph.D. Students (2020), and the Best Ph.D. Thesis Award. As a Research Fellow at NTU, he developed advanced electromagnetic simulation algorithms and educational tools. He also served as a consultant at RM Associates, collaborating with Dr. Raj Mittra to create a parallel time-domain electromagnetic simulator. His work bridges theoretical research and practical engineering applications in electromagnetics.

Ravi K. Arya is a Distinguished Professor and Director of the Xiangshan Laboratory Wireless Group at the Zhongshan Institute of Changchun University of Science and Technology (ZICUST), China. He earned his Ph.D. in Electrical Engineering from Pennsylvania State University, USA, under the supervision of Prof. Raj Mittra, following an M.Tech in RF and Microwave Engineering from the Indian Institute of Technology (IIT) Kharagpur (advised by Prof. Ramesh Garg) and a B.Tech from Delhi Technological University, India. With a career spanning both academia and industry, Dr. Arya has held positions at ECIL (India), C-DOT (India), Ansys Inc. (USA), and ALL.SPACE (USA), as well as academic roles at NIT Delhi (India) and JNU (India). He has authored over 90 peer-reviewed publications, seven book chapters, and four patents. His research focuses on antenna design, computational electromagnetics, machine learning applications in electromagnetics, and RF system modeling.

A Stable Subgridding 2D-FDTD Method for Ground Penetrating Radar Modeling

Xiao Yan Zhang and Rui Long Chen

The School of Information and Software Engineering
East China Jiao Tong University, Nanchang 330013, China
xy_zhang3129@ecjtu.edu.cn, 2465246593@qq.com

***Abstract* –** The subgridding finite-difference time-domain (FDTD) method has a great attraction in ground penetrating radar (GPR) modeling. The challenge is that the interpolation of the field unknowns at the multi-scale grid interfaces will aggravate the asymmetry of the numerical system which results in its instability. In this paper, an explicit unconditionally stable technique for a lossy object is introduced into the subgridding FDTD method. It removes the eigenmodes of the coefficient matrix which make the algorithm unstable. Therefore, the proposed approach not only maintains the advantages of simple implementation of the traditional FDTD method but also adopts a relatively large time step in both coarse and fine grid, which breaks through the restriction of the Courant-Friedrichs-Lewy (CFL) stability condition. The proposed method is applied in simulating the transverse magnetic (TM) wave backscattering of the two-dimensional buried objects in lossy media. Its accuracy and efficiency are examined by comparison with conventional FDTD and subgridding FDTD approaches.

***Index Terms* –** Courant-Friedrichs-Lewy (CFL) stability condition, ground penetrating radar (GPR), subgridding finite-difference time-domain (FDTD) method, unconditionally stable algorithm.

I. INTRODUCTION

Ground penetrating radar (GPR) plays an important role in geological detection, resource exploration, and urban construction. In order to identify the targets detected by the GPR equipment, some approaches, such as a Born approximation [1], a method of moments (MoM) [2], and a finite-difference time-domain (FDTD) method [3–4], are proposed to establish a half-space model to study the backscattering of the buried objects in advance. Among these methods, FDTD is the most popular because of its relatively simple implementation. However, the efficiency of the traditional explicit FDTD approach is low when simulating such GPR models. The reason is that, on the one hand, the underground object usually has a fine structure or its or soil's dielectric constant is large, so that the FDTD method has to use the fine grid to guarantee its accuracy, which increases the memory requirement. On the other hand, due to restriction by the Courant-Friedrichs-Lewy (CFL) stability condition, the time step of the traditional FDTD is shortened correspondingly, which increases the time cost.

An efficient way to overcome the above issues is to introduce a subgridding technique into the traditional FDTD approach [5–7]. This method divides the solution domain into several coarse and fine grids. The inner fields of the different grids are updated separately by using a local time increment. This process is stable, but the fields at the coarse/fine grids interface need to be estimated by certain interpolation schemes, which will lead to asymmetry of the numerical system and result in its instability [8]. Meanwhile, influenced by the CFL condition and numerical dispersion of the FDTD, the discontinuity in time of the temporal subgridding method will increase the algorithm's implementation complexity and limit the flexibility of the grid ratio [6]. Therefore, a good subgridding FDTD should be stable, have acceptable accuracy, and be simple to implement.

In recent years, some explicit subgridding FDTD approaches, such as Huygens subgridding FDTD method [9–10], FDTD hybrid method [11], and FDTD subgridding method with two separate interfaces in time and space [12], were proposed to improve the efficiency of the traditional subgridding FDTD. However, the time increments of these algorithms are restricted by the CFL condition. To break through such restriction, hybrid methods of the implicit and the explicit algorithm were proposed to make the time increment of the subgrid as large as that of the coarse grid [13–14]. However, the introduction of the implicit operation will increase the FDTD's complexity and may degrade the algorithm's performance since a matrix needs to be solved. In addition, unstable eigenmodes still exist in these methods, so the late time stability is still a problem to be faced [15].

In order to identify the root cause of the algorithm's instability, the system matrix of the subgridding FDTD

Submitted On: October 19, 2024
Accepted On: May 8, 2025

https://doi.org/10.13052/2025.ACES.J.400602

was analyzed in [8, 16–18]. They achieved late time stability by removing the eigenmodes of the system matrix that make the algorithm unstable [15] or by deriving a new iterative approach [8, 17–18]. In those studies, the scattering of objects in free space or cavities is of concern. To retain the original FDTD code and extend the CFL limit, a spatial filtering technique based on Fourier transform was developed in [19] and successfully applied in the GPR detect simulation. Its computational overhead was related to the number of sampling points in the spatial frequency domain. Therefore, when the number of the unknowns is much less than that of the sampling, the efficiency of the algorithm will decline.

In this paper, a subgridding 2D-FDTD method [20] based on the explicit unconditionally stable technique for a lossy media is proposed. Different from those global modeling methods, the proposed method only performs the explicit unconditional stable technique in the subgrid region, and the traditional FDTD algorithm with a uniaxial medium perfect matched layer (UPML) absorbing boundary is used in the other grids. In this way, the implement simplicity of the traditional FDTD algorithm can be maintained. Furthermore, by removing the eigenmodes of the coefficient matrix that make the subgridding FDTD unstable, its time step can be extended to be a relatively large one, so the proposed algorithm can use a unified time increment in both coarse and fine grids and achieve the late time stability.

This paper is arranged in the following manner. In section II, theories and mathematics of 2D-FDTD formulation with a lossy medium, subgridding scheme and unconditional stable algorithm for a lossy medium are derived. In section III, the computation performance of the algorithm is examined by comparing it with conventional FDTD and subgridding schemes. Numerical results of 2D GPR simulation with the transverse magnetic (TM) wave proves the validity and efficiency of the proposed algorithm. In section IV, conclusions are drawn.

II. THEORIES AND MATHEMATICS

As Fig. 1 shows, the half-space 2D GPR model is composed of air (ε_0, μ_0, representing the dielectric permittivity and the magnetic permeability of free space, respectively), the lossy soil (its parameters are ε_1, μ_1, and a conductivity of σ_1. The soil extends into the absorbing boundary), and the underground objects (ε_2, μ_2, σ_2). The electromagnetic signal is sent from the Tx, and the backscattering of the soil and the buried objects is received by the Rx (Tx, Rx denote the transmitting antenna and the receiving antenna, respectively).

The air layer is a small proportion in the model. Therefore, its spatial increment is set to be the same as that of the soil in this research, which will only slightly increase the computational cost of the algorithm. In this case, the computational domain is divided into two parts: the coarse grid area of the background and the subgridding area of the buried objects. The outward traveling wave is absorbed by the UPML absorption boundary, which also uses the coarse mesh and is implemented using traditional FDTD methods. Since the explicit unconditional stable technique only performs in the subgrid region, we can skip the UPML, because its electrical parameters change with distance, making it almost impossible to apply the unconditional stable explicit methods to it.

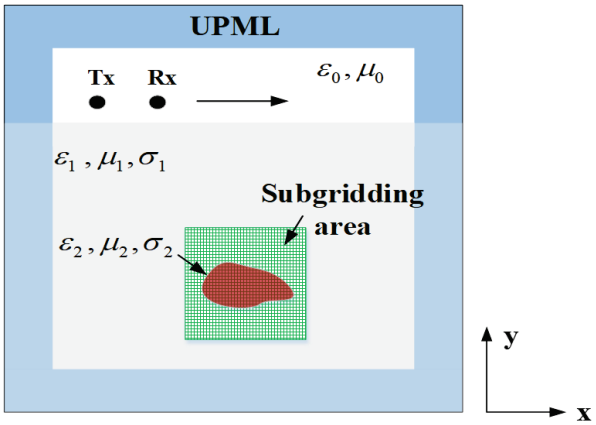

Fig. 1. Configuration of the two-dimensional GPR model.

A. Overall algorithm of the model

To describe the algorithm principle of the model, the coarse/fine grid size ratio of 3:1 is taken as an example. Figure 2 shows the spatial distributions of the electric field intensity (***E*** or ***e***) and the magnetic field intensity (***H*** or ***h***) at grid nodes. As Fig. 2 shows, the meshes in the model mainly include the coarse mesh nodes (in cell #1),

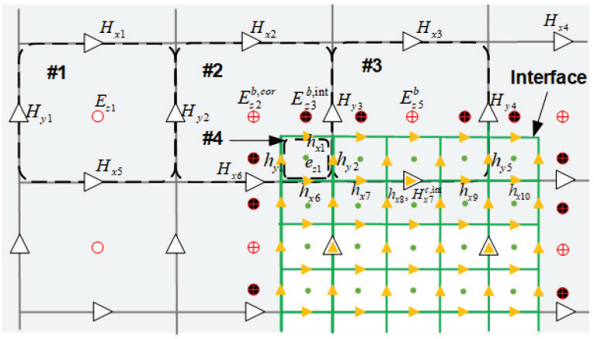

Fig. 2. Spatial distributions of the electric field intensity and the magnetic field intensity at grid nodes (take TM_z wave as example).

the fine mesh nodes (in cell #4), and the border nodes (in cells #2 and #3). In cell #1, the traditional FDTD method is employed to obtain the transient values of $\boldsymbol{E}$ and $\boldsymbol{H}$ at the coarse nodes. In cell #4, the unconditionally stable explicit FDTD method in lossy media is used to calculate the field quantities of $\boldsymbol{e}$ and $\boldsymbol{h}$ in the fine grids. In cells #2 and #3, the $\boldsymbol{E}$ field is calculated by the $\boldsymbol{H}$ field of a portion of the coarse grids and the $\boldsymbol{h}$ field of a portion of the fine grids. It should be noted that the time steps used in all regions are the same.

Following, we will describe the calculation methods for different regions.

B. Explicit unconditional stable FDTD formulations in cell #4

A two-dimensional (2D) TM$_z$ wave propagating in a lossy medium is considered. Its Maxwell's equation in time domain (t) can be written as:

$$\begin{bmatrix} \varepsilon\partial_t+\sigma & \partial_y & -\partial_x \\ \partial_y & \mu\partial_t & 0 \\ \partial_x & 0 & -\mu\partial_t \end{bmatrix} \begin{bmatrix} E_z \\ H_x \\ H_y \end{bmatrix} = 0, \tag{1}$$

where ∂_ς represents the operator of $\partial/\partial\varsigma$, ε and σ are the dielectric constant and the conductivity of the media, respectively, and μ is the media's permeability. The wave equation corresponding to (1) is:

$$\partial_t^2 E_z + \frac{\sigma}{\varepsilon}\partial_t E_z - \partial_y^2 E_z/\varepsilon\mu - \partial_x^2 E_z/\varepsilon\mu = 0, \tag{2}$$

where ∂_ς^2 represents the second-order derivative of ς. Let $\tilde{E} = \partial_y^2 E_z/\varepsilon\mu + \partial_x^2 E_z/\varepsilon\mu$ and expand $\tilde{E}$ using the difference method to obtain:

$$\begin{aligned} \tilde{E}(i,j) = &\frac{1}{\varepsilon\mu}\left\{\frac{1}{\Delta y^2}\left[E_z(i,j+1)-2E_z(i,j)\right.\right. \\ &\left.+E_z(i,j-1)\right]+\frac{1}{\Delta x^2}\left[E_z(i+1,j)-\right. \\ &\left.\left.2E_z(i,j)+E_z(i-1,j)\right]\right\}, \end{aligned} \tag{3}$$

where i and j represent the grids in space. The matrix form of (3) is:

$$\tilde{\boldsymbol{E}} = \boldsymbol{M}\boldsymbol{E}. \tag{4}$$

Here, $\boldsymbol{M}$ is a sparse matrix representing the operator $\partial_y^2/\varepsilon\mu + \partial_x^2/\varepsilon\mu$, $\boldsymbol{E}$=[E_z(0,0), E_z(0,1), E_z(0,2), …, E_z(1,0), E_z(1,1), E_z(1,2), …, E_z(2,0), E_z(2,1), E_z(2,2), …]^T.

Taking $\tilde{E}(1,1)$ as an example, its expansion equation is:

$$\begin{aligned} \tilde{E}^n(1,1) = \frac{1}{\varepsilon\mu}\Big[&0\ \ \frac{1}{\Delta x^2}\ \ 0\ \cdots\ \frac{1}{\Delta y^2} \\ &\frac{-2}{\Delta x^2}+\frac{-2}{\Delta y^2}\ \ \frac{1}{\Delta y^2}\ \cdots\ 0\ \ \frac{1}{\Delta x^2}\ \ 0\ \cdots\Big]\boldsymbol{E} \end{aligned}. \tag{5}$$

Substituting (4) into (2), we have:

$$\frac{\partial^2 \boldsymbol{E}}{\partial t^2} + \boldsymbol{D}_\sigma\frac{\partial \boldsymbol{E}}{\partial t} - \boldsymbol{M}\boldsymbol{E} = 0, \tag{6}$$

with $\boldsymbol{D}_\sigma$ the diagonal matrix of element σ/ε.

Since $\boldsymbol{E}$ is a vector, the characteristic equation of (6) is:

$$\left(\lambda^2+\boldsymbol{D}_{\sigma N\times N}\lambda-\boldsymbol{M}_{N\times N}\right)\boldsymbol{V}_{N\times 1} = 0, \tag{7}$$

where $\boldsymbol{V}$ is the right eigenvector corresponding to each eigenvalue λ. The quantity of λ is $2N$ (N represents the number of grids), so the corresponding number of columns in $\boldsymbol{V}$ is also $2N$ [21].

After some manipulations, (7) becomes a typical eigenvalue problem as:

$$\boldsymbol{A}_{2N\times 2N}\boldsymbol{u}_i = \lambda_i\boldsymbol{u}_i, i = 1,2,\cdots,2N, \tag{8}$$

with:

$$\boldsymbol{A}_{2N\times 2N} = \begin{bmatrix} \boldsymbol{O}_{N\times N} & \boldsymbol{I}_{N\times N} \\ \boldsymbol{M}_{N\times N} & -\boldsymbol{D}_{\sigma N\times N} \end{bmatrix} \text{ and } \boldsymbol{u}_i = \begin{bmatrix} \boldsymbol{V}_i \\ \lambda_i\boldsymbol{V}_i \end{bmatrix}. \tag{9}$$

It can be seen that $\boldsymbol{A}$ is determined by space discretization and the size of $\boldsymbol{A}$ will expand as the unknown number increases. $\boldsymbol{A}$ is an asymmetric matrix and does not have orthogonality, so its eigenvalue vector $\boldsymbol{u}$ also does not have orthogonality, and λ is the eigenvalue of $\boldsymbol{A}$.

Usually, the generation of unstable modes comes from space discretization. For example, for an object with a large ε or a fine structure, the explicit FDTD algorithm requires very fine mesh generation. Thus, Δx and Δy must be very small and subject to CFL condition [22]:

$$\Delta t \le \frac{\min(\Delta x,\Delta y)}{\sqrt{2\varepsilon_r}c}, \tag{10}$$

where c is the speed of light. Therefore, Δt will become very small. According to the Nyquist sampling theorem, Δt only needs to meet $\le 1/f_{\max}$ (f_{max} is the maximum frequency of the incident wave), and the high-frequencies $>f_{max}$ corresponding to very small Δt is redundant [16]. In terms of (8), if Δt is selected beyond the CFL condition, the modes corresponding to eigenvalues that do not meet:

$$|\lambda_i| \le \frac{2}{\Delta t}, \tag{11}$$

will lead to algorithm instability. In fact, these modes correspond to redundant frequencies. Theoretically, the removal of these unstable modes will not affect the accuracy of the algorithm. Therefore, the key to breaking free from CFL constraints in algorithms lies in being able to find the unstable modes in $\boldsymbol{A}$ and remove them. However, due to the large size of $\boldsymbol{A}$, directly solving the eigenvalues of $\boldsymbol{A}$ would be time-consuming.

To achieve matrix compression, an orthogonal matrix $\boldsymbol{F}_E^T$ is left multiplied into (7):

$$\boldsymbol{F}_E^T\left[\left(\lambda^2\boldsymbol{I}+\boldsymbol{D}_\sigma\lambda-\boldsymbol{M}\right)V\right]. \tag{12}$$

According to the property that orthogonal matrix $\boldsymbol{F}_E^T$ has $\boldsymbol{F}_E^T\boldsymbol{F}_E = \boldsymbol{I}_r$, (12) can be transformed into:

$$\left(\lambda^2\boldsymbol{F}_E^T\boldsymbol{F}_E + \boldsymbol{F}_E^T\boldsymbol{D}_\sigma\boldsymbol{F}_E\lambda - \boldsymbol{F}_E^T\boldsymbol{M}\boldsymbol{F}_E\right)\boldsymbol{F}_E^T\boldsymbol{V} = 0, \quad (13)$$

i.e.

$$\left(\lambda^2\boldsymbol{I}_r + \boldsymbol{D}_{\sigma,r}\lambda - \boldsymbol{M}_r\right)\boldsymbol{V}_r = 0, \quad (14)$$

where $\boldsymbol{D}_{\sigma,r} = \boldsymbol{F}_E^T\boldsymbol{D}_\sigma\boldsymbol{F}_E$, $\boldsymbol{M}_r = \boldsymbol{F}_E^T\boldsymbol{M}\boldsymbol{F}_E$, $\boldsymbol{V}_r = \boldsymbol{F}_E^T\boldsymbol{V}$.

$\boldsymbol{F}_E$ are obtained through preprocessing, and its matrix size is $N\times a$ ($a<N$). Therefore, the matrix sizes of $\boldsymbol{D}_{\sigma,r}$, $\boldsymbol{M}_r$, and $\boldsymbol{V}_r$ are correspondingly reduced to $a\times a$, $a\times a$, and $a\times 2N$. The eigenvalue problem becomes:

$$\boldsymbol{A}_{r2a\times 2a}\boldsymbol{u}_{r2a\times 2N} = \lambda\boldsymbol{u}_{r2a\times 2N}, \quad (15)$$

with:

$$\boldsymbol{A}_{r2a\times 2a} = \begin{bmatrix} \boldsymbol{O}_r & \boldsymbol{I}_r \\ \boldsymbol{M}_r & -\boldsymbol{D}_{\sigma,r} \end{bmatrix} \text{ and } \boldsymbol{u}_{r2a\times 2N} = \begin{bmatrix} \boldsymbol{V}_r \\ \lambda\boldsymbol{V}_r \end{bmatrix}. \quad (16)$$

Obviously, the eigenvalues of (15) have not changed, but the scale of matrices A_r and u_r has significantly decreased.

By executing:

$$\boldsymbol{V}_{st} = \boldsymbol{F}_E\boldsymbol{V}_r, \quad (17)$$

the eigenvector containing stable modes can be obtained. The size of V_{st} is the same as that of $\boldsymbol{V}_r$. The stable transient $\boldsymbol{E}_{st}(t)$ can be represented as:

$$\boldsymbol{E}_{st}(t) = \boldsymbol{V}_{st}\boldsymbol{y}(t). \quad (18)$$

Substituting (18) into (2) and performing the central difference scheme on the equation, we have:

$$\left(\boldsymbol{I} + \frac{\Delta t}{2}\boldsymbol{C}_b\right)\boldsymbol{y}^{n+1} = \left(2\boldsymbol{I} + \Delta t^2\boldsymbol{C}_c\right)\boldsymbol{y}^n - \left(\boldsymbol{I} - \frac{\Delta t}{2}\boldsymbol{C}_b\right)\boldsymbol{y}^{n-1}. \quad (19)$$

C_b and C_c are calculated by:

$$\boldsymbol{C}_b = \left(\boldsymbol{V}_{st}^H\boldsymbol{V}_{st}\right)^{-1}\boldsymbol{V}_{st}^H\boldsymbol{D}_\sigma\boldsymbol{V}_{st}.$$
$$\boldsymbol{C}_c = \left(\boldsymbol{V}_{st}^H\boldsymbol{V}_{st}\right)^{-1}\boldsymbol{V}_{st}^H\boldsymbol{M}\boldsymbol{V}_{st}. \quad (20)$$

Therefore, (19) can be written as:

$$y^{n+1} = C_d y^n + C_e y^{n-1}, \quad (21)$$

in which C_d and C_e are given by:

$$\boldsymbol{C}_d = \left(\boldsymbol{I} + \frac{\Delta t}{2}\boldsymbol{C}_b\right)^{-1}\left(2\boldsymbol{I} + \Delta t^2\boldsymbol{C}_c\right)$$
$$\boldsymbol{C}_e = -\left(\boldsymbol{I} + \frac{\Delta t}{2}\boldsymbol{C}_b\right)^{-1}\left(\boldsymbol{I} - \frac{\Delta t}{2}\boldsymbol{C}_b\right). \quad (22)$$

Execute (21) and (18) to compute unconditional stable $\boldsymbol{E}_{st}(t)$ and then substitute $\boldsymbol{E}_{st}(t)$ into (1). The value of $\boldsymbol{H}_{st}(t)$ can be obtained simultaneously.

To improve efficiency, $\boldsymbol{V}_r$ and λ are not directly solved but are obtained by iterating FDTD for some steps. The specific method is as described in Algorithm 1.

Algorithm 1: Scheme procedure of finding stable eigenmodes

1. While $|y_h^n y_h| / |y_l^n y_l| > e_1$,
2. performing n steps of traditional FDTD ($n \geq \Delta t_p/\Delta t_{CFL}$. Δt_p is the time increasement of the unconditionally stable algorithm, Δt_{CFL} is the time increasement of CFL limitation);
3. $\boldsymbol{F}_E = [\boldsymbol{F}_E \quad E_z^n]$, $\boldsymbol{F}_E = \text{orth}(\boldsymbol{F}_E)$;
4. $\boldsymbol{D}_{\sigma,r} = \boldsymbol{F}_E^T\boldsymbol{D}_\sigma\boldsymbol{F}_E$, $\boldsymbol{M}_r = \boldsymbol{F}_E^T\boldsymbol{M}\boldsymbol{F}_E$. Calculate the eigenvalues and eigenvectors of matrix $[\boldsymbol{O}_r \quad \boldsymbol{I}_r;\quad \boldsymbol{M}_r \quad -\boldsymbol{D}_{\sigma,r}]$;
5. if $|\lambda_i^n - \lambda_i^{n-1}| / |\lambda_i^n| \leq e_2$, then $\boldsymbol{V}_{r,l} = [\boldsymbol{V}_{r,l} \quad V_i]$; else $\boldsymbol{V}_{r,h} = [\boldsymbol{V}_{r,h} \quad V_i]$; here, $\boldsymbol{V}_{r,l}$ is a repetitive eigenvalue, and $\boldsymbol{V}_{r,h}$ is a non-repetitive eigenvalue. V_i is the eigenvector corresponding to λ_i^n.
6. orthogonalize the eigenvectors; $\boldsymbol{V}_{r,l} = \text{orth}(\boldsymbol{V}_{r,l})$, $\boldsymbol{V}_{r,h} = \text{orth}(\boldsymbol{V}_{r,h} - \boldsymbol{V}_{r,l}\boldsymbol{V}_{r,l}^H\boldsymbol{V}_{r,h})$.
7. determine the weight of $\boldsymbol{V}_{r,l}$ and $\boldsymbol{V}_{r,h}$; $y_l = \boldsymbol{V}_{r,l}^H\boldsymbol{F}_E^H\boldsymbol{E}_z^n$, $y_h = \boldsymbol{V}_{r,h}^H\boldsymbol{F}_E^H\boldsymbol{E}_z^n$.
8. $\boldsymbol{V}_{st} = \boldsymbol{F}_E\boldsymbol{V}_{r,st}$, where $\boldsymbol{V}_{r,st}$ is the vectors of $\boldsymbol{V}_{r,l}$ whose eigenvalue satisfy (11);
9. perform iteration by (21) to calculate $\boldsymbol{y}$, and $\boldsymbol{E}_{st}$ is determined by (18).

C. Subgridding scheme in cells #2 and #3

In the subgridding scheme, properly dealing with coupling between the base and fine grid interfaces is crucial because it determines the stability and accuracy of the algorithm. However, the algorithms that can improve accuracy are often complex. In this paper, we adopt the improved separated temporal and spatial interfaces subgridding method to solve the above issues. Due to the application of the unconditional stability technique, both coarse and fine grids use the same time increment, which further reduces the complexity of the algorithm.

Taking the 2D TM wave subgridding interface shown in Fig. 2 as an example: H_{x2}, H_{x3}, H_{x6}, H_{y2}, H_{y3}, H_{y4} are the magnetic fields of the coarse grid; h_{x1}, h_{x6}, h_{x7}, h_{x8}, h_{x9}, h_{x10}, h_{y1}, h_{y2}, h_{y5} are the magnetic fields of the fine grid; $E_{z2}^{b,cor}$, $E_{z3}^{b,int}$, E_{z5}^{b}, $H_{x7}^{c,int}$ are the fields of coarse/fine grid interface, in which $E_{z2}^{b,cor}$ is located at the boundary corner. All these fields need to be particularly treated.

According to [20], E_z on the interface can be solved by:

$$E_z^{n+1} = E_z^n + \frac{\Delta t}{\mu}\frac{1}{\Delta S}\sum_i l_i H_i, \quad (23)$$

where Δt is the time step of the FDTD method and ΔS is the area of a grid. Thus:

$$E_{z5}^{b,n+1} = E_{z5}^{b,n} + \frac{\Delta t}{\mu}\frac{1}{\Delta x_c \Delta y_c}\left[\Delta x_c (H_{x7}^{c,int,n+\frac{1}{2}} - H_{x3}^{n+\frac{1}{2}}) + \frac{\Delta y_c + \Delta y_f}{2}(H_{y4}^{n+\frac{1}{2}} - H_{y3}^{n+\frac{1}{2}}) + \Delta y_f (h_{y5}^{n+\frac{1}{2}} - h_{y2}^{n+\frac{1}{2}})\right], \quad (24)$$

and:

$$E_{z2}^{b,cor,n+1} = E_{z2}^{b,cor,n} + \frac{\Delta t}{\mu}\frac{1}{\Delta x_c \Delta y_c}\left[\left(\frac{\Delta x_c + \Delta x_f}{2} H_{x6}^{n+\frac{1}{2}} + \Delta x_f h_{x6}^{n+\frac{1}{2}} - \Delta x_c H_{x2}^{n+\frac{1}{2}}\right) + \left(\frac{\Delta y_c + \Delta y_f}{2} H_{y3}^{n+\frac{1}{2}} + \Delta y_f h_{y2}^{n+\frac{1}{2}} - \Delta y_c H_{y2}^{n+\frac{1}{2}}\right)\right]. \quad (25)$$

$H^{c,int}$ comes from the interpolation of h in the fine grid [20]:

$$H^{c,int} = \sum_{i=1}^{2m-1} \frac{m - |m-i|}{m^2} h_i. \quad (26)$$

Hence, $H_{x7}^{c,int}$ can be estimated by:

$$H_{x7}^{c,int} = \frac{1}{9}h_{x6} + \frac{2}{9}h_{x7} + \frac{1}{3}h_{x8} + \frac{2}{9}h_{x9} + \frac{1}{9}h_{x10}. \quad (27)$$

Use $E_z^{b,int}$ to update h_x and h_y on the boundary. $E_z^{b,int}$ is calculated through linear interpolation. Taking $E_{z3}^{b,int}$ as an example:

$$E_{z3}^{b,int} = \frac{2}{3}E_{z2}^{b,cor} + \frac{1}{3}E_{z5}^{b}. \quad (28)$$

For ease of understanding, suppose that the current time step is n and all fields are known. We summarize the update process of the proposed subgridding scheme into the following steps:

Step #1: Calculate E^{n+1} and $H^{n+\frac{3}{2}}$(such as H_{x2}, H_{x3}, H_{x6}, H_{y3}, H_{y4}) for coarse grids by using the traditional FDTD method.

Step #2: Calculate e^{n+1} and $h^{n+\frac{3}{2}}$(such as h_{x6}, h_{x7}, h_{x8}, h_{x9}, h_{x10}, h_{y2}, h_{y5}) for fine grids by using the explicit unconditional stable FDTD formulations.

Step #3: Substitute (27) into (24) to obtain $E_{z5}^{b,n+1}$, and substitute (24), (25), into (28) to obtain $E_{z3}^{b,int,n+1}$. Thus, the fields on the coarse/fine grids interface can be updated accordingly.

It should be noted that the subgridding scheme and the unconditional stable algorithm above are analyzed and derived based on TM_z waves. The proposed method in this paper is applicable for 2D GPR numerical simulation in TM mode.

III. NUMERICAL RESULTS

A. Accuracy

To demonstrate the accuracy of this proposed subgridding unconditional stable algorithm, a square object (ε_{r2} =5, μ_{r2} =1, σ_2 =0.02 S/m) in a homogeneous medium (ε_{r1} =3, μ_{r1} =1, σ_1=0.1 S/m) is illustrated (see Fig. 3). The object has a size of 0.21×0.21 m with a center located at (0.675 m, 0.495 m). It is illuminated by a TM_z wave in the form of:

$$J_z = \delta(x - x_0, y - y_0) e^{(-((t-t_0)/t_d)^2)}. \quad (29)$$

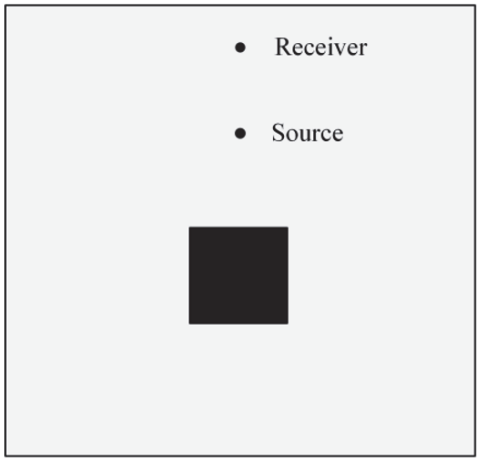

Fig. 3. Model for algorithm accuracy verification.

Here, (x_0, y_0) is the location of the source, $\delta(x - x_0, y - y_0) = 1/(\Delta x \Delta y)$, $t_0 = 0.9/f_c$, $t_d = t_0/4$, and f_c=5 MHz. The source is placed at (0.66 m, 0.9 m), and the receiver is located at (0.66 m, 1.2 m).

Two sizes of grids with Δl_{base} =30 mm and Δl_{fine} =10 mm are adopted. Their size ratio is 3. A temporal step of CFL stability condition of uniform base grids is chosen, which is three times beyond CFL condition of uniform fine grids. The total number of the eigenmodes is 800, of which 773 unstable eigenmodes need to be removed. Furthermore, we also compute the numerical problem when the size ratio increases to 5, 15, 25, 75, and the removed eigenmodes are 2287, 21621, 60542, 549121, with the total eigenmodes number 2312, 21632, 60552, 549152. When selecting different grid size ratios, the number of grids applying unconditional stable algorithm vary, so the total eigenmodes number will be different and this leads to different stable eigenmodes size. On the other side, error e_1, e_2 and FDTD step n in the unconditional stable algorithm also affects the number of stable eigenmodes. In this problem, we choose the parameters e_1, e_2, n in the procedure of finding stable eigenmodes with $e_1 = 10^{-4}$ and $e_2 = 10^{-3}$ with n=3 (grid size ratio equals 3), $e_2 = 10^{-2}$ with n=5 (grid size ratio equals 5), $e_2 = 10^{-2}$ with n=15 (grid size ratio equals 15), $e_2 = 10^{-4}$ with n =25 (grid size ratio equals 25), $e_2 = 10^{-4}$ with n=30 (grid size ratio equals 75).

The transient $E_z(t)$ at the receiver computed using the proposed algorithm are compared with the results of traditional FDTD method based on uniform grid

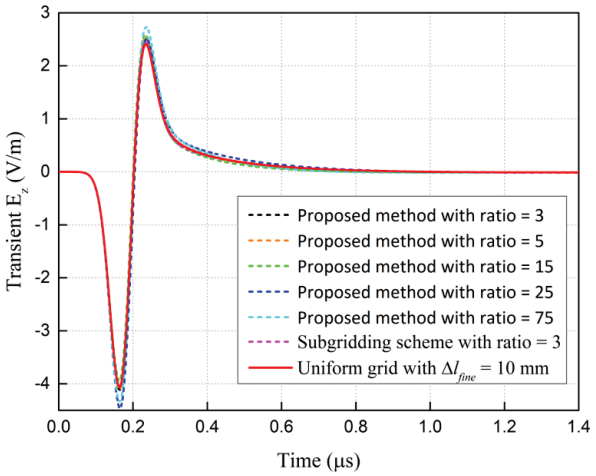

Fig. 4. Electric field computed by conventional FDTD, subgridding FDTD, and subgridding unconditional stable algorithm.

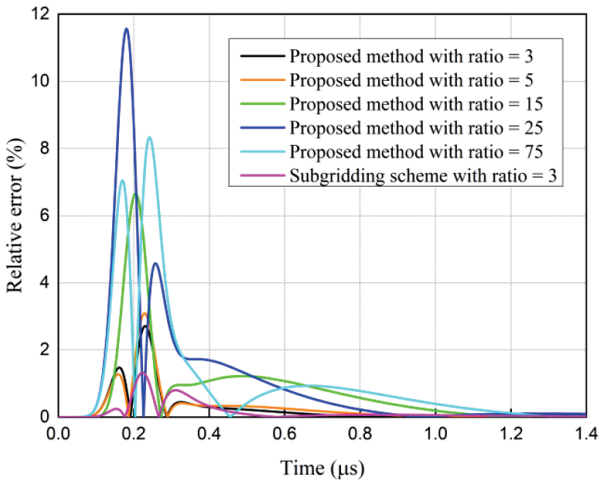

Fig. 5. Relative error of the traditional subgridding scheme and the proposed subgridding unconditional stable algorithm.

(Δl_{fine}) and traditional subgridding approach. As shown in Fig. 4, the proposed method with ratio=3 and 5 has the best agreement in our simulation; a larger ratio will lead to some accuracy loss. Although there is a gradually increasing error when ratio=15, 25, 75, it indicates that the proposed method is feasible when we use a large ratio. This proposed method will have more advantages in multi-scale electromagnetic problem simulation.

To measure the accuracy of the algorithm, a relative error is defined as:

$$\text{Error}(t) = \frac{\left|E_z(t) - E_{z,ref}(t)\right|}{\left|E_{z,ref}(t)\right|_{\max}} \times 100\%. \qquad (30)$$

The reference solution $E_{z,ref}(t)$ is obtained by conventional FDTD with Δl_{fine}. The relative errors of the traditional subgridding FDTD and the proposed method are shown in Fig. 5. It can be seen that the relative error of the proposed method with ratio=3 is less than 3%, and there is only a slight difference when ratio=3 and 5. It must be pointed out that when selecting an appropriate grid size ratio, the computational accuracy of the proposed approach is slightly lower than the subgridding scheme.

Table 1 lists the computational resource consumption of three methods. From Table 1, the following observations are made:

- The number of unknowns in the proposed method with ratio = 3, 5, 15 is 0.19, 0.22, 0.64 compared to the conventional FDTD. The proposed method with ratio = 3 reduces memory cost by 52.48% and saves computational time by 84.84% compared to that of conventional FDTD. The proposed method with ratio=5, 15 has advantages in terms of time consumption.

Table 1: Computational resource consumption of the three methods

Method	Grid Ratio	Grid Number	Memory (MB)	Time (s)
FDTD	1	70840	1.01	62.06
Subgridding Scheme	3	13364	1.80	20.05
Proposed Method	3	13364	0.48	9.41
	5	15716	1.44	9.97
	15	45116	1.90	25.06
	25	103916	5.32	84.68
	75	838916	130.13	10825.27

- Compared to the subgridding scheme, the proposed method with ratio = 3, 5 reduces memory cost by 73.33%, 20%, and saves computational time by 53.07%, 50.27%. The proposed method with ratio=15 has advantages in terms of time consumption.

In our experiment, as the grid size ratio increases from 3 to 75, the CPU time of the preprocessing procedure to find stable eigenmodes is 0.33 s, 0.49 s, 0.87 s, 1.99 s, 125.89 s, respectively. It is clear that the preprocessing time only accounts for a small portion of the total time in Table 1. In this numerical example, when we select inappropriate parameter e_1, e_2 and step size n, the main resource consumption increment will come from the preprocess of finding the stable vector $\boldsymbol{V}_{r,st}$. In our experience, e_1 is on the order of 10^{-4}, e_2 is $10^{-4}\sim10^{-2}$, and n usually equals the grid size ratio when it is not too large.

B. GPR model

Next, we apply the algorithm to the 2D GPR model, as Fig. 6 shows, while keeping the time step and spatial step unchanged. A lossy square ($\varepsilon_{r1} = 2$, $\mu_{r1} = 1$, $\sigma_1 = 0.97$ S/m) is buried under the dispersive soil ($\varepsilon_{r0} = 4$, $\mu_{r0} = 1$, $\sigma_0 = 0.004$ S/m). The size of the simulation domain is 3×3.6 m, with the object located at a depth of 1.89 m below the surface and the center at (1.245 m, -1.965 m). Its scale is 0.15×0.15 m. Tx and Rx are placed at (0.48 m, 0.09 m) and (2.46 m, 0.09 m), respectively.

A TM wave is excited by the z-component of a current source $J_z(t)$ with first derivative of the Blackman-Harris pulse as:

$$J_z(t) = \begin{cases} -\frac{2\pi}{T_s}\sum_{n=0}^{3} a_n n \sin\left(\frac{2\pi n t}{T_s}\right), & 0 < t < T_s \\ 0, & otherwise \end{cases}, \quad (31)$$

with f_c=100 MHz, T_s=0.9/f_c, $a_0 = 0.3532$, $a_1 = -0.488$, $a_2 = 0.145$, and $a_3 = -0.0102$.

Figure 7 shows comparisons of the transient $E_z(t)$ at Rx. It can be seen that the proposed method agrees well with the results of other methods. In the proposed algorithm, we compute the problem with grid ratio 3 and 5, scale of coefficient matrix $\boldsymbol{A}$ is 392×392, 1152×1152, and number of stable modes is 7 and 3. In the unconditional stable process, parameter e_1 =10^{-4}, e_2 =10^{-2}, and step size n=3, 5.

Figure 8 shows time snapshots of the electric field amplitudes in the computational domain at n = 150, 220, 290, and 330, where the Tx and Rx antennas are static.

In B-Scan simulation, Tx is moved from (0.09 m, 0.09 m) to (2.91 m, 0.09 m), with a spatial increment of 0.06. Rx also moves with Tx, and the distance between them is always 0.09 m in the x-axis direction. Figure 9 shows the contour of the echo z-component of the electric field received by Rx.

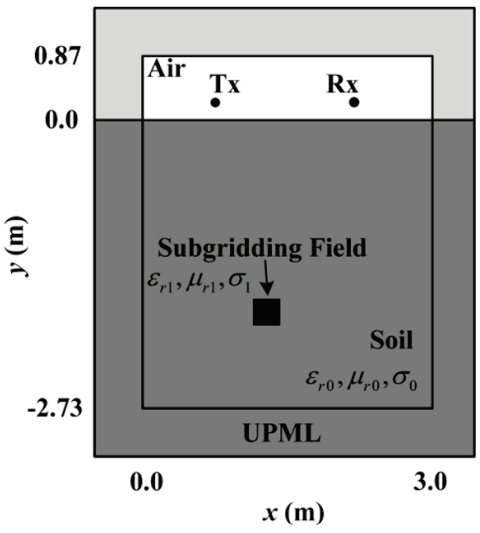

Fig. 6. Two-dimensional GPR model.

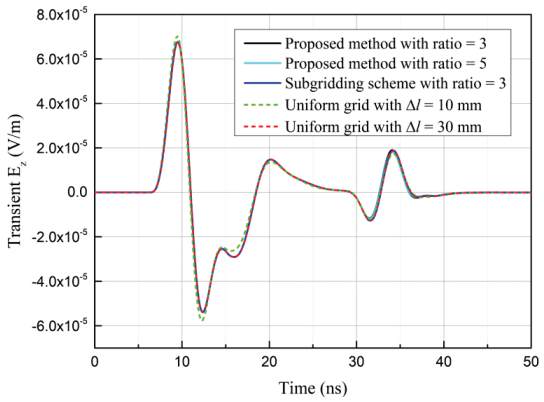

Fig. 7. Comparison of the electric fields computed by different methods.

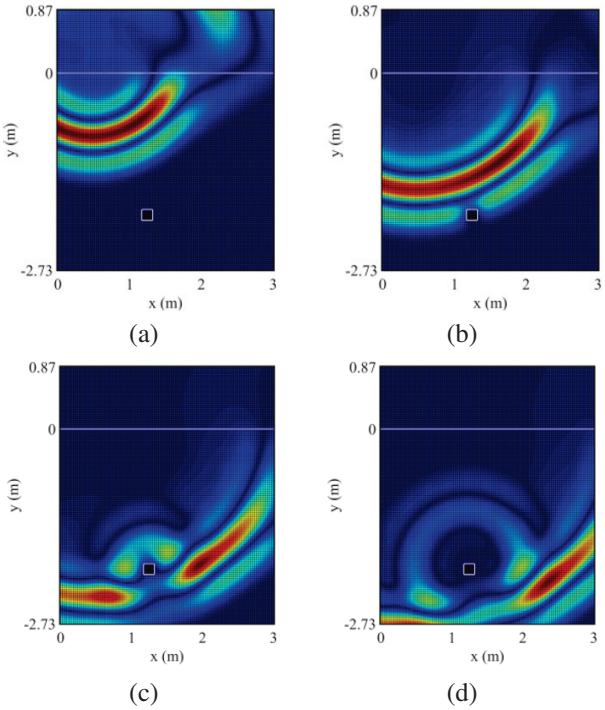

Fig. 8. Time snapshot of electric field amplitude in the computational domain: (a) n=150, (b) n=220, (c) n=290, and (d) n=330.

Computational resource consumption of the three methods in the GPR simulation are listed in Table 2. The efficiency of the proposed algorithm has been validated again. It can be seen that the proposed method has superiority in memory consuming compared to the other two methods with acceptable time increment and showing its potential in GPR simulation.

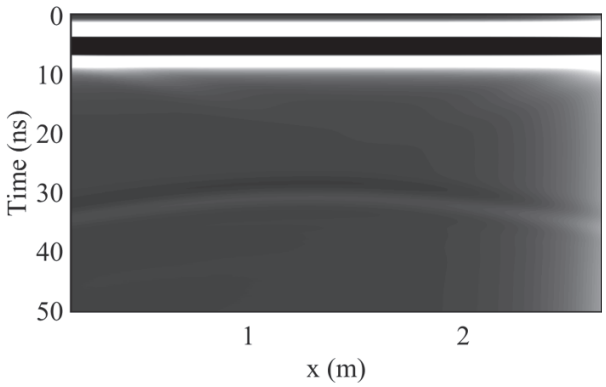

Fig. 9. Contour of the echo electric field received by Rx.

Table 2: Computational resource consumption of the three methods

Method	Grid Ratio	Grid Number	Memory (MB)	Time (s)
FDTD with $\Delta l =$ (mm) 10	1	362005	2.47	1342.11
FDTD with $\Delta l =$ (mm) 30	1	49365	0.63	12.02
Subgridding Scheme	3	49985	1.98	12.75
Proposed Method	3	49985	1.09	13.67
	5	51185	1.47	13.05

Finally, we carried out an experiment to test the performance of the proposed method when simulated in media with different electrical properties. We changed the buried object by selecting material parameter $\varepsilon_{r1} = 2$, 4, 8, and $\sigma_1 = 0$ S/m, 4 S/m, 16 S/m, respectively. There are no obvious variations in memory cost and time consumption, and the accuracy is also stable with relative error below 6%. Long-term instability will occur from the interface of the base and fine grid when low ε_{r1} and σ_1 are chosen, and can be a direction to improve the proposed method.

IV. CONCLUSION

In this paper, an explicit unconditionally stable technique is introduced into the subgridding 2D-FDTD approach and applied in GPR modeling with TM mode. A subgridding algorithm with separated temporal and spatial interfaces is proposed to solve the multiscale problem. The unconditional stable algorithm can find all the stable eigenmodes to keep numeric stability without compromising accuracy when the time step does not meet CFL conditions, and the numerical results demonstrate its good performance in terms of accuracy. In GPR simulation, this proposed method's potential in solving multiscale problems is demonstrated.

ACKNOWLEDGMENT

The authors wish to acknowledge the support of the National Natural Science Foundation of China (Grants #61761017).

REFERENCES

[1] G. Bozza, C. Estatico, M. Pastorino, and A. Randazzo, "Application of an inexact-Newton method within the second-order born approximation to buried objects," *IEEE Geoscience & Remote Sensing Letters*, vol. 4, pp. 51-55, 2007.

[2] Y. Altuncu, "A numerical method for electromagnetic scattering by 3-D dielectric objects buried under 2-D locally rough surfaces," *IEEE Transactions on Antennas and Propagation*, vol. 63, no. 8, pp. 3634-3643, 2015.

[3] K. Yee, "Numerical solution of initial boundary value problems involving Maxwell's equations in isotropic media," *IEEE Trans. Antennas Propag.*, vol. 14, no. 3, pp. 302-307, 1966.

[4] A. Taflove and S. C. Hagness, *Computational Electrodynamics: The Finite-Difference Time-Domain Method.* Boston, MA: Artech House, 2000.

[5] D. T. Prescott and N. V. Shuley, "A method for incorporating different sized cells into the finite-difference time-domain analysis technique," *IEEE Microwave and Guided Wave Letters*, vol. 2, no. 11, pp. 434-436, 1992.

[6] S. S. Zivanovic, K. S. Yee, and K. K. Mei, "A subgridding method for the time-domain finite-difference method to solve Maxwell's equations," *IEEE Transactions on Microwave Theory and Techniques*, vol. 39, no. 3, pp. 471-479, 1991.

[7] M. J. White, M. F. Iskander, and Z. Huang, "Development of a multigrid FDTD code for three-dimensional applications," *IEEE Transactions on Antennas and Propagation*, vol. 45, no. 10, pp. 1512-1517, 1997.

[8] J. Yan and D. Jiao, "An unsymmetric FDTD subgridding algorithm with unconditional stability," *IEEE Transactions on Antennas and Propagation*, vol. 66, no. 8, pp. 4137-4150, 2018.

[9] H. Al-Tameemi, J. P. Berenger, and F. Costen, "Singularity problem with the one-sheet Huygens subgridding method," *IEEE Transactions on Electromagnetic Compatibility*, vol. 99, pp. 1-4, 2016.

[10] J. Hartley, A. Giannopoulos, and C. Warren, "A Huygens subgridding approach for efficient modelling of ground penetrating radar using the finite-difference time-domain method," in *2018 17th International Conference on Ground Penetrating Radar (GPR)*, 2018.

[11] N. V. Venkatarayalu, R. Lee, Y.-B. Gan, and L.-W. Li, "A stable FDTD subgridding method based

on finite element formulation with hanging variables," *IEEE Transactions on Antennas & Propagation*, vol. 55, no. 3, pp. 907-915, 2007.

[12] K. Xiao, D. J. Pommerenke, and J. L. Drewniak, "A three-dimensional FDTD subgridding algorithm with separated temporal and spatial interfaces and related stability analysis," *IEEE Transactions on Antennas and Propagation*, vol. 55, no. 7, pp. 1981-1990, 2007.

[13] N. Diamanti and A. Giannopoulos, "Implementation of ADI-FDTD subgrids in ground penetrating radar FDTD models," *Journal of Applied Geophysics*, vol. 67, no. 4, pp. 309-317, 2009.

[14] M. R. Cabello, L. D. Angulo, J. Alvarez, I. D. Flintoft, S. Bourke, J. F. Dawson, R. G. Martin, and S. G. Garcia, "A hybrid Crank-Nicolson FDTD subgridding boundary condition for lossy thin-layer modeling," *IEEE Transactions on Microwave Theory & Techniques*, vol. 65, no. 5, pp. 1397-1406, 2017.

[15] M. Zhou, Z. David Chen, W. Fan, X. Bo, and W. Wei, "A subgridding scheme with the unconditionally stable explicit FDTD method," in *IEEE MTT-S International Conference on Numerical Electromagnetic & Multiphysics Modeling & Optimization*, Beijing, China, pp. 1-3, 2016.

[16] M. Gaffar and D. Jiao, "An explicit and unconditionally stable FDTD method for electromagnetic analysis," *IEEE Transactions on Microwave Theory and Techniques*, vol. 62, no. 11, pp. 2538-2550, 2014.

[17] J. Yan and D. Jiao, "Symmetric positive semidefinite FDTD subgridding algorithms for arbitrary grid ratios without compromising accuracy," *IEEE Transactions on Microwave Theory and Techniques*, vol. 65, no. 12, pp. 5084-5095, 2017.

[18] K. Zeng and D. Jiao, "Symmetric positive semidefinite FDTD subgridding algorithms in both space and time for accurate analysis of inhomogeneous problems," *IEEE Transactions on Antennas and Propagation*, vol. 68, no. 4, pp. 3047-3059, 2020.

[19] X.-K. Wei, X. Zhang, N. Diamanti, W. Shao, and C. D. Sarris, "Subgridded FDTD modeling of ground penetrating radar scenarios beyond the courant stability limit," *IEEE Transactions on Geoscience & Remote Sensing*, vol. 12, pp. 1-10, 2017.

[20] Z. Ye, C. Liao, X. Xiong, and M. Zhang, "A novel FDTD subgridding method with improved separated temporal and spatial subgridding interfaces," *IEEE Antennas and Wireless Propagation Letters*, vol. 16, pp. 1011-1015, 2017.

[21] F. Tisseur and K. Meerbergen, "The quadratic eigenvalue problem," *SIAM Review*, vol. 43, no. 2, pp. 235-286, 2001.

[22] R. Courant, K. Friedrichs, and H. Lewy, "Über die partiellen differenzengleichungender mathematischen physik [in German]," *Math. Ann.*, vol. 100, no. 1, pp. 32-74, 1928.

Xiao Yan Zhang received the B.S. degree in applied physics and the M.S. degree in physical electronics from Yunnan University, Kunming, China, in 2001 and 2004, respectively, and the Ph.D. degree in electromagnetic field and microwave technology from the Institute of Electronics, Chinese Academy of Sciences, Beijing, China, in 2007. Her research interests include electromagnetic computation and antenna design.

Rui Long Chen was born in Hengyang, Hunan, China, in 1996. He received the B.S. degree in communication engineering from Beijing Union University, Beijing, China, in 2018, and the M.S. degree in communication engineering from East China Jiao Tong University, Nanchang, China, in 2021. Currently, he is pursuing the Ph.D. degree in Xiangtan University, Xiangtan, China. His research interests focus on electromagnetic computation and numerical methods of partial differential equations.

Sparse Array Optimization Based on Modified Particle Swarm Optimization and Orthogonal Matching Pursuit

Daren Li and Qiang Guo

College of Information and Communication Engineering
Harbin Engineering University, Harbin, 150001, China
lidaren@hrbeu.edu.cn, guoqiang@hrbeu.edu.cn

Abstract – This paper addresses the low degree of freedom in optimization, primarily attributed to the conventional antenna array optimization methods that solely focus on the optimization of element positions, without considering the influence of element excitations. To address this issue, a sparse array optimization method is proposed based on modified Particle Swarm Optimization (PSO) algorithm and Orthogonal Matching Pursuit (OMP). This method simultaneously optimizes both the element positions and excitations to achieve the desired pattern. Initially, the compressive sensing principle is employed to establish a compressive sensing optimization model for the antenna array. Subsequently, OMP is utilized to simultaneously optimize the element positions and excitations within the antenna array. An improved PSO algorithm is then applied to iteratively update the obtained parameters, thereby further enhancing the peak sidelobe level. Experimental results demonstrate that the proposed algorithm can achieve satisfactory optimization performance.

Index Terms – Compressive sensing, orthogonal matching pursuit, particle swarm optimization algorithm, sparse array antenna.

I. INTRODUCTION

As the radio technology continues to advance, antennas have played a pivotal role in various applications such as communications, remote sensing, navigation, and radar, profoundly influencing every aspect of social life and national defense and military affairs. As the device for receiving and transmitting electromagnetic waves [1], antennas play an irreplaceable role in radio communication systems. The optimization of array antenna deployment is a crucial step in radio communication systems. To enhance performance and meet system requirements, researchers conduct optimizations of array structures by analyzing the relationship between antenna array performance and its geometric configuration [2, 3]. When the spacing between array elements adheres to certain constraints, mutual coupling among elements can be effectively reduced. Nevertheless, this often triggers the issue of grating lobes. Consequently, researchers have embarked on optimizing sparse array antenna technologies. Sparse array antennas, characterized by a smaller number of elements, offer advantages of higher degrees of freedom and broader optimization space [4], attracting extensive research and applications.

In recent years, several studies on sparse array synthesis have attempted to achieve a certain pattern definition with the minimum number of antenna elements by optimizing the excitation coefficients and positions of individual antenna elements. Pinchera et al. proposed a deterministic iterative method for synthesizing isophoric radiation patterns of aperiodic arrays with arbitrary upper limits, which can scan over a wide angle range without violating the sidelobe level constraints [5]. To address the problem of array structure design, Cui et al. introduced a novel Consensus Penalty Dual Decomposition (CPDD) method based on the concept of consensus computing. CPDD utilizes a virtual star topology network, where the central node corresponds to the global variable and each edge node corresponds to a single beam synthesis task. In the outer loop, the algorithm collects excitation vector information from the edge nodes through the central node, then integrates the information to obtain a better co-array structure [6]. Xia and Zhang proposed a new method for synthesizing sparse arrays with discrete phase constraints using Mixed-Integer Programming (MIP). The proposed method optimizes antenna positions and amplitude/phase excitations under given discrete phase constraints [7].

Existing literature on sparse array antenna optimization can be broadly categorized into global optimization [8–13], matrix pencil method (MPM) [14, 15], and compressed sensing-based array optimization algorithms [16–19]. Moreover, the intuitionistic fuzzy toolbox based on fuzzy divergence calculation will allow for more effective modeling of the implicit uncertainties and trade-offs in array optimization[20]. Global optimization algorithms transform the synthesis problem into a binary

Submitted On: October 5, 2024
Accepted On: May 27, 2025

https://doi.org/10.13052/2025.ACES.J.400603

optimization problem, systematically exploring the solution space to find the global optimal solution or a solution close to it. These algorithms are particularly suitable for optimization problems with complex, non-convex objective functions, effectively addressing the nonlinear optimization challenges in sparse arrays. Among them, evolutionary algorithms such as the Genetic Algorithm (GA) [8, 10], Particle Swarm Optimization (PSO) [11], and Differential Evolution (DE) [12, 13] have demonstrated the best performance. However, these algorithms are characterized by high computational complexity. The MPM [14, 15] can be applied to the synthesis of non-uniform arrays. By performing matrix transformations on the signals from the array antenna, MPM efficiently estimates signal sources, making it particularly effective in sparse arrays. MPM can simultaneously optimize the number of elements, element positions, and excitations in a sparse array, allowing the synthesis of sparse arrays to no longer be limited to minimizing the peak sidelobe level by optimizing element positions (and sometimes element excitations) given a fixed number of elements. This opens up new research directions for the synthesis and design of sparse arrays. Nevertheless, the complex matrix operations involved in the MPM algorithm lead to challenges in terms of high computational complexity and implementation difficulty.

Compressed Sensing (CS) technology was introduced in 2006, primarily targeting the solution of sparse signal problems. Research on the application of compressive sensing in array antennas started relatively late. Professor L. Carin from Duke University was the first to theoretically analyze the connection between random sparse arrays and compressive sensing, proving that random sparse arrays are a special case of compressive sensing [21]. The ELEDIA Research Center at the University of Trento in Italy has established a dedicated research group to explore the application of compressive sensing in the field of sparse array antennas, and they have achieved preliminary research results [22]. Experimental results have verified the potential and advantages of applying compressive sensing to the synthesis of sparse array antennas. The emergence of the CS paradigm [17] has significantly advanced the design of sparse arrays. By applying CS techniques to array antenna synthesis, sparse solutions for array antennas are sought. CS-based optimization methods for array antennas effectively reduce the number of array elements, thereby lowering the cost of array construction. Convex optimization [18] minimizes the number of elements by optimizing the weights of each element, converting the solution of the $\ell 0$ norm into that of the $\ell 1$ norm, and incorporating certain decision criteria. [19] proposes an algorithm combining Multi-Objective Particle Swarm Optimization (MOPSO) with convex optimization. Through optimization of sparse circular arrays, this algorithm suppresses grating lobes, significantly enhancing the recognizability of the main beam and improving the optimization efficiency of the algorithm. However, these methods overlook the influence of element positions on optimizing array antennas. Furthermore, it is easy for the use of optimization algorithms to get stuck in local optima during the search for global optimal solutions.

To address this, this paper proposes a joint array optimization algorithm based on the Modified Particle Swarm Optimization (MPSO) and Orthogonal Matching Pursuit (OMP), which is applied to both linear arrays and concentric circular arrays. Firstly, the optimization of linear arrays is achieved. With the main beamwidth fixed, the element positions and excitations are optimized. The results show that compared to other algorithms, this proposed algorithm can achieve a lower Peak Side-Lobe Level (PSLL). PSLL refers to the ratio of the maximum value in the sidelobes to the maximum value in the main lobe, and it is an important indicator for evaluating antenna performance, typically expressed in decibels (dB). Generally, radar systems require extremely low sidelobe levels to meet anti-interference requirements and effectively perform target search. Therefore, this parameter is often used as one of the optimization criteria in array synthesis. Secondly, considering the complexity of the array antenna model, the proposed algorithm is further applied to concentric circular arrays. By solving for the excitations of continuous current loops, relevant information about discrete elements can be obtained. According to the simulation results, under the premise of a fixed main beamwidth, although the number of required elements slightly increases, there is a significant improvement in reducing the PSLL.

The structure of this paper is organized as follows: Section II presents the proposed algorithm and model. Section III conducts simulations and analyses of the proposed algorithm, along with a comparative analysis with existing sparse array optimization algorithms. Section IV summarizes and concludes the paper.

II. METHOD DESCRIPTION

A. Array structure model

1. Linear array

As shown in Fig. 1, there are $2N+1$ array elements symmetrically distributed on both sides of the x axis, with a spacing of $\Delta x_i, i \in [1,N]$ between adjacent elements. The directional pattern, as a direct representation of an antenna's radiation characteristics, can be used to determine the antenna's directional properties. It not only depicts the spatial distribution of energy when the antenna emits electromagnetic waves but also characterizes the spatial filtering characteristics when receiving electromagnetic waves. Based on the obtained directional pattern, the parameters of the main lobe and side

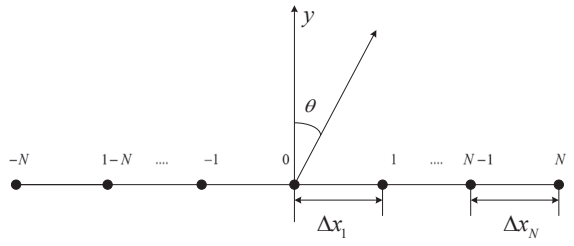

Fig. 1. A symmetric linear array with $2N+1$ elements.

lobes can be determined. Based on the superposition principle, the directional pattern function expression of this linear array is

$$F(\theta) = I_0' f_0(\theta) + \sum_{n=1}^{N} (I_{-n}' e^{jkx_{-n}\sin\theta} f_{-n}(\theta)) + \sum_{n=1}^{N} (I_n' e^{jkx_n \sin\theta} f_{-n}(\theta)), \quad (1)$$

where $I_n' = I_n e^{j\beta}$ represents the excitation of the nth element, $k = 2\pi/\lambda$, λ is the wavelengths, x_n is the position of the nth element, θ is the signal elevation angle, and $\theta \in [-\pi/2, \pi/2]$. When the element factor $f_n(\theta) = n$, $n \in [-N, N]$, and when each element adopts equal amplitude and phase excitation (let $I_n' = 1$), then (1) can be simplified as

$$F\left(\theta\right) = 1 + 2\sum_{n=1}^{N} \cos(kx_n \sin\theta). \quad (2)$$

2. Concentric Ring Array

The Concentric Ring Array (CRA) is composed of multiple concentric circles, with its array elements located on the circles under certain constraints. Its structure is shown in Fig. 2. Assuming there are N_r circles, the radius of the nth circle is $r_n (1 \le n \le N_r)$, and its pattern is shown in (3)

$$F(u,v) = 1 + \sum_{n=1}^{N_r} \omega_n \sum_{m=1}^{N_n} \exp[j\frac{2\pi}{\lambda} r_n(\cos\varphi_m u + \sin\varphi_m v)], \quad (3)$$

where ω_n is the excitation weight of the nth ring, and the array element positions are $(r_n \cos\varphi_m u, r_n \sin\varphi_m v)$, $u = \sin\theta\cos\varphi$, $v = \sin\theta\sin\varphi$, $\varphi_m = 2\pi(m-1)/N_n$. When $\omega_n = 1$, i.e., the excitation of each array element is fixed, (3) can be transformed into (4)

$$F(\theta,\varphi) = 1 + \sum_{n=1}^{N_r} \sum_{m=1}^{N_n} e^{j\frac{2\pi}{\lambda} r_n \sin\theta\cos(\varphi-\varphi_m)}. \quad (4)$$

For a concentric ring array with uniformly distributed array elements, if the spacing between adjacent array elements in the nth ring is d_n, then, given the radius

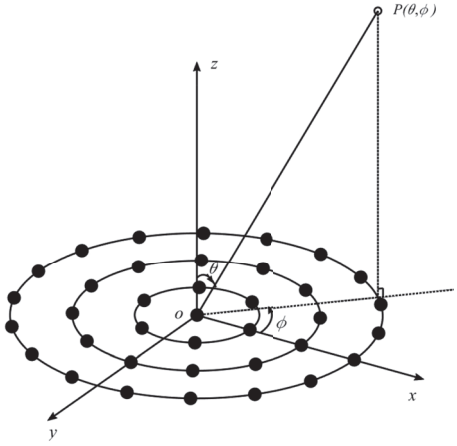

Fig. 2. Concentric ring array structure.

of the ring, the number of array elements in that ring is

$$N_n = \left[\frac{2\pi r_n}{d_n}\right], d_c \le d_n \le \lambda, n = 1,2,...,N_r, \quad (5)$$

where d_c is the defined minimum spacing between array elements, and it is assumed that the spacing between adjacent array elements is not greater than λ. Then, the number of array elements on the ring should satisfy

$$N_{n-\min} = \left[\frac{2\pi r_n}{d_c}\right] \le N_n \le \left[\frac{2\pi r_n}{\lambda}\right] = N_{n-\max}. \quad (6)$$

When the total number of concentric ring arrays is N, then it needs to satisfy

$$\sum_{n=1}^{N_r} N_n = N. \quad (7)$$

When this model imposes constraints on the total number of array elements, i.e., satisfying (7), controlling the total number of array elements becomes a critical issue. It is necessary to ensure that the total number of array elements remains constant during the optimization process while also ensuring a reasonable distribution of array elements on each ring. [23] proposes a method of linearly weighting the number of array elements, comparing linear models with Gaussian models, and ultimately derives a relationship between the radius of the array elements and the proportion of the total number of array elements, as shown in (8)

$$f(r_n) = a(\sin(r_n - \pi)) + b((r_n - 10)^2) + c, \quad (8)$$

where $f(r_n)$ represents the full array occupancy ratio of the number of array elements in the nth ring, r_n is the radius of the nth concentric ring. a, b, and c are three constants, which can be solved according to the optimization results in the known literature. After determining the full array occupancy ratio, the number of array elements on

each ring can be determined

$$N_n = \lfloor f(r_n) N_{n-\max} \rfloor = \left\lfloor f(r_n) \frac{2\pi r_n}{\lambda} \right\rfloor. \quad (9)$$

B. Modified Particle Swarm Optimization

The PSO algorithm is combined with adaptive mutation and crossover operations, where the mutation vector is influenced by the individual optimal vector. This process not only maintains the diversity of the population during the iteration process but also ensures that the information of high-quality particles is not destroyed. Adaptive mutation can intervene when the population gets trapped in a local optimum by randomly changing the position or velocity of some particles, enabling them to escape the current optimal region and explore other under-explored areas. The flow of the proposed MPSO algorithm is as follows:

Step 1: Initialize the population

Taking the concentric circular array as an example, suppose the aperture of the concentric circular array is R, the minimum spacing between adjacent rings is Δd, the minimum spacing between array elements in the same ring is d_c, the number of populations is NP, where C is the minimum interval between rings to meet the requirements of the array antenna, and $[x_1, x_2, ..., x_{N_r}]$ is the margin of the rings to form the original mapping vector. Then, the radius of the rings can be expressed as

$$\begin{cases} [r_1, r_2, ..., r_{N_r}] = C + [x_1, x_2, ..., x_{N_r}] \\ C = [\Delta d, 2\Delta d, ..., N_r \Delta d] \end{cases}. \quad (10)$$

When the total number of array elements is fixed, the number of elements on each ring can be determined by (8) and (9). According to (10), the value of its peak sidelobe level is related to $[x_1, x_2, ..., x_{N_r}; N_1, N_2, ..., N_{N_r}]$. Based on the obtained initial population, the peak sidelobe level corresponding to any vector in the population can be determined. Based on the merits of the obtained results, the partial optimal solution *pbest* and the globally optimal solution *gbest* are determined. Optimizing $[x_1, x_2, ..., x_{N_r}]$ can reduce the search space from $[0, R]$ to $[0, R - N_r \Delta d]$, accelerating the search speed and facilitating the acquisition of the optimal solution.

Step 2: Update speed and location information

Based on the characteristics of the PSO algorithm, during each iteration process, the position and velocity variables are updated according to the obtained information, as follows

$$\begin{aligned} \mathbf{v}_i = & \omega(k) \cdot \mathbf{v}_i + C_1 rand \cdot (\mathbf{p}_i - \mathbf{v}_i) + \\ & C_2 rand \cdot (\mathbf{g} - \mathbf{v}_i), \end{aligned} \quad (11)$$

$$\mathbf{x}_i = \mathbf{v}_i + \mathbf{x}_i, \quad (12)$$

where C_1 and C_2 are acceleration factors, with C_1 being the individual learning factor for each particle and C_2 being the social learning factor for particles. $\mathbf{p}_i$ represents the position vector corresponding to the individual extremum $pbest_i$ of the ith swarm, and $\mathbf{g}$ represents the position vector corresponding to the global optimum $gbest$. $\omega(k)$ is the inertia factor, which is non-negative. In this paper, a linearly decreasing inertia weight is adopted.

$$\omega(k) = \omega_{start} (\omega_{start} - \omega_{end})(T_{\max} - k)/T_{\max}, \quad (13)$$

where $T_{\max}$ represents the maximum number of iterations, and k indicates the current iteration number. ω_{start} stands for the initial weight, ω_{end} for the final weight, and $\omega_{start} > \omega_{end}$. During the iteration process, the inertia weight decreases linearly from ω_{start} to ω_{end}. At the initial stage of iteration, the inertia weight is larger, which leads to stronger global search capability; as the number of iterations increases, the inertia weight gradually decreases, which facilitates the algorithm's precise search in local areas. The obtained v_{ij} and x_{ij} need to satisfy the following formula

$$\begin{cases} v_{\min} \le v_{ij} \le v_{\max}, i = 1, 2, ..., NP; j = 1, 2, ..., N_r \\ 0 \le x_{ij} \le R - N_r \Delta d \end{cases}. \quad (14)$$

Step 3: Mutation

This paper adopts adaptive mutation, and the generated mutation vector is as follows

$$\mathbf{y}_i^k = \mathbf{g}^k + F \cdot (\mathbf{x}_{r_1}^k - \mathbf{x}_{r_2}^k), i = 1, 2, ..., NP, \quad (15)$$

where $\mathbf{g}^k$ represents the position vector corresponding to the global optimal solution during the kth iteration. r_1, r_2 are distinct positive integers in $[1, NP]$, and none of them are equal to the target vector index i.

Step 4: Crossover

To increase the diversity of disturbance variables, a crossover operation is introduced. Define the test variable $\mathbf{u}_i$ as

$$\mathbf{u}_i = (u_{i1}, u_{i2}, ..., u_{iN}) \; i = 1, 2, ..., NP, \quad (16)$$

$$u_{ij} = \begin{cases} y_{ij}, b(j) \le CR \text{ or } j = br(i) \\ x_{ij}, b(j) > CR \text{ and } j \ne br(i) \end{cases}, \quad (17)$$

$$i = 2, ..., NP; j = 1, 2, ..., N,$$

where CR is the crossover operator, $b(j)$ represents the jth estimated value generated from a set of random numbers between $[0, 1]$. $br(i) \in [2, NR]$ denotes a randomly selected integer, used to ensure that at least one set of parameters can undergo crossover.

Step 5: Update the optimal solution

Calculate the fitness function to determine whether $\mathbf{u}_i$ can become a member of the next generation. Compare the fitness of vector $\mathbf{u}_i$ in the experiment with that of vector $\mathbf{x}_i$ in the population, and retain the better one. Then, based on the obtained population, update the individual optimal and global optimal solutions, and proceed to the next iteration until the specified conditions are met.

The flowchart of this algorithm is shown in Fig. 3.

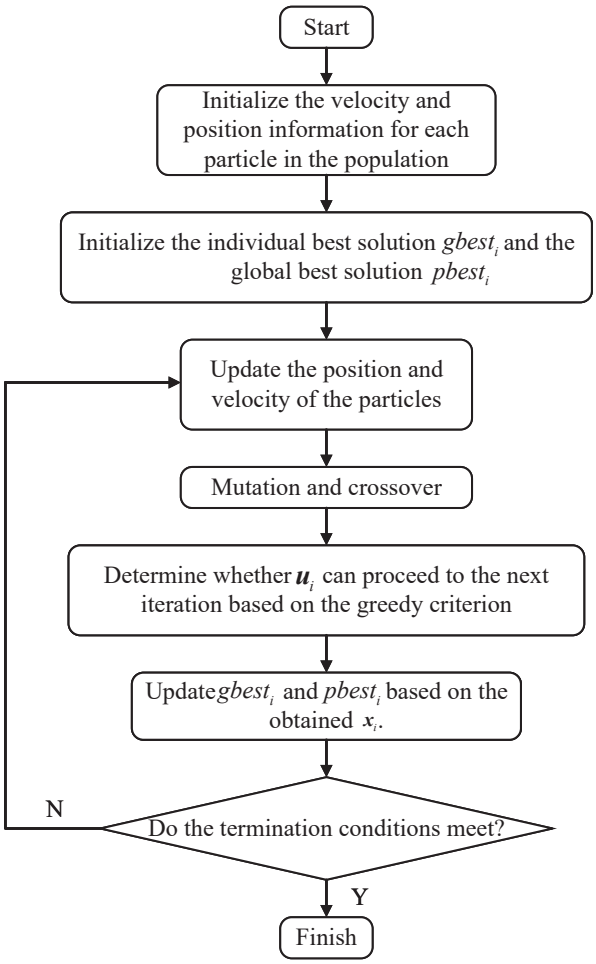

Fig. 3. Flow chart of MPSO.

C. Optimization of linear array by MPSO-OMP

For sparse linear arrays, their array structure is simple, and it is often difficult to obtain the desired radiation characteristics by optimizing only the array element positions. Moreover, the degree of freedom for position optimization is low, resulting in limited optimization of peak sidelobe levels. Therefore, this section utilizes the OMP algorithm to simultaneously optimize the positions and excitations of the array elements in the linear array, and combines the proposed MPSO algorithm to iteratively update the obtained parameters, which is conducive to achieving better peak sidelobe levels. The algorithm flow is as follows:

Step 1: Optimization model construction

For a linear array with N array elements, its pattern function is as follows

$$F(d,\theta)=\sum_{i=1}^{N}\omega_i e^{(j\frac{2\pi}{\lambda}d_i\sin\theta)}=\mathbf{A}(d)\omega. \tag{18}$$

From the above equation, it can be seen that the two vectors that affect its pattern function are the array element positions and the array element excitations. In the process of joint optimization, the obtained PSLL is used as the performance evaluation index. Assuming that the minimum spacing between adjacent array elements is d_c, and the desired main beam is $F_d(\theta_k)(\theta_k\in\Theta_M)$, where Θ_M is the shaping area of the main beam, the optimization model can be expressed as

$$\begin{cases}\min PSLL(\mathbf{d},\omega)\\ PSLL(\mathbf{d},\omega)=\max\left\{\left|\frac{F(\mathbf{d},\omega)}{\max F}\right|\right\}\\ d_{i+1}-d_i\geq d_c, 1\leq i\leq N-1\\ d_1=0\\ |F(\theta_k)-F_d(\theta_k)|<\varepsilon,\theta_k\in\Theta_M\end{cases}. \tag{19}$$

Step 2: Population initialization

Initialize the position vector d, and establish an OMP sparse recovery model based on the desired shaping main beam $F_d(\theta_k)$. Solve for the corresponding array element excitation vector of the position vector d.

$$\begin{cases}\min PSLL(\mathbf{d},\omega)\\ s.t.\left|F(\theta_k)-F_d(\theta_k)\right|<\varepsilon,\theta_k\in\Theta_M\end{cases}. \tag{20}$$

Based on $\sum_{n=1}^{N_r}\omega_n J_0(\frac{2\pi}{\lambda}r_n\sin\theta)$, the corresponding PSLL is solved, and the individual best value and the global optimal value in the population are determined. The obtained results are then carried over to the next iteration.

Step 3: Information updating and mutation

Utilize the velocity information of the PSO algorithm to update its position information. Generate a mutation vector through adaptive mutation based on the global optimal solution, and select the results. The specific operation process is detailed in II.B.

Step 4: Optimal solution update

Substitute the obtained array element positions into (20), with the peak sidelobe level as the optimization objective, and determine the array element excitations under the condition that the main beam does not change significantly. Based on the results obtained, update the individual optimal solution and the global optimal solution, and carry the results into the next iteration process. When the number of iterations reaches the maximum iteration count, stop the iteration, and the global optimal solution obtained is the optimal result from the optimization process.

D. Optimization of concentric ring array by MPSO-OMP

Unlike linear arrays, concentric ring arrays have more parameters that affect the radiation pattern,

including element positions, ring radii, the number of elements, and element excitations. To achieve a lower peak sidelobe level, this section conducts a multi-variable joint optimization of concentric circular arrays with uniformly distributed elements to obtain better radiation characteristics. For the concentric circular array structure shown in Fig. 2, its radiation pattern can be represented by (4). The radiation pattern function of the concentric circular array can be equivalently substituted using the zeroth-order Bessel series, and the substituted formula is shown below

$$\begin{aligned} F(\theta) &= \sum_{n=1}^{N_r} \omega_n J_0\left(\frac{2\pi}{\lambda} r_n \sin\theta\right) \\ &= \left[J_0\left(\frac{2\pi}{\lambda} r_1 \sin\theta\right), ..., J_0\left(\frac{2\pi}{\lambda} r_{N_r} \sin\theta\right) \right] \begin{bmatrix} \omega_1 \\ \omega_2 \\ \vdots \\ \omega_{N_r} \end{bmatrix} \\ &= \mathbf{A}(\theta)\omega. \end{aligned} \tag{21}$$

As can be seen from, (21) the radiation pattern function at this time only depends on the radiation angle θ, the ring radius r_n, and the excitation matrix ω. This section also adopts the equivalent form of the Bessel series to solve the radiation pattern of the circular array. Similarly, the excitation vector of the continuous current loop is first obtained, and then it is equivalently replaced by discrete elements. The number of elements and excitation amplitudes on the corresponding ring are determined based on minimizing the matching error value. Different from the reconstruction process, for the radius variable in the steering vector $\mathbf{A}(\theta)$, this section does not adopt a small step size Δr similar to that established in the reconstruction process. Instead, it utilizes a set of random numbers that meet the requirements, which are randomly generated during the initialization process of the MPSO algorithm. The specific steps are as follows:

Step 1: Optimization model construction

Based on the above description, under the constraint of satisfying the main beam conditions, the optimization process for the concentric circular array mainly consists of two parts. Firstly, the corresponding ring radii and excitation matrices under continuous current loop excitation are obtained. Then, the discrete elements are used for equivalent substitution to determine the number of uniformly distributed elements and the excitation amplitudes of each ring. The optimization model can be composed of two parts, as shown (22) and (23)

$$\begin{cases} \min PSLL(\mathbf{r}, \omega) \\ PSLL(\mathbf{r}, \omega) = \max\left\{ \left| \frac{F(\mathbf{r}, \omega)}{\max F} \right| \right\} \\ r_{i+1} - r_i \geq \Delta d, 1 \leq i \leq N_r \\ |F(\theta_k) - F_d(\theta_k)| < \varepsilon, \theta_k \in \Theta_M \end{cases}, \tag{22}$$

$$\begin{cases} \min \gamma(N_1, N_2, ..., N_{N_r}) \\ \gamma = \dfrac{\int_0^{2\pi} \int_0^{\pi/2} \left| \sum_{n=1}^{N_r} I_n \sum_{m=1}^{N_n} e^{j\frac{2\pi}{\lambda} r_n \sin\theta \cos(\varphi - \varphi_{nm})} - \omega_n J_0\left(\frac{2\pi}{\lambda} r_n \sin\theta\right) \right|^2 d\theta d\varphi}{2\pi \int_0^{\pi/2} \left| \omega_n J_0\left(\frac{2\pi}{\lambda} r_n \sin\theta\right) \right|^2 d\theta} \\ I_n = \omega_n / N_n, 1 \leq n \leq N_r \end{cases}. \tag{23}$$

Step 2: Population initialization

For this model, the initial values of the ring radii are first determined. When the minimum spacing between adjacent rings is constrained to Δd, and the array aperture is R, the initialization of the radii for N rings can be set as follows

$$\begin{cases} \mathbf{r} = rand(1, N_r) \cdot (R - \Delta d \cdot N_r) \\ \mathbf{r} = sort(\mathbf{r}, 2) \end{cases}. \tag{24}$$

Based on the initialized vector, the OMP algorithm is utilized to solve for the excitation matrix ω of the continuous current loop, with the obtained element radii as known quantities, under the condition of a fixed main beam. Through calculations based on the obtained information, the individual optimal solution $pbest_i$ and the global optimal solution $gbest$ within the population can be determined.

Step 3: Information update and mutation

The initialization results are brought into the iteration process to update the particle information. To increase population diversity, mutation and selection operations are performed on relevant particles, with the specific operational process as described earlier.

Step 4: Update optimal solutions

The individual optimal solution and global optimal solution are updated based on the obtained results. The criterion for whether to update is to determine if the peak sidelobe level of the obtained result is more optimal, and

the particle information corresponding to the lower peak sidelobe level is retained.

Step 5: Equivalent substitution of discrete elements for continuous current loop

After obtaining the optimal solution corresponding to the continuous current loop excitation matrix ω through iteration, according to (25), the number of uniformly distributed elements on each ring can be determined simply by specifying the total number of elements. Based on the number of elements on each concentric ring, the matching error value between the concentric circular array under discrete element conditions and the continuous current loop excitation can be determined. By finding the number of elements that minimizes matching error value, the equivalent substitution of the continuous current loop can be completed, and the excitation amplitudes of the discrete elements on the rings can be obtained.

$$N_n = \begin{cases} floor(N \times \omega_n / \sum_{i=1}^{N_r} \omega_i), n = 1 \\ floor\left\{ \frac{(N - \sum_{i=1}^{n-1} N_i)\omega_n}{\sum_{i=1}^{N_r} \omega_i} \right\}, n = 2,3,...,N_r \end{cases} . \quad (25)$$

III. NUMERICAL EXAMPLES

A. MPSO-OMP optimization for linear array

For sparse linear arrays, their array structure is simple, and it is often difficult to obtain the desired radiation characteristics by optimizing only the element positions. Moreover, the degree of freedom for position optimization is low, limiting the optimization of PSLL. [24] proposes the IGA-EDSPSO algorithm to jointly optimize the element positions and excitations in linear arrays. This algorithm combines Improvements of Genetic Algorithm (IGA) and the modified PSO algorithm. By comparing the results obtained by the hybrid algorithm with those of the two individual algorithms, it is found that the optimization results of the hybrid algorithm are relatively excellent. This section will utilize the MPSO-OMP algorithm to jointly optimize the element positions and excitations in linear arrays. In the simulation process of [24], the array aperture is constrained to 9.744λ, the total number of elements is 17, and the minimum spacing between adjacent elements is 0.5λ. Under these conditions, the IGA-EDSPSO algorithm achieves a PSLL of -26.67 dB, with a corresponding main beam width (FNBW) of 17.4° in the pattern diagram. [25] proposes the IWO-CVX algorithm, which combines CVX technology with Invasive Weed Optimization (IWO) and applies it to the optimization process of sparse linear arrays. The simulation conditions are the same as those for IGA-EDSPSO.

To verify the effectiveness of the proposed algorithm in optimizing sparse linear arrays, the optimization of sparse linear arrays is conducted under the same conditions. The results obtained by this algorithm are compared with those in [24] and [25]. During the optimization process, the main beam width is also constrained to 17.4°. First, 10 independent simulation experiments are conducted for the proposed algorithm, with $C_1 = C_2 = 1.492$, $F_0 = 0.5$, $CR = 0.9$, population size $NP = 30$, and maximum number of iterations $T_{\max} = 50$. The convergence curves of the Monte Carlo simulation values obtained from the 10 independent experiments are shown in Fig. 4.

According to Fig. 4, during the optimization process with a total of 50 iterations, most of the results tend to stabilize after 15 iterations and remain unchanged in the later stages. However, a few results show variations during the 30th to 45th iterations. Although the convergence curves of the obtained results exhibit some fluctuations in the later stages of optimization, the number of iterations is only 50 and, under a limited number of iterations, the results obtained are relatively impressive. The Monte Carlo simulation values, i.e., PSLLs, obtained from the 10 independent experiments are shown in Table 1.

According to Table 1, the optimal PSLL obtained from 10 independent experiments is -35.17 dB, the worst PSLL is -34.21 dB, and the average PSLL is -34.84 dB. Compared with the results obtained by the IGA-EDSPSO algorithm, the optimal PSLL obtained by the MPSO-OMP algorithm is optimized by 8.5 dB, and the worst PSLL is optimized by 7.54 dB, with an optimization ratio of approximately 28.3% to 31.9%. Therefore, taking PSLL as the performance evaluation index and under the condition of the same main beamwidth, the proposed algorithm exhibits significant superiority in optimizing sparse linear arrays compared to the IGA-EDSPSO algorithm. This paper also compares the results

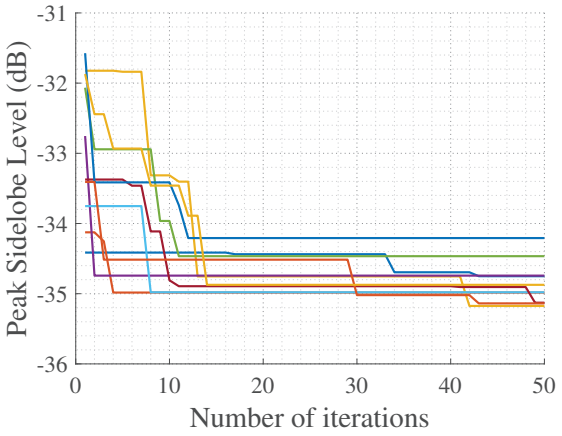

Fig. 4. The convergence curves corresponding to the results of the 10 independent experiments.

Table 1: PSLLs obtained from 10 independent experiments

No.	1	2	3	4	5	6	7	8	9	10
PSLL	37.45	34.98	35.17	34.74	34.74	34.98	35.13	34.21	35.14	34.87

with those obtained by the IWO-CVX algorithm proposed in [25]. Under the same conditions, the optimal PSLL obtained by the IWO-CVX algorithm after 10 independent experiments with a maximum number of iterations of 50 is -33.85 dB, and the worst PSLL is -33.62 dB. The results obtained by the proposed algorithm, both optimal and worst PSLL, are superior to those obtained by the IWO-CVX algorithm. Moreover, the worst PSLL obtained by the proposed algorithm is approximately 0.36 dB better than the optimal PSLL obtained by the IWO-CVX algorithm. This result demonstrates that under the condition of the same main beamwidth, the optimization results of the MPSO-OMP for sparse linear arrays are superior to those obtained by the IWO-CVX algorithm, making it more suitable for joint optimization of element positions and element excitations. Figure 5 shows the comparison of the optimal array patterns, and Table 2 presents the excitation amplitudes and element positions obtained from the experiments.

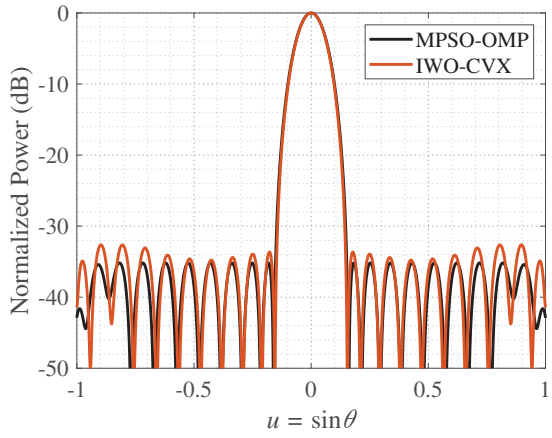

Fig. 5. Comparison of optimal array pattern obtained by MPSO-OMP and IWO-CVX.

B. MPSO-OMP optimization for concentric ring array

Chen et al. employ a Modified Genetic Algorithm (MGA) to optimize a concentric ring array, jointly optimizing the array element positions and the number of array elements for a 6-ring array under the condition that the aperture $R = 4.7\lambda$ [9]. The experimental results indicate that this algorithm achieves a PSLL of -28.33 dB, with a total of 142 array elements in the array. This paper compares with this algorithm by optimizing the relevant parameters of the concentric ring array under the same aperture width and number of rings, using the peak sidelobe level as the performance evaluation metric for simulation experiments.

To ensure that the main beam correlation coefficient remains unchanged after the experiment, the main beam width is constrained during this simulation process. The main beam width obtained in the pattern generated by the MGA algorithm is 16.9° and, similarly, this paper also constrains the main beam width to 16.9° during the simulation process. Based on the above analysis, the simulation analysis of the concentric ring array using the MPSO-OMP algorithm consists of two parts: first, solving the continuous current loop excitation variables using OMP to determine the ring radii and continuous current loop excitations; second, determining the number of array elements for each ring under a uniform distribution based on the obtained results. This section conducts five independent simulation experiments for the first part of the operation, which are carried out when the population size $NP = 30$ and there are 50 iterations. The convergence curves obtained from the results are shown in Fig. 6.

As shown in Fig. 6, the algorithm exhibits excellent convergence performance under continuous current loop excitation. Despite only 50 iterations, the results gradually stabilize after the 25th iteration, approaching the final optimized results. Moreover, the results from the five experiments show little variation, all converging around -31.5 dB. Therefore, this paper analyzes the

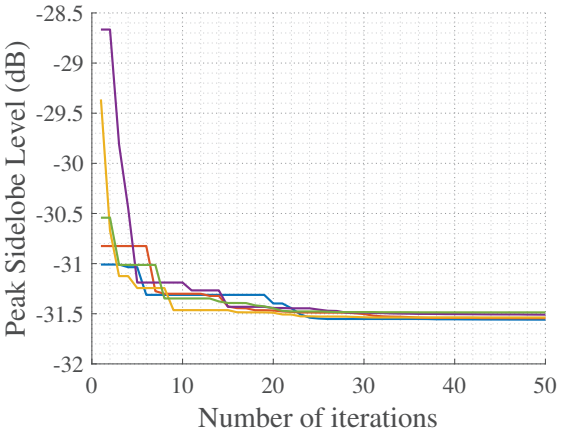

Fig. 6. Convergence curves corresponding to the five independent experiments.

‘

Table 2: Comparison of joint optimization results for sparse array of array elements

Element Number	IWO-CVX Optimal Array		MPSO-OMP Worst Array		MPSO-OMP Optimal Array	
	Element Positions	Excitation Amplitudes	Element Positions	Excitation Amplitudes	Element Positions	Excitation Amplitudes
1	0	0.225	0	0.155	0	0.193
2	0.765	0.315	0.726	0.219	0.702	0.270
3	1.353	0.289	1.282	0.338	1.339	0.388
4	1.867	0.524	1.910	0.501	1.952	0.513
5	2.581	0.788	2.606	0.628	2.561	0.667
6	3.270	0.769	3.113	0.548	3.171	0.752
7	3.770	0.661	3.645	0.835	3.711	0.727
8	4.313	0.854	4.314	0.997	4.241	0.870
9	4.820	0.709	4.994	1	4.849	1
10	5.383	1	5.641	0.920	5.482	0.924
11	6.091	0.975	6.237	0.718	6.019	0.687
12	6.728	0.652	6.738	0.602	6.522	0.718
13	7.238	0.574	7.313	0.636	7.101	0.645
14	7.834	0.487	7.890	0.415	7.680	0.523
15	8.354	0.327	8.412	0.326	8.310	0.447
16	8.948	0.321	9.027	0.307	9.034	0.229
17	9.744	0.228	9.744	0.163	9.744	0.187

Table 3: Parameters corresponding to the optimal array obtained by MPSO-OMP

Number of Rings	1	2	3	4	5	6
Current Loop Excitation	0.2434	6.271	0.9919	1	0.8384	0.9586
Ring Radius	0.5436	1.2703	2.0792	2.9170	3.7587	4.7
PSLL (dB)	-31.5445					

optimal array obtained from the five experiments and determines the number of array elements on the rings based on the relevant continuous current loop excitations and ring radii obtained under these conditions. The normalized continuous current loop excitations and ring radii corresponding to the optimal array are shown in Table 3.

By minimizing the matching error as the criterion, the total number of corresponding array elements can be determined, thereby obtaining the number of array elements uniformly distributed on each ring. The results obtained are presented in Table 4 along with the relevant data from the MGA algorithm.

According to Table 4, when the array aperture is $R = 4.7\lambda$, the number of rings is 6, and the main beam width remains consistent, the PSLL obtained by MPSO-OMP is approximately 3.2145 dB lower than the optimal PSLL achieved by the MGA algorithm reported in the literature, demonstrating a significant optimization effect. Although the number of array elements increases by 5, which is about 3.5% of the original array, the PSLL has been greatly improved, thus, the impact of the increased number of array elements can be neglected. The results obtained in this paper correspond to the three-dimensional pattern and array elements as shown in Fig. 7. The comparison of patterns at $\varphi = 0°$ between the results obtained in this paper and those by MGA is illustrated in Fig. 8.

As can be seen from Fig. 8, the MPSO-OMP

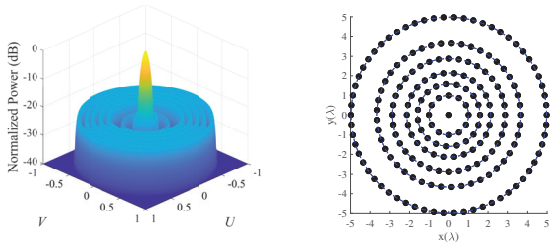

(a) (b)

Fig. 7. The optimal array's three-dimensional pattern and element distribution obtained by MPSO-OMP.

Table 4: Comparison of results obtained by MPSO-OMP and MGA

Method Number	MGA		MPSO-OMP		
	Ring Radius	Number of Elements	Ring Radius	Number of Elements	Excitation Amplitudes
1	0.7604	9	0.5436	7	1
2	1.3180	16	1.2703	20	0.9019
3	2.0969	26	2.0792	29	0.9124
4	2.9305	30	2.9170	32	0.8989
5	3.7852	27	3.7587	27	0.8931
6	4.7000	33	4.7000	33	0.8355
Number of elements	142		149		
Main beam width	16.9°		16.9°		
PSLL (dB)	-28.33		-31.5445		

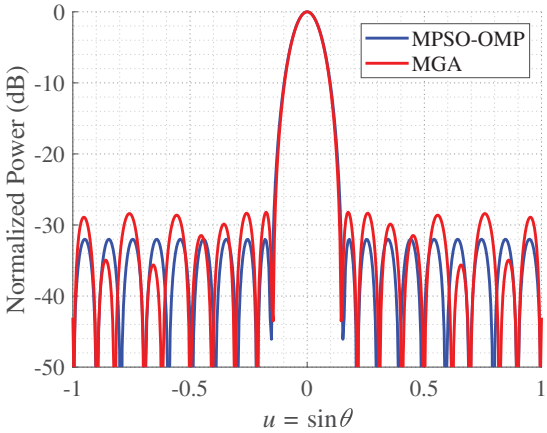

Fig. 8. Comparison of directional patterns between results obtained by MPSO-OMP and MGA.

algorithm can achieve a lower PSLL. This is because MPSO-OMP optimizes the excitation of the array elements in the array by utilizing the OMP sparse recovery principle, while keeping the fitness calculation function unchanged. Although this algorithm can achieve a lower sidelobe level, it requires a relatively large amount of computation and a longer calculation time, making it suitable for antenna systems with high requirements for sidelobe levels.

IV. CONCLUSION

In this paper, the application of compressive sensing-related techniques in the optimization of sparse arrays is investigated. Analyzing both linear arrays and concentric circular arrays, the MPSO-OMP algorithm is proposed for joint optimization of multiple variables, including array element excitations. Firstly, an MPSO algorithm is introduced, incorporating adaptive mutation and crossover operations within the PSO framework. The mutation vector in this process is influenced by the individual best vector, which not only maintains the diversity of the population during iterations but also ensures that the information of high-quality particles is preserved. Furthermore, by integrating the OMP algorithm and making reasonable choices regarding array element excitations, the number of array elements, and the radius of the circular rings, a reduction in the peak sidelobe level is achieved. Simulation results demonstrate that the proposed algorithm can achieve satisfactory optimization performance for array antenna systems.

ACKNOWLEDGMENT

This work was supported in part by the National Natural Science Foundation of China under Grant 62071140.

REFERENCES

[1] R. L. Haupt, *Antenna Arrays: A Computational Approach*. Hoboken, NJ: Wiley, 2010.

[2] S. A. Hamza and M. G. Amin, "Sparse array design for optimum beamforming using deep learning," *IEEE Transactions on Aerospace and Electronic Systems,* vol. 60, no. 1, pp. 133-144, Feb. 2024.

[3] N. Amani, A. Farsaei, S. R. Aghdam, T. Eriksson, M. V. Ivashina, and R. Maaskant, "Sparse array synthesis including mutual coupling for MU-MIMO average capacity maximization," *IEEE Transactions on Antennas and Propagation,* vol. 70, no. 8, pp. 6617-6626, Aug. 2022.

[4] M. G. Amin, *Sparse Arrays for Radar, Sonar, and Communications.* Hoboken, NJ: John Wiley & Sons, pp. i-xxiv, 2024.

[5] D. Pinchera, M. D. Migliore, and G. Panariello, "Isophoric inflating deflating exploration algorithm (I-IDEA) for equal-amplitude aperiodic arrays," *IEEE Transactions on Antennas and Propagation,* vol. 70, no. 11, pp. 10405-10416, Nov. 2022.

[6] Z. M. Cui, Q. H. Zhang, J. F. An, Y. Yu, and B. B. Cheng, "Multibeam synthesis for a reconfigurable sparse array via a vew consensus PDD framework," *IEEE Transactions on Antennas and Propagation,* vol. 72, no. 2, pp. 1541-1555, Feb. 2024.

[7] D. N. Xia and X. J. Zhang, "Synthesis of sparse arrays with discrete phase constraints via mixed-integer programming," *IEEE Antennas and Wireless Propagation Letters,* vol. 23, no. 3, pp. 1030-1034, Mar. 2024.

[8] K. S. Chen, H. Chen, L. Wang, and H. G. Wu, "Modified real GA for the synthesis of sparse planar circular arrays," *IEEE Antennas and Wireless Propagation Letters,* vol. 15, pp. 274-277, 2016.

[9] K. S. Chen, Y. Y. Zhu, X. L. Ni, and H. Chen, "Low sidelobe sparse concentric ring arrays optimization using modified GA," *International Journal of Antennas and Propagation,* vol. 2015, p. 147247, 2015.

[10] K. S. Chen, Z. S. He, and C. L. Han, "A modified real GA for the sparse linear array synthesis with multiple constraints," *IEEE Transactions on Antennas and Propagation,* vol. 54, no. 7, pp. 2169-2173, July 2006.

[11] Y. Li, F. Yang, J. Ouyang, Z. P. Nie, and H. J. Zhou, "Synthesis of nonuniform array antennas using particle swarm optimization," *Electromagnetics,* vol. 30, no. 3, pp. 237-245, 2010.

[12] Z. Y. He, K. S. Chen, Z. S. He, and C. L. He, "Sparse circular arrays method based on modified DE algorithm," *Systems Engineering and Electronics,* vol. 31, no. 3, p. 497-499, 2009.

[13] K. Du, Z. K. Chen, D. L. Peng, and X. T. Zhu, "Sparse optimization of uniform array based on hybrid mutation differential evolution algorithm," *Modern Radar,* vol. 54, no. 7, pp. 2169-2173, July 2006.

[14] Y. H. Liu, Z. P. Nie, and Q. H. Liu, "Reducing the number of elements in a linear antenna array by the matrix pencil method," *IEEE Transactions on Antennas and Propagation,* vol. 56, no. 9, pp. 2955-2962, Sep. 2008.

[15] H. O. Shen, B. H. Wang, and X. Li, "Shaped-beam pattern synthesis of sparse linear arrays using the unitary matrix pencil method," *IEEE Antennas and Wireless Propagation Letters,* vol. 16, pp. 1098-1101, 2017.

[16] E. J. Candès, J. Romberg, and T. Tao, "Robust uncertainty principles Exact signal reconstruction from highly incomplete frequency information," *IEEE Transactions on Information Theory,* vol. 52, no. 2, pp. 489-509, Feb. 2006.

[17] E. J. Candès and M. B. Wakin, "An introduction to compressive sampling," *IEEE Signal Processing Magazine,* vol. 25, no. 2, pp. 21-30, Mar. 2008.

[18] T. Hong, X. P. Shi, and X. S. Liang, "Synthesis of sparse linear array for directional modulation via convex optimization," *IEEE Transactions on Antennas and Propagation,* vol. 66, no. 8, pp. 3959-3972, Aug. 2018.

[19] A. H. Cao, H. L. Li, S. L. Ma, J. Tan, and J. J. Zhou, "Sparse circular array pattern optimization based on MOPSO and convex optimization," in *2015 Asia-Pacific Microwave Conference (APMC),* Vols 1-3, 2015.

[20] M. Versaci, G. Angiulli, F. La Foresta, F. Laganà, and A. Palumbo, "Intuitionistic fuzzy divergence for evaluating the mechanical stress state of steel plates subject to bi-axial loads," *Integrated Computer-Aided Engineering,* vol. 31, no. 4, pp. 363-379, 2024.

[21] L. Carin, "On the relationship between compressive sensing and random sensor arrays," *IEEE Antennas and Propagation Magazine,* vol. 51, no. 5, pp. 72-81, 2009.

[22] G. Oliveri and A. Massa, "Bayesian compressive sampling for pattern synthesis with maximally sparse non-uniform linear arrays," *IEEE Transactions on Antennas and Propagation,* vol. 59, no. 2, pp. 467-481, 2011.

[23] K. Chen, Y. Li, and J. Shi, "Optimization of sparse concentric ring arrays for low sidelobe," *International Journal of Antennas and Propagation*, vol. 2019, no. 1, pp. 1485075, June 2019.

[24] S. Zhang, S. X. Gong, Y. Guan, P. F. Zhang, and Q. Gong, "A novel IGA-EDSPSO hybrid algorithm for the synthesis of sparse arrays," *Progress in Electromagnetics Research-PIER,* vol. 89, pp. 121-134, 2009.

[25] Y. Liu, Y. R. N. Zhang, and S. Gao, "Suppress sideband radiation in time-modulated linear arrays by an effective hybrid algorithm," in *Proceedings of 2020 IEEE 10th International Conference on Electronics Information and Emergency Communication (ICEIEC 2020),* pp. 257-260, 2020.

Daren Li was born in Harbin, Heilongjiang Province, China, in 1990. He received the M.S. degree in shipbuilding and ocean engineering from the College of Shipbuilding Engineering, Harbin Engineering University, Harbin, China, where he is currently working toward the Ph.D. degree in information and communication engineering with Harbin Engineering University of Information and Communication Engineering.

His research interests include antenna array synthesis, radar signal processing and target comprehensive identification.

Qiang Guo received the B.S., M.S., and Ph.D. degrees in information and communication engineering from Harbin Engineering University, China, in 1994, 2003, and 2007, respectively. In 2009, he joined the Faculty with the School of Information and Communication Engineering, Harbin Engineering University, where he is currently a Full Professor. His research interests include antenna array synthesis, machine learning, radar signals sorting, and recognition.

He is also a Foreign member of the Ukrainian Academy of Engineering, Review Expert of the Science and Technology Commission of the Military Commission, the National Natural Science Foundation of China and Technology Department evaluation expert and the Chinese Institute of Electronics Science and Technology Award evaluation expert.

A Brief Review of Non-invasive Systems for Continuous Glucose Monitoring

Lisa K. Elmiladi, Atef Z. Elsherbeni, and Peter H. Aaen

Department of Electrical Engineering
Colorado School of Mines, Golden, CO 80401, USA
lelmiladi@mines.edu, aelsherb@mines.edu, paaen@mines.edu

Abstract – This paper explores the pros and cons of using Vector Network Analyzers (VNAs) and radar systems for non-invasive glucose concentration testing. While VNAs provide precise measurement capabilities, radar systems offer a more portable and cost-effective solution. The research discusses the application of both technologies in medical settings, focusing on their potential for glucose monitoring and the challenges associated with each. This paper also considers radar unit options for experimental setups below 40 GHz, with a focus on simulations for glucose concentration detection in finger tissues using the 3-term Debye model.

Index Terms – Debye model, glucose monitoring, radar, VNA.

I. INTRODUCTION

The need for continuous and non-invasive glucose monitoring is growing as diabetes affects millions worldwide. Traditional monitoring methods like glucometers are invasive and uncomfortable for patients, leading to the exploration of alternative techniques involving electromagnetic methods. The use of both nano-Vector Network Analyzers (nano-VNAs) and miniaturized radar systems boards have been investigated for their potential in detecting glucose concentrations through changes in the dielectric properties of blood or the radar cross-section (RCS) from blood vessels having high glucose concentrations. RCS detects glucose concentration by observing the reflection of electromagnetic waves through human tissues.

VNAs have been extensively utilized for detecting glucose concentration changes through the measurement of scattering parameters (S-parameters), which reflect the dielectric properties of biological tissues. Figure 1 shows a simple VNA with internal S-parameter test set.

Studies such as those by Choi et al. [1] demonstrated the feasibility of microwave sensors to monitor blood glucose concentrations. Their work showed that the dielectric properties of blood are closely correlated with glucose levels, making VNAs a viable option for glucose sensing. Similarly, Flaherty [2] demonstrated that mmWave-based techniques using VNAs could detect glucose concentrations in anesthetized rats, further validating the potential of electromagnetic methods.

On the other hand, radar systems operating in the mmWave band provide an alternative solution, offering greater portability and reduced cost. Figure 2 shows a 60 GHz mmWave radar system developed for applications such as driver monitoring and touchless interfaces. This radar system operates at mmWave frequencies, which provides high-resolution detection capabilities. It is manufactured by Acconeer AB, a company specializing in high-frequency radar solutions for automotive and consumer applications [3]. The radar system's compact size and advanced integration make it ideal for non-invasive applications, including gesture recognition, motion tracking, and medical monitoring.

Saha et al. [4] investigated the use of microstrip patch antennas operating at 60 GHz for glucose detection. Their study highlighted how changes in the transmission and reflection coefficients of the radar signal could accurately monitor glucose levels. In a similar vein, Cano-Garcia et al. [5] conducted experiments using radar systems to detect glucose variability in saline solutions, demonstrating that radar systems can effectively monitor glucose concentrations non-invasively.

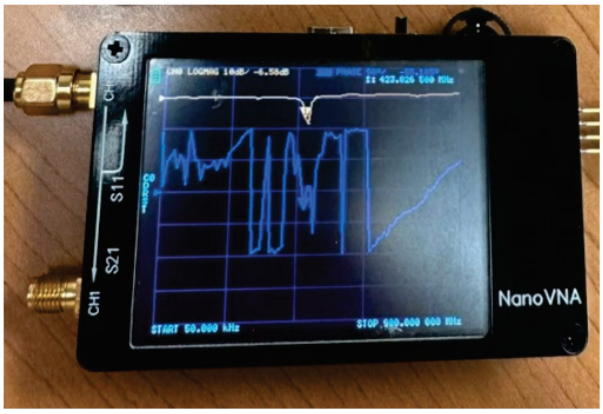

Fig. 1. Nano-Vector Network Analyzer demonstrating a magnitude and phase plot.

Submitted On: December 23, 2024
Accepted On: June 20, 2025

https://doi.org/10.13052/2025.ACES.J.400604

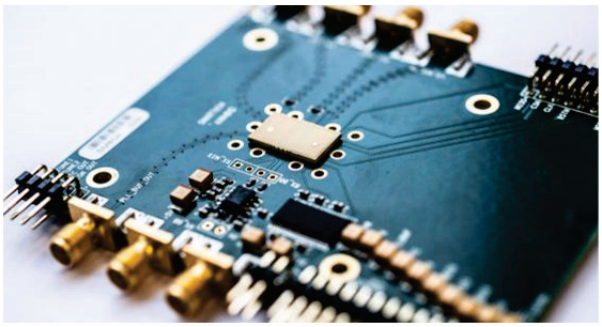

Fig. 2. 60 GHz mmWave radar. Adapted from [3].

Despite the advancements in radar-based glucose monitoring, challenges remain in ensuring accuracy and sensitivity, especially when compared to the use of VNAs. Kim et al. [3] explored the sensitivity of microwave biosensors to different glucose concentrations in aqueous solutions, illustrating the need for higher precision equipment. Additionally, Guo et al. [6] studied alternative non-invasive methods, such as breath signal analysis for glucose monitoring, but found them less effective than electromagnetic approaches.

This paper examines the advantages and disadvantages of these two methods, considering cost, precision, portability, and the stage of development

II. VECTOR NETWORK ANALYZER

VNA has been widely used in material characterization due to its ability to measure S-parameters, making it a valuable tool for analyzing the dielectric properties of biological tissues, including blood glucose levels. VNAs operate by emitting electromagnetic waves and analyzing their interaction with materials, providing high-precision measurements. The use of VNAs for glucose monitoring, in particular, has shown promising results in detecting changes in the dielectric properties of blood, which correlate with glucose concentration. These measurements are often performed at higher frequencies, enhancing sensitivity to variations in glucose levels.

A. Advantages

One of the key advantages of the use of VNAs is their precision in measuring electromagnetic behavior. VNAs provide highly accurate readings of S-parameters, which are instrumental in quantifying the dielectric properties of biological tissues. This level of precision allows for detailed analysis of subtle variations in glucose concentration. They support a broad frequency range, with some models operating at frequencies as high as 67 GHz. The ability to work in higher frequency ranges enhances the VNA's capacity to detect minute changes in electromagnetic behavior, particularly in relation to glucose sensing [7].

Additionally, VNAs are well-studied for medical applications. Their use in glucose detection has been extensively documented, with research demonstrating reliable results in measuring the dielectric properties of blood and correlating them with glucose levels [7].

B. Disadvantages

Despite their precision, VNAs present several limitations. The most notable drawback is their high cost, with prices over US$100,000 for those capable of measurements above 40 GHz. VNAs are not a cost-effective solution for widespread deployment in non-invasive glucose monitoring [7]. This limits their practical application to large research institutions and specialized medical facilities.

Another challenge is the bulky nature of VNAs. They are typically large and not portable, making them impractical for real-time, continuous glucose monitoring in everyday settings. Though advancements such as nano-VNAs offer more compact solutions, these smaller versions may sacrifice some precision and frequency range [7].

Finally, the complex setup required for VNAs can pose challenges. Accurate measurements depend on careful calibration and maintenance, which may be cumbersome in a clinical setting compared to more user-friendly alternatives, such as radar systems [7].

III. RADAR SYSTEM (60 GHz MMWAVE)

The mmWave radar systems, particularly those operating around 60 GHz, have gained attention as an alternative to VNAs for non-invasive glucose monitoring. These systems function by emitting electromagnetic waves and analyzing the reflected signals, allowing for the detection of changes in dielectric properties related to glucose concentrations in biological tissues. Radar systems offer a compact, portable, and potentially cost-effective solution for continuous glucose monitoring.

A. Advantages

Radar systems, especially those based on mmWave technology, provide significant advantages in terms of portability. Systems like the Google Soli radar are small and lightweight, making them well-suited for wearable applications. This portability facilitates non-invasive glucose monitoring in daily life without the need for intrusive devices or continuous finger pricking [7].

Another advantage is their cost-effectiveness compared to VNAs. Radar systems are considerably less expensive, making them a more viable option for large-scale deployment in medical applications. This affordability opens the possibility of continuous glucose monitoring for a broader patient population.

Radar systems also demonstrate good sensitivity to glucose concentrations. Research has shown that radar

systems can effectively detect variations in the dielectric properties of glucose solutions, making them suitable for tracking glucose levels in the blood [7]. Moreover, radar-based systems allow for non-invasive monitoring, which reduces patient discomfort and improves the feasibility of frequent or continuous glucose testing [7].

B. Disadvantages

Radar systems also come with limitations. Most affordable radar units operate at frequencies below 40 GHz, which can reduce their sensitivity compared to higher-frequency VNAs. The lower frequency range may limit the system's ability to detect small variations in glucose concentration, especially when applied to deeper biological tissues [7].

Another challenge lies in the radar systems' sensitivity to physiological and environmental factors. Changes in body temperature, moisture, or surrounding environmental conditions can affect the accuracy of glucose readings, posing challenges for real-time monitoring [7].

Finally, radar-based glucose detection technology remains in the experimental stage. While research has demonstrated the feasibility of radar systems for glucose monitoring, further validation and development are needed before these systems can be deployed in clinical or personal health settings [7].

IV. RADAR UNIT SELECTION

A suitable and cost-effective radar unit is available on SparkFun that operates below 40 GHz. Operating below 40 GHz allows for compatibility with most existing VNA systems, ensuring that both radar systems and VNAs can be used in tandem for comparison studies. Additionally, radar units operating in this frequency range typically provide a balance between performance and cost, making them more feasible for practical applications in continuous glucose monitoring. One potential option is the SparkFun Radar Breakout - A111 Pulsed Radar Sensor shown in Fig. 3.

Although this unit operates at 60 GHz, which is higher than the preferred range, it may still be useful due to its versatility and potential for adaptation in medical applications. The A111 Radar Sensor is a compact pulsed radar sensor, which is capable of detecting motion [8], which makes it suitable for non-invasive applications where detecting minute changes in dielectric properties is crucial, such as in glucose monitoring.

The sensor is capable of detecting objects at distances of up to two meters and can be used for gesture recognition, motion detection, and distance measurement. It includes built-in antennae and supports communication via an SPI interface with speeds up to 50 MHz [8]. The breakout board for the A111 sensor comes with a 1.8 V regulator, voltage-level translation, and breaks out all pins for easy integration with Raspberry Pi or other development platforms [8]. Figure 4 demonstrates a sample configuration with a Raspberry Pi attached to the A111 radar.

It can be adapted for glucose monitoring by analyzing the reflection of electromagnetic waves through biological tissues, such as skin and blood. The radar system's ability to detect subtle variations in reflected signals makes it a good candidate for measuring changes in the dielectric properties of blood, which vary with glucose concentration [2]. By calibrating the radar system to measure these variations, the A111 could be used to continuously monitor glucose levels in a non-invasive manner. If selecting an ideal radar unit under 40 GHz is critical, modifications to the experimental setup may be necessary, or modern sensors with broader operational ranges could be considered.

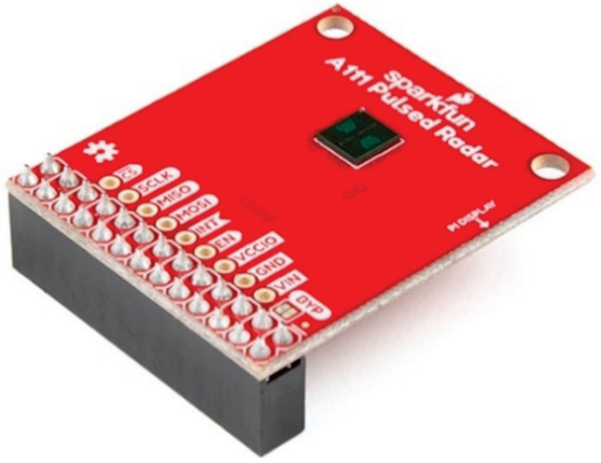

Fig. 3. SparkFun A111 Pulsed Radar. Adapted from [8].

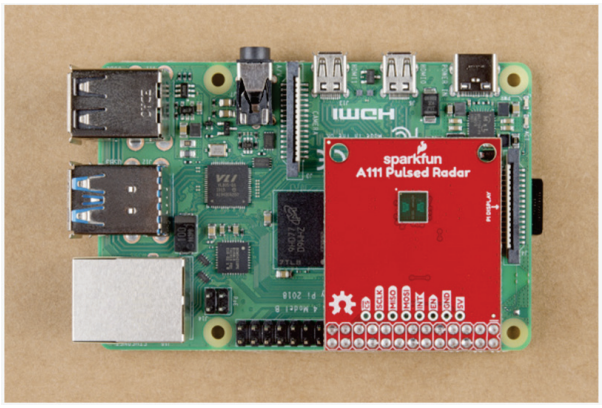

Fig. 4. A111 HAT v1.1 and v1.0 stacked on a Raspberry Pi. Adapted from [8].

V. SIMULATION AND EXPERIMENTAL SETUP

Once the radar units are selected, electromagnetic simulations can be performed using the 3-term Debye model [9] for dielectric properties of finger or shoulder tissues. The modeling provides a detailed representation of the frequency-dependent behavior of biological tissues. The simulation should analyze amplitude and phase variations of the received radar signal as it passes through the simulated human tissues with varying glucose concentrations. Several electromagnetic simulation tools can be used to set up such simulation environment similar to those in [10].

To ensure simulation fidelity, it is recommended to model multilayered tissue geometries (e.g., skin, fat, muscle, blood vessels) with distinct Debye parameters. A parameter sweep across a realistic range of glucose concentrations should be used to observe sensitivity trends. Full-wave modeling tools should utilize the accurate presentation of these tissues' dielectric properties [9, 10].

Further, radar time-domain modeling—such as simulating pulse response or transient S-parameters—can help evaluate the system's response to changes in tissue permittivity due to glucose variability. These simulations should be conducted across the radar's operating frequency band, particularly around 60 GHz, to match practical device capabilities [5, 7].

In terms of usability, VNAs—especially high-frequency models—are bulky and expensive, limiting their feasibility for patient-operated devices [7]. However, they can be valuable tools for calibration and controlled lab testing [1, 2]. Radar systems, on the other hand, are more promising for integration into non-invasive, wearable systems. For example, compact radar sensors like the SparkFun A111 (Fig. 3) demonstrate the feasibility of embedding such sensors into consumer-friendly form factors (e.g., smart rings or finger clips). For practical deployment, attention must be given to energy efficiency, signal processing accuracy, wireless communication (e.g., via Bluetooth or USB CDC [8]), and overall comfort and safety for the user. The system should be tested under dynamic conditions (e.g., blood flow or motion) to mimic real-world variability [4, 5].

VI. CONCLUSION

Both VNAs and radar systems present viable options for non-invasive glucose monitoring. VNAs offer higher precision and are well-studied but are costly and not portable. Radar systems, while more affordable and portable, are still in the experimental phase and may face challenges related to physiological and environmental variability. Future research and experimental validation will determine the most practical solution for continuous glucose monitoring.

REFERENCES

[1] H. Choi, J. Naylon, S. Luzio, J. Beutler, J. Birchall, C. Martin, and A. Porch, "Design and in vitro interference test of microwave noninvasive blood glucose monitoring sensor," *IEEE Transactions on Microwave Theory and Techniques*, vol. 63, no. 10, pp. 3016-3025, 2015.

[2] N. Flaherty, "60GHz mmWave radar for driver monitoring and touchless interfaces," *eeNews Europe* [Online], Aug. 04 2020. Available: https://www.eenewseurope.com/en/60ghz-mmwave-radar-for-driver-monitoring-and- touchless-interfaces (accessed July 04 2025).

[3] J. Kim, A. Babajanyan, A. Hovsepyan, K. Lee, and B. Friedman, "Microwave dielectric resonator biosensor for aqueous glucose solution," *Review of Scientific Instruments*, vol. 79, no. 8, p. 086107, Aug. 2008.

[4] S. Saha, H. Cano-Garcia, I. Sotiriou, O. Lipscombe, I. Gouzouasis, M. Koutsoupidou, G. Palikaras, R. Mackenzie, T. Reeve, P. Kosmas, and E. Kallos, "A glucose sensing system based on transmission measurements at millimetre waves using microstrip patch antennas," *Scientific Reports*, vol. 7, no. 1, 2017.

[5] H. Cano-Garcia, P. Kosmas, I. Sotiriou, I. Papadopoulos-Kelidis, C. Parini, I. Gouzouasis, G. Palikaras, and E. Kallos, "Detection of glucose variability in saline solutions from transmission and reflection measurements using V-band waveguides," *Measurement Science and Technology*, vol. 26, no. 12, p. 125701, Oct. 2015.

[6] D. Guo, D. Zhang, L. Zhang, and G. Lu, "Non-invasive blood glucose monitoring using breath signal analysis," *Sensors and Actuators B: Chemical*, vol. 173, pp. 106-113, 2012.

[7] A. E. Omer, G. Shaker, and S. Safavi-Naeini, "Non-invasive glucose monitoring at mm-Wave frequencies," *International Journal of Mobile Human Computer Interaction*, vol. 10, no. 3, pp. 10-29, 2018.

[8] SparkFun, *Getting Started with the A111 Pulsed Radar Sensor* [Online]. Available: https://learn.sparkfun.com/tutorials/getting-started-with-the-a111-pulsed-radar-sensor/all

[9] R. Lumnitzer, A. Tanner, and A. Z. Elsherbeni, "Debye coefficients for biological tissues from 100 MHz to 100 GHz," *Applied Computational Electromagnetics Society (ACES) Journal*, vol. 35, no. 11, pp. 613-621, 2020.

[10] F. Kaburcuk and A. Z. Elsherbeni, "Efficient electromagnetic analysis of a dispersive head model due to smart glasses embedded antennas at Wi-Fi and 5G frequencies," *Applied Computational*

Electromagnetics Society (ACES) Journal, vol. 36, no. 2, pp. 159-167, 2021.

Lisa K. Elmiladi is a graduate student in the Electrical Engineering Department at Colorado School of Mines in Golden, Colorado, USA. With a keen interest in the practical and theoretical aspects of her field, Lisa is intent on furthering her education with a Ph.D. in Electrical Engineering. Her academic endeavors are not solely restricted to coursework; they extend to diverse interests such as VLSI Circuit Design, biomedical device applications, electromagnetics and RF, as well as Embedded Systems. Lisa's research interests are centered around medical devices and antennas, reflecting her passion for leveraging technology to improve health outcomes.

Atef Z. Elsherbeni received his Ph.D. degree in Electrical Engineering from Manitoba University, Winnipeg, Manitoba, Canada, in January 1987. He started his engineering career as a Software and System Design Engineer from March 1980 to December 1982 at the Automated Data System Center, Cairo, Egypt. From January to August 1987, he was a Post-Doctoral Fellow at Manitoba University. Elsherbeni joined the faculty at the University of Mississippi in August 1987 as an Assistant Professor of Electrical Engineering and progressed to the full professor and the Associate Dean of the College of Engineering for Research and Graduate Programs. He then joined the Electrical Engineering and Computer Science Department at Colorado School of Mines in August 2013. Elsherbeni is an IEEE Life Fellow and ACES Fellow. He is the Editor-in-Chief for *Applied Computational Electromagnetics Society (ACES) Journal*, and a past Associate Editor to *Radio Science*. He was the Chair of the Engineering and Physics Division of the Mississippi Academy of Science, the Chair of the Educational Activity Committee for IEEE Region 3 Section, and the past President of ACES Society. He received the 2023 IEEE APS Harington-Mittra Award for his contribution to computational electromagnetics with hardware acceleration and the ACES 2025 Computational Electromagnetics Award.

Peter H. Aaen received the B.A.Sc. degree in Engineering Science and the M.A.Sc. degree in Electrical Engineering from the University of Toronto, Toronto, ON, Canada, in 1995 and 1997, respectively, and the Ph.D. degree in Electrical Engineering from Arizona State University, Tempe, AZ, USA, in 2005. He was the Manager of the RF Division, RF Modeling and Measurement Technology Team, Freescale Semiconductor Inc., Tempe, AZ, USA, a company which he joined in 1997, then the Semiconductor Product Sector, Motorola Inc. In 2013, he joined the Faculty of Engineering and Physical Sciences, University of Surrey, Guildford, UK, where he was a Reader of microwave semiconductor device modeling. He was also the Director of the Nonlinear Microwave Measurement and Modeling Laboratory, a joint University of Surrey/National Physical Laboratory, and the Director of National Physical Laboratory – South of England, Guildford, UK. In 2019, he joined the Colorado School of Mines as a Professor and Head of the Electrical Engineering Department. He has co-authored *Modeling and Characterization of RF and Microwave Power FETs* (Cambridge University Press, 2007). Aaen is a member of the Microwave Theory and Techniques and Electron Device Societies, served as an Executive Committee Member and Vice-President of the Automatic RF Techniques Group, and was the Chair of the IEEE Technical Committee (MTT-1) on Computer-Aided Design.

Ultra-thin Coating Materials Sensor Based on Constitutive Parameters Near-zero Media

Si Hui Jia[1], Yu Wei Mao[1], Qiao Yu Li[1], Zi Jian Gao[1], Zi Peng Shan[2], and Yong Jin Zhou[1,2]

[1]Shanghai Collaborative Innovation Center of Intelligent Sensing Chip Technology
Laboratory of Specialty Fiber Optics and Optical Access Networks, Shanghai University, Shanghai 200444, China
22820144@shu.edu.cn, maoyuwei@shu.edu.cn, 20820117@shu.edu.cn, zijiangao2333@shu.edu.cn

[2]State Key Laboratory of Millimeter Waves
School of Information Science and Engineering, Southeast University, Nanjing 210096, China
yjzhou@shu.edu.cn

Abstract – Microwave absorbing materials, which serve as essential functional components, are increasingly vital to stealth systems in military equipment. Accurate measurement of the electromagnetic parameters of absorbing coatings is crucial for achieving stealth effects. This study introduces a high-precision curved microwave sensor based on constitutive parameters near-zero (CPNZ) media, which uses thickness and complex permittivity as key test parameters. The complex permittivity and thickness of several typical absorbing materials were evaluated and benchmarked against other sensors. The detection limit of a CPNZ sensor for curved thickness is 0.5 mm, and the relative error of relative dielectric constant is less than 8%. Given the material thickness and resonant frequency, the relative error in the inversion of the dielectric constant is less than 3%. The calculated values closely correspond with the reference values, highlighting the CPNZ sensor's enhanced accuracy and reliability for material characterization.

Index Terms – Constitutive parameters near-zero media, high accuracy, microwave sensor, ultra-thin coating material.

I. INTRODUCTION

Material stealth technology is extensively applied in radar stealth design for ships, aircraft, missiles, and other platforms due to its superior stealth effect, ease of application, and lack of restrictions on body shape. Microwave absorbing materials, as vital military components, play an increasingly critical role in the stealth systems of military equipment [1]. To accurately design stealth absorbing materials, precise measurement of their complex dielectric constant is crucial for radar stealth applications [2–4]. To meet aerodynamic requirements, the carrier's shape is often streamlined to reduce radar signal reflections. When applied to the carrier's surface, the absorbing material bends, altering its electromagnetic parameters, and its thickness also affects absorbing performance. Therefore, accurate measurement of the complex permittivity of ultra-thin surface materials holds significant research value for radar defense system design. Since the 1940s, when Horner et al. used the perturbation method to measure the complex permittivity of materials, measurement technology has developed vigorously [5]. Numerous researchers worldwide have conducted extensive research on methods to measure complex permittivity, such as the free space method, transmission/reflection method, and resonance method [6]. As material performance requirements increase, new measurement technologies have been proposed [6–11]. Noncontact measurement methods are commonly employed to determine the complex permittivity and thickness of materials under test (MUT) [12]. However, these methods are primarily used to measure high-loss materials [12, 13], with measurement errors too large to accurately characterize low-loss dielectric materials [13, 14]. A magnetic dielectric material characterization sensor, based on an improved complex split-ring resonator, can simultaneously measure both complex permittivity and permeability changes [11]. By locating the highest field strengths of the electric and magnetic fields in two independent regions, the measured resonant frequency and quality factor can be analyzed to determine the real and imaginary parts of the complex permittivity and permeability. The relative permittivity and loss tangent of the measured materials range from 3.25 to 6.2 and 0.0022 to 0.027, respectively, providing accurate measurements for low-loss materials. Additionally, a dual-band nondestructive sensor for measuring relative permittivity based on a complementary split resonant ring has been developed [14]. The measured relative dielectric constant, loss tangent, and material thickness range from 2 to 10, 0 to 0.1, and 2 to 10 mm, respectively,

Submitted On: February 28, 2025
Accepted On: June 16, 2025

https://doi.org/10.13052/2025.ACES.J.400605

with relative errors of permittivity and low-loss tangent less than 4% and 16.7%, indicating a high level of accuracy. However, these methods for measuring solid materials often neglect the influence of material thickness on the complex dielectric constant [7, 10]. In the nondestructive measurement of relative permittivity for objects with varying thicknesses, the measurement error increases as material thickness decreases. Yet, the measurement of the complex dielectric constant for ultra-thin curved materials has not been addressed in the existing work.

Microwave sensor measurement technology offers advantages such as high integration, measurement accuracy, and real-time performance, emerging as the leading technology for measuring complex permittivity [15, 16]. Metamaterials, artificial electromagnetic structures composed of subwavelength resonators, exhibit novel electromagnetic properties and are widely used in sensing, antennas, and stealth technology [17–19]. Among these metamaterials, constitutive parameters near-zero (CPNZ) media have garnered significant interest for their unique wave phenomena [20]. In printed circuit design, substrate-integrated photon doping facilitates the use of near-zero refractive index media in dielectric constant measurements [21, 22]. A small change in the relative dielectric constant of the measured object leads to a significant shift in the tunneling frequency, and the transmission coefficient amplitude decreases significantly with moderate doping loss, indicating that the near-zero refractive index medium is sensitive to doped complex permittivity [6, 23, 24]. This sensitivity has potential applications in material characterization, sensing, and related fields. For example, a wireless sensor system based on the relative permittivity near-zero effect measures the complex permittivity of liquids with relative errors of 3.72% and 9.67%, respectively, using only a small volume of liquid [23]. In addition to complex permittivity, microwave sensors based on relative permeability near-zero media can also measure the permeability of magnetic dielectric materials [24]. Research on sensing platforms based on relative permittivity near-zero metamaterials has demonstrated that relative permittivity near-zero sensors can detect changes in both the relative dielectric constant and position. However, effective transmission requires the waveguide height to exceed the relative permittivity near-zero channel height, complicating experimental verification [25]. The relative permittivity near-zero sensor is sensitive to both low-loss and high-loss materials, and relative permittivity near-zero medium doping allows for the measurement of materials of varying shapes by altering the doping configuration. Despite these advancements, the measurement of complex permittivity in ultra-thin curved surfaces using near-zero refractive index media sensors remains unexplored. To address the challenge of multi-parameter measurement for curved materials, this paper proposes a novel sensor structure based on CPNZ media with elliptical doping. High-accuracy measurements are achieved through optimization of the field distribution and implementation of a polynomial regression model parameter inversion.

In this paper, a high-precision curved microwave sensor based on CPNZ medium is proposed, focusing on the thickness and complex permittivity of curved materials as test parameters. The sensor is modeled and benchmarked against other advanced sensors. The sensor successfully achieves accurate measurement of the thickness and complex permittivity of curved materials.

II. STRUCTURES AND RESULTS

A. Design and simulation of CPNZ sensor

Considering the curvature distribution of typical curved surface coatings, the study adopts elliptical doping as a representative case to improve the generalizability and applicability of the proposed approach. This paper adopts elliptical doping, defines the operating frequency range between 1.5 GHz and 3 GHz, and uses electromagnetic simulation software CST to perform a full-wave simulation of the sensor. The relative permittivity near-zero cavity is modeled using a rectangular air waveguide operating near the cutoff frequency of the TE10 mode. The length and width of the rectangular air waveguide are $L = 260$ mm and $W = 85$ mm, respectively. The cutoff frequency of the simulated relative permittivity near-zero cavity is 1.97 GHz. The input and output terminals are both 50-ohm microstrip lines, connected via gradient microstrip lines. The dielectric substrate is F4B with a relative permittivity of 2.65 and a loss tangent of 0.002. The length and width of the entire structure are $l = 100$ mm and $w = 76$ mm, respectively. The substrate thickness is $h = 6.5$ mm, and the diameter of the metal through-hole is $d = 2.4$ mm. The hole spacing is $s = 4$ mm and the copper thickness on the upper and lower surfaces of the dielectric substrate is 0.035 mm. The length of ceramic doping is $X_d = 50$ mm, and the width of ceramic doping is $Y_d = 20$ mm.

The overall schematic diagram of the sensor structure and the top view of the elliptical doping part are shown in Fig. 1. Figure 2 (a) presents the transmission curve S_{21} of the CPNZ structure, showing a resonant frequency at 1.97 GHz. To simulate effects that may be introduced during the actual fabrication process, we vary the lengths of the major and minor axes of the doping in the simulation, with a step of 0.2 mm. As shown in Fig. 2 (a), it can be seen that the fabrication tolerance has little impact on the results. The electric and magnetic field distributions of the CPNZ structure at 1.97 GHz are illustrated in Figs. 2 (b) and (c). The electric field

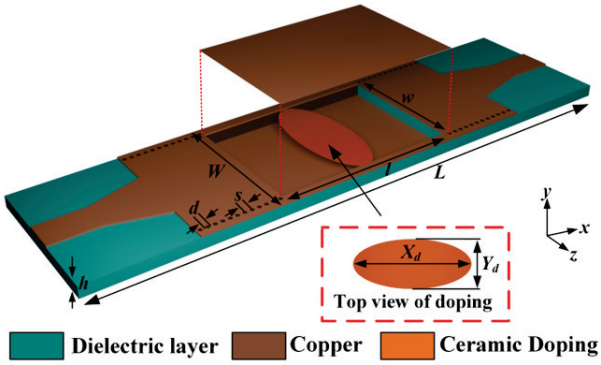

Fig. 1. Structure diagram of CPNZ microwave sensor.

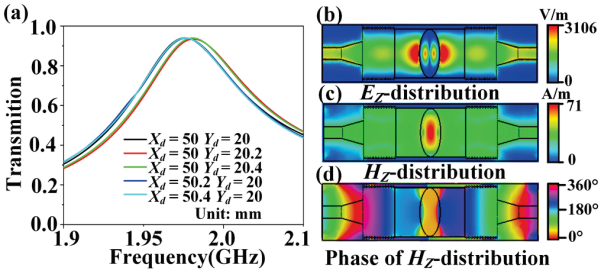

Fig. 2. Simulation results of CPNZ sensor: (a) transmission coefficients, (b) electric field distribution, (c) magnetic field distribution, and (d) magnetic field phase distribution.

is largely concentrated at the edge of the doping, while the magnetic field is primarily concentrated in the inner part of the doping. The local enhancement of the electric and magnetic fields makes the structure feasible to the precise measurement of small variations in the electromagnetic parameters of the material. The phase distribution of the magnetic field is illustrated in Fig. 2 (d). It can be seen that the phase of the magnetic field is uniformly distributed at the resonant frequency. At this frequency, the equivalent relative permittivity and equivalent relative permeability of the doped relative permittivity near-zero cavity are both zero, consistent with the characteristics of CPNZ media.

B. Sensor simulation data acquisition

To better measure the thickness and complex permittivity of the absorbing material coated, elliptical doping grooves were employed for applying the absorbing material. The structure after grooving is shown in Fig. 3 (a). Due to processing technology limitations, the groove wall thickness was selected as 0.7 mm. In the absence of coating material, the transmission curve after grooving is shown in Fig. 3 (b), demonstrating a transmission peak at 2.9 GHz. To simulate effects that may be introduced during the actual fabrication process, we vary the lengths of the major and minor axes of the elliptical doping trench, in the simulation, with a step of 0.2 mm. In Fig. 3 (b), it can be seen that the fabrication tolerance in the minor axis has a greater impact on the results. Grooving altered the elliptical doping, resulting in a nonzero equivalent relative permeability, while the equivalent relative permittivity remained unaffected. As a result, the resonant frequency undergoes a blue shift, and the field distribution inside the doping is altered. Specifically, the magnetic field inside the doping is no longer uniformly distributed, and the electric field shifts from being concentrated at the doping edge prior to grooving to the doping interior, while the magnetic field shifts from being concentrated inside the doping prior to grooving to the doping edge, as shown in Figs. 3 (c) and (d). The local concentration of the electric field inside the doping is advantageous for accurately measuring the thickness and complex permittivity of curved materials.

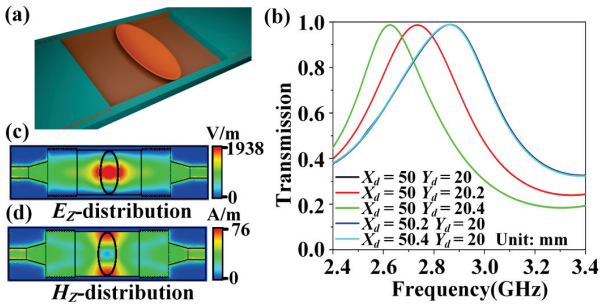

Fig. 3. (a) Structure diagram after grooving (upper metal is hidden), (b) transmission coefficients, (c) electric field distribution, and (d) magnetic field distribution.

Next, the designed sensor is employed to simulate and analyze the thickness and complex permittivity of the absorbing material. The absorbing material bends when coated on the surface of the elliptical groove, which is made of ceramic doping, as shown in Fig. 4 (a). According to the absorption mechanism of the coating, its performance depends not only on its complex permittivity but also on its thickness. Therefore, the coating thickness must be analyzed before measuring its complex permittivity. Figure 4 (b) displays the corresponding transmission curves for different thicknesses, where the thickness is given in millimeters (mm). It is evident that the sensor is sensitive to slight changes in coating thickness. When the coating thickness is increased by 0.25 mm, it can be clearly observed that the peak of the resonance frequency is shifted to the lower frequency by about 40 MHz, and when the coating thickness is increased by 0.1 mm, the peak of the resonance frequency is shifted to the lower frequency by about 17 MHz. The simulation results demonstrate a consistent red shift in resonance frequency with increasing coating thickness.

If the coating is too thin, absorption and stealth performance will be markedly reduced. Conversely, if the coating is too thick, the maneuverability of the aircraft or weapon will be compromised. Here, the chosen thickness for the absorbing coating is 1.3 mm. The electric field of the sensor varies with changes in the complex permittivity of the absorbing coating, which is manifested in changes to the resonant frequency and transmission amplitude of the sensor. The relative permittivity of the absorbing coating increases from 6 to 11 in steps of 0.5, and the loss tangent of the coating increases from 0 to 1.3 in steps of 0.1. This process results in 154 sets of data. Figure 5 (a) shows the transmission curve when the loss tangent of the absorbing coating is zero and only the relative permittivity is varied. It is evident that as the relative permittivity of the absorbing coating gradually increases, the resonant frequency of the sensor red-shifts accordingly. When the relative permittivity of the absorbing coating is 8, only the loss tangent of the coating is varied, and its transmission curve is shown in Fig. 5 (b). It is observed that as the loss tangent of the coating increases successively, the sensor's transmission amplitude decreases correspondingly. The simulation results demonstrate a clear relation between the transmission coefficient for both the relative permittivity and loss tangent. Additionally, the absorbing performance of the coatings is shown to be closely dependent on both their electromagnetic properties and thickness. To evaluate the sensitivity and the detection limit of the sensor, a polynomial regression model is developed.

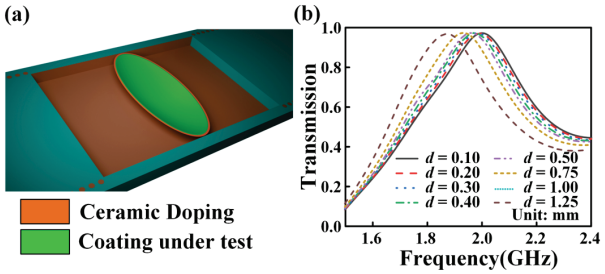

Fig. 4. (a) Schematic diagram after loading absorbing coating under test and (b) transmission coefficients corresponding to different thicknesses.

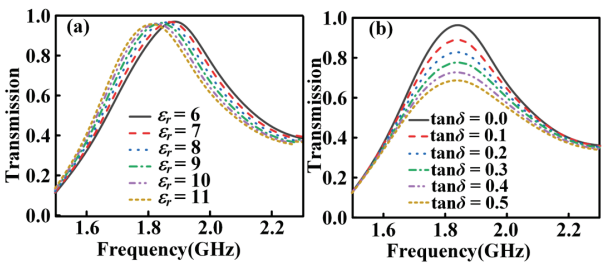

Fig. 5. (a) Transmission coefficients corresponding to different relative permittivity and (b) transmission coefficients corresponding to different loss tangent.

C. Parameter inversion based on polynomial regression model

The absorbing effect of the coating depends heavily on its thickness and complex permittivity. This paper employs a polynomial regression model to establish an inversion model based on simulated data at different thicknesses, thus enabling the determination of the detection limit of coating thickness using the CPNZ media sensor. First, absorbing coatings with thicknesses of 0.3 mm, 0.4 mm, and 0.5 mm are selected, where the resonant frequency is primarily determined by the relative permittivity of the coating. Through the extraction of simulation results, the relationship between relative permittivity and resonant frequency of coatings with thicknesses of 0.3 mm, 0.4 mm, and 0.5 mm is derived through a quadratic regression model, as shown in Figs. 6 (a), (b), and (c), respectively. The coefficients of determination for thicknesses of 0.3 mm, 0.4 mm, and 0.5 mm are 0.9699, 0.9870, and 0.9877, respectively. The obtained quadratic equations are given in equations (1-3). It can be concluded that the minimum sensitivities are 8.21 MHz/RIU, 7.11 MHz/RIU, and 10.45 MHz/RIU at coating thicknesses of 0.3 mm, 0.4 mm, and 0.5 mm, respectively:

$$y = 2.025 - 0.006526p + 0.0001678p^2, \quad (1)$$

$$y = 2.03 - 0.01071p + 0.0004429p^2, \quad (2)$$

$$y = 2.026 - 0.01046p + 0.0003403p^2, \quad (3)$$

where p represents the relative dielectric constant of the coating, and y represents the resonant frequency.

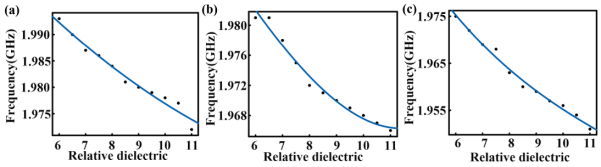

Fig. 6. Relationship between relative permittivity of coating and resonant frequency: (a) 0.3 mm, (b) 0.4 mm, and (c) 0.5 mm.

To better determine the detection limit of the sensor's coating thickness, the relative permittivity of substrates of six types of media with thicknesses of 0.3 mm, 0.4 mm, and 0.5 mm is inverted, and the relative errors for the three thicknesses are compared, as shown in Fig. 7. The relative error of measurement is defined as:

$$e = \frac{cp - cr}{cr} \times 100\%. \quad (4)$$

c_p represents the predicted inversion value of coating thickness, while c_r represents the reference value.

When the coating thickness is 0.3 mm and 0.4 mm, the relative errors in permittivity exceed 10% for these thicknesses, but remain below 8% for a coating thickness of 0.5 mm, demonstrating high accuracy. Therefore, we determined that the minimum thickness detectable by the CPNZ media sensor is 0.5 mm, where e_1 represents the relative error in the permittivity of the materials.

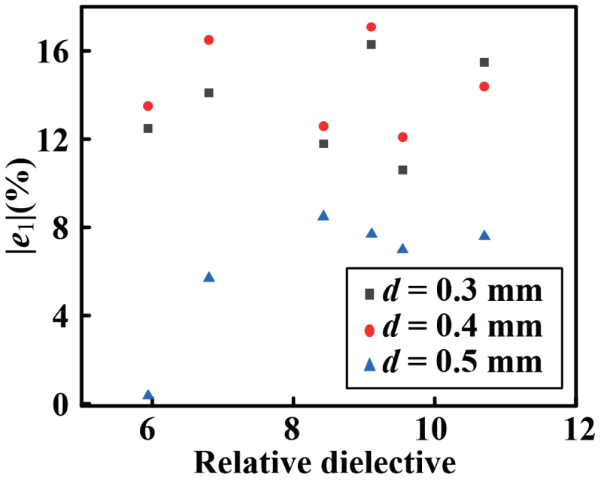

Fig. 7. Relative error comparison of relative permittivity under different thickness.

We compare the performances of the CPNZ sensor with other works in Table 1. Santra and Limaye [6] evaluated cylindrical samples, reporting a minimum detectable thickness of 4 mm and a relative error of less than 5% in dielectric constant measurement. Wang et al. [14] investigated cubic samples, achieving a minimum detectable thickness of 2 mm with a relative error of less than 4%. The proposed sensor is tailored for ellipsoidal wave-absorbing coatings, achieving a lower detection limit of 0.5 mm and a relative error in dielectric constant measurement of less than 8%. These results indicate that the proposed method offers clear advantages in the non-destructive evaluation of thickness and electrical parameters in complex curved films, combining high sensitivity with low measurement error.

Table 1: Performance comparison with other works

Ref.	Shape	Frequency Band (GHz)	Minimum Detectable Thickness	$\|e_1\|$
[6]	Cylinder	3.2-4	4 mm	5%
[14]	Cube	2.8, 4.9	2 mm	4%
This Work	Elliptic surface	2.9	0.5 mm	8%

The resonant frequency of the sensor is influenced by both the relative permittivity and the thickness of the coating. We first consider the case without loss, that is, the loss tangent of the material is set to zero. The coating thickness increases from 0.5 mm to 1.5 mm with a step value of 0.1 mm, and the relative permittivity of the coating increases from 6 to 11 with a step value of 0.5, yielding a total of 121 data sets. In the simulation, the data are directly obtained, and the resonant frequency is then extracted. A polynomial regression model was used to nonlinearly fit the 121 data sets extracted above, producing the relationship surface between coating thickness, relative permittivity, and resonant frequency, as shown in Fig. 8. The coefficient of determination is 0.9961.

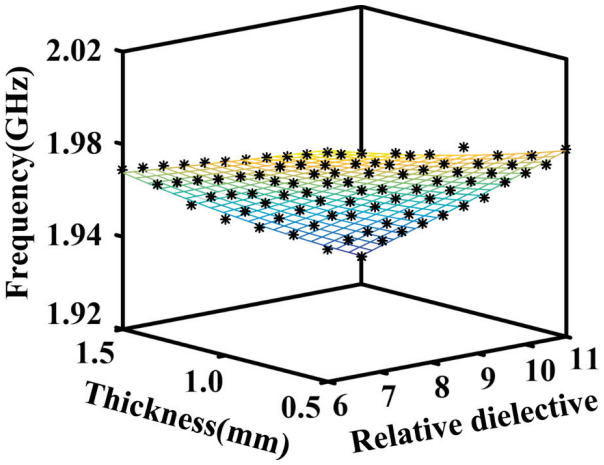

Fig. 8. Relationship between relative permittivity and thickness of coating and resonant frequency.

Since the resonant frequency is related to both the relative permittivity and the thickness of the material, two inversion methods are available. First, the resonant frequency and relative permittivity are used to determine the thickness through the inversion model. Second, the resonant frequency and thickness are used to obtain the relative permittivity from the inversion model.

Four types of dielectric substrates with varying thicknesses and complex permittivity were selected, analyzed, and compared using the two inversion approaches. For the first inversion approach, when the relative permittivity and resonant frequency of the four materials are known, the relative error in material thickness, as shown in Table 2, is computed. Here, e_2 represents the relative error of the material thickness, and the four materials are abbreviated as S_1, S_2, S_3, and S_4, respectively. The calculation equation for e_1, e_2 is based on equation (1).

For the second inversion approach, when the thickness and resonant frequency of the four materials are known, the relative error of the relative permittivity of the materials can be obtained as shown in Table 3.

By comparing the relative errors of material thickness and relative permittivity, the relative error from the

Table 2: The first inversion approach: Inversion thickness with known relative permittivity

MUT	ε_r'	Reference Thickness (c_r)	Predicted Thickness (c_p)	$\lvert e_2 \rvert$
Rogers 4003(S_1)	3.55	0.814 mm	0.695 mm	14.6%
FR4(S_2)	4.4	0.814 mm	0.710 mm	12.8%
FR4(S_3)	4.4	1.187 mm	1.077 mm	9.3%
Rogers 5880(S_3)	2.2	1.576 mm	1.456 mm	7.6%

Table 3: The second inversion approach: Inversion of relative permittivity with known thickness

MUT	Thickness	ε_r' (c_r)	ε_r' (c_p)	$\lvert e_1 \rvert$
Rogers 4003(S_1)	0.814 mm	3.55	3.45	2.8%
FR4(S_2)	0.814 mm	4.4	4.35	1.1%
FR4(S_3)	1.187 mm	4.4	4.35	1.1%
Rogers 5880(S_4)	1.576 mm	2.2	2.17	1.4%

second inversion algorithm is smaller than that from the first inversion algorithm. In other words, the elliptically doped CPNZ media sensor is more suitable for obtaining the relative permittivity of a material with known thickness and resonant frequency.

Furthermore, keeping the thickness of the material to be measured and the relative permittivity the same, we compared the accuracy of the proposed elliptically doped CPNZ media sensor, compared with the single-compound triple complementary split-ring resonator (SC-TCSRR) sensor [11] and interdigital capacitor (IDC) sensor [26], using four dielectric substrates with varying thicknesses and relative permittivity. To ensure a fair comparison, different sensors were operated in the same frequency band. The obtained relative permittivity relative error comparisons are shown in Fig. 9 (b).

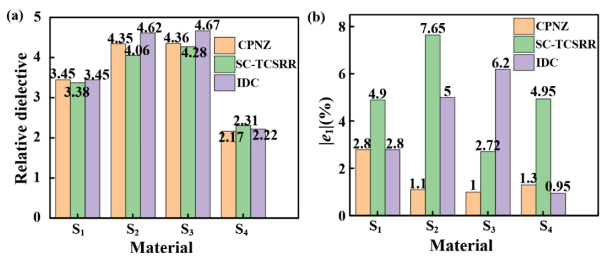

Fig. 9. The results of elliptically doped CPNZ media sensor, SC-TCSRR sensor and IDC sensor relative permittivity relative error.

In the same frequency band, Fig. 9 shows that the relative permittivity errors for the elliptically doped CPNZ media sensor remain below 2.8%, with an average relative error of 1.55%, while the errors for the SC-TCSRR sensor are below 7.7%, with an average relative error of 5.055%. The relative permittivity error of the IDC sensor remains below 6.2%, with an average relative error of 3.737%. The relative permittivity measurement accuracy of the elliptically doped CPNZ media sensor is better than that of other sensors, even when the material is bent. This confirms the high accuracy of the elliptically doped CPNZ media sensor in measuring ultra-thin surface coatings.

In addition to coating thickness and relative permittivity, which are crucial for material structure design and evaluation, the loss tangent is another important factor. However, most existing work does not thoroughly analyze the influence of material thickness, relative permittivity, and loss tangent on sensor transmission amplitude. Instead, it typically examines the relationship between relative permittivity, loss tangent, and sensor transmission amplitude, without considering the impact of thickness. Since thickness also affects the properties of materials, this simplified analysis compromises the accuracy of electromagnetic property measurements of their electromagnetic properties. Therefore, this paper analyzes the relationship among material thickness, relative permittivity, loss tangent, and sensor transmission amplitude.

First, the coating thickness, relative permittivity, and loss tangent were set. When the thickness increased from 0.5 mm to 1.5 mm in steps of 0.1 mm, the relative permittivity increased from 6 to 11 in steps of 0.5, and the loss tangent increased from 0 to 1.2 in steps of 0.1. A total of 1573 sets of data were obtained. The coating thickness, relative permittivity, and loss tangent were set as independent variables, with the transmission amplitude of the sensor as the dependent variable. The relationship between coating thickness, relative permittivity, loss tangent, and transmission amplitude was obtained through polynomial regression model fitting. As shown in Fig. 10, with a coefficient of determination of 0.9965.

In practical applications, the complex permittivity of most absorbing coatings is known, while the thickness is unknown. The absorbing properties of coatings with different thicknesses also vary. Therefore, five types of absorbing coatings with unknown thickness and known complex permittivity were selected as measurement objects. The five coatings are Al doped Ti3SiC2/paraffin wax, Ti3SiC2/paraffin, 12% CB/MAS, 4%CB/MAS, and 7% MWCNTs/MAS. The thicknesses of these five coatings, denoted as X_1, X_2, X_3, X_4, and X_5, were predicted. The thickness range of the five coatings was set to increase from 0.5 mm to 1.5 mm in steps

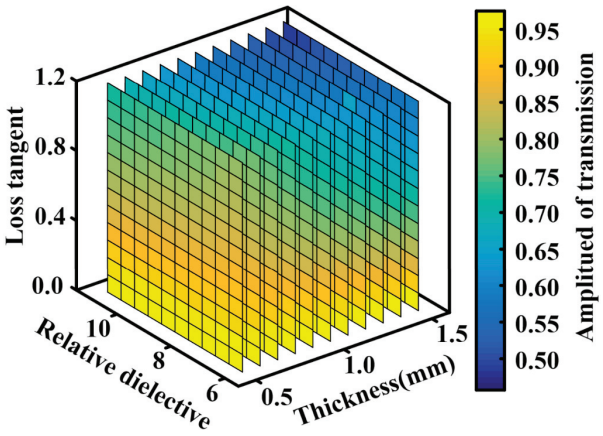

Fig. 10. Relationship between thickness of absorbing coating, relative permittivity, loss tangent, and transmission amplitude.

of 0.1 mm. A total of 55 sets of data were obtained. The obtained polynomial was used to invert the 55 sets of data from the simulation, and the relative errors of the five coatings at different thicknesses were compared to determine the most likely thickness. The thickness prediction values and relative errors obtained from the inversion are shown in Table 4. It can be seen that the relative thickness error for the five coatings is less than 1.1%, indicating good predictability.

Table 4: Thickness prediction and relative error of absorbing coatings with different complex permittivity

MUT	ε_r'	tanδ	Predicted Thickness (c_p)	$\lvert e_2 \rvert$
$\mathbf{X}_1$	5.94	0.0724	1.2 mm	0.17%
$\mathbf{X}_2$	8.42	0.641	1 mm	1%
$\mathbf{X}_3$	9.10	0.297	0.8 mm	0.04%
$\mathbf{X}_4$	9.54	0.521	0.9 mm	1.1%
$\mathbf{X}_5$	10.70	1.21	1.1 mm	0.06%

III. DISCUSSION

We have proposed a promising CPNZ sensor for ultra-thin coating materials measurement. We will fabricate and experimentally validate the sensors and to discuss the effects of fabrication and measurement tolerances on the sensing performance. In our work, it is assumed that the temperature and humidity are controlled within a small range of variations. The CPNZ sensor can be used in conjunction with an on-site reflectance measurement system. First, a suitable CPNZ sensor structure is modeled based on the curved surface geometry of the practical equipment under test. The reflectivity of the ultra-thin microwave-absorbing coating on the equipment is measured, and its complex permittivity can be inverted. By using the first inversion approach, inversion thickness with known relative permittivity, we can obtain the thickness of the microwave-absorbing coating. On the other side, if we have measured the thickness of the ultra-thin microwave-absorbing coating by using a thickness gauge, we can obtain the complex permittivity by using the second inversion approach, inversion of relative permittivity with known thickness. Additionally, for multi-physical-field detection, the CPNZ sensor could be extended by incorporating environmental sensing capabilities such as temperature and humidity sensors to construct a composite sensing platform. This would enable simultaneous acquisition of dielectric properties, coating thickness, and environmental conditions in complex operating environments.

IV. CONCLUSION

The proposed high-precision CPNZ medium microwave sensor offers a significant advancement for measuring the complex permittivity and thickness of ultra-thin surface materials. It overcomes the limitations of traditional sensors, which struggle with measuring the complex permittivity of curved materials and provides an effective solution for material thickness measurement. Simulation results demonstrate that the elliptically doped CPNZ media sensor outperforms other sensors in accurately measuring the complex permittivity of ultra-thin surface materials. The detection limit for thickness is 0.5 mm, with a measurement accuracy of up to 97% for relative permittivity. This sensor is capable of accurately measuring the complex permittivity of absorbing coatings of varying thicknesses and can predict the thickness of different types of absorbing coatings. It is expected to be an ideal choice for applications involving curved surface materials.

ACKNOWLEDGMENT

This work is supported by the National Natural Science Foundation of China under Grant No. 61971469 and Fundamental Research Funds of Shaanxi Key Laboratory of Artificially-Structured Functional Materials and Devices (AFMD-KFJJ-24212).

REFERENCES

[1] X. Weng, B. Li, Y. Zhang, X. Lv, and G. Gu, "Synthesis of flake shaped carbonyl iron/reduced graphene oxide/polyvinyl pyrrolidone ternary nanocomposites and their microwave absorbing properties," *Journal of Alloys and Compounds*, vol. 695, pp. 508-519, 2017.

[2] Z. Li, X. Wei, F. Luo, W. Zhou, and Y. Hao, "Microwave dielectric properties of Ti3SiC2 synthesized by solid state reaction," *Ceramics International*, vol. 40, pp. 2545-2549, 2014.

[3] J. Su, W. Zhou, Y. Liu, Y. Qing, F. Luo, and D. Zhu, "Effect of carbon black on dielectric and microwave absorption properties of carbon black/cordierite plasma-sprayed coatings," *Journal of Thermal Spray Technology*, vol. 24, pp. 826-835, 2015.

[4] J. Su, W. Zhou, Y. Liu, Y. Qing, F. Luo, and D. Zhu, "Atmosphere plasma-sprayed carbon nanotubes/cordierite nanocomposite coatings for microwave absorption applications," *Journal of Thermal Spray Technology*, vol. 23, pp. 1065-1072, 2014.

[5] F. Horner, T. A. Taylor, R. Dunsmuir, J. Lamb, and W. Jackson, "Resonance methods of dielectric measurement at centimetre wavelengths," *Electrical Engineers Part III: Radio and Communication Engineering*, vol. 93, no. 21, pp. 53-68, 1946.

[6] M. Santra and K. U. Limaye, "Estimation of complex permittivity of arbitrary shape and size dielectric samples using cavity measurement technique at microwave frequencies," *IEEE Transactions on Microwave Theory and Techniques*, vol. 53, no. 2, pp. 718-722, 2005.

[7] H. Miyagawa, K. Wakino, Y. D. Lin, and T. Kitazawa, "Simultaneous determination of complex permittivity and permeability of columnar materials with arbitrarily shaped cross section," *IEEE Transactions on Microwave Theory and Techniques*, vol. 57, no. 9, pp. 2249-2256, 2009.

[8] A. Yasin, F. Rehman, U. Naeem, S. A. Khan, and M. F. Shafique, "Top loaded TM01δ mode cylindrical dielectric resonator for complex permittivity characterization of liquids," *Radio Engineering*, vol. 25, no. 4, pp. 714-720, 2016.

[9] M. Saadat-Safa, V. Nayyeri, M. Khanjarian, M. Soleimani, and O. M. Ramahi, "A CSRR-based sensor for full characterization of magneto-dielectric materials," *IEEE Transactions on Microwave Theory and Techniques*, vol. 67, no. 2, pp. 806-814, 2019.

[10] R. Moolat, M. Mani, S. V. Abdulrahiman, A. Pradeep, V. Kesavath, and M. Pezholil, "Liquid permittivity sensing using planar open stub resonator," *Journal of Electronic Materials*, vol. 49, no. 3, pp. 2110-2117, 2020.

[11] C. L. Yang, C. S. Lee, K. W. Chen, and K. Z. Chen, "Noncontact measurement of complex permittivity and thickness by using planar resonators," *IEEE Transactions on Microwave Theory Techniques*, vol. 64, no. 1, pp. 247-257, 2016.

[12] J. K. Pakkathillam, B. T. Sivaprakasam, J. Poojali, C. V. Krishnamurthy, and K. Arunachalam, "Tailoring antenna focal plane characteristics for a compact free-space microwave complex dielectric permittivity measurement setup," *IEEE Transactions on Instrumentation and Measurement*, vol. 70, pp. 1-12, 2021.

[13] Y. Xiang, J. Huang, L. Fu, Y. Chen, W. Gu, and Y. Wu, "A folded substrate integrated waveguide reentrant cavity for full characterization of magneto-dielectric powder materials," *IEEE Sensors Journal*, vol. 21, no. 9, pp. 10657-10666, 2021.

[14] C. Wang, X. Liu, L. Gan, and Q. Cai, "A dual-band non-destructive dielectric measurement sensor based on complementary split-ring resonator," *Frontiers in Physics*, vol. 9, p. 669707, 2021.

[15] Z. Abbasi, P. Shariaty, M. Nosrati, Z. Hashisho, and M. Daneshmand, "Dual-band microwave circuits for selective binary gas sensing system," *IEEE Transactions on Microwave Theory and Techniques*, vol. 67, no. 10, pp. 4206-4219, Oct. 2019.

[16] N. Javanbakht, G. Xiao, and R. E. Amaya, "Portable microwave sensor based on frequency-selective surface for grain moisture content monitoring," *IEEE Sensors Letters*, vol. 5, no. 11, pp. 1-4, 2021.

[17] Y. Cao, K. Chen, C. Ruan, and X. Zhang, "Robust and sensitive metamaterial-inspired microfluidic sensor for liquids with low dielectric constants," *Sensors and Actuators A-Physical*, vol. 331, p. 112869, 2021.

[18] E. Rahamim, D. Rotshild, and A. Abramovich, "Performance enhancement of reconfigurable metamaterial reflector antenna by decreasing the absorption of the reflected beam," *Applied Sciences-Basel*, vol. 11, p. 8999, 2021.

[19] W. Zhou, Z. Zhu, and R. Bai, "Low-frequency broadband lightweight magnetic composite absorber based on metamaterial structure," *OPTIK*, vol. 244, p. 167619, 2021.

[20] A. K. Jha and M. J. Akhtar, "Elevated and tapered microstrip coupled ENZ SIW sensor for microwave testing of radome and building materials in 3G and ISM bands," in *URSI Asia-Pacific Radio Science Conference (URSI AP-RASC)*, Seoul, Korea (South), pp. 1761-1764, 21-25 Aug. 2016.

[21] Z. Zhou, Y. Li, H. Li, W. Sun, I. Liberal, and N. Engheta, "Substrate-integrated photonic doping for near-zero-index devices," *Nature Communications*, vol. 10, no. 1, p. 4132, 2019.

[22] H. Lobato-Morales, A. Corona-Chávez, J. L. Olvera-Cervantes, R. A. Chávez-Pérez, and J. L. Medina-Monroy, "Wireless sensing of complex dielectric permittivity of liquids based on the RFID," *IEEE Transactions on Microwave Theory and Techniques*, vol. 62, no. 9, pp. 2160-2167, 2014.

[23] A. K. Jha, N. Delmonte, A. Lamecki, M. Mrozowski, and M. Bozzi, "Novel MNZ-type microwave sensor for testing magnetodielectric materials," *Scientific Reports*, vol. 10, no. 1, pp. 1-3, 2020.

[24] S. Mário and E. Nader, "Tunneling of electromagnetic energy through subwavelength channels and bends using epsilon-near-zero materials," *Physical Review Letters*, vol. 97, p. 157403, 2006.

[25] V. Pacheco-Peña, M. Beruete, P. Rodríguez-Ulibarri, and N. Engheta, "On the performance of an ENZ-based sensor using transmission line theory and effective medium approach," *New Journal of Physics*, vol. 21, no. 4, p. 043056, 2019.

[26] L. Ali, C. Wang, F. Y. Meng, K. K. Adhikari, Y. C. Wei, J. H. Li, Z. W. Song, and M. Zhao, "Design and optimization of interdigitated microwave sensor for multidimensional sensitive characterization of solid materials," *IEEE Sensors Journal*, vol. 21, no. 20, pp. 22814-22822, 2021.

Si Hui Jia is currently pursuing the doctor's degree in Electronic Science and Technology at Shanghai University, Shanghai 200444, China. He received the master's degree in electronics and communication engineering from Yangtze University, Jingzhou 434023, China, in 2022. His current research is in the direction of microwave sensing.

Yu Wei Mao received the B.S. degree from Bengbu College, Bengbu, China, in 2015, and the master's degree in Communication and Information Engineering at Shanghai University, Shanghai 200444, China, in 2018. Her current research is focused on near-zero medium sensor technology.

Qiao Yu Li is currently pursuing the doctor's degree in Electromagnetic Field and Microwave Technology in Shanghai University, Shanghai 200444, China. She received the B.S. degree in Engineering from Henan Normal University, Xinxiang, China, in 2016, received the master's degree in Electromagnetic Field and Microwave Technology from Shanghai University, Shanghai 200444, China, in 2019. Her current research is focused on plasmonic sensor devices.

Zi Jian Gao was born in Tongcheng, Anhui Province, China, in 1998. Currently, he is pursuing a master's degree in communication and information systems at Shanghai University, China, and his research interests are microwave sensing and algorithms.

Zi Peng Shan was born in 1974. He received the B.S. degree in Industrial Automation from Shanghai University, Shanghai, China, in 1997, and the M.S. degree in Software Engineering from Beijing Institute of Technology, Beijing, China, in 2010, respectively. He currently serves as the Director of Modern Educational Technology Center at Shanghai University. Additionally, he acts as the Director of the Cloud Computing Joint Laboratory, Virtual Simulation Experimental Center, and "Cloud + Humanities" Experimental Teaching Demonstration Center. His recent research focuses on machine learning, cloud computing and virtualization technologies.

Yong Jin Zhou received the B.S. degree in communication engineering from Shandong University, Jinan, China, in 2006, and Ph.D. degree in electromagnetic field and microwave technology from Southeast University, Nanjing, China, in 2011. From 2009 to 2010, he was a visiting scholar of University of Houston. From 2011 to 2012, he was a software engineer with EEBU of Marvell Technology (Shanghai) Ltd. From 2012 to 2015, he was an Assistant Professor with School of Communication & Information Engineering, Shanghai University, Shanghai, China. From 2015, he was an Associate Professor with School of Communication & Information Engineering, Shanghai University, Shanghai, China. From 2020, he was a Professor with School of Communication & Information Engineering, Shanghai University, Shanghai, China. His current research interests include plasmonic metamaterials, millimeter wave and THz functional devices, wireless energy transmission, and computational electromagnetism. He has served as *Applied Computational Electromagnetics Society (ACES) Journal* guest editor and is serving as a Youth Editorial Board Member *Journal of Electronics & Information Technology*. He is serving as a Reviewer for over 20 peer-reviewed journals, such as *Nature Electronics, Photonic Research, Optics Letter, Optics Express, Appl. Phys. Express, IEEE Access, IEEE MTT,* and *IEEE MWCL*. He has served as a session chair for several International Symposiums.

An Angularly Stable and Polarization Insensitive Miniaturized Frequency Surface for WiMAX Applications

Ze Wang, Huaxin Zhu, Dongming Guo, Xu Gan, and Xianzheng Lyu

School of Science
Jiangnan University, Wu Xi 214122, China
6231206032@stu.jiangnan.edu.cn, zhuhuaxin1312@163.com, 1422737299@qq.com,
2722309952@qq.com, 2103496771@qq.com

Abstract **–** This paper presents a miniaturized, polarization insensitive and angularly stable frequency selective surface (FSS) for WiMAX (3.5 GHz) applications. The proposed FSS structure improves upon conventional curved units by incorporating 45° tilted dipoles with extended lengths to increase the effective electrical size. The proposed FSS is printed on float glass with a dielectric constant of 8. The unit cell dimensions are $0.062\lambda_0 \times 0.062\lambda_0$ (where λ_0 is the free space wavelength at the first resonant frequency). It exhibits a bandstop characteristic at 3.5 GHz with a bandwidth of 540 MHz (-10 dB). This FSS demonstrates a stable frequency response under incident angles ranging from 0° to 80° for both horizontal and polarization angles. Furthermore, the proposed structure is further analyzed through the derivation of an equivalent circuit model. Finally, a prototype of adequate size is fabricated to validate the simulation results. Both the simulation and measured results confirm the stable performance of the proposed FSS.

Index Terms **–** Angular stability, bandstop filters, frequency selective surface (FSS), miniaturization, polarization insensitive.

I. INTRODUCTION

With the ongoing miniaturization trend in wireless communication devices, developing miniaturized frequency selective surfaces (FSS) has become essential to address stringent size limitations in modern system integration. As two-dimensional periodic arrays fabricated on dielectric substrates [1–2], FSS exhibit unique frequency-dependent properties that enable selective control of electromagnetic wave transmission, reflection, and absorption [3–4]. Given these features, FSS is extensively employed in centimeter-wave and millimeter wave domains, serving roles in hybrid antenna radomes, radar cross-section (RCS) reduction, antenna reflectors, absorbers, high impedance surfaces, and electromagnetic shielding [5–9]. However, practical applications are often constrained by limited spatial availability. It becomes challenging to accommodate larger physical components to achieve enhanced FSS performance. Therefore, miniaturizing the FSS offers the potential for more precise performance metrics.

Recent years have witnessed significant progress in the development of miniaturized FSS. Jayanandan and Alex proposed a miniaturized FSS operating at 2.45 GHz, which achieved cell miniaturization and stable polarization response by loading distributed reactive elements such as square patches (SP) and meander lines. However, its miniaturized period only reached $0.12\lambda_0 \times 0.12\lambda_0$ [10]. Li et al. developed a compact FSS employing capacitive, inductive, and resonant-type surface impedance elements that attained a remarkable miniaturization factor of $0.056\lambda_0 \times 0.056\lambda_0$, though the multilayer configuration increased fabrication complexity and the structure maintained satisfactory resonant stability only within a limited 45° incidence angle range [11]. Vardaxoglou and Alexandridis designed a steady-state FSS with $0.025\lambda_0 \times 0.025\lambda_0$ miniaturization through combined square and triangular structures, but the asymmetric metallic configuration resulted in poor polarization symmetry. These limitations highlight the pressing need for a miniaturized FSS that combines simplified fabrication with excellent polarization response and wide-angle stability [12].

In this study, we propose a miniaturized FSS with a convoluted structure based on the conventional winding technique, and our proposed FSS has excellent miniaturization characteristics compared to other element designs, with a design size of $0.062\lambda_0 \times 0.062\lambda_0$. In addition, the working mechanism is investigated by surface current distribution and equivalent circuit. Finally, we fabricate the FSS structure as a prototype. Good reflections were obtained in the WiMAX band, and the agreement between the measured and simulated results was very obvious.

II. MINIATURIZED STRUCTURE AND ITS PERFORMANCE

The evolutionary geometry of the proposed miniaturized unit is depicted in Fig. 1. The first design

Submitted On: March 7, 2025
Accepted On: May 26, 2025

https://doi.org/10.13052/2025.ACES.J.400606

phase features a cross-shaped dipole unit, while the second phase involves a cross-convoluted unit. A cross-convoluted unit is a commonly used structure for miniaturized frequency selective surfaces [13].

The proposed design evolved from the cross-convoluted unit and is comprised of four symmetrically bent units. This tight packing serves to reduce the resonating dimensions of the FSS while increasing the effective electrical size. Based on the conventional cross-curled unit cell, this work introduces an additional 45° tilted dipole to each horizontal strip dipole. Compared to traditional 90° vertical dipoles, this modified configuration occupies a larger physical footprint while effectively enhancing the electrical size. The compact arrangement contributes to the reduction of the FSS's resonant dimensions. Furthermore, the 45° inclination optimizes the structural coverage ratio, resulting in additional resonant frequency reduction. Meanwhile, the 90° symmetric unit cell facilitates polarization insensitivity. This FSS is printed on float glass with a thickness of 1.6 mm and a dielectric constant of 8, ensuring a low manufacturing cost. The parameters of the final structure unit are provided in Fig. 1 (d) and Table 1. For ease of visualization, Fig. 1 (e) provides a partial enlarged detail. All simulated structures were realized using the ANSYS High Frequency Structure Simulator (HFSS). The proposed FSS structure was modeled under periodic boundary conditions with Floquet port excitation [14].

To systematically investigate the frequency response

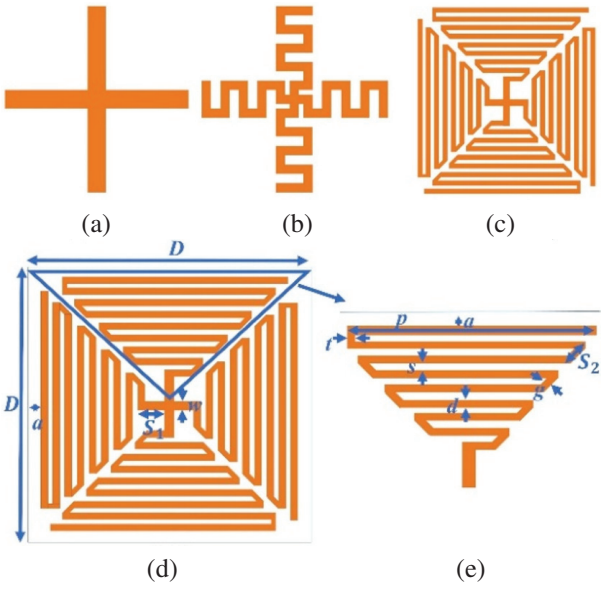

Fig. 1. Design evolution of the structure: (a) cross-shaped dipole unit, (b) cross-convoluted unit, (c) final structure unit, (d) proposed FSS unit, and (e) partial enlarged detail.

Table 1: Dimensions and parameters of Fig. 1

Parameter	***D***	***w***	***d***	***g***	***s***
Value (mm)	5.3	0.2	0.15	0.11	0.1
Parameter	S_1	S_2	***p***	***a***	***t***
Value (mm)	0.55	0.35	4.65	0.05	0.1

evolution of the FSS structure, our analysis begins with fundamental unit cell configurations: the basic cross-shaped dipole and its convoluted counterpart. The periodicity of this cross-shaped dipole unit and cross-convoluted unit aligns unit with that of the final structure unit. Figure 2 presents the transmission curves for three designs. As observed in Fig. 2, with increasing coiling, the resonant frequency of the FSS structure decreased dramatically from 13.3 GHz to 3.5 GHz, representing a 74% reduction. Likewise, bandwidth (-10 dB) dropped from 2.99 GHz to 0.54 GHz, a decrease of 79%, but this bandwidth perfectly covers WiMAX (3.5 GHz). Hence, from our observations, we discerned that, as the degree of coiling increases, both the resonant frequency and the resonant bandwidth decrease. The decline in resonant frequency can be elucidated using $f = \frac{1}{2\pi\sqrt{LC}}$ in which L and C represent the equivalent inductance and capacitance, respectively. By amplifying the equivalent inductance and capacitance, the resonant frequency can be reduced. The equivalent inductance, L, is related to the structure's length, while the equivalent capacitance, C, is associated with the width between structures [15]. The transition from the cross-shaped dipole unit to the final structure unit is marked by an increase in the structural perimeter and a reduction in the inter row spacing, leading to an observed decrease in the resonant frequency. The bandwidth of a bandstop FSS is associated with the ratio of the FSS's equivalent capacitance to its equivalent inductance ($\mathrm{BW} \propto \sqrt{\frac{C}{L}}$) [16]. From the cross-shaped dipole unit to the final structure unit, the change in the structural perimeter is more pronounced than the interspace alteration, resulting in the observed bandwidth reduction.

Moving forward, we now discuss the impact of varying geometric parameters on the proposed FSS. Figure 3 (a) showcases the effect of line variations on the FSS. As evident from Fig. 3 (a), when parameter d increases from 0.05 mm to 0.2 mm, the resonant frequency of the FSS rises with the widening of the line width, moving from 3.2 GHz to 3.8 GHz. This phenomenon is primarily attributed to the reduction in the corresponding capacitance as the line width increases, thereby elevating the resonant frequency. Furthermore, we examined the influence of variations in the relative permittivity of the dielectric substrate on the FSS. From Fig. 3 (b), it can be observed that, as the dielectric

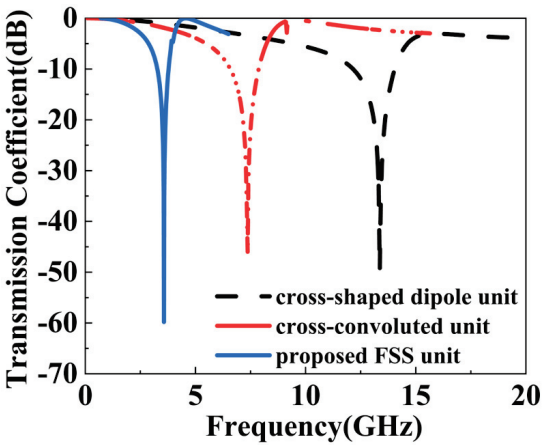

Fig. 2. Different structure responses.

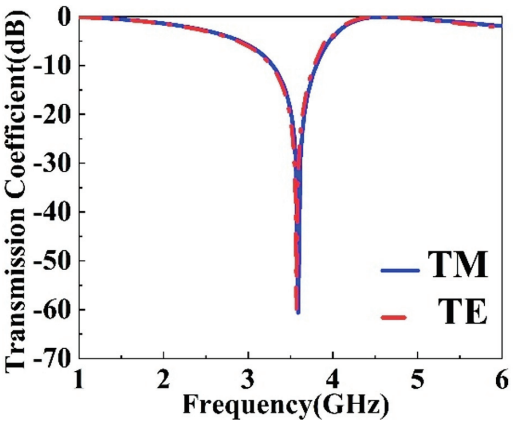

Fig. 4. Frequency curves for TE and TM polarization at 0° θ angle.

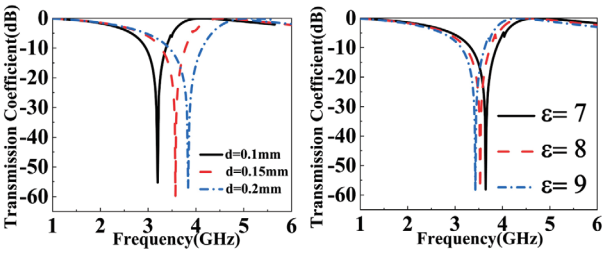

(a) (b)

Fig. 3. (a) Different line variation responses and (b) different relative permittivity responses.

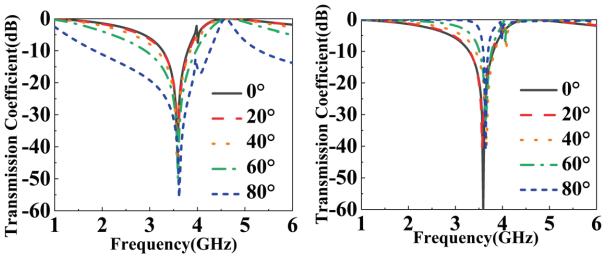

(a) (b)

Fig. 5. Frequency curves for different angles: (a) 0-80° θ angle TE polarization, and (b) 0-80° θ angle TM polarization.

constant increases from 7 to 9, the corresponding resonant frequency decreases from 3.64 GHz to 3.42 GHz. This change stems from the inverse relationship between the resonant frequency and permittivity, as depicted in $f = \frac{f_0}{\sqrt{1+\frac{\varepsilon_r}{2}}}$, where f_0 in the formula indicates the resonant frequency in a vacuum [17].

For practical implementations, the angular stability of miniaturized FSS becomes critical as these structures are routinely exposed to oblique wave incidence spanning 0° to 80° in typical deployment environments [18]. Thus, an FSS that exhibits a stable frequency response under varying angles of incidence is considered a benchmark for quality. Simulations were conducted on the central frequency of the miniaturized FSS using the HFSS software. Figure 4 presents the simulated curves for both TE and TM polarizations at a 0° angle. From Fig. 4, it is evident that the FSS provides consistent responses under both TE and TM polarizations.

Figures 5 (a) and (b) present the simulated curves for both TE and TM polarizations at θ incidence angle. The results demonstrate that the designed FSS structure exhibits a stable response under both TE and TM polarizations. It is clear from the results that, for TE polarization, the maximum frequency shift for θ is no more than 0.05 GHz (1.4%). Similarly, for TM polarization, the maximum frequency shift for θ does not exceed 0.07 GHz (2%).

As the angle of incidence increases, the bandwidth under TE polarization expands, while it narrows under the TM mode. This is attributed to the fact that with the rise in angle of incidence, according to $Z_{TE} = \frac{Z_0}{cos\ \theta}$ and $Z_{TM} = Z_0 \times cos\ \theta$, Z_{TE} is increasing and Z_{TM} is decreasing as the angle of incidence increases further [19]. Z_{TE} and Z_{TM} represent the wave impedance of TE and TM.

The equivalent current distribution at 3.5 GHz is shown in Fig. 6 (a), where green and blue regions represent high and low current intensities, respectively. At this resonant frequency, the current density is predominantly concentrated on the dipole elements along both lateral edges. Specifically, in the horizontal direction, the current flows sequentially from the leftmost edge dipole to the central cross-shaped unit, and subsequently to the rightmost edge dipole, forming a complete current loop. This distinct current path suggests the establishment of strong current circulation between the lateral dipoles under electromagnetic excitation. In contrast, the vertical

current flow between the topmost and bottommost edge dipoles exhibits relatively weaker intensity compared to its horizontal counterpart. Notably, the current magnitude on the lateral dipoles significantly exceeds that on the vertical dipoles. This asymmetric current distribution plays a crucial role in generating the FSS's stopband characteristics. The enhanced horizontal current response, particularly the strong currents along the lateral edges, contributes substantially to the formation of the stopband effect at specific frequencies. Based on this analysis, the metallic dipoles can be effectively modeled as equivalent inductors (L), while the inter-element gaps are represented as capacitors (C) in the circuit analogy. Figure 6 (b) presents the corresponding equivalent circuit model, which visually demonstrates these electromagnetic characteristics through lumped-element representations [20].

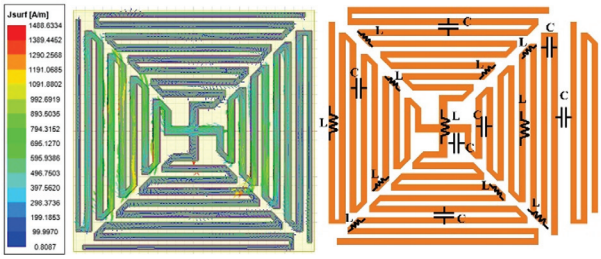

Fig. 6. (a) Surface current distribution at 3.5 GHz and (b) FSS circuit schematic.

To validate the full-wave simulation results and further understand the working mechanism of the FSS, we derived an equivalent circuit model of the FSS, as shown in Fig. 7 (a). Here, Z_0 represents the wave impedance of free space, with a value of 377 Ω, and ε_r denotes the relative permittivity of the dielectric substrate. The wave impedance of the dielectric substrate, *Zsub*, can be determined by $Z_{sub} = \frac{Z_0}{\sqrt{e_r}}$. Based on the equivalent circuit model in Fig. 7 (a), the impedance at the center frequency of 3.5 GHz is expressed by:

$$Z_{3.5GHz} = \frac{1}{j\omega C_1} + j\omega L_1 + \frac{1-\omega^2 (L_2+L_3) C_2}{j\omega C_2}. \quad (1)$$

Here, the capacitance *C1* represents the gap capacitance between adjacent unit cells, primarily determined by the spacing width and electric field distribution. The inductance *L1* corresponds to the structural inductance of the dipole, closely related to its length and current path. Meanwhile, *L3* denotes the inductance of the 45° inclined dipole, while *L2* and *C2* represent the internal inductance of the cross-shaped unit and the gap capacitance between the dipole and the cross-shaped structure, respectively. According to the resonant frequency formula $f = \frac{1}{2p\sqrt{L}}$, increasing parameters a or s enhances the coupling area between unit cells and reduces the electric field intensity between metallic structures, thereby increasing the equivalent capacitance *C1*. Conversely, increasing parameters p, S2, or the edge dipole length extends the current path, leading to higher equivalent inductances *L1* and *L2*, which shifts the resonant frequency toward lower frequencies. The inductance of the 45° tilted dipole, denoted as *L3*, can be effectively tuned by adjusting parameters d and w. Increasing these parameters reduces the metallic trace inductance, consequently decreasing the equivalent inductance *L3*. This reduction in *L3* shifts the resonant frequency toward higher frequencies.

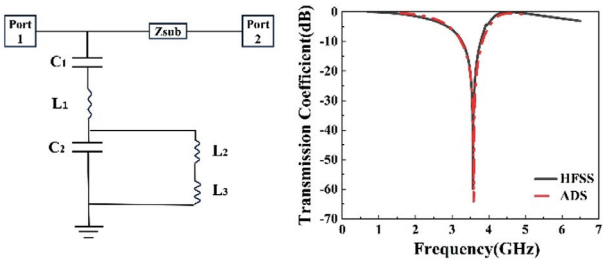

(a) (b)

Fig. 7. (a) Equivalent circuit of the proposed bandstop FSS structure and (b) ADS software and HFSS software transmission coefficient.

Within the Advanced Design System (ADS), the equivalent circuit model for the FSS was simulated. Based on the equivalent current distribution and the circuit schematic of the FSS, we imported the equivalent circuit structure into the ADS software and derived the values of the superimposed components. To accurately extract the capacitance and inductance values in the equivalent circuit, we employed an optimization-based fitting method that considers transmission zeros and bandwidth characteristics. The inductance (L) and capacitance (C) values were constrained within ranges of 0.01-10 nH and 0.01-10 pF, respectively, for random sampling using ADS software. These parameter ranges were determined through systematic analysis of the FSS's geometric parameters and electromagnetic properties, ensuring comprehensive coverage of the potential parameter space. During the optimization process, the built-in optimization tools in ADS were employed to perform curve fitting for the equivalent circuit model. The model's accuracy was evaluated by comparing the S_{21} parameters obtained from ADS simulations with HFSS simulation results. The specific optimization strategy consisted of two main steps. First, adjusting the inductance and capacitance values to align the transmission zero and pole of the equivalent circuit model with the HFSS simulation results and, subsequently, further optimizing these values to ensure the bandwidth characteristics matched

the HFSS results. Figure 7 (b) illustrates the response of ADS and HFSS, showing that the transfer coefficients of both are in good agreement. In each iteration, the error between the simulated results and HFSS data was calculated. Systematic adjustments of the inductance and capacitance values were made to progressively reduce this error until the iterative error converged below 5%. Through multiple optimization iterations, precise inductance and capacitance values were ultimately obtained, as presented in Table 2.

Table 2: Circuit parameters of FSS

Parameter	L_1	L_2	L_3	C_1	C_2
Value (nH/pF)	1.27	1.86	0.84	0.64	0.15

III. EXPERIMENTAL RESULTS AND DISCUSSION

The proposed fabricated FSS prototype is shown in Fig. 8 (a), where an array of 18×18 cells with a size of 20×20 cm was printed on float glass by photolithography process. Figure 8 (b) shows the photograph of the measurement setup. It consists of two horn antennas operating in the 1-18 GHz range, both of which are connected to a FieldFox N9918A handheld vector network analyzer. During the transmission curve measurement, the horn antennas were positioned at a certain distance apart, facing each other. Measurements were taken in a standard indoor environment surrounded by absorber material.

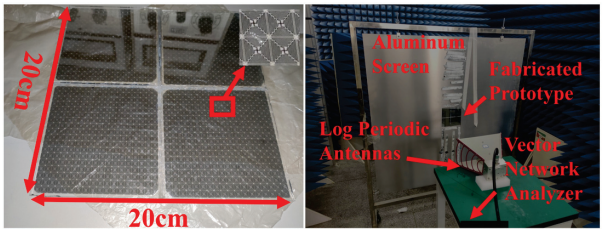

(a) (b)

Fig. 8. FSS finite prototype and measurement equipment: (a) fabricated prototype and (b) measurement setup.

Based on the measurement results depicted in Fig. 9, a slight deviation in the measured resonant frequency is observed, with an offset of 70 MHz. This deviation has a negligible impact at 3.5 GHz.

Concurrently, angular stability tests were performed on the FSS prototype, with results presented in Figs. 10 (a) and (b). When angle θ is set to 80°, the fabricated FSS displays a stable response at the resonant frequency under TE polarization and TM polarization. In the context of TE polarization, angle θ exhibits a

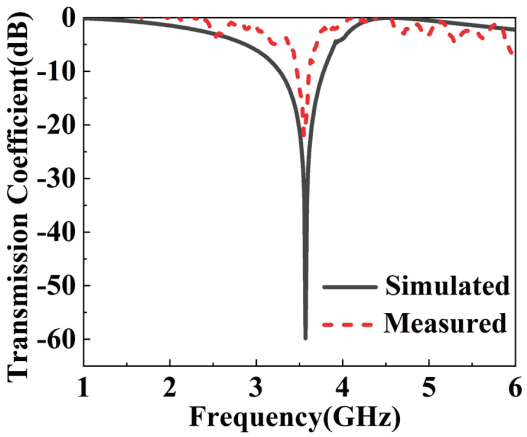

Fig. 9. Comparison of simulated curve and measured result.

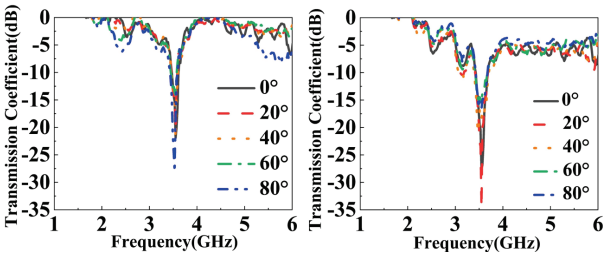

(a) (b)

Fig. 10. Measured frequency response curve: (a) 0-80° θ angle TE polarization and (b) 0-80° θ angle TM polarization.

maximum frequency shift of 40 MHz (1.3%), Similarly, for TM polarization, angle θ reveals a shift of only 60 MHz (2.0%) in the same range.

We fabricated the FSS cells in smaller sizes. Some of the designs in Table 3 have neither high angular stability nor polarization insensitivity, and most of the FSS structures have lower angular stability than our designs. As can be seen in Table 3, the single-layer FSS structures we designed and printed are ultra-miniaturized, highly polarization-insensitive, and angularly stable.

Table 3: Comparison of the proposed FSS structure with previous miniaturized FSS studies

Ref.	Unit Cell Size (mm)	Periodicity (λ_0)	Angular Stability	Polarization Insensitive
[21]	11.4	0.091	80°	YES
[22]	25	0.29	60°	YES
[24]	9.5	0.125	45°	YES
[25]	6.25	0.05	75°	NO
This Work	5.3	0.062	80°	YES

IV. CONCLUSION

In this study, we introduce a miniaturized and polarization-stabilized FSS design based on the improvement of a conventional cross-convolutional unit. The improved design has higher polarization stability and smaller cell size than the conventional cross-convolution FSS. The resonant frequency is 3.5 GHz and the suppression bandwidth is 540 MHz (-10 dB), which perfectly covers the WiMAX band (3.5 GHz). In addition, the design has been proven to show a stable frequency response over a range of incidence angles from 0° to 80° for both TE and TM polarization.

ACKNOWLEDGMENT

This work was supported by the National Natural Science Foundation of China (61605067); Open Fund of Key Laboratory of Optical System Advanced Manufacturing Technology, Chinese Academy of Sciences (KLOMT190103).

REFERENCES

[1] B. A. Munk, *Frequency Selective Surfaces Theory and Design*. New York, NY: Wiley, 2000.

[2] J. Yiannis and C. Vardaxoglou, *Frequency Selective Surfaces Analysis and Design*. New York, NY: Wiley, 1997.

[3] T. K. Wu, *Frequency Selective Surface and Grid Array*. New York, NY: Wiley, 1995.

[4] J. C. Vardaxoglou, *Frequency Selective Surfaces: Analysis and Design*. New York, NY: Wiley, 1997.

[5] A. Malekara, C. Ghobadi, and J. Nourinia, "A frequency selective absorber with anisotropic reflection band for radar cross section reduction," *IEEE Access*, vol. 11, pp. 132557-132566, 2023.

[6] A. Ericsson, M. Zhou, S. B. Sørensen, T. Rubæk, M. Riel, and N. J. G. Fonseca, "Modulated frequency-selective doubly curved sub-reflector for a dual-band multiple spot beam communication satellite antenna system," *IEEE Transactions on Antennas and Propagation*, vol. 72, pp. 9152-9163, 2024.

[7] Y. Fu, F. Ding, J. Jin, H. Cheng, Y. Yang, X. Zhou, Y. Dai, and H. Yang, "Conformal frequency selective rasorber in S, C, X-band with low backward-scattering," *Opt. Express*, vol. 32, pp. 16879-16890, 2024.

[8] M. Li, C. Zhang, X. Yang, D. Zeng, and Z. Yi, "An ultrawideband and wide-angle absorber based on mushroom-type high impedance surface," *IEEE Antennas and Wireless Propagation Letters*, vol. 23, pp. 4368-4372, 2024.

[9] Q. Li, Q. Wang, H. Zhang, J.-Q. Hou, and J. Zhao, "A new miniaturized double stop-band frequency selective surface," *Applied Computational Electromagnetics Society (ACES) Journal*, vol. 39, pp. 9-16, 2024.

[10] T. Jayanandan and Z. C. Alex, "A miniaturized embedded frequency selective surface-based EMI shield for microwave ovens," *International Journal of Communication Systems*, vol. 38, no. 5, 2025.

[11] Z. Li, X. Weng, X. Yi, W. Duan, K. Li, M. Bi, T. Pan, and Y. Lin, "A miniaturized ultrawideband dual-bandpass frequency-selective surface with high selectivity," *IEEE Transactions on Antennas and Propagation*, vol. 72, pp. 6510-6519, 2024.

[12] Y. Vardaxoglou and A. A. Alexandridis, "Frequency selective surface with a bistable auxetic geometry," *Electronics Letters*, vol. 60, no. 12, 2024.

[13] S. Nan, Z. Hou, L. Guiyuan, and X. Haiyang, "Miniaturized frequency selective surface based on meander lines unit," *Journal of Detection & Control*, vol. 32, pp. 87-89, 2010.

[14] A. Chatterjee and S. K. Parui, "Frequency-dependent directive radiation of monopole-dielectric resonator antenna using a conformal frequency selective surface," *IEEE Transactions on Antennas and Propagation*, vol. 65, pp. 2233-2239, 2017.

[15] N. Marcuvitz, *Waveguide Handbook*. Lexington, MA: Boston Technical Publishers, 1964.

[16] P. C. Zhao, Z. Y. Zong, B. Li, W. Wu, and D. G. Fang, "Miniaturized bandstop frequency selective surface based on quasi lumped inductor and capacitor," *Electronics Letters*, vol. 53, pp. 642-643, 2017.

[17] M. B. Yan, S. B. Qu, J. F. Wang, J. Q. Zhang, H. Zhou, H. Y. Chen, and L. Zheng, "A miniaturized dual band FSS with stable resonance frequencies of 2.4 GHz/5 GHz for WLAN applications," *IEEE Antennas and Wireless Propagation Letters*, vol. 13, pp. 895-898, 2014.

[18] K. Z. Zhang, W. Jiang, J. Y. Ren, and S. X. Gong, "An annular-ring miniaturized stopband frequency selective surface with ultra-large angle of incidence," *Progress in Electromagnetics Research M*, vol. 65, pp.19-27, 2010.

[19] P. S. Wei, C. N. Chiu, and T. L. Wu, "Design and analysis of an ultraminiaturized frequency selective surface with two arbitrary stopbands," *IEEE Transactions on Electromagnetic Compatibility*, vol. 61, pp. 1447-1456, 2019.

[20] A. B. Varuna, S. Ghosh, and K. V. Srivastava, "A miniaturized element bandpass frequency selective surface using meander line geometry," *Microwave and Optical Technology Letters*, vol. 59, pp. 2484-2489, 2017.

[21] D. M. Liu, B. Chen, S. W. Ji, and J.-F. Ruan, "A thin and miniaturized bandpass frequency selective surface with superior angular stability," *Journal of Electromagnetic Waves and Applications*, vol. 39, no. 7, pp. 743-753, 2025.

[22] M. Idrees, S. Buzdar, S. Khalid, and M. A. Khalid, "A miniaturized polarization independent frequency selective surface with stepped profile for shielding applications," *Applied Computational Electromagnetics Society (ACES) Journal*, vol. 31, pp. 531-536, 2021.

[23] S. Das, A. Rajput, and B. Mukherjee, "A novel FSS-based bandstop filter for TE/TM polarization," *IEEE Letters on Electromagnetic Compatibility Practice and Applications*, vol. 6, pp. 11-15, 2024.

[24] L. Murugasamy and R. Sivasamy, "A single layer interdigitated loop elements-based miniaturized frequency selective surface for WLAN shielding," *IEEE Transactions on Consumer Electronics*, vol. 70, pp. 617-626, 2024.

[25] Z. U. Abidin, Q. Cao, and G. Shah, "Design of a compact single-layer frequency selective surface with high oblique stability," *IEEE Transactions on Electromagnetic Compatibility*, vol. 64, pp. 2060-2066, 2022.

Ze Wang was born in Puyang, Henan, China, in 1999. He received the B.S. degree from the Xiamen University of Technology, Xiamen, China, in 2023. Currently, he is focusing on antenna and microwave devices.

Huaxin Zhu received his Ph.D. degree in 2011. Since 2011, he has worked on optical thin film design, preparation and frequency selective surfaces. Currently, he is an Associate Professor in the Jiangnan University, School of Science, China.

Dongming Guo was born in Quanzhou, Fujian, China, in 2000. He received the B.S. degree from the Xiamen University of Technology, Xiamen, China, in 2022. Currently, he is focusing on antenna and microwave devices.

Xu Gan was born in Zaozhuang, Shandong, China, in 2000. He received the B.S. degree from the Xiamen University of Technology, Xiamen, China, in 2024. Currently, he is focusing on antenna and microwave devices.

Xianzheng Lyu was born in Jining, Shandong, China, in 2000. He received the B.S. degree from the Xiamen University of Technology, Xiamen, China, in 2024. Currently, he is focusing on antenna and microwave devices.

Compact Single and Dual-Band Branch-Line Coupler with Effective Fractional Bandwidth for Wireless Communication Systems

G. Srividhya and S. Maheswari

Department of ECE
Panimalar Engineering College, Poonamallee, Chennai, Tamil Nadu 600123, India
srividhyakrishiv@gmail.com, maheswarisp@yahoo.co.in

Abstract **–** Multiple wireless communication systems make use of a branch-line coupler (BLC), which is a passive microwave component. For the purpose of splitting and combining microwave signals, as well as providing a 90-degree phase shift between the output ports, this 4-port device is made from four quarter-wavelength ($\lambda/4$) transmission lines. Having recently developed a dual-band branch-line coupler (DBBLC), there has been a lot of attention paid to this development. When it comes to getting dual-band (DB) functioning of a BLC, one of the most common approaches is stub loaded transmission lines. For the BLC, stubs may be positioned either in the center of the arms or at the input of the arms. Stepped-impedance stubs, orthogonal coupled branches, and coupled lines are some of the strategies that have been shown to be effective in achieving DB functioning of a coupler. Through the utilization of the Elongated T-Shape Transmission Line (ETSTL), this work presents a one-of-a-kind design for each single-band branch-line coupler (SBBLC) and DBBLC that is of a compact proportion. Based on the information presented in this article, the SBBLC operates at a frequency of 0.9 GHz, whereas the DBBLC operates at 0.9 and 2.4 GHz. Using a fractional bandwidth (FBW) of 44%, the coupler that has been proposed is able to function at both 0.9 GHz (GSM) and 2.4 GHz (wireless). Efforts are done on reducing the size of the coupler to be ready for fabrication.

Index Terms **–** Branch-line coupler, dual-band branch-line coupler, single-band branch-line coupler, wireless communication systems.

I. INTRODUCTION

Branch-line couplers (BLC) are an essential component of wireless communication systems, since they enable the development of crossovers, Butler matrices (BMs), and antenna arrays. They play an important role in radio frequency (RF) and microwave systems, and they are also an essential component of wireless communication systems. There are several benefits associated with BLC, some of which include a broad bandwidth, balanced power division, and excellent isolation between output ports. The use of microstrip or strip line transmission lines, which provide the advantages of compactness and ease of integration into microwave circuits, is often used in their construction. The compactness, fractional bandwidth (FBW), and harmonic suppression that are desired in single-band (SB) BLCs have been accomplished via the use of a number of different strategies [1–7]. A T-shaped section was used in [1] in order to accomplish the combination of small sizes and harmonic reduction. Transmission lines that are stub loaded are used for the purpose of achieving compactness, FBW, and harmonic suppression [2]. For the purpose of achieving a compact form and FBW, a T-shape with an open stub [3] and open stubs with high-low impedance [4] were used. The meander T-shaped line [5] and the symmetric structure [6] both increase isolation, return loss, and harmonic attenuation, which ultimately leads to ideal frequency response without increasing the size of the circuit. For the construction of the coupler, a microstrip-slot BLC made up of two sections was used [7]. When it comes to the miniaturization of the structure and the suppression of harmonics, low-pass filters (LPFs) [8] are used as coupler branches in a number of different designs [10] This method tends to provide satisfactory outcomes. Additionally, dual-band (DB) BLC [11–18] were explored.

In recent times, DB components have earned a great deal of attention as a result of the potential opportunities they provide for use in BM [11] and crossovers [12]. In response to this, a number of other DBBLCs have been created. A DBBLC is often created by simply exchanging every quarter-wave line from a single-band branch-line coupler (SBBLC) with an equal number of DB quarter-wave blocks. This is the most common method. In order to investigate DB approaches, many strategies are used. These techniques include π-shaped lines [13], T-network [14], open-ended stub [15], coupled line [16], feature-based optimization [17], port extension [18, 19], and cross coupled [20].

Submitted On: September 3, 2024
Accepted On: May 22, 2025

https://doi.org/10.13052/2025.ACES.J.400607

Two novel couplers, a Single-Band Branch-Line Coupler (SBBLC) and a Dual-Band Branch-Line Coupler (DBBLC), are proposed using Elongated T-Shape Transmission Lines (ETSTL). The same SBBLC structure can be adapted for DBBLC operation by adjusting the electrical length of the transmission line and the open stub. Through even-odd mode analysis, the impedance values are determined. It was necessary to model, build, and evaluate a coupler operating at 0.9 GHz and 2.4 GHz using a FR4 substrate in order to verify the idea. The remaining sections of the article may be organized as follows: section II provides an illustration of the work that is suggested, section III presents the findings and discussion, and section IV draws the conclusion.

II. PROPOSED WORK

The conventional BLC is shown in Fig. 1 (a). It is composed of four branches with quarter-wavelength, which are two series arms with an impedance of 35.35Ω and two shunt arms with an impedance of 50Ω. Using a FR4 substrate with a thickness of 1.6 mm and ε_r value of 4.4, the conventional coupler dimensions are 51.2×56.6 mm. However, the size of the device is a disadvantage of this typical technique, which is one of its problems.

A. Design of proposed SBBLC

Figure 1 (b) illustrates the construction of a SBBLC that makes use of an ETSTL with series and shunt arm. This kind of coupler is responsible for providing a connectivity between the transmission lines that have open stubs.

An Elongated T-Shape as seen in Fig. 2 comprised of three transmission lines and a stub.

The three impedances that are associated with ETSTL are Z_{1S}, Z_{1H}, and Z_{1L}. The electrical lengths that correlate to these impedances are θ_{1s}, θ_{1H}, and θ_{1L}. The

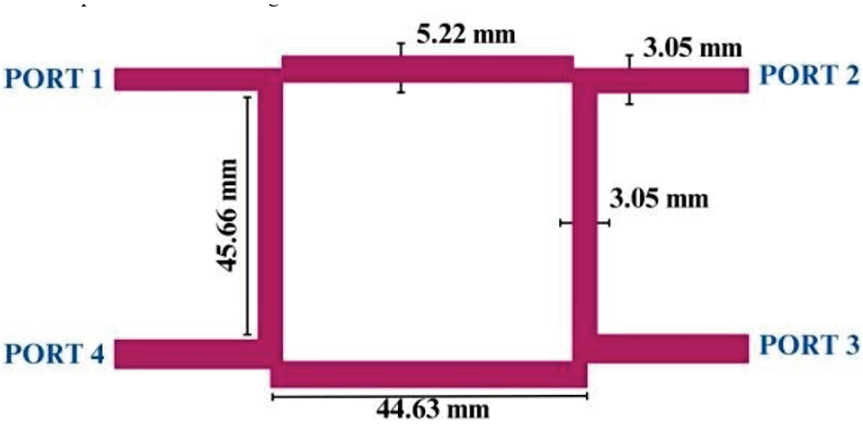

(a)

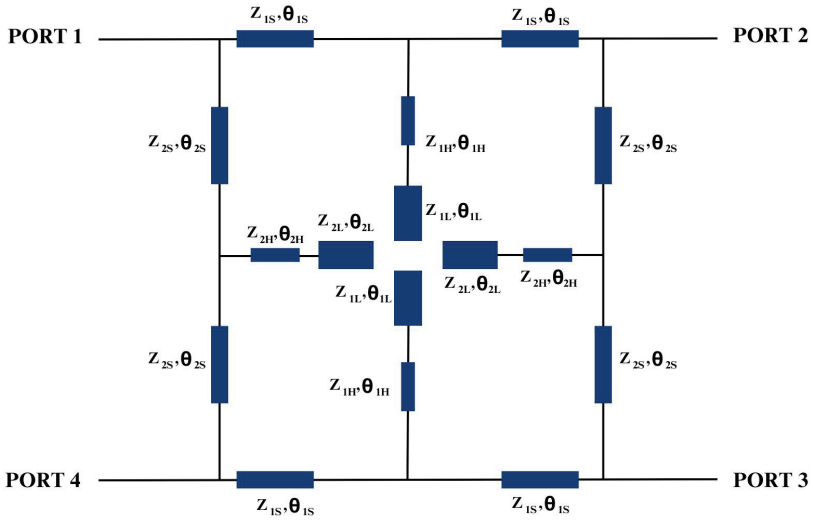

(b)

Fig. 1. Layout of (a) conventional BLC and (b) proposed SBBLC with ETSTL.

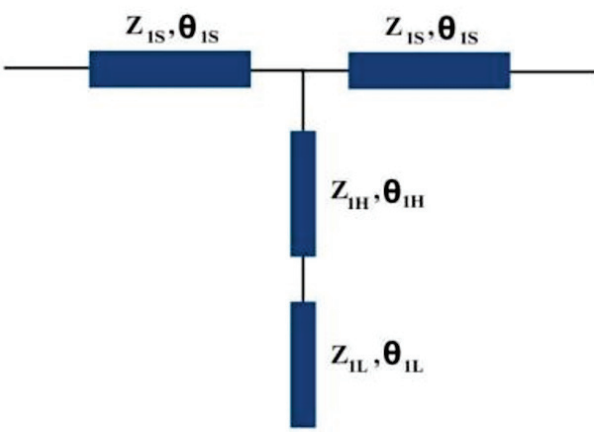

Fig. 2. Elongated T-Shape Transmission Line.

impedance of the transmission lines is represented by the symbols Z_{1S} and Z_{1H} in Fig. 2. The impedance of the stub is represented by Z_{1L}. The symbols θ_{1S} and θ_{1H} may be used to represent the electrical lengths of the transmission lines. The electrical length of the stub is represented by the symbol θ_{1L}.

B. Design of proposed DBBLC

The coupler is designed to operate at two different frequency bands, hence termed DBBLC. The operating frequencies are $f_1 = 0.9$ GHz and $f_2 = 2.4$ GHz, where the frequency ratio, $p = 2.66$, $\theta_1 = 49°$,$\theta_2 = 131°$.

$$\text{frequency ratio, } p = \frac{f_2}{f_1}. \tag{1}$$

$$\theta_1 = \frac{\pi}{1+p}. \tag{2}$$

$$\theta_2 = \frac{p\pi}{1+p}. \tag{3}$$

Frequency ratio is determined by equation (1). To further comprehend the phase connection between these frequencies, we compute two crucial angles. The first angle θ_1 simplifies to about 49°.

The second angle θ_2 is roughly 131°, calculated using equation (3). These angles, determined from the frequency ratio, reflect the phase angles connected with the frequencies, allowing for a clear understanding of their phase connection. In the proposed structure, θ_2 is divided into θ_{1H} and θ_{1L} for transmission line and stub, respectively.

C. Analysis of the proposed coupler

An even and odd mode equivalent circuit analysis is performed on the ETSTL, as can be seen in Fig. 3. When it comes to identifying the impedance and electrical lengths that are required, in order to obtain the acceptable coupling qualities, the findings of this research are useful in understanding what those dimensions are [10].

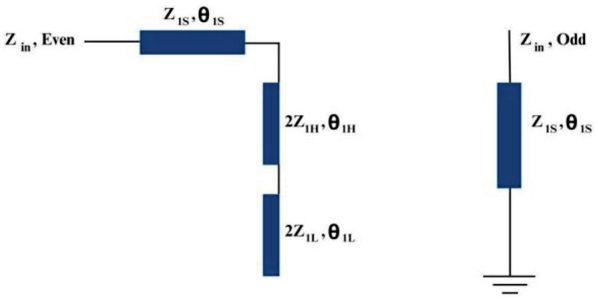

Fig. 3. Even and odd mode analysis of ETSTL.

The even and odd mode impedance of the proposed ETSTL can be written as

$$Z_{in,even} = \frac{Z_{1S}(Z_a + jZ_{1S}\tan\theta_{1S})}{Z_{1S} + jZ_a\tan\theta_{1S}}, \tag{4}$$

$$Z_{in,odd} = jZ_{1S}\tan\theta_{1S}, \tag{5}$$

where

$$Z_a = \frac{2Z_{1H}(Z_b + 2jZ_{1H}\tan\theta_{1H})}{2Z_{1H} + jZ_b\tan\theta_{1H}}, \tag{4a}$$

$$Z_b = -2jZ_L\cot\theta_L. \tag{4b}$$

It is possible to express the typical transmission line for even and odd mode impedance as

$$Z_{even,conv} = -jZ_o\cot\theta_o, \tag{5}$$

$$Z_{odd,conv} = jZ_o\tan\theta_o. \tag{6}$$

The impedance characteristics may be computed in the following manner, taking into account both the conventional design and the design that was suggested:

$$Z_{1S} = Z_0\frac{\tan\left(\frac{\theta_0}{2}\right)}{\tan\theta_1} \tag{7}$$

$$Z_{1H} = \frac{Z_{1S}B\left[Z_{1S}\tan\theta_{1S} + Z_0\cot\left(\frac{\theta_0}{2}\right)\right]}{2A\left[Z_0\cot\left(\frac{\theta_0}{2}\right) - Z_{1S}\right]} \tag{8}$$

where

$$A = \tan\theta_{1H} - \frac{1}{K}\cot\theta_{1L}, \tag{8a}$$

$$B = 1 + \frac{1}{K}\cot\theta_{1L}\tan\theta_{1H}, \tag{8b}$$

$$K = \frac{Z_{1H}}{Z_{1S}}. \tag{8c}$$

Figure 4 is a representation of the equivalent series arm transmission line. The impedances that are distinctive of the series arms are what give them their identity Z_{1S}, Z_{1H}, and Z_{1L}. As a result of these arms being linked in series between the ports, it is possible to send signals or power from one port to another. In addition to being in charge of the coupling mechanism, the series arms are also responsible for determining how power is distributed among the ports.

The equivalent shunt arm transmission line is shown in Fig. 5. The shunt arms are represented by the

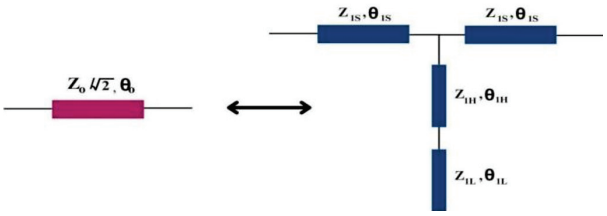

Fig. 4. Equivalent series arm transmission line.

impedances Z_{2S}, Z_{2H}, Z_{2L}. The ground reference and the series arms are linked to these arms in a parallel fashion and provide the connection. It is the shunt arms that are responsible for ensuring that the ports remain isolated and that the impedance matching that is sought is maintained. In addition to this, they further contribute to the overall coupling qualities of the coupler.

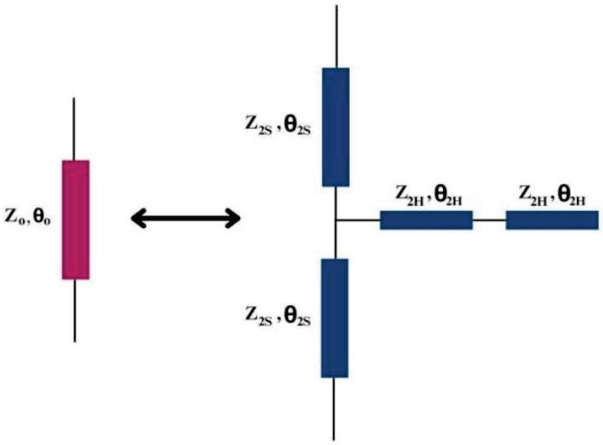

Fig. 5. Equivalent shunt arm transmission line.

The design curve for Z_{1S}, Z_{1H} is shown in Fig. 6, against the value of θ_{1S} for the series arm. To get the value of θ_{1S}, it is necessary to solve equations (7) and (8) mathematically. This allows one to derive the impedance of Z_{1S}, Z_{1H} by altering the electrical length. Under the assumption that K is equal to one, θ_{1H} is equal to θ_{1L} for 20. In order to produce an SBBLC using ETSTL on a FR4 substrate with a dielectric constant $\varepsilon_r = 4.4$ and a substrate thickness of 1.6 mm, it is necessary to replace the traditional BLC with similar ETSTL units.

Figure 6 shows the design curve for Z_{1S}, Z_{1H} versus θ_{1S} for a series arm by solving equations (7) and (8) graphically to obtain the impedance of Z_{1S}, Z_{1H} by varying the electrical length by assuming K = 1,θ_{1H} = θ_{1L}= 20 in order to determine the θ_{1S} value.

Figure 7 shows the design curve for Z_{2S}, Z_{2H} versus θ_{2S} for the shunt arm by solving equations (7) and (8) graphically to obtain the impedance of Z_{2S}, Z_{2H} by varying the electrical length by assuming K=1,θ_{2H}=θ_{2L}= 20,

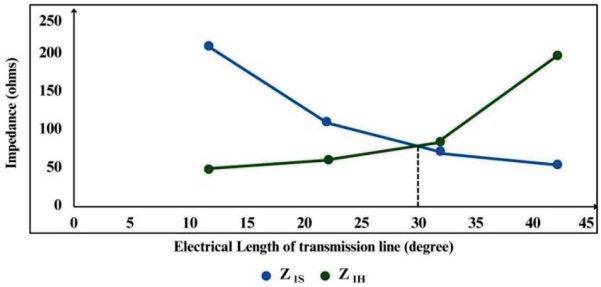

Fig. 6. Impedance versus electrical length of series SBBLC.

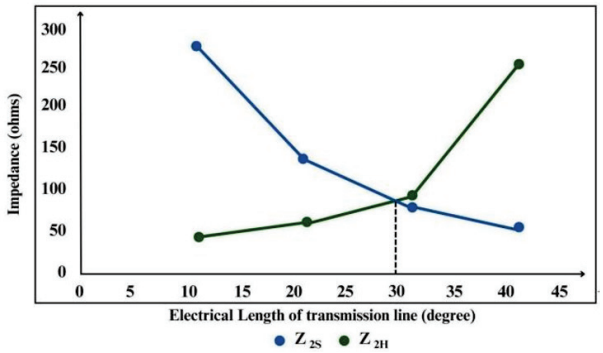

Fig. 7. Impedance versus electrical length of shunt SBBLC.

in order to determine θ_{2S} . The following values are obtained for the ETSTL for SBBLC (Series Arm), Z_{1S}=61.26, Z_{1H}=69.76, Z_{1L}=61.26 when we substitute the electrical length values as in equations (7) and (8). In same way, for shunt arm, the impedance values are Z_{2S}=86.60, $Z_{2H=}$98.72, Z_{2L}=86.60. Table 1 shows the series and shunt value analysis of SBBLC.

Figure 8 (a) shows the impact of Impedance versus electrical length for series arm of DBBLC. In the equivalent series arm, the characteristics impedance of the coupler for k = 1, Z_{1H} at Z_0 tends to fall between 327Ω to 229Ω. Similarly for k = 2, Z_{1H} at Z_0 tends to fall between 166Ω to 110Ω which is not feasible for fabrication because the impedance is not suitable for the FR4

Table 1: Series and shunt value analysis of SBBLC

ARM	IMPEDANCE (Ω)	WIDTH (mm)	LENGTH (mm)
SERIES	$Z_{1S} = 61.26$	2.14	15.43
	$Z_{1H} = 69.76$	1.66	10.38
	$Z_{1L} = 61.26$	2.14	10.28
SHUNT	$Z_{2S} = 86.60$	1.03	15.81
	$Z_{2H} = 98.72$	0.73	10.64
	$Z_{2L} = 86.60$	1.03	10.54

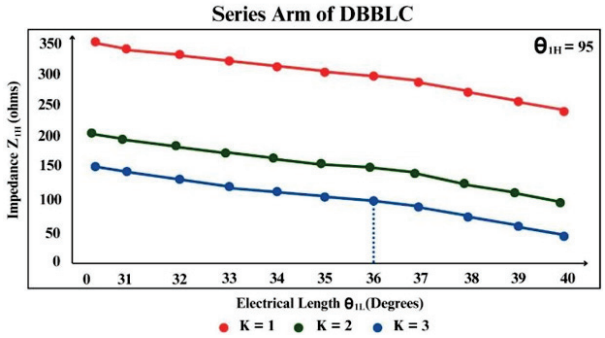

Fig. 8. (a) Impedance versus electrical length for series arm of DBBLC.

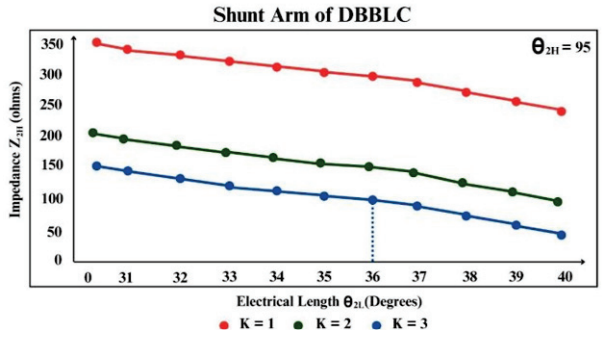

Fig. 8. (b) Impedance versus electrical length for shunt arm of DBBLC.

substrate. When k = 3, Z_{1H} at Z_0 tends to fall between 102Ω to 68Ω at $\theta_{1H} = 95$ and $\theta_{1L} = 30$, which provides the feasibility to fabricate the FR4 substrate of the proposed design.

Figure 8 (b) shows the impact of Impedance versus electrical length for shunt arm of DBBLC. In the equivalent shunt arm, the power division ratio of the equal power division coupler for k=1, Z_{2H} at $Z_0/\sqrt{2}$ tends to fall between 475Ω to 332Ω. Similarly for k=2, Z_{2H} at $Z_0/\sqrt{2}$ tends to fall between 240Ω to 160Ω which is not feasible for fabrication because the impedance is not suitable for a FR4 substrate. Hence, when k=3, Z_{2H} at $Z_0/\sqrt{2}$ tends to fall between 155Ω to 99Ω at $\theta_{2H} = 95$ and $\theta_{2L} = 30$ provides the feasibility to fabricate in the FR4 substrate of the proposed design. The overall parameter value obtained on series and shunt arm for DBBLC are illustrated in Table 2.

III. PERFORMANCE ANALYSIS

Evaluation of the designed architecture is done in this section. Commercial electromagnetic simulation software ADS is used for the optimization of physical parameters. For the conventional BLC, characteristic impedance of the shunt arm is 50, and impedance of the series arm is 35.35Ω.

Table 2: Calculated parameter values of DBBLC

	Circuit Parameters (Ω)	Structure Parameters (mm)
Series	$Z_{1S} = 30.729$ $Z_{1H} = 83.91$ $Z_{1L} = 30.729$	$l_1 = 30.86$ mm $l_2 = 49.97$ mm $l_3 = 17.69$ mm $w_1 = 6.35$ mm $w_2 = 1.11$ mm $w_3 = 6.35$ mm
Shunt	$Z_{2S} = 43.46$ $Z_{2H} = 118.60$ $Z_{2L} = 43.46$	$l_4 = 49.24$ mm $l_5 = 51.21$ mm $l_6 = 18.09$ mm $w_4 = 3.83$ mm $w_5 = 0.42$ mm $w_6 = 3.83$ mm

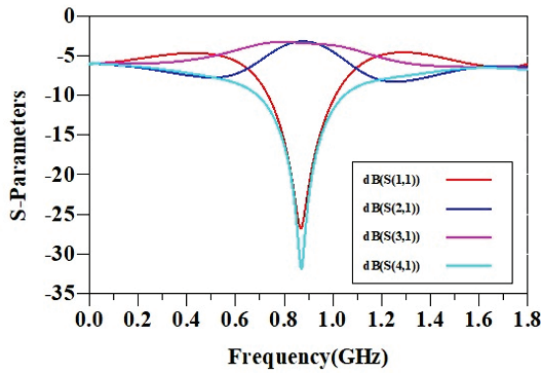

Fig. 9. Simulation result of conventional BLC.

Figure 9 shows the S-parameters of the conventional BLC. From the plot, the output characteristics of the BLC can be observed, including the insertion loss, coupling, isolation, and return loss at the output ports.

A. Simulation result of proposed SBBLC

Figures 10 (a) and (b) show the simulation results of SBBLC. Ideally, S_{11} and S_{41} should be greater than -15 dB and the proposed SBBLC has achieved -24.8 dB and -22.4 dB, respectively.

Ideally, S_{21} and S_{31} should be -3 dB and the proposed SBBLC achieves -3.5 dB and -3.2 dB, respectively. When compared to a conventional coupler, SBBLC achieved 55% size reduction and 33% FBW.

B. Simulation result of proposed DBBLC

For the DBBLC, the center frequency is located at 0.9 to 2.4 GHZ, maximal measured insertion losses |S21|/|S31| are -3.5 to -4.7 dB and -3.6 to -3.7 dB, respectively.

S_{11} and S_{41} should be greater than -15 dB and the proposed DBBLC has achieved -16.7 to -18.4 dB and -17.6 to -18.1 dB for 0.9 GHz and 2.4 GHz, respectively.

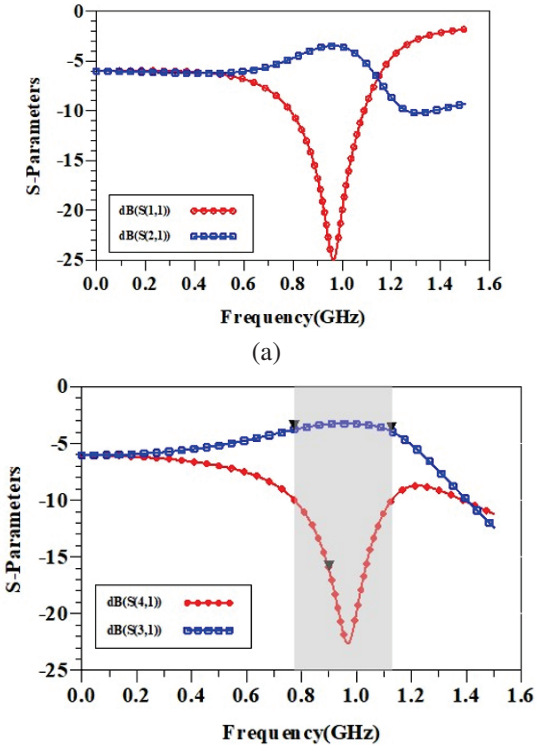

Fig. 10. (a) Simulation result of Return Loss S_{11} and Insertion Loss S_{21} of SBBLC and (b) simulation result of Isolation S_{41} and Coupling S_{31} of SBBLC.

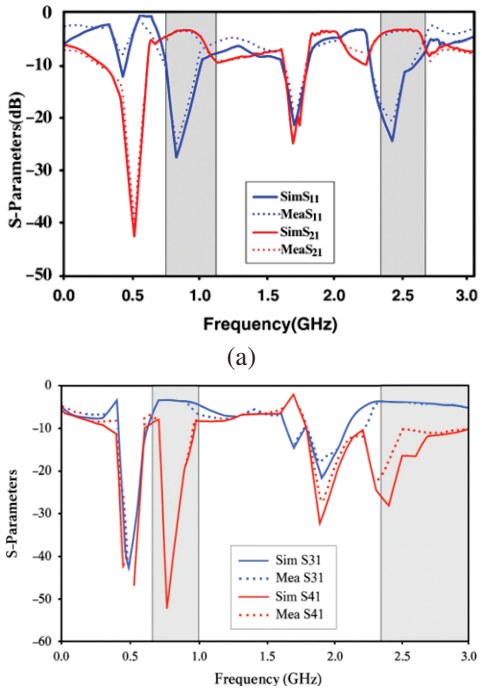

Fig. 11. (a) S_{11} and S_{21} parameter value analysis of DBBLC and (b) S_{31} and S_{41} parameter value analysis of DBBLC.

Similarly, S_{21} and S_{31} should be -3 dB and the proposed DBBLC has achieved -3.5 to -4.7 dB and -3.6 to -3.7 dB for 0.9 GHz and 2.4 GHz, respectively.

FBW achieved nearly 400 MHz (44%). The size of the proposed coupler is reduced by 67% compared to the conventional structure.

Suggested BLC simulated S-parameters are shown in Figs. 11 (a) and (b). The down peaks show the mid-point frequencies of the two comparison pass bands. The most that may be seen in the amplitude imbalance between the output ports is 0.3 dB. At mid-frequency ranges, isolation loss, and return loss are both significantly below -20 dB.

Figure 12 shows the layout of the DBBLC. Following fabrication (Fig. 13) and measurement of the coupler prototype, the suggested design idea is evaluated to see whether it is feasible. Both the SNA4400 network analyzer and ADS Keysight were used to do simulations and analyses on the proposed DBBLC.

From the above discussions, the proposed model has dimensions of $0.29\lambda g \times 0.32\lambda g$ (λg is the full transmission wavelength at the center frequency).

The even-odd mode analysis and practical design impedance curves provide explicit design formulae. A 0.9/2.4 GHz DBBLC is manufactured for the purpose of

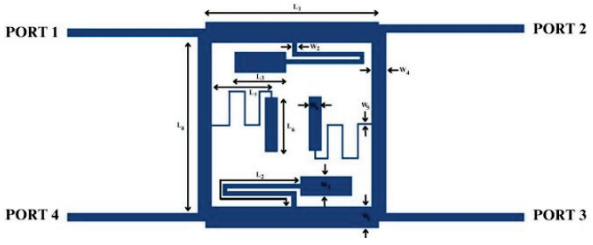

Fig. 12. Layout of the DBBLC.

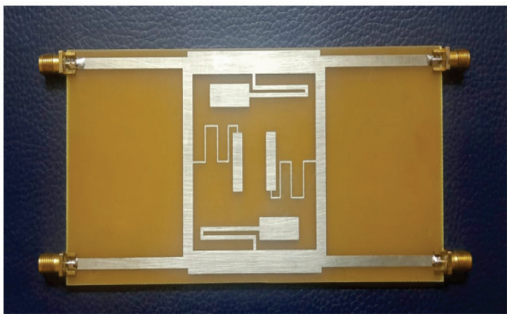

Fig. 13. Fabricated prototype of the DBBLC.

verification. The findings from the simulations and the measurements are in good agreement. The coupler has an

easy-to-understand architecture with strategically placed ports, and it also provides some leeway in the design for potential other uses. Figure 14 shows the experimental setup for DBBLC.

Compared with other works (see Tables 4 and 5), the suggested architecture output performs better than other existing architectures. DBBLC exhibits significant performance slightly higher than SBBLC.

Fig. 14. Experimental setup for DBBLC.

Table 3: Proposed architectures performance comparison

	F (GHz)	Return Loss (dB)	Isolation (dB)	Size (λg^2)	FBW (%)
SBBLC	0.9	24.83	24.47	0.17× 0.18	33
DBBLC	0.9/2.4	16.7/ 18.41	17.8/18.1	0.28× 0.32	44

Table 4: Comparison between proposed SBBLC and others

Ref.	F (GHz)	Return Loss (dB)	Isolation (dB)	Size (λg^2)	Size Reduction (%)	FBW (%)
[2]	2.45	<20	28	-	29	50
[3]	3.55	30.69	29.28	0.27 ×0.16	-	32.2
[4]	2.45	21.7	36.2	-	64.21	22.08
[6]	2.82	29.5	31.3	0.29 ×0.26	-	-
[7]	3.5	<8	<11	-	31	34.4
This SBBLC	**0.9**	**24.83**	**24.47**	**0.17 ×0.18**	**55**	**33**

IV. CONCLUSION

In this work, two novel couplers for SBBLC and DBBLC are proposed. In addition, design equations are offered through the use of even-odd mode analysis. The results of the simulations indicate that the coupler constructed has good degrees of matching and isolation at both center frequencies. Folding the stub towards the inner section of the coupler in order to make it suitable for manufacture is one of the methods used to reduce the size of the coupler. By using a simple design formula, the coupler presented has the potential to provide the needed output at the dual frequencies stated. The architecture proposed has a number of benefits, including a small size and FBW. Both the simulated and measured results of the structures exhibit a high degree of consistency.

REFERENCES

[1] K. V. Phani Kumar and S. S. Karthikeyan, "Miniaturized quadrature hybrid coupler using modified T-shaped transmission line for wide-range harmonic suppression," *IET Microwaves, Antennas, and Propagation*, vol. 10, no. 14, pp. 1522-1527, Nov. 2016.

[2] W. Nie, K.-D. Xu, M. Zhou, L.-B. Xie, and X.-L. Yang, "Compact narrow/wide band branch-line couplers with improved upper-stopband," *International Journal of Electronics and Communications*, vol. 98, pp. 45-50, Jan. 2019.

[3] A. A. Abdulbari, S. K. A. Rahim, M. Z. A. Abd Aziz, K. G. Tan, N. K. Noordin, and M. Z. M. Nor, "New design of wideband microstrip branch line coupler using T-shape and open stub for 5G application," *International Journal of Electrical and Computer Engineering,* vol. 11, no. 2, pp. 1346-1355, Apr. 2021.

[4] M. Y. O. Elhiwaris, S. K. A. Rahim, and U. A. K. Okonkwond, N. M. Jizat, "Miniaturized size branch line coupler using open stubs with high-low impedances," *Progress in Electromagnetics Research Letters*, vol. 23, pp. 65-74, Apr. 2011.

Table 5: Comparison between proposed DBBLC and other works

Ref.	F (GHz)	Return Loss (dB)	Insertion Loss (dB)	Coupling(dB)	Isolation (dB)	PhaseDifference (deg)	Size (λg^2)	FBW(MHz)
[16]	0.756/1.42	>15	3.35/3.74	4.0/4.10	>14	87,89	-	-
[13]	0.9/2.0	26.8/35.6	3.5/3.4	3.1/3.3	23.4/27.2	-	0.79x0.1	-
[15]	0.9/1.63	>20	3.2/3.5	3.3/4.1	>14	90.3,89.2	0.53x0.34	-
[14]	0.92/2.03	Below 24/19	3.17/3.76	3.50/3.83	Below 24/19	89.1,89.6	-	-
[17]	0.92/1.9	36.4/23.5	3.18/3.37	3.14/3.46	33.8/39.8	90,90	0.18x0.15	-
[19]	1.0/2.0	36.7/25.3	3.3/3.1	3.1/3.7	32.9/29.9	90,89	-	-
[20]	0.99/1.97	35.5/24.1	3.22/2.95	3.06/3.53	32.6/22	91,90	-	-
This Work (DBBLC)	**0.9/2.4**	**16.7/18.41**	**3.5/4.7**	**3.6/3.7**	**17.8/18.1**	86,91	**0.28x0.32**	400

[5] K.-S. Choi, K.-C. Yoon, J.-Y. Lee, C.-K. Lee, S.-C. Kim, K.-B. Kim, and J.-C. Lee, "Compact branch-line coupler with harmonics suppression using meander T-shaped line," *Microwave and Optical Technology Letters*, vol. 56, no. 6, pp. 1382-1384, June 2014.

[6] A. Rezaei and L. Noori, "Microstrip hybrid coupler with a wide stop-band using symmetric structure for wireless applications," *Journal of Microwaves, Optoelectronics and Electromagnetic Applications*, vol. 17, no. 1, Mar. 2018.

[7] N. A. M. Shukor and N. Seman, "Enhanced design of two-section microstrip-slot branch line coupler with the overlapped $\lambda/4$ open circuited lines at ports," *Wireless Personal Communications*, vol. 88, pp. 467-478, Nov. 2015.

[8] K. V. Phani Kumar and S. S. Karthikeyan, "Microstrip low pass filter with flexible roll-off rates," *International Journal of Electronics and Communications*, vol. 86, pp. 63-68, Jan. 2018.

[9] S. Roshani, S. I. Yahya, S. Roshani, and M. Rostami, "Design and fabrication of a compact branch-line coupler using resonators with wide harmonics suppression band," *Electronics,* vol. 11, no. 793, Mar. 2022.

[10] F. Hosseinkhani and S. Roshani, "A compact branch-line coupler design using low-pass resonators and meandered lines open stubs," *Turkish Journal of Electrical Engineering & Computer Sciences*, vol. 26, pp. 1164-1170, 2018.

[11] A. M. Zaidi, M. T. Beg, B. K. Kanaujia, J. Kishor, and K. Rambabu, "A novel dual band branch line coupler and its application to design a dual band 4 X 4 Butler matrix," *IEEE Access*, vol. 8, Apr. 2020.

[12] M. A. Maktoomi, M. S. Hashmi, and F. M. Ghannouchi, "Systematic design technique for dual-band branch-line coupler using T- and Pi-networks and their application in novel wideband-ratio crossover," *IEEE Transactions on Components, Packaging and Manufacturing Technology*, vol. 6, no. 5, May 2016.

[13] X.-Y. Zhang and J.-C. Lee, "A dual-band branch-line coupler with ultra-wideband harmonic suppression," *Journal of Electromagnetic Engineering and Science*, vol. 23, no. 1, pp. 57-62, Jan. 2023.

[14] H. Zhang and K. J. Chen, "A stub tapped branch-line coupler for dual-band operations," *IEEE Microwave and Wireless Components Letters*, vol. 17, no. 2, Feb. 2007.

[15] W. Feng, X. Duan, Y. Shi, X. Y. Zhou, and W. Che, "Dual-band branch-line couplers with short/open-ended stubs," *IEEE Transactions on Circuits and Systems—II: Express Briefs*, vol. 67, no. 11, Nov. 2020.

[16] W. Feng, Y. Zhao, W. Che, H. Chen, and W. Yang, "Dual-/tri-band branch line couplers with high power division isolation using coupled lines," *IEEE Transactions on Circuits and Systems—II: Express Briefs*, vol. 65, no. 4, Apr. 2018.

[17] S. Koziel and A. Lukasiewicz, "Fast simulation-driven feature-based design optimization of compact dual-band microstrip branch-line coupler," *International Journal of RF and Microwave Computer-Aided Engineering,* vol. 26, no. 1, Jan. 2016.

[18] M. A. Maktoomi, M. S. Hashmi, and F. M. Ghannouchi, "A dual-band port-extended branch-line coupler and mitigation of the band-ratio and power division limitations," *IEEE Transactions on Components, Packaging and Manufacturing Technology*, vol. 7, no. 8, pp. 1313-323, Aug. 2017.

[19] H. Kim, B. Lee, and M. J. Park, "Dual-band branch-line coupler with port extensions," *IEEE Transactions on Microwave Theory and Techniques,* vol. 58, no. 3, pp. 651-655, 2010.

[20] M. J. Park and B. Lee, "Dual-band, cross coupled branch line coupler," *IEEE Microwave and Wireless Components Letters*, vol. 15, no. 10, pp. 655-657, 2005.

G. Srividhya is currently pursuing her Ph.D. in Information and Communication Engineering at Anna University, Chennai, India. She earned her M.Tech. in VLSI Design from Bharath University, Chennai, India (2013), and B.E. in Electronics and Communication Engineering from SCSVMV University, Kanchipuram, India (2011). She serves as Assistant Professor in the Department of Electronics and Communication Engineering at Panimalar Engineering College, Poonamallee, Chennai, India. She has published extensively in international journals and conferences. Her research interests include VLSI design, RF devices, antenna systems, artificial intelligence, and machine learning, bridging traditional electronics with emerging technologies in modern communication systems.

S. Maheswari received the Ph.D. degree in Microwave Engineering and the M.E. degree in Applied Electronics from Sathyabama Institute of Science and Technology, Chennai, India, in 2016 and 2009, respectively. She received the B.E. degree in ECE from University of Madras. Her area of research includes microwave and millimeter wave circuits. She has more than two decades of teaching experience. Currently she is working as a Professor in Panimalar Engineering College, Chennai, India. She is a recognized supervisor for doing research in Anna University. She has published more than 30 papers in Web of Science, Scopus indexed journals, and IEEE conferences. She is a Fellow of IETE.

De-embedding Technique for Extraction and Analysis of Insulator Properties in Cables

Wei-Hsiu Tsai[1], Ding-Bing Lin[1], Po-Jui Lu[1], and Tzu-Fang Tseng[2]

[1]Department of Electronic and Computer Engineering
National Taiwan University of Science and Technology, Taipei 10607, Taiwan
D10802006@mail.ntust.edu.tw, dblin@mail.ntust.edu.tw, boblu0910@gmail.com

[2]Department of CTO Office
Bizlink International Corporation, New Taipei 23533, Taiwan
tzufang_tseng@optiworks.com

***Abstract* –** This work utilizes the Nicolson-Ross-Weir (NRW) method to analyze the frequency-dependent material properties of the insulator inside cables. These properties include $\varepsilon(f)$, $\mu(f)$, and $\tan\delta$. Common methods for this analysis include the open-ended coaxial probe method, free space method, resonant method, and transmission/reflection line method. Each method has a suitable structure and may require additional samples for measurement. Our proposed method can calculate the real material properties of the insulation after foaming in the cable following extrusion, up to 40 GHz. This study also compiles the effects of various factors on the extraction of material parameters and provides a detailed analysis of potential sources of error. We observed that variations in production can introduce discrepancies after de-embedding, which can result in anomalies at the dissipation factor curve. Finally, we propose a correction method that effectively improves the accuracy of the extracted dielectric constant.

***Index Terms* –** Cable, characterization, de-embedding, dielectric constant, Nicolson-Ross-Weir (NRW) method.

I. INTRODUCTION

The rapid development of artificial intelligence (AI) and cloud computing has driven a surge in demand for data processing, storage, and transmission. These advancements have heightened the performance requirements for servers and data centers. To meet these demands, high-performance computing (HPC) and AI servers are increasingly adopting the PCIe 6.0 standard, which delivers significantly faster data transfer rates, enabling bidirectional throughput of up to 128 GB/s.

However, the increase in transmission rates implies greater signal bandwidth. For instance, the PCIe 6.0 specification requires that when transmitting at 64 GT/s using 4-Level Pulse Amplitude Modulation (PAM4) signal modulation, the signal frequency reaches 16 GHz. Additionally, the Insertion Loss ($|S_{21}|$) target must be greater than -7 dB for a cable and -36 dB for the total channel. Nevertheless, with modern Printed Circuit Boards (PCBs), signal attenuation increases significantly at such high frequencies, and issues such as Electromagnetic Interference (EMI) and crosstalk increasingly affect signal integrity. As a result, reducing signal attenuation within the channel, increasing signal speed, and maintaining good signal integrity have become pressing challenges in the development of cable solutions today. Extracting accurate Relative Permittivity and Loss Tangent parameters is crucial [1].

TwinAx cables play an important role in modern communication systems due to their high transmission rates, excellent anti-interference capability, and relatively low cost. Consequently, many manufacturers are now incorporating more TwinAx cable architectures in system designs as signal transmission channels, extending the effective length of PCIe channels. This enables all high-speed devices to be integrated into a single system or allows for more efficient transmission between different systems.

However, as the number of high-speed cables used increases, the quality of these cables becomes crucial. The manufacturing process of TwinAx cables includes steps such as wire drawing, insulation extrusion, twisting, and braiding. These processes are often susceptible to process errors, leading to various non-ideal effects such as insufficient concentricity and outer diameter tolerance. Ensuring the design precision of these cables is crucial, as manufacturing defects can lead to impedance mismatches, thereby disrupting system performance [2–10].

Accurate characterization of material properties, such as $\varepsilon(f)$, $\mu(f)$, and $\tan\delta(f)$, across different frequencies is essential to ensuring high-frequency performance

Submitted On: February 21, 2025
Accepted On: June 9, 2025
https://doi.org/10.13052/2025.ACES.J.400608

and system stability. By addressing these issues, future research and applications can improve the quality and reliability of TwinAx cable manufacturing, ensuring consistency in high-speed data transmission.

Currently, there are several methods for inspecting the quality of cable insulators, with the most used in the manufacturing industry being the Electro Capacitive Method of Control [11–13] and the Spark Method of Control [14].

The process for the Electro Capacitive Method involves passing the cable through a circular electrode and applying a low voltage source across the insulator on both sides of the cable [15]. The capacitance value between the insulator's sides is then measured. If there are defects in the cable's insulator structure, fluctuations in the measured capacitance value may occur. To ensure full contact between the insulator surface and the electrode surface, the entire measurement process takes place in a cooling tank, which is why this method is also known as the "Water Capacitive Method." This method is widely adopted by most cable manufacturers for Statistical Process Control (SPC) monitoring of production line quality.

The Spark Method of Control, on the other hand, involves applying high voltage to the insulator surface through different types of electrodes, including Chain-type, Spring-type, or Brush-type. If there is a defect in the cable's insulation layer and it passes through the high-voltage area, an electrical breakdown will occur.

However, both cable inspection methods are only suitable for examining cables at low frequencies (≈50 MHz). For microwave frequencies (300 MHz∼300 GHz), other methods are required to obtain the material characteristics of the cable insulator.

With technological advancements, various methods have been developed to obtain the complex properties of materials at high frequencies. In the microwave domain, S-parameters measured using a network analyzer are often processed numerically to convert them into the dielectric properties of insulators. The most common methods currently include the Open-ended Coaxial Probe Method [16–18], Free Space Method [19–21], Resonant Method [22–25], and Transmission/Reflection Line Method [26–28]. Each method is suited to specific structures, and the extracted dielectric properties of the insulating materials may vary slightly.

In the past, most cable manufacturers used these methods for measurement, requiring large, thin samples, typically molded by material manufacturers. However, there are discrepancies between these measurements and those of actual cables, as the cable insulators are formed through foaming and extrusion processes.

We reference the method in [26] and propose a measurement framework using the Transmission/Reflection Line Method. Although our goal is to extract the dielectric constant of the insulator in a high-speed PCIe dual-core cable, we measure a coaxial cable instead. Since the manufacturing process is identical, we can obtain the dielectric constant of the foamed insulator in the same way. Using a 2-port vector network analyzer (VNA), it is possible to measure the S-parameters required for the calculations. Section II explains the theory and calculation equations. Section III discusses the extraction of dielectric material properties, while section IV simulates the impact of manufacturing deviations in coaxial cables on the extracted material properties. Section V is simulation and validation. Section VI is measurement. Finally, section VII presents the conclusion.

II. MEASUREMENT INSTRUCTIONS AND METHOD

The measurement framework for the Transmission Line Method includes the Device Under Test (DUT) and fixtures attached to both ends of the DUT. The DUT can be a transmission line that propagates electromagnetic waves in TEM mode or a rectangular waveguide that propagates electromagnetic waves in TE mode, such as coaxial cables or microstrip lines. During measurement, the DUT is connected to a VNA via fixtures or adapters. The impedance of the DUT and the measurement system (fixture) are denoted as Z_d and Z_0, respectively.

In the calculation process, the length of the DUT, l, must be known in advance, and the propagation constant of the DUT is assumed to be γ_D. The propagation factor (T) of the DUT is expressed as $e^{-\gamma_D l}$, as shown in equation (1). Using the impedance of the DUT and the system, the reflection coefficient ρ and transmission coefficient τ between the DUT and fixture can be calculated, as illustrated in equations (2) and (3):

$$T = e^{-\gamma_D l}, \tag{1}$$

$$\rho = \frac{Z_d - Z_0}{Z_d + Z_0}, \tag{2}$$

$$\tau = \frac{2Z_0}{Z_d + Z_0} = 1 + \rho\ . \tag{3}$$

Subsequently, employing the Lattice Diagram method, as depicted in Fig. 1, the effects of multiple reflections are calculated by summing the reflected and transmitted signals. This allows for the establishment of relationships between the measured S-parameters, the reflection coefficient ρ, and the propagation factor T of the DUT, as shown in equations (4) and (5):

$$\begin{aligned} S_{11} = \rho &+ (1+\rho)(1-\rho)(-\rho)T^2 \\ &+ (1+\rho)(1-\rho)\left(-\rho^3\right)T^4 \\ &+ (1+\rho)(1-\rho)\left(-\rho^5\right)T^6 + \ldots, \end{aligned} \tag{4}$$

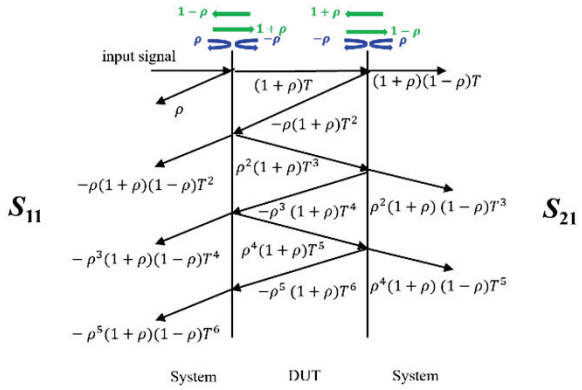

Fig. 1. Multiple reflections of a single frequency in the fixture.

$$S_{21} = (1+\rho)(1-\rho)T + (1+\rho)(1-\rho)\rho^2 T^3 + (1+\rho)(1-\rho)\rho^4 T^5 + \ldots. \quad (5)$$

After establishing the relationship between the measured S_{11} and S_{21}, the reflection coefficient ρ, and the propagation factor T of the DUT, simultaneous equations can be solved to derive equations (6-8). During this process, it is important to note that there may be two possible solutions for the reflection coefficient ρ. However, since the measurement is performed on passive components, where gain is not present, only the solution with ρ less than 1 is valid. This enables the calculation of the reflection coefficient ρ and the propagation factor T of the DUT from the measured S-parameters without prior knowledge of the characteristic impedance of either the DUT or the system:

$$\rho = K \pm \sqrt{K^2 - 1}\,, \quad |\rho| < 1, \quad (6)$$

$$K = \frac{S_{11}{}^2 - S_{21}{}^2 + 1}{2S_{11}}, \quad (7)$$

$$T = \frac{S_{11} + S_{21} - \rho}{1 - (S_{11} + S_{21})\rho}. \quad (8)$$

Once the reflection coefficient ρ and the propagation factor T have been derived from the measured S-parameters, the relationship between the propagation constant γ_D of the DUT and the propagation factor T can be obtained, as shown in (9):

$$\gamma_D = \frac{1}{l} \cdot ln\left(\frac{1}{T}\right). \quad (9)$$

However, in the calculation process, since S-parameters not only include the magnitude of the voltage wave propagation ratio but also contain important phase information, they are typically represented in complex form. This implies that, during calculations, the reflection coefficient ρ, the propagation factor T, and the propagation constant γ_D of the DUT may exhibit phase ambiguity as a function of frequency. This occurs because the same imaginary value may correspond to different phase angles, requiring careful attention during analysis. To address phase ambiguity, numerical methods such as the *unwrap* algorithm in MATLAB can be employed to adjust the phase angles. By applying phase continuity correction, the imaginary part of the propagation constant γ_D is $ln(1/T)$, as shown in (10):

$$ln\left(\frac{1}{T}\right) = real\left(ln\left(\frac{1}{T}\right)\right) + j * unwrap\left(imag\left(ln\left(\frac{1}{T}\right)\right)\right). \quad (10)$$

After obtaining the propagation constant γ_D of the DUT structure, the next step is to derive the relationship between the wave number k, cutoff wave number k_c, and phase constant β of the DUT through Faraday's Law and Ampere's Law from Maxwell's equations in the source-free region. From (11), when the wave number k exceeds the cutoff wave number k_c, the phase constant β in the propagation constant γ_D of the DUT becomes a real number. Electromagnetic waves can only propagate within the structure when β is a real number, which leads to the concept of the cutoff wave number k_c. The cutoff frequency f_c can be obtained from the cutoff wave number k_c as shown in (12):

$$\gamma_D^2 + k^2 = k_c{}^2, \quad (11)$$

$$f_c = \frac{k_c}{2\pi\sqrt{\mu\varepsilon}}. \quad (12)$$

This study uses coaxial cables to extract the dielectric material properties. During the propagation of electromagnetic waves within a coaxial cable, the electric field, magnetic field, and wave propagation direction are mutually orthogonal. The propagation mode in coaxial cables is the TEM mode. According to the definition of the TEM mode, there are no longitudinal (propagation direction) electromagnetic field components (Ez, Hz) in the guided wave structure.

From (13), the cutoff wave number k_c for the TEM mode in a coaxial cable is zero. Therefore, by using the propagation constant γ_D of the DUT calculated from the measured S-parameters and the wave number k, which is related to the material, as shown in (14), and substituting it into (13), a crucial relationship is obtained as shown in (15), which can then be simplified to (16). In this equation, c is the speed of light in a vacuum (3×10^8 m/sec), which is inversely proportional to the square root of the vacuum permittivity (ε_0) and vacuum permeability (μ_0), as described in (17). Here, ω represents the angular

frequency, and f represents the frequency:

$$k = \omega\sqrt{\mu\varepsilon}, \tag{13}$$

$$\gamma_D^2 + k^2 = 0\,, \tag{14}$$

$$(\gamma_D)^2 + (\omega\sqrt{\mu\varepsilon})^2 = 0, \tag{15}$$

$$\gamma_D = j\sqrt{\frac{\omega^2\mu_r\varepsilon_r}{c^2}} = j2\pi\sqrt{\frac{f^2\mu_r\varepsilon_r}{c^2}}, \tag{16}$$

$$c = \frac{1}{\sqrt{\varepsilon_0\mu_0}}\,. \tag{17}$$

The intrinsic impedance η of a wave in the dielectric material of the DUT, also known as the wave impedance, is defined in (18). According to the definition of wave impedance, it is proportional to μ/γ. Assuming that the wave impedance of the system is η_1 and the wave impedance of the dielectric material in the DUT is η_D, we can proceed to calculate the reflection coefficient ρ between the system and the DUT using the S-parameters through equation (6). The reflection coefficient ρ is related to the wave impedance η_1 of the system and the wave impedance η_D of the DUT's dielectric material, as shown in (19):

$$\eta = \frac{j\omega\mu}{\gamma} \propto \frac{\mu}{\gamma}, \tag{18}$$

$$\rho = \frac{\eta_2 - \eta_1}{\eta_2 + \eta_1}. \tag{19}$$

Assuming that the wave impedance in the system is equal to the wave impedance in a vacuum, i.e., η_1=η_0=377 ohm, we substitute the relationship from (18) into (19) and rewrite it as (20). Simplifying further, we obtain (21).

Using equation (21), we can then calculate the relative permeability $\mu_r(f)$ of the DUT, as shown in (22). By expressing the propagation constant in a vacuum γ_0 using equation (16) and calculating the propagation constant γ_D of the DUT from equation (9), we can compute $\mu_r(f)$, as described in (23):

$$\rho = \frac{\frac{\mu_2}{\gamma_D} - \frac{\mu_0}{\gamma_0}}{\frac{\mu_2}{\gamma_D} + \frac{\mu_0}{\gamma_0}}\,, \tag{20}$$

$$\rho = \frac{\frac{\gamma_0}{\gamma_D}\cdot\mu_r - 1}{\frac{\gamma_0}{\gamma_D}\cdot\mu_r + 1}, \tag{21}$$

$$\mu_r = (\frac{1+\rho}{1-\rho})\frac{\gamma_D}{\gamma_0}, \tag{22}$$

$$\mu_r = \left(\frac{1+\rho}{1-\rho}\right)\frac{\gamma_D}{j2\pi\sqrt{\frac{f^2}{c^2}}}\,. \tag{23}$$

After obtaining the relative permeability $\mu_r(f)$ of the DUT, it can be substituted into equation (15) to calculate the relative permittivity $\varepsilon_r(f)$, as shown in (24). The resulting expression can be simplified as (25). Permittivity ε is a physical property that describes the material's response to polarization under the influence of an electric field. The real part of ε represents the dielectric's ability to refract electromagnetic waves, which can be used to calculate how the direction of electromagnetic waves changes as they move from one medium to another. The imaginary part, on the other hand, represents the energy loss within the dielectric, which is caused by the generation of heat from the oscillation of polarized dipoles in the material. Due to energy conservation, the imaginary part of ε must be negative, as described in (26):

$$(\gamma_D)^2 + (\omega\sqrt{\mu_r\varepsilon_r\mu_0\varepsilon_0})^2 = 0, \tag{24}$$

$$\varepsilon_r = -\frac{c^2}{\mu_r}\cdot\left(\frac{\gamma_D}{\omega}\right)^2, \tag{25}$$

$$\varepsilon = \varepsilon^{'} - j\varepsilon^{''} = \varepsilon^{'}(1 - jtan\delta)\,. \tag{26}$$

In the calculation process using the Transmission Line Method, the loss term includes both dielectric loss and conductor loss from the coaxial cable, resulting in equation (27). From this, the loss tangent tanδ of the DUT's dielectric material (including the metal) can be derived, as shown in (28).

However, it is important to note that, if the dielectric material has very low dielectric loss, the loss tangent value tanδ calculated from equation (29) may be dominated by the metal losses, preventing an accurate determination of the dielectric material's tanδ:

$$\nabla\times\overrightarrow{H} = j\omega\varepsilon\overrightarrow{E} + \overrightarrow{J}, \tag{27}$$

where

$$\overrightarrow{J} = \sigma\overrightarrow{E}\,,$$

$$\nabla\times\overrightarrow{H} = j\omega\varepsilon\overrightarrow{E} + \sigma\overrightarrow{E} = j\omega\varepsilon^{'}\overrightarrow{E} + (\omega\varepsilon^{''} + \sigma)\overrightarrow{E}, \tag{28}$$

$$tan\delta = \frac{\omega\varepsilon^{''} + \sigma}{\omega\varepsilon^{'}}. \tag{29}$$

III. EXTRACT INSULATOR PARAMETERS FROM MEASUREMENT

A. Equation formatting

This study prepared three different lengths of coaxial cable samples, with lengths of 15 cm, 30 cm, and 50 cm, and quantities of 10, 10, and 5, respectively, as shown in Fig. 2. According to the manufacturer's data, the dielectric constant (ε_r) of the insulation in the coaxial cables is 2.04±1% at 1 GHz, and the loss tangent (tanδ) ranges from 0.0002 to 0.0004.

Aside from manufacturing tolerances, the three test samples are identical in structure, differing only in length, see Fig. 3. Therefore, two coaxial cables of different lengths were selected for the experiment. The shorter cable was used as the calibration object, while the longer one was used as the error model. The 2X-Thru de-embedding technique was employed to remove the effects of the 3.5 mm SMA connectors, preserving the characteristics of the coaxial cable in between. As a result, the extracted material parameters are free from the influence of the SMA connectors, as illustrated in Fig. 4.

Fig. 2. Coaxial cables used for measurement.

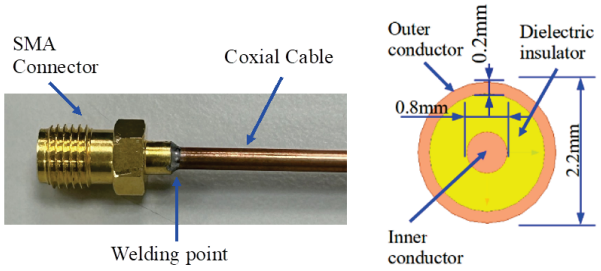

Fig. 3. (a) Hand-soldered coaxial cable to SMA connector. (b) Cross-section of the coaxial cable.

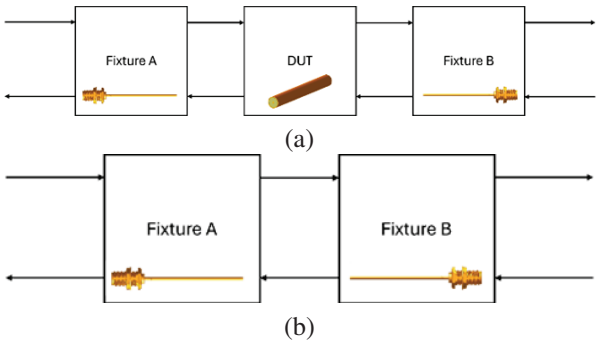

Fig. 4. 2X-Thru de-embedded technique. (a) Error model. (b) Thru line.

In this experiment, we used two sets of coaxial cables, each comprising ten cables of 15 cm and 30 cm in length, respectively. The S-parameters of each cable were measured using a VNA. Subsequently, a 2X-Thru de-embedding process was applied. The objective was to obtain the parameters of the DUT, which in this case is a 15 cm cable. The error model was based on the measurement of the 30 cm coaxial cable, while the thru line measurement was based on the 15 cm cable. After applying the de-embedding process, we derived 100 sets of S-parameters for the DUT, where the middle 15 cm represents the difference between the 30 cm and 15 cm cables. Using these S-parameters, we calculated 100 sets of ε_r and tanδ, as shown in Fig. 5.

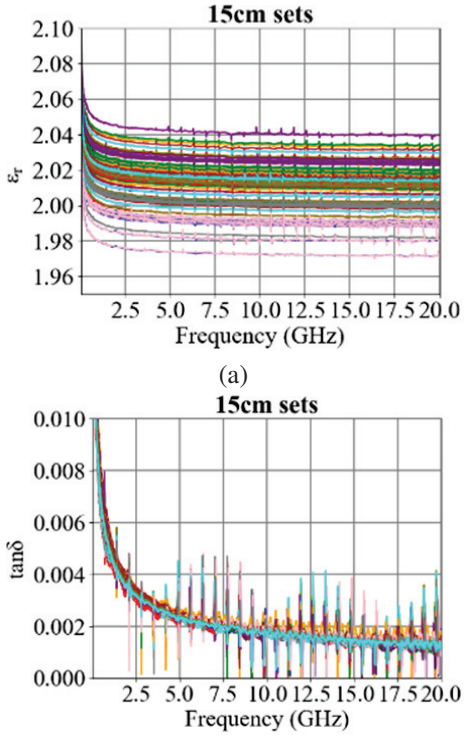

Fig. 5. Insulator parameters of the 15 cm coaxial cable are by calculation (a) ε_r and (b) tanδ.

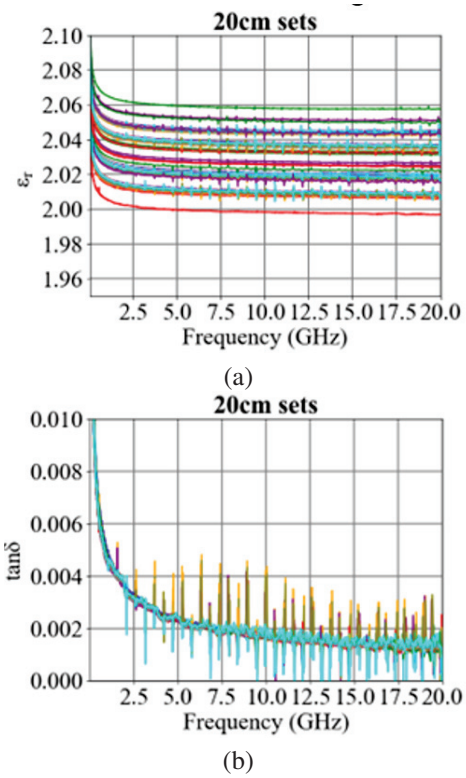

Fig. 6. Insulator parameters of the 20 cm coaxial cable are by calculation (a) ε_r and (b) tanδ.

It is important to note that several frequency points exhibited spark-like anomalies. Typically, these issues can be mitigated through more advanced correction methods. The characteristics of the insulator obtained in this study are presented as a range of values.

Next, we selected ten coaxial cables, each 30 cm in length, and five coaxial cables, each 50 cm in length. After measuring the S-parameters of each cable using a VNA, we applied the 2X-Thru de-embedding process. The objective was to obtain the parameters of a 20 cm coaxial cable, which represents the difference between the lengths of the 50 cm and 30 cm cables. The error model was based on measurements of the 50 cm coaxial cable, while the thru line measurement was based on the 30 cm cable. After the de-embedding process, we obtained 50 sets of S-parameters for DUT. From these, we calculated 50 sets, as shown in Fig. 6.

Notably, we observed a reduction in the spike, indicating that the issues associated with the 2X-Thru de-embedding process were mitigated to some extent. As in the previous experiment, the characteristics of the insulator were determined as a range of values.

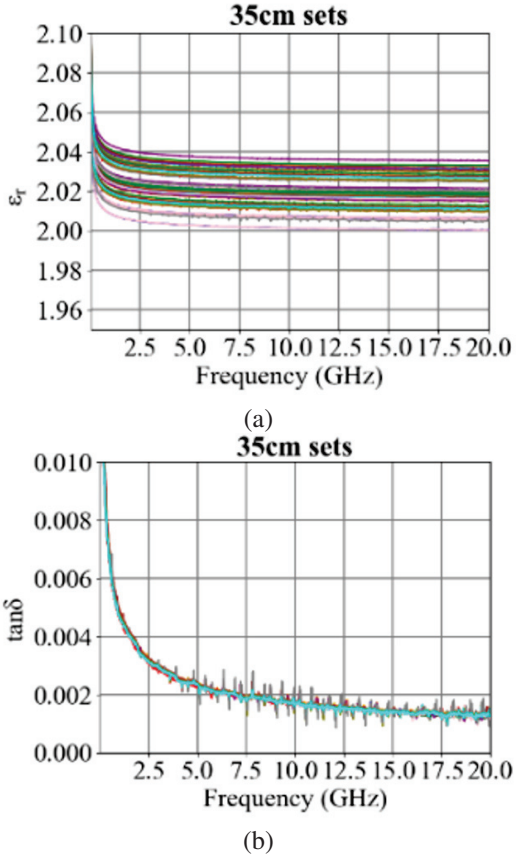

Fig. 7. Insulator parameters of the 35 cm coaxial cable are by calculation (a) ε_r and (b) tanδ.

In the third set of experiments, we selected ten coaxial cables, each 15 cm in length, and five coaxial cables, each 50 cm in length. The S-parameters of these cables were measured to obtain the parameters of a 35 cm coaxial cable, representing the difference between the 50 cm and 15 cm cables. The error model was based on measurements of the 50 cm coaxial cable, while the thru line measurement was taken from the 15 cm cable. From these measurements, we calculated 50 sets, as shown in Fig. 7.

We observed a further reduction in the spikes, indicating continued improvement in the issues associated with the de-embedding process. As before, the characteristics of the insulator were presented as a range of values, and this range became more concentrated in this experiment.

Based on the results of the three experiments, we observed a decrease in the anomalous peaks in the extracted material parameters as the length of the DUT increased. This may be due to the fact that, when the DUT is smaller, the discrepancies between the calibration objects and the actual fixtures, as well as manufacturing errors of the DUT itself, have a more pronounced effect. However, as the length of the DUT increases, these non-ideal effects are likely averaged out, leading to more stable extracted material parameters. In the next section, we will use simulations to confirm this hypothesis.

Another issue is the standard deviation of the range of values observed. This variability could stem from differences in the cables, including length, diameter of the conductor and insulator, circularity, surface roughness of the copper conductor, and the degree of foaming in the dielectric layer. When extreme variations exist between cables, the range of values after de-embedding will differ. However, as the DUT length increases, these differences tend to be diluted, resulting in a narrower range of values. To investigate this further, we conducted three additional experiments.

In the first experiment, we used a 15 cm thru line as the calibration object to perform 2X-Thru de-embedding on the 30 cm error model for all cables. The results, shown in Fig. 8, indicate a reduction in the range of values.

In the second experiment, we reversed the setup, using ten 15 cm cables as the calibration objects to perform 2X-Thru de-embedding on a single 50 cm error model. The results, shown in Fig. 9, demonstrate an even more concentrated narrowing of the range.

However, we observed that the results of these experiments were unable to yield precise values. Instead, they provide only an estimate of the general range for a batch of produced cables.

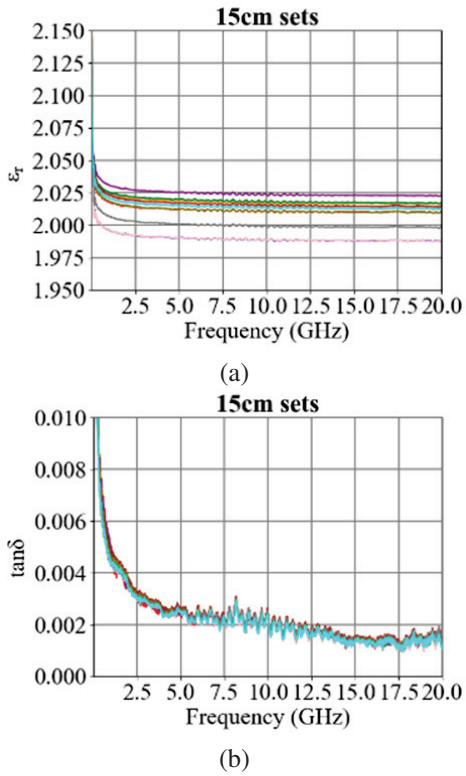

Fig. 8. Insulator parameters of the 30 cm by 10sets and 15 cm by 1set (a) ε_r and (b) tanδ.

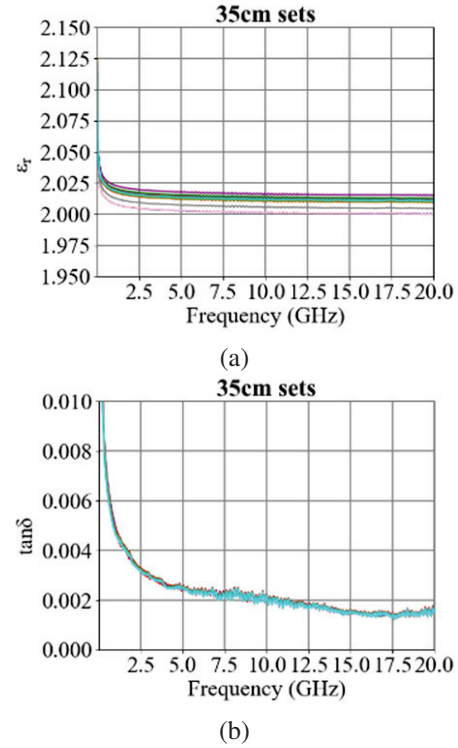

Fig. 9. Insulator parameters of the 50 cm by 1set and 15cm by 10sets (a) ε_r and (b) tanδ.

IV. DE-EMBEDDING THEORY

A. Time domain gating

In the standard 2X-Thru calibration method [29], a fixture is connected to create a through line calibration object, which is then used to remove fixture effects from the error model. However, differences between the calibration fixture and the actual fixtures attached to the DUT, or variations in the connections during assembly or measurement, can introduce discrepancies. These differences can be observed through the time-domain response of the fixture in the calibration object and the error model, as shown in Fig. 10.

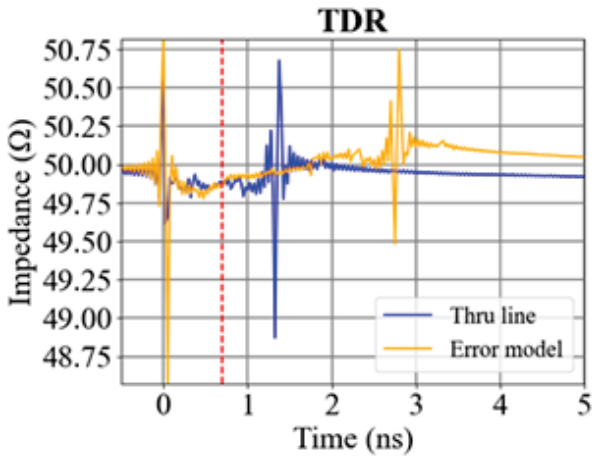

Fig. 10. TDR variations in connectors and welding points.

B. De-embedding method

The improved 2X-Thru de-embedding method proposed in this study begins with the same initial steps as the conventional process. However, it assumes excellent impedance matching between the DUT and the fixtures, minimizing reflection at their interface. This assumption aligns with the concept of the Line in TRL calibration [30], where the DUT's propagation characteristics are represented by $e^{-\gamma l}$. In this study, a fixture containing a segment of coaxial cable was selected as the Thru calibration structure to meet these requirements.

In this study, the primary difference between the error model and the calibration object is the presence or absence of the DUT. Assuming that the impedance between the DUT and the fixture is nearly matched, the propagation constant of the DUT, denoted as γ_{ini}, can be preliminarily estimated using the S-parameters of the error model ($|S_{Total}|$) and the thru calibration object ($|S_{Thru}|$). When the magnitude of S_{21} of the DUT is high (indicating minimal transmission loss), its value can be expressed by (30). Through (30), the attenuation constant α_{ini} of the DUT can be estimated. Here, Δl represents the physical length of the DUT in meters. Next, the

phase angles of the transmission coefficients from both the error model and the calibration object are unwrapped to determine the difference in electrical length. This difference corresponds to the electrical length θ_D of the DUT. Consequently, the phase constant β_{ini} of the DUT can be estimated using (31):

$$\alpha_{ini} = \frac{ln(\text{mag}\left(S_{21,Thru}\right)) - ln(\text{mag}\left(S_{21,Total}\right))}{\lambda l}, \quad (30)$$

$$\beta_{ini} = \frac{Phase\left(S_{21,Total}\right) - Phase\left(S_{21,Thru}\right)}{\lambda l}. \quad (31)$$

By combining (30) and (31), the propagation constant γ_{ini} of the DUT can be estimated. Subsequently, by analyzing the signal flow in the error model, equations (32-35) can be derived. In this context, the DUT is assumed to be an ideal transmission line with a propagation characteristic of $e^{-\gamma ini}$, as shown in Fig. 11.

$$S_{11}=S_{11A}+\frac{S_{11B}\cdot S_{21A}^2\cdot e^{-2\gamma_{ini}\Delta l}}{1-S_{22A}\cdot S_{11B}\cdot e^{-2\gamma_{ini}\Delta l}}, \quad (32)$$

$$S_{21}=\frac{S_{21A}\cdot S_{21B}\cdot e^{-\gamma_{ini}\Delta l}}{1-S_{22A}\cdot S_{11B}\cdot e^{-2\gamma_{ini}\Delta l}}, \quad (33)$$

$$S_{22}=S_{22B}+\frac{S_{22A}\cdot S_{12B}^2\cdot e^{-2\gamma_{ini}\Delta l}}{1-S_{11B}\cdot S_{22A}\cdot e^{-2\gamma_{ini}\Delta l}}, \quad (34)$$

$$S_{12}=\frac{S_{12B}\cdot S_{12A}\cdot e^{-\gamma_{ini}\Delta l}}{1-S_{11B}\cdot S_{22A}\cdot e^{-2\gamma_{ini}\Delta l}}. \quad (35)$$

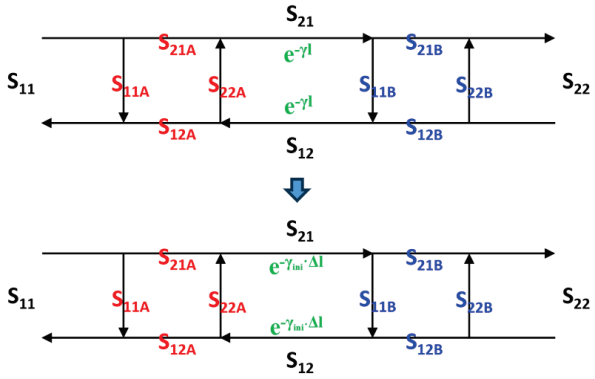

Fig. 11. Signal flow graph of error model.

Combine and simplify (32) and (33) into (36), and (34) and (35) into (37):

$$S_{11} = S_{11A} + S_{11B}\cdot e^{-\gamma_{ini}\Delta l}\cdot S_{21}, \quad (36)$$

$$S_{22} = S_{22B} + S_{22A}\cdot e^{-\gamma_{ini}\Delta l}\cdot S_{12}. \quad (37)$$

To determine the reflection coefficients of fixture A and fixture B, we start similarly with $|S_{11A}|$ from (36) and $|S_{22B}|$ from (37). However, the process will differ slightly from the existing 2X-Thru calibration procedure.

After obtaining $|S_{11A}|$ and $|S_{22B}|$, we use (36) and (37) to derive $|S_{11B}|$ and $|S_{22A}|$, as given by (38) and (39). Equations (32) and (34) are employed to determine $|S_{21A}|$, $|S_{12B}|$, $|S_{12A}|$, and $|S_{21B}|$ as detailed in (41) and (42):

$$S_{11B} = \frac{S_{11} - S_{11A}}{S_{21}}\cdot e^{\gamma_{ini}\Delta l}, \quad (38)$$

$$S_{22A} = \frac{S_{22} - S_{22B}}{S_{12}}\cdot e^{\gamma_{ini}\Delta l}, \quad (39)$$

$$S_{21A}=\sqrt{S_{21}\cdot\left(1-S_{22A}\cdot S_{11B}\cdot e^{-2\gamma_{ini}\Delta l}\right)\cdot e^{\gamma_{ini}\Delta l}} = S_{21B}, \quad (40)$$

$$S_{12B}=\sqrt{S_{12}\cdot\left(1-S_{11B}\cdot S_{22A}\cdot e^{-2\gamma_{ini}\Delta l}\right)\cdot e^{\gamma_{ini}\Delta l}} = S_{12A}. \quad (41)$$

When the actual S-parameters of the fixtures are obtained, we convert both the fixture S-parameters and the error model S-parameters into T-parameter matrices. By performing the de-embedding calculations, we derive the DUT's T-parameters, which are then converted back to S-parameters.

V. SIMULATION AND VALIDATION

A. Simulation

In this section, a circuit simulator is used to simulate two-port networks with COAX components to model the S-parameters of the calibration object and error model. The DUT is a 50-ohm, 150-mm COAX component. The simulation accounts for connector transition effects and variations in the coaxial cable's insulation diameter (Do), reflecting connector characteristics and dis-continuities. Simulation data are presented in Tables 1–3.

Table 1: Cross-section dimensions of DUT

	Outer Radius (Do)	Length (L)	Characteristic Impedance (Z_0)
DUT	1.072 mm	150 mm	50.02Ω

COAX inner diameter (Di) is fixed at 0.32 mm

Table 2: Cross-section dimensions of Calibration Object

	Outer Radius (Do)	Length (L)	Characteristic Impedance (Z_0)
Fixture A	1.062 mm	2 mm	49.63Ω
	1.078 mm	10 mm	50.25Ω
	1.065 mm	2 mm	49.75Ω
	1.072 mm	50 mm	50.02Ω
Fixture B	1.072 mm	50 mm	50.02Ω
	1.065 mm	2 mm	49.75Ω
	1.078 mm	10 mm	50.25Ω
	1.062 mm	2 mm	50.02Ω

COAX inner diameter (Di) is fixed at 0.32 mm

Table 3: Cross-section dimensions of Calibration Object-1

	Outer Radius (Do)	**Length (L)**	**Characteristic Impedance (Z_0)**
Fixture A	1.059 mm	2 mm	49.51Ω
	1.066 mm	10 mm	49.78Ω
	1.074 mm	2 mm	50.10Ω
	1.072 mm	50 mm	50.02Ω
Fixture B	1.072 mm	50 mm	50.02Ω
	1.074 mm	2 mm	50.10Ω
	1.066 mm	10 mm	49.78Ω
	1.059 mm	2 mm	49.51Ω

COAX inner diameter (Di) is fixed at 0.32 mm

This study compares two main aspects. First, it examines the de-embedding results before and after improvements when the calibration fixtures match the DUT fixtures. Second, it analyzes the results using a different calibration object (Calibration Object-1) when the fixtures differ. Both the IEEE P370 standard 2X-Thru de-embedding algorithm and an enhanced Python-based algorithm are employed to process the S-parameters of the DUT.

B. Validation

The S-parameters of the calibration fixtures obtained through different algorithms are compared with the S-parameters of the DUT fixtures (Golden Standard) simulated in a circuit simulator, as illustrated in Fig. 12. The blue line represents the S-parameters obtained using the existing 2X-Thru de-embedding algorithm, while the yellow line indicates those obtained with the improved method proposed in this study. The green line shows the S-parameters from the circuit simulator for a single fixture. The results demonstrate that the improved 2X-Thru de-embedding algorithm yields S-parameters that closely align with both the existing algorithm and the simulated fixture S-parameters, as shown in Fig. 13.

In practical applications, measurement or fabrication errors can cause slight differences between the calibration fixtures and those used next to the DUT. This study uses Calibration Object-1 to de-embed the error model. Analysis of the time-domain reflection impedance reveals a minor discrepancy between the trace impedance of the left fixture in Calibration Object-1 and that in the error model, as indicated by the impedance before the red dashed line in Fig. 14. The calibration and de-embedding results are shown in Figs. 15 and 16.

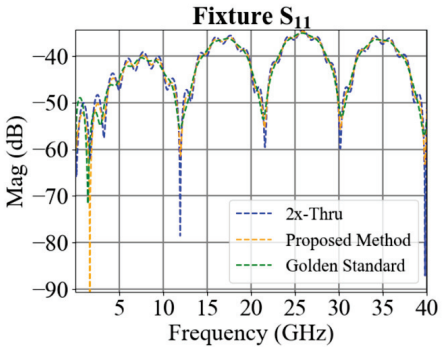

(a)

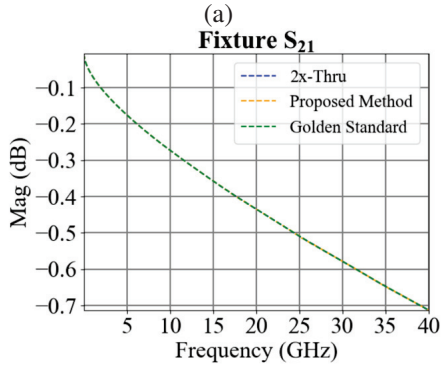

(b)

Fig. 12. Fixture S-parameter comparison (match) (a) $|S_{11}|$ and (b) $|S_{21}|$.

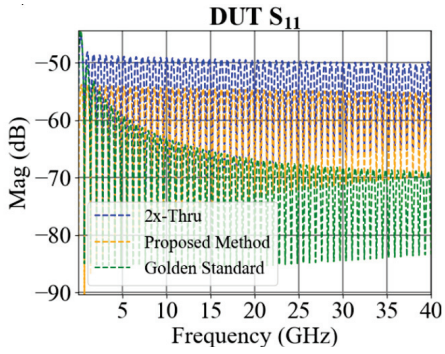

(a)

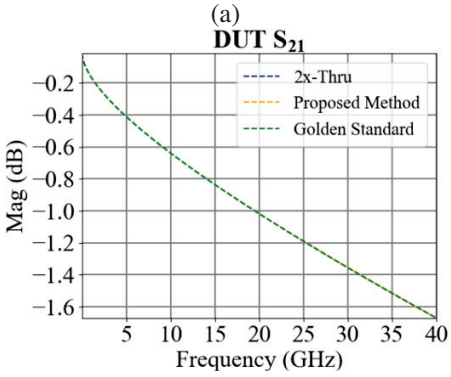

(b)

Fig. 13. DUT S-parameter comparison (match) (a) $|S_{11}|$ and (b) $|S_{21}|$.

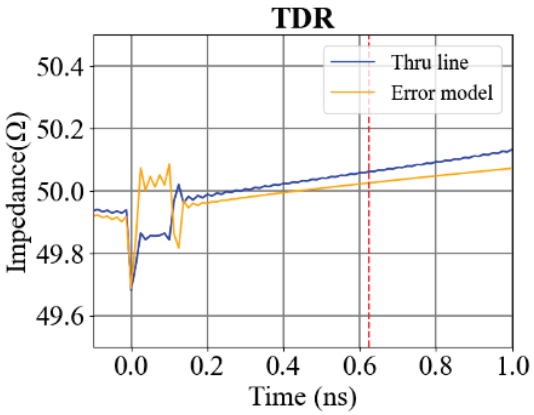

Fig. 14. Difference in time domain reflection.

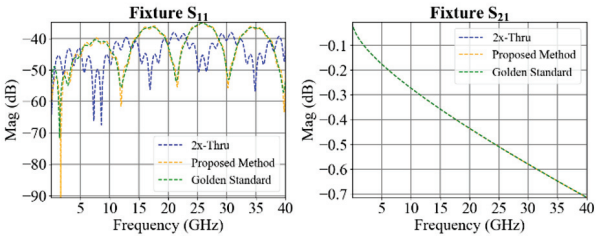

(a) (b)

Fig. 15. Fixture S-parameter comparison (differ) (a) $|S_{11}|$ and (b) $|S_{21}|$.

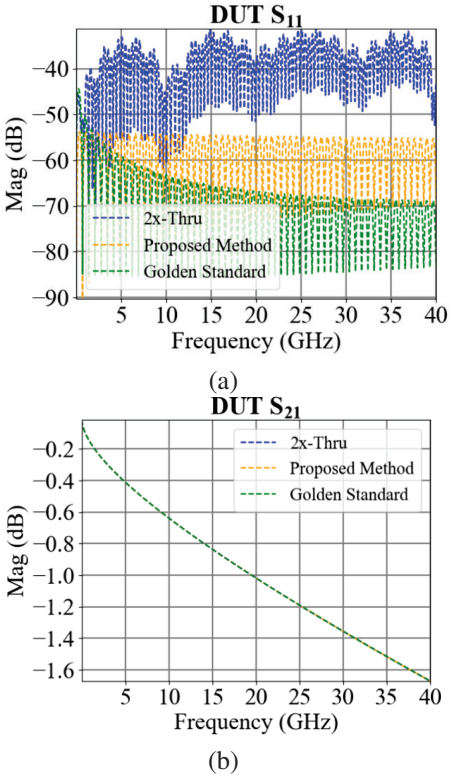

(a)

(b)

Fig. 16. DUT S-parameter comparison (differ) (a) $|S_{11}|$ and (b) $|S_{21}|$.

VI. MEASUREMENT

Here, we use the Nicolson-Ross-Weir (NRW) method to validate the parameter extraction methods for coaxial cable insulation. Ignoring manufacturing errors, the samples differ only in length. Both the existing 2X-Thru de-embedding algorithm and the improved version were used to remove the 3.5 mm connector effects and isolate the coaxial cable properties.

We analyzed the extracted ε_r and $\tan\delta$ across different combinations. We identified the maximum and minimum values at each frequency using various de-embedding methods, as illustrated in Fig. 17. Observation shows that the improved 2X-Thru de-embedding algorithm effectively reduces numerical errors caused by differences between calibration objects and actual fixtures. Our method effectively reduces the spikes caused by after de-embedding at specific frequencies, enhancing the precision of the extracted values. However, due to manufacturing tolerances, the extracted ε_r and $\tan\delta$ result in a range of values rather than a single point.

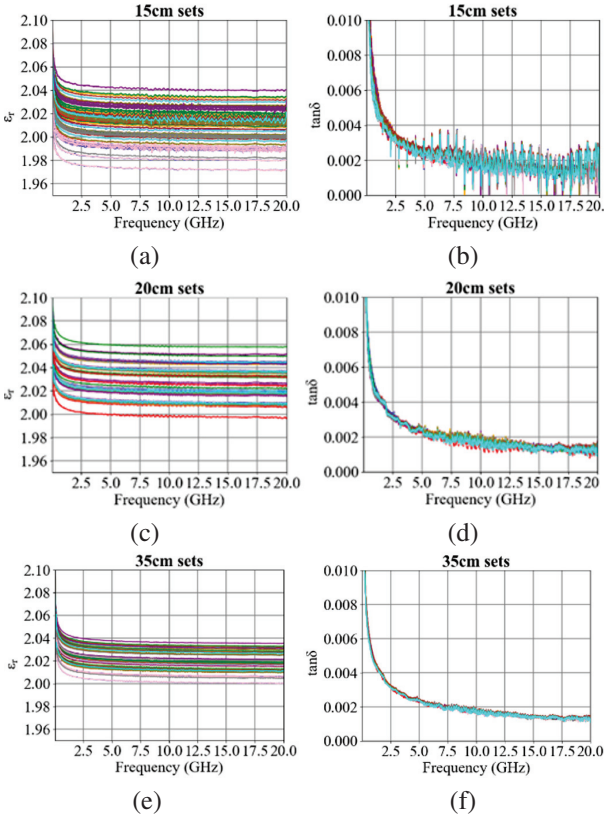

(a) (b) (c) (d) (e) (f)

Fig. 17. Extracted values of cable insulators by the improved 2X-Thru method (a) 15 cm, ε_r (b) 15 cm, $\tan\delta$ (c) 20 cm, ε_r (d) 20 cm, $\tan\delta$ (e) 35 cm, ε_r (f) 35 cm, $\tan\delta$.

We also observed that, under the same length configuration, slight variations are present in the extracted

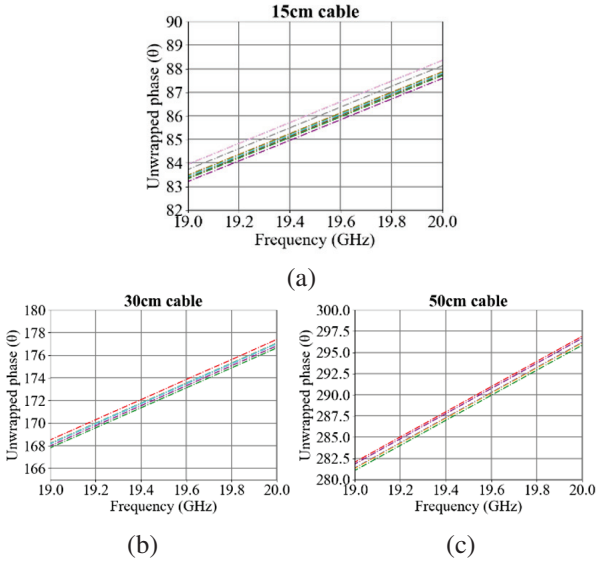

Fig. 18. Original phase $|S_{21}|$ of coaxial cable (a) 15 cm, (b) 30 cm, and (c) 50 cm.

results regardless of whether the same error model is de-embedded using different calibration artifacts or the same calibration artifact is used to de-embed different error models. These variations can be attributed to measurement differences. The coaxial cable lengths and labels provided by manufacturers typically have a tolerance of approximately ± 3 mm, as verified through the measured phase of $|S_{21}|$, as shown in Fig. 18. By examining the $|S_{21}|$ original phase of the coaxial cables, it is evident that the electrical length of each sample labeled with the same length exhibits minor differences. Since the electrical length is related to the phase constant and physical dimensions, as indicated in (42), these length tolerances result in discrepancies in the extracted material parameters. Finally, the advantages summarized in Table 4 are validated:

$$\theta = \beta l. \tag{42}$$

Table 4: Comparison among the classical methods

	[16]	[19]	[31]	This work
Method	Open-ended Coaxial	Free space	Waveguide	Coaxial line
DUT Material	PTFE	Flat plastic	Flat plastic	Cable insulator
Fixture	SMA	Antenna	X-band Waveguide	SMA
Input	S_{11}, S_{12}	S_{11}, S_{12}	S_{11}, S_{12}	S_{11}, S_{12}
Output	ε_r	ε_r	ε_r	ε_r, tan δ
Frequency	0-20 GHz	8.2-12 GHz	8.2-12 GHz	0-20 GHz
Range	Broad band	Wide	Wide	Broad band
For production inspection	No	No	No	Yes

VII. CONCLUSION

This study proposes a method for extracting the relative permittivity of cables that more closely reflects their actual properties. Compared to the traditional open-end coaxial line structure, we adopt an extruding machine to injection-mold the insulator, resulting in a device with virtually no air gaps. During the measurement process, manufacturing tolerances in the production of the sample and the actual length of the coaxial cables introduce variability. Additionally, inconsistencies in the size of solder joints between the coaxial cable and SMA connectors further contribute to de-embedding errors. To address these challenges, we present an improved version of the 2X-Thru de-embedding method and conduct comparative evaluations. The proposed method significantly reduces numerical errors, offering a more reliable approach for accurately extracting material parameters in practical applications. Results indicate that as the measured cable length increases, the extracted values converge within a narrower range, and the occurrence of spikes is reduced. This improvement may be attributed to the greater impact of calibration object discrepancies and cable manufacturing tolerances when the cable size is smaller. However, as the cable length increases, the non-ideal effects become more evenly distributed, resulting in smoother and more stable material parameter extraction.

ACKNOWLEDGMENT

This work was supported by BizLink International Corporation.

REFERENCES

[1] *IEEE Standard for Ethernet Amendment 2: Physical Layer Specifications and Management Parameters for 100 GB/s Operation Over Backplanes and Copper Cables*, IEEE Std 802.3bj-2014 (Amendment to IEEE Std 802.3-2012 as amended by IEEE Std 802.3bk-2013), pp. 1-368, 3 Sep. 2014.

[2] E. Mayevskiy and H. James, "Limitations of the intra-pair skew measurements in gigabit range interconnects," *DesignCon*, 2016.

[3] Z. Chen, M. Prasad, D. O'Connor, P. Bond, and A. Muszynski, "Differential TwinAx cable modeling by measured 4-port S-parameters," in *Proc. IEEE 14th Topical Meeting Elect. Perform. Electron. Package*, pp. 87-90, 2005.

[4] Y. Shlepnev and C. Nwachukwu, "Modelling jitter induced by fibre weave effect in PCB dielectrics,"

Proc. IEEE Int. Symp. Electromagnet. Compat., pp. 803-808, 2014.

[5] E. J. Denlinger, "Frequency dependence of a coupled pair of microstrip lines (correspondence)," *IEEE Trans. Microwave Theory Tech.*, vol. 18, no. 10, pp. 731-733, Oct. 1970.

[6] Y. Liu, S. Bai, C. Li, V. S. De Moura, B. Chen, and S. Venkataraman, "Inhomogeneous dielectric induced skew modeling of TwinAx cables," *IEEE Transactions on Signal and Power Integrity*, vol. 2, pp. 94-102, 2023.

[7] A. Talebzadeh, K. Koo, P. K. Vuppunutala, J. Nadolny, A. Li, and Q. Liu "SI and EMI performance comparison of standard QSFP and flyover QSFP connectors for 56+ GBps applications," *Proc. IEEE Int. Symp. Electromagnet. Compat. Signal/Power Integrity*, pp. 776-781, 2017.

[8] W. H. Tsai, D. B. Lin, T. F. Tseng, and C. H. Ho, "Analysis of electrical characteristics of TwinAx cable with asymmetric structures," in *2024 IEEE Joint International Symposium on Electromagnetic Compatibility, Signal & Power Integrity: EMC Japan / Asia-Pacific International Symposium on Electro-magnetic Compatibility (EMC Japan /APEMC Okinawa)*, Ginowan, Okinawa, Japan, pp. 342-345, 2024.

[9] R. Joshi, S. K. Podilchak, C. Constantinides, and B. Low, "Flexible textile-based coaxial transmission lines for wearable applications," *IEEE Journal of Microwaves*, vol. 3, no. 2, pp. 665-675, Apr. 2023.

[10] A. Lago, C. M. Penalver, J. Marcos, J. D. Gandoy, A. A. N. Melendez, and O. Lopez, "Electrical design automation of a twisted pair to optimize the manufacturing process," *IEEE Trans. on Components, Packaging and Manufacturing Technology*, vol. 1, no. 8, pp. 1269-1281, Aug. 2011.

[11] *Telephone cable. Test methods*, Moscow: Standards Publishing House, GOST (State Standard) 27893-88, 1989.

[12] S. Yasufuku, T. Umemura, and Y. Ishioka, "Phenyl methyl silicone fluid and its application to high-voltage stationary apparatus," *IEEE Transactions on Electrical Insulation*, vol. EI-12, no. 6, pp. 402-410, Dec. 1977.

[13] R. M. Hakim, R. G. Olivier, and H. St-Onge, "The dielectric properties of silicone fluids," *IEEE Transactions on Electrical Insulation*, vol. EI-12, no. 5, pp. 360-370, Oct. 1977.

[14] *Cables, wires and cords. Methods of voltage testing*, Moscow: Standards Publishing House, GOST (State Standard) 2990-72, 1986.

[15] A. Goldshtein, G. Vavilova, and S. Mazikov, "Capacitance control on the wire production line," *IME&T,* 2016.

[16] I. Dilman, M. N. Akinci, T. Yilmaz, M. Çayören, and I. Akduman, "A method to measure complex dielectric permittivity with open-ended coaxial probes," *IEEE Transactions on Instrumentation and Measurement*, vol. 71, pp. 1-7, 2022.

[17] D. Popovic, L. McCartney, C. Beasley, M. Lazebnik, M. Okoniewski, and S. C. Hagness, "Precision open-ended coaxial probes for in vivo and ex vivo dielectric spectroscopy of biological tissues at microwave frequencies," *IEEE Transactions on Microwave Theory and Techniques*, vol. 53, no. 5, pp. 1713-1722, May 2005.

[18] M. J. Da Silva, E. Schleicher, and U. Hampel, "A novel needle probe based on high-speed complex permittivity measurements for investigation of dynamic fluid flows," *IEEE Trans. on Instrumentation and Measurement*, vol. 56, no. 4, pp. 1249-1256, Aug. 2007.

[19] H. Shwaykani, J. Costantine, A. El-Hajj, and M. Al-Husseini, "Monostatic free-space method for relative permittivity determination using horn antenna near-field measurements," *IEEE Antennas and Wireless Propagation Letters*, vol. 23, no. 4, pp. 1336-1340, Apr. 2024.

[20] B. Moon and J. Oh, "FSS-enhanced quasi-optical dielectric measurement method for liquid crystals in sub-THz band," *IEEE Antennas and Wireless Propagation Letters*, vol. 22, no. 12, pp. 3062-3066, Dec. 2023.

[21] L. S. Rocha, C. C. Junqueira, E. Gambin, A. N. Vicente, A. E. Culhaoglu, and E. Kemptner, "A free space measurement approach for dielectric material characterization," in *2013 SBMO/IEEE MTT-S International Microwave & Optoelectronics Conference (IMOC)*, Rio de Janeiro, Brazil, 2013.

[22] J.-M. Heinola, P. Silventoinen, K. Latti, M. Kettunen, and J.-P. Strom, "Determination of dielectric constant and dissipation factor of a printed circuit board material using a microstrip ring resonator structure," in *15th International Conference on Microwaves, Radar and Wireless Communications (IEEE Cat. No.04EX824)*, Warsaw, Poland, vol. 1, pp. 202-205, 2004.

[23] G. Galindo-Romera, F. Javier Herraiz-Martínez, M. Gil, J. J. Martínez-Martínez, and D. Segovia-Vargas, "Submersible printed split-ring resonator-based sensor for thin-film detection and permittivity characterization," *IEEE Sensors Journal*, vol. 16, no. 10, pp. 3587-3596, May 2016.

[24] H. Shwaykani, A. El-Hajj, J. Costantine, F. A. Asadallah, and M. Al-Husseini, "Dielectric spectroscopy for planar materials using guided and unguided electromagnetic waves," in *2018 IEEE Middle East and North Africa Communications*

Conference (MENACOMM), Jounieh, Lebanon, pp. 1-5, 2018.

[25] H. B. Wang and Y. J. Cheng, "Broadband printed-circuit-board characterization using multimode substrate-integrated-waveguide resonator," *IEEE Transactions on Microwave Theory and Techniques*, vol. 65, no. 6, pp. 2145-2152, June 2017.

[26] W. B. Weir, "Automatic measurement of complex dielectric constant and permeability at microwave frequencies," *Proceedings of the IEEE,* vol. 62, no. 1, pp. 33-36, Jan. 1974.

[27] B. Chen, X. Ye, B. Samaras, and J. Fan, "A novel de-embedding method suitable for transmission-line measurement," in *2015 IEEE APEMC*, Taipei, Taiwan, 2015.

[28] Y.-C. Luo, Y.-H. Chen, C.-Y. Zhuang, J.-H. Lu, and D.-B. Lin, "The bandwidth limitation of de-embedding technique for microstrip line measurement," in *2023 VTS Asia Pacific Wireless Communications Symposium (APWCS)*, Tainan City, Taiwan, 2023.

[29] *IEEE Standard for Electrical Characterization of Printed Circuit Board and Related Interconnects at Frequencies up to 50 GHz*, IEEE Std 370-2020, pp. 1-147, 8 Jan. 2021

[30] B. Hofmann and S. Kolb, "A multi standard method of network analyzer self-calibration-generalization of multiline TRL," *IEEE Transactions on Microwave Theory and Techniques*, vol. 66, no. 1, pp. 245-254, Jan. 2018.

[31] C. Yang and H. Huang, "Extraction of stable complex permittivity and permeability of low-loss materials from transmission/reflection measurements," *IEEE Transactions on Instrumentation and Measurement*, vol. 70, pp. 1-8, 2021.

Wei-Hsiu Tsai received the B.S. degree in Mathematics from the Fu Jen Catholic University, New Taipei, Taiwan, in 1999, and the M.B.A. degree in industrial management from the National Taiwan University of Science and Technology (Taiwan Tech), Taipei, Taiwan, in 2019. He is pursuing a Ph.D. degree in the Department of Electronic and Computer Engineering, National Taiwan University of Science and Technology (Taiwan Tech) under the supervision of Professor Ding-Bing Lin. He is currently an Engineer with BizLink International Corp., New Taipei, Taiwan. His research interests include high-speed transmission techniques and high-frequency measurement techniques.

Ding-Bing Lin (S'89-M'93-SM'14) received the M.S. and Ph.D. degrees in electrical engineering from National Taiwan University, Taipei, Taiwan, in 1989 and 1993, respectively. From August 1993 to July 2016, he was in the faculty of the Electronic Engineering Department, National Taipei University of Technology, Taipei, Taiwan, where he was an Associate Professor, a Professor and a Distinguished Professor in 1993, 2005 and 2014, respectively. Since August 2016, he had been with National Taiwan University of Science and Technology, Taipei, Taiwan, where he is currently a Professor in the Electronic and Computer Engineering Department. His research interests include wireless communication, antennas, high-speed digital transmission and microwave engineering. From 2015 to 2018, he served as the Taipei Chapter Chair, IEEE EMC society. Since 2022, he serves as the Taipei Chapter Chair, IEEE AP society. He also serves as Associate Editor of *IEEE Transactions of Electromagnetic Compatibility* since 2019 and Editorial Board member of the *International Journal of Antennas and Propagation* since 2014. He has published more than 250 papers in international journals and conferences. Lin was the recipient of the Annual Research Outstanding Award of the College of Electrical Engineering and Computer Science in 2004, 2006 and 2008. Subsequently, the College of Electrical Engineering and Computer Science awarded him the College Research Outstanding Award to highlight his research achievements. He was also the recipient of the Taipei Tech Annual Outstanding Research Award in 2008. Lin was the recipient of the Annual Research Outstanding Award of the National Taiwan University of Science and Technology in 2024.

Po-Jui Lu received the B.S. degree from Department of Electrical Engineering, National University of Kaohsiung, Kaohsiung, Taiwan, in 2022, and the M.S. degree in Electronic and Computer Engineering from the National Taiwan University of Science and Technology, Taipei, Taiwan, in 2024. His research interests includes high-frequency measurement techniques, signal integrity and power integrity.

Tzu-Fang Tseng received the B.S. degree in electrical engineering from National Taiwan University, Taipei, Taiwan, in 2009, and the Ph.D. degree in photonics and opto-electronics from National Taiwan University, Taipei, Taiwan, in 2015. She started working in industry in 2015. Her research interests include MMW signal transmission, signal integrity in high-speed cables and connectors, and optical planar lightwave circuit design and applications.

Investigations on the Influence of Augmented Rail Geometry on Rail Gun Design Parameters using Finite Element Method

M. N. Saravana Kumar[1], R. Murugan[2], J. Lydia[3], and S. Leones Sherwin Vimalraj[4]

[1]Department of Electronics and Communication Engineering
Kings Engineering College, Chennai, Tamil Nadu, India
dr.mnskphd@gmail.com

[2]Department of Electrical and Electronics Engineering
Bharath Institute of Higher Education and Research, Chennai, Tamil Nadu, India
ramumurugan_r@rediffmail.com

[3]Department of Electrical and Electronics Engineering
Easwari Engineering College, Chennai, Tamil Nadu, India
lydia.jeec@gmail.com

[4]Department of Electronics and Communication Engineering
Panimalar Engineering College, Chennai, Tamil Nadu, India
sherwin_leo@yahoo.com

Abstract **–** This paper investigates the effect of augmented rail geometry on rail gun key parameters such as mutual inductance gradient between the main and augmented rail (M'), maximum current density, and maximum magnetic flux density distribution in the rail cross-section, as well as repulsive force acting on the rails. The research study was conducted using a rectangular main rail with several augmented rail designs, including rectangular T, rectangular E, rectangular U, rectangular Convex, and rectangular Concave under inward and outward modes. The ANSYS MAXWELL 2-D eddy current field solver, which computes the magnetic field distributions for a given configuration using the finite element method, was used to calculate the rail gun essential parameters. Using the obtained results, a comparison study was conducted. It was found that the rectangular main rail with the inward circular convex augmented form rail cross-section had a greater value of M' than other geometries; hence, it could be utilized to increase the armature's velocity.

Index Terms **–** Current density, magnetic flux density, mutual inductance, repulsive force, velocity.

I. INTRODUCTION

One weapon technology that can be utilized to increase the projectile's velocity is the rail gun [1]. In order to accelerate the projectile with a faster velocity, the rail gun must overcome numerous obstacles and hurdles during design and construction [2]. Getting a greater electromagnetic force on a projectile to increase its acceleration and velocity is one of the primary issues in rail gun design.One of the traditional ways to increase force on the armature is to typically excite the rails with a high current magnitude for a brief period of time. This results in an uneven current density distribution in the rail and armature, which damages the rail and armature because it increases local heat and erosion in the rails [3].

Increasing the inductance gradient of the rails is another method of increasing the projectile's acceleration in a traditional rail cannon. This is a crucial element in rail gun design because it directly affects the force applied on the projectile [4, 5].

The dimensions, shape, and material properties of the rail all affect the inductance gradient values. Using analytical and computational techniques, numerous researchers have proposed different rail shapes in the past year to raise the inductance gradient value of the rails [6–12]. Researchers discovered that attaining a uniform current density distribution in the rail is the primary challenge in rail gun design. Therefore, without reducing the armature force with uniform current density distribution the researchers followed one of the advanced techniques is the augmented rail gun, as seen in Fig. 1, which involves connecting extra rails to the main rails either in series or parallel to create an additional magnetic field between them. This lowers the current flowing to the rail and helps to accelerate the projectile with a higher velocity [13].

Submitted On: March 6, 2025
Accepted On: May 23, 2025

https://doi.org/10.13052/2025.ACES.J.400609

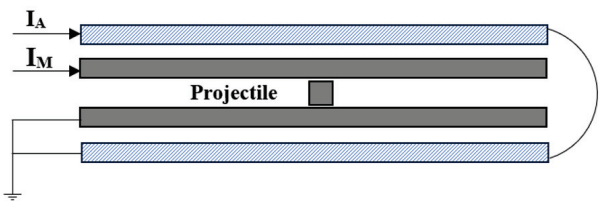

Fig. 1. Basic rectangular augmented rail gun [14].

The railgun Lorentz force is determined by

$$F = \frac{1}{2}L'I^2. \tag{1}$$

For an improved rail gun, the electromagnetic force operating on the armature is [15]

$$F = \frac{1}{2}L'I_M^2 + M'I_M I_A, \tag{2}$$

where I_A is the current flowing through the augmenting rail, M' is the mutual inductance gradient between the main rail and the augmenting rail, I_M is the electrical current flowing through the main rail, F is the armature's accelerating force, and L' is the main rail's inductance gradient. The force acting on the armature is directly proportional to the L' and M', according to the equation. Since the M' value is dependent on the dimensions and shape of the main and augmented rail, research has been conducted in recent years to raise the M' value by altering these elements. Simulation and experimentation have been used in recent years to improve the performance of augmented rail [14–23].

This study uses the ANSYS MAXWELL 2-D finite element method to analyze the impact of augmented rail geometries' shape on rail gun key design parameters like L' and M', the main rails' maximum current density distribution (J_{MR}) and magnetic flux density distribution (B_{MR}), and the repulsive force acting on the main rails (F_{MR}) and augmented rails (F_{AR}).

II. GOVERNING EQUATIONS FOR RAILGUN DESIGN PARAMETER CALCULATION

When the displacement current is ignored, and Maxwell's equations are used to calculate the electric and magnetic fields [24–26], we have

$$\nabla \times \vec{H} = \vec{J}, \tag{3}$$

$$\nabla \times \vec{E} = -\frac{\partial \vec{B}}{\partial t}, \tag{4}$$

$$\nabla \cdot \vec{B} = 0, \tag{5}$$

$$\nabla \cdot \vec{J} = 0, \tag{6}$$

$$\vec{J_C} = \sigma \vec{E}. \tag{7}$$

Additionally, in the transitory case, the differential equation for the magnetic vector potential $\vec{A}$ is:

$$\nabla \times \left(\frac{1}{\mu}\nabla X\ \vec{A}\right) = \sigma\frac{\partial \vec{A}}{\partial t} = \vec{J}, \tag{8}$$

$$\vec{B} = \nabla \times \vec{A}. \tag{9}$$

The magnetic flux density, permeability, conductivity, and impressed current density are denoted by $\vec{A}$, μ, σ, and J, respectively. The following is the induced eddy current:

$$\vec{J_e} = -\sigma\frac{\partial \vec{A}}{\partial t}. \tag{10}$$

For the 2-D situation, equation (8) reduces to

$$\nabla \cdot \left(\frac{1}{\mu}\nabla A\right) - \sigma\frac{\partial \vec{A}}{\partial t} = -\vec{J}. \tag{11}$$

This formula can be used in any 2-D time-varying scenario that involves non-linear magnetic materials. If J is a time harmonic excitation with frequency ω (rad/s), then (10) can be expressed as follows by substituting $j\omega$ for $\partial/\partial t$

$$\nabla \cdot \left(\frac{1}{\mu}\nabla A\right) - \sigma jw\vec{A} = -\vec{J}. \tag{12}$$

Solving this equation yields magnetic vector potential (A). B may be derived from (8). The magnetic energy per length is then determined using

$$W_m = \frac{1}{2}\iint \frac{\left|\nabla \times \vec{A}\right|^2}{\mu} ds. \tag{13}$$

This is the force exerted to the armature and may be expressed as

$$F = W_m = \frac{1}{2}\sum_i \frac{1}{\mu_i}\left|\vec{B_i}\right| S_i, \tag{14}$$

where i is the element index and S_i is the area of the i^{th} element. The inductance gradient L' is defined as the ratio of magnetic energy per length to current squared. Then, using equations (14) and (1), we may write:

$$L' = \frac{2F}{I^2}, \tag{15}$$

the equation we used to calculate the inductance gradient, L'.

III. THE EFFECT OF AUGMENTED RAIL GEOMETRY ON RAIL GUN DESIGN PARAMETERS

A. Validation of basic rectangular augmented rail gun

To examine the effect of augmented rail geometry form on rail gun design parameters, the ANSYS Maxwell is first validated by simulating the 2-D basic rectangular augmented rail gun as shown in Fig. 2.

The main rails (MR) and augmented rails (AR) are assumed to supply a current of 250 kA with a maximum frequency of 2000 Hz. In Fig. 2 the cross indicates the current supplied to the rail is passes into the rail and the dot indicates the current comes out of the rails. The main rail height (H_M), width (W_M), and rail separation (S_M) are assumed to be 15 mm, 30 mm, and 10 mm,

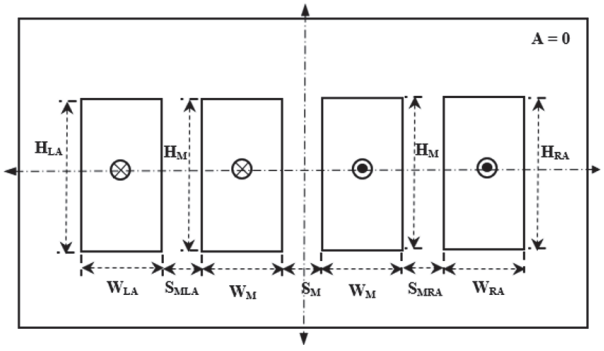

Fig. 2. A simple rectangular enhanced rail gun.

respectively. The height and width of the left- and right-hand augmented rails (H_{LA} and W_{LA}, H_{RA} and W_{RA}) are considered to be 30 mm and 15 mm, respectively. The spacing between the main rail and the left and right augmented rails (SM_{LA} and SM_{RA}) is expected to be 10 mm. The main and supplemental rails are supposed to be copper with a conductivity of 5.8×10^7 S. The magnetic vector potential (A) at the external border is taken to be zero.The rail geometry is symmetrical about the X and Y axes; therefore one-fourth of the rail structure might be utilized to imitate the rail cannon. In this study, the rail construction is mimicked without using the symmetrical characteristic. The enlarged rail gun geometry is simulated with ANSYS Maxwell, and the inductance gradient L' and mutual inductance M' are measured to be 0.492 μH/m and 0.225 μH/m, respectively. These values are consistent with the findings [14].

B. Augmented rail geometry's impact on various configurations

Several rails augmented geometry designs, including the rectangular T, E, Convex, Concave, and U shapes shown in Figs. 3 and 4, were considered and simulated in order to assess their impact in this study. The augmented geometry always has an area of 450 mm^2, which is equivalent to the area of a rectangular augmented rail.

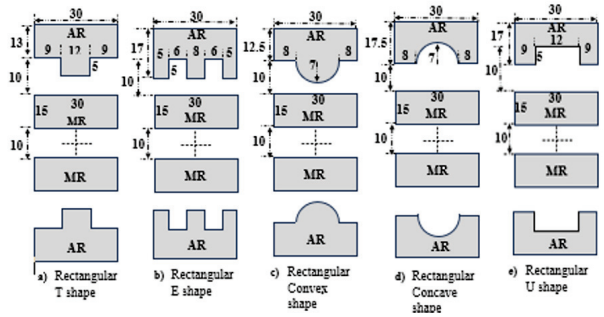

Fig. 3. Different types of augmented inward rail geometries.

The dimensions of the rails, for each rail configuration are in millimeter (mm) which is given in the Fig. 3 and in order to get the constant cross-sectional area of augmented rail geometry the width of the rail is adjusted.

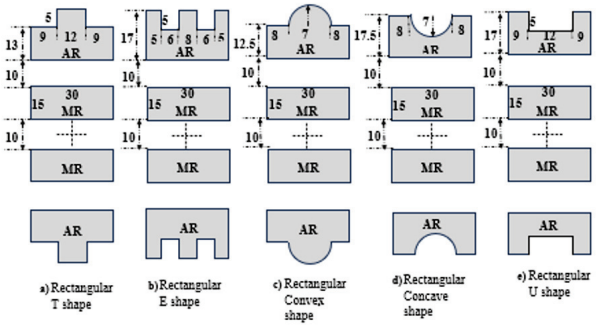

Fig. 4. Different types of augmented outward rail geometries.

IV. SIMULATION RESULTS

Figures 5 and 6 demonstrate the current density distribution over rail cross-sections generated from simulations for various shapes of augmented rail geometry. Due to the symmetrical structure of the rail geometry, only the upper portion is represented in the illustrations.

Figures 5 and 6 show that the current density distribution in the rail is not uniform, with the majority of the current distributed nearer to the surface of the

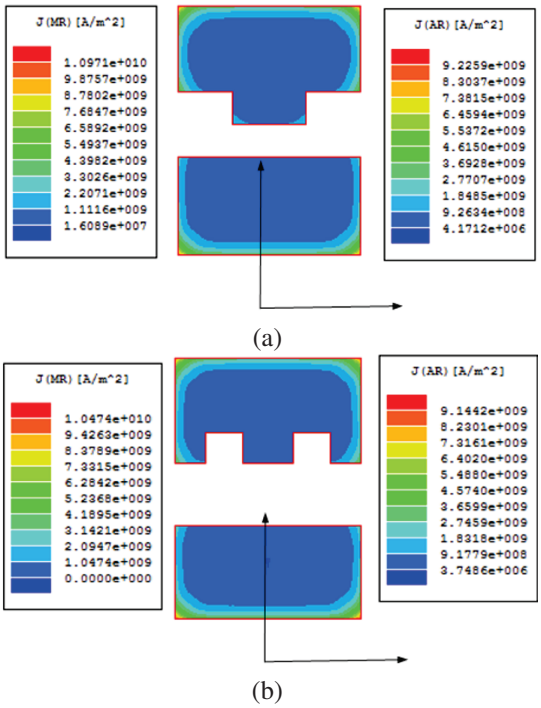

Fig. 5. *Continued*

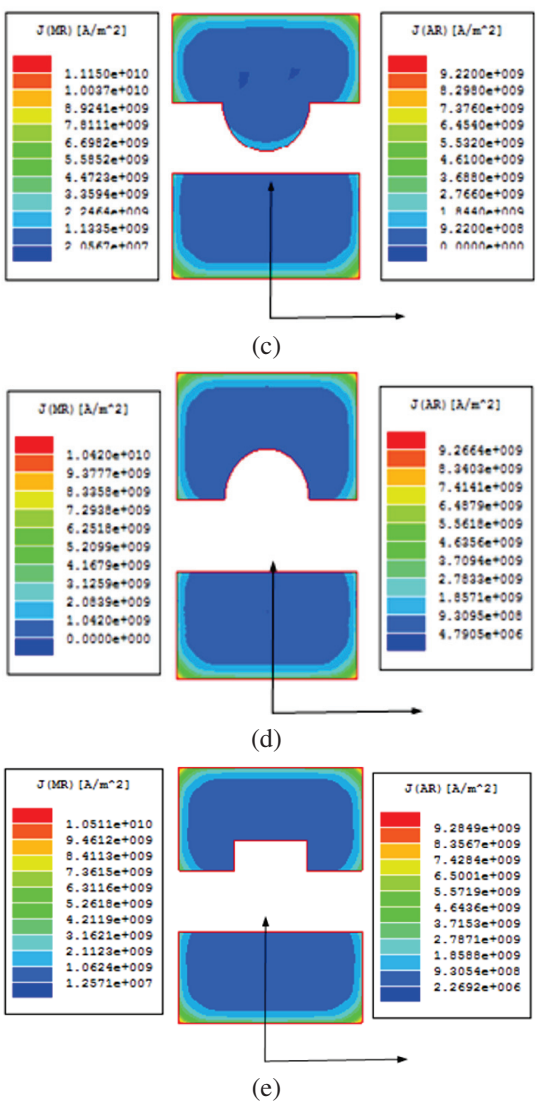

Fig. 5. Current density distribution over different inwards augmented rail geometries: (a) rectangular T shape, (b) rectangular E shape, (c) rectangular Convex shape, (d) rectangular Concave shape, and (e) rectangular U shape.

conductors, known as the skin effect. It is also discovered that the current density distribution is highest at the inside surface edges of the main rail and the outer surface edges of the enhanced rail.This results in substantial ohmic losses at the surface of the rail cross-section, as well as non-uniform temperature distribution in the rail, which causes damage. This can be adjusted by adjusting the current provided to enhanced rails. Tables 1 and 2 demonstrate the rail gun essential design characteristics acquired from simulations for various rail augmented rail geometries under inward and outward situations.

Tables 1 and 2 show that adding augmented rail and modifying the shape of its cross-section has no effect on the value of the main rail's inductance gra-

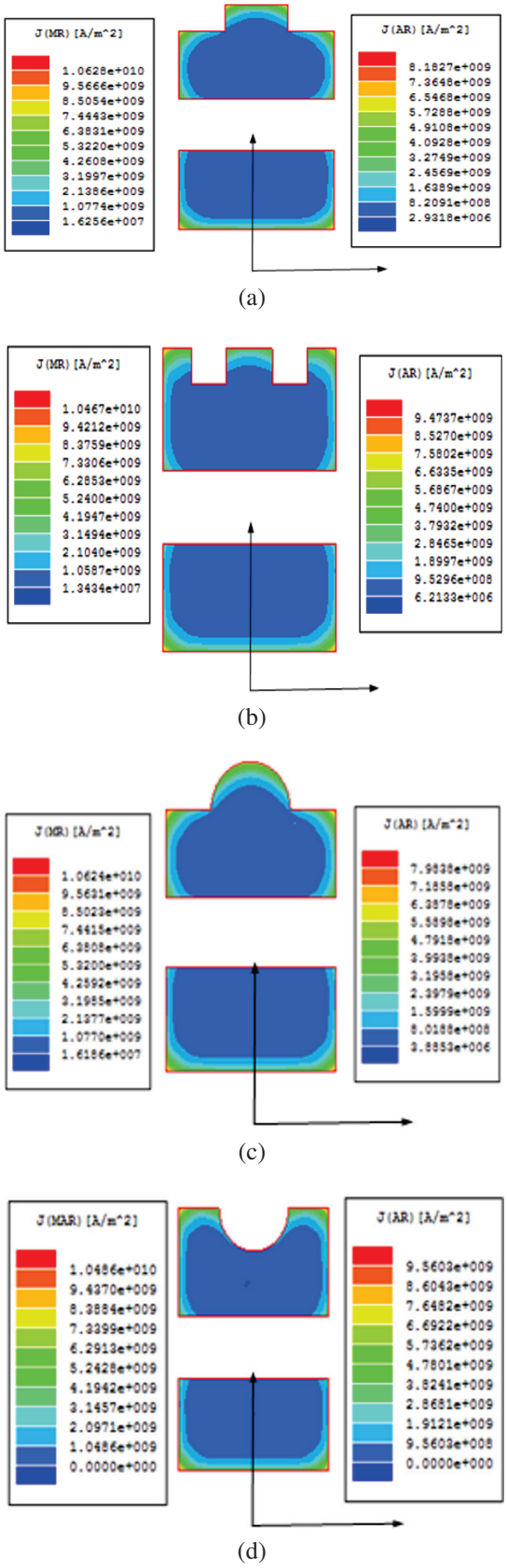

Fig. 6. *Continued*

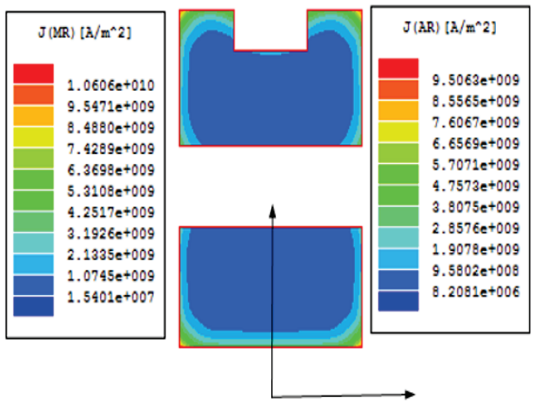

(e)

Fig. 6. Current density distribution over different outwards augmented rail geometries: (a) rectangular T shape, (b) rectangular E shape, (c) rectangular Convex shape, (d) rectangular Concave shape, and (e) rectangular U shape.

Table 1: Rail gun key design characteristics for various inwardly enhanced rail cross-sections

Augmented Rail Shape	**L' (μH/m)**	**M' (μH/m)**	**J_{MR} ($\times 10^{10}$) (A/m^2)**	**J_{AR} ($\times 10^{9}$) (A/m^2)**	**B_{MR} (Tesla)**	**B_{AR} (Tesla)**	**F_{MR} & F_{AR} (kN)**
Rectangular	0.492	0.225	1.065	9.236	9.12	7.84	110.9
T	0.492	0.256	1.097	9.226	9.40	7.78	132.02
E	0.492	0.218	1.047	9.144	9.04	7.89	97.64
Convex	0.492	0.263	1.115	9.22	9.97	7.92	142.7
Concave	0.492	0.207	1.042	9.266	9.26	8.23	84.03
U	0.492	0.215	1.05	9.284	9.00	8.02	93.01

Table 2: Rail gun key design characteristics for various outwardly expanded rail cross-sections

Augmented Rail Shape	**L' (μH/m)**	**M' (μH/m)**	**J_{MR} ($\times 10^{10}$) (A/m^2)**	**J_{AR} ($\times 10^{9}$) (A/m^2)**	**B_{MR} (Tesla)**	**B_{AR} (Tesla)**	**F_{MR} & F_{AR} (kN)**
Rectangular	0.492	0.225	1.065	9.236	9.12	7.84	110.9
T	0.492	0.221	1.063	8.183	9.13	7.08	105.3
E	0.492	0.214	1.047	9.474	8.98	8.18	92.05
Convex	0.492	0.223	1.07	7.98	9.15	7.35	103.3
Concave	0.492	0.213	1.04	9.56	9.34	8.5	90.8
U	0.492	0.217	1.06	9.50	9.11	8.05	105

dient, whereas other rail gun critical design parameters are altered by the augmented rail shape change. Table 1 shows that M' values are higher for the rectangular T and Convex augmented rail geometries. This may be due to the rail bulging inwards which decreases the separation between the main and augmented rail. The rectangular Convex augmented rail geometry has a high mutual inductance (0.263 μH/m) compared to other structures. However, the current density and magnetic flux density distribution over the rail cross-section, as well as the repulsive force acting on the rails, are higher. It is also observed that the repulsive force acting on the main rail and enhanced rail is the same for each rail cross-section, indicating that the repulsive force operating on the rail is primarily determined by the current flowing through the rails rather than the distance between the rails.Tables 1 and 2 show that M' values are lower for all configurations when compared to the basic rectangular augmented rail geometry in the outward mode. As a result, the rectangular Convex enhanced rail geometry in inward mode might be used to increase the armature's velocity.

V. CONCLUSION

This research investigates the effect of modifying the form of an augmented rail cross-section on rail gun critical design parameters using the finite element approach. Rail gun essential design characteristics are estimated for several enhanced rail geometries, including rectangular T shape, rectangular E shape, rectangular U shape, rectangular Convex, and rectangular Concave, in both inward and outward modes. A detailed comparison analysis was performed utilizing the collected results, and it was discovered that the M' value is higher in values for inward mode that enhanced the rail geometry when compared to outward mode. When compared to the standard rectangular augmented rail geometry, the rectangular T shape and rectangular Convex augmented rail geometries have greater M' values. As a result, the rectangular Convex enhanced rail geometry in inward mode might be used to increase the armature's velocity.

REFERENCES

[1] M. Asgari, M. B. Heydari, L. Gharib, A. Keshtkar, N. Jafari, and M. Zolfaghari, "A novel augmented railgun using permanent magnets," *Advanced Electromagnetics*, vol. 8, pp. 99-105, 2019.

[2] M. B. Heydari, M. Asgari, and A. Keshtkar, "A novel structure of augmented railgun using multilayer magnets and sabots," *IEEE Transactions on Plasma Science*, vol. 47, no. 7, pp. 3320-3325, July 2019.

[3] M. Putnam, "An experimental study of electromagnetic Lorentz force and rail recoil," Naval Postgraduate School, Monterey, CA, USA, Tech. Rep. 0704-0188, 2009.

[4] R. Murugan and K. Udayakumar, "Effect of rail dimensions on rail gun design parameters," in *2005 Annual IEEE India Conference - Indicon*, pp. 623-626, 2005.

[5] A. Keshtkar, "Effect of rail dimension on current distribution and inductance gradient," *IEEE Trans. Magn.*, vol. 41, no. 1, pp. 383-386, Jan. 2005.

[6] M. S. Bayati and A. Keshtkar, "Study of the current distribution, magnetic field, and inductance gradient of rectangular and circular rail guns," *IEEE*

Trans. Plasma Sci., vol. 41, no. 5, pp. 1376-1381, May 2013.

[7] M. N. Saravana Kumar and R. Murugan, "Analysis of inductance gradient and current density distribution over different cross-section of rails," *International Journal of Electrical and Computer Engineering*, vol. 8, pp. 723-729, 2018.

[8] M. N. Saravana Kumar, R. Murugan, and S. Poorani, "Inductance gradient and current density distribution for T-shaped convex and concave rail cross-sections," *International Journal of Engineering & Technology (UAE)*, vol. 7, no. 01, pp. 237-240, 2018.

[9] J. Lydia, R. Karpagam, and R. Murugan, "A novel technique for dynamic analysis of an electromagnetic rail launcher using FEM coupled with Simplorer," *Applied Computational Electromagnetics Society (ACES) Journal*, vol. 37, no. 2, pp. 229-237, Feb. 2022.

[10] M. S. Bayati and A. Keshtkar, "Study of the current distribution, magnetic field, and inductance gradient of rectangular and circular railguns," *IEEE Transactions on Plasma Science*, vol. 41, no. 5, pp. 1376-1381, May 2013.

[11] A. Keshtkar, L. Gharib, M. S. Bayati, and M. Abbasi, "Simulation of a two-turn railgun and comparison between a conventional railgun and a two-turn railgun by 3-D FEM," *IEEE Transactions on Plasma Science*, vol. 41, no. 5, pp. 1392-1397, May 2013.

[12] M. S. Bayati and A. Keshtkar, "Novel study of the rail's geometry in the electromagnetic launcher," *IEEE Transactions on Plasma Science*, vol. 43, no. 5, pp. 1652-1656, May 2015.

[13] A. Keshtkar, L. Gharib, M. S. Bayati, and M. Abbasi, "Simulation of a two-turn railgun and comparison between a conventional railgun and atwo-turnrailgunby3-DFEM," *IEEE Trans. Plasma Sci.*, vol. 41, no. 5, pp. 1392-1397, May 2013.

[14] J. Gallant, "Parametric study of an augmented railgun," *IEEE Transactions on Magnetics*, vol. 39, pp. 451-455, 2003.

[15] J. Gallant and P. Lehmann, "Experiments with brush projectiles in a parallel augmented railgun," *IEEE Transactions on Magnetics*, vol. 41, no. 1, pp. 188-193, Jan. 2005.

[16] Z. Su, W. Guo, Z. Dong, J. Yang, H. Zhang, and W. Zhou, "Design and simulation of a large muzzle kinetic energy railgun," in *2012 16th International Symposium on Electromagnetic Launch Technology, Beijing, China*, pp. 1-4, 2012.

[17] T. Watt and M. Crawford, "Experimental results from a two-turn 40 mm railgun," in *2008 14th Symposium on Electromagnetic Launch Technology,* Victoria, BC, Canada, pp. 1-6, 2008.

[18] E. Poltanov, A. K. Kondratenko, A. P. Glinov, and V. N. Ryndin, "Multi-turn railguns: Concept analysis and experimental results," *IEEE Transactions on Magnetics*, vol. 37, no. 1, pp. 457-461, Jan. 2001.

[19] M. Coffo and J. Gallant, "Modeling and analysis of the current distribution between the brushes of a multiple brush projectile in a parallel augmented railgun," in *2008 IEEE International Power Modulators and High-Voltage Conference,* Las Vegas, NV, USA, pp. 419-422, 2008.

[20] M. Coffo and J. Gallant, "Modelling of a parallel augmented railgun with Pspice validation of the model and optimization of the augmenting circuit," in *2007 16th IEEE International Pulsed Power Conference,* Albuquerque, NM, USA, pp. 1814-1817, 2007.

[21] S. Mozafari and M. S. Bayati, "Design and simulation of a slice-rail and cylindrical for multi-projectile electromagnetic launchers: electromagnetic," *Applied Computational Electromagnetics Society (ACES) Journal*, vol. 38, no. 3, pp. 214-223, Mar. 2023.

[22] M. Roch, S. Hundertmark, M. Löffler, and P. Zacharias, "First experiment with the modular augmented staged electromagnetic launcher," *IEEE Transactions on Plasma Science*, vol. 42, no. 10, pp. 3239-3244, Oct. 2014.

[23] M. Roch, S. Hundertmark, M. Löffler, and P. Zacharias, "Augmented electromagnetic accelerators: Technical solutions and new ideas," *IEEE Transactions on Plasma Science*, vol. 41, no. 10, pp. 2810-2814, Oct. 2013.

[24] M. J. Loeffler and F. Zellmer, "Augmented three phase AC railgun: Basic considerations," *IEEE Transactions on Plasma Science*, vol. 51, no. 1, pp. 249-253, Jan. 2023.

[25] A. Keshtkar, S. Bayati, and A. Keshtkar, "Effect of rail's material on railgun inductance gradient and losses," in *2008 14th Symposium on Electromagnetic Launch Technology*, pp. 1-4, 2008.

[26] K. Hsieh, "A Lagrangian formulation for mechanically, thermally coupled electromagnetic diffusive processes with moving conductors," *IEEE Transactions on Magnetics,* vol. 31, no. 1, pp. 604-609, Jan. 1995.

M. N. Saravana Kumar received a bachelor's degree in Electronics and Communication Engineering from Bhajarang Engineering College, Chennai, India, in 2009. He received his master's degree in Power electronics and drives from Rajalakshmi Engineering College, Chennai, India, in 2013, and Ph.D. degree in Electrical and Electronics Engineering department from St. Peter's Institute of Higher Education and Research, Chennai, India, in 2019. His main areas of interest are power electronics and drives, electrical machine design, electromagnetic field computation and modelling.

R. Murugan received bachelor's degree in Electrical and Electronics Engineering from University of Madras, Tamil Nadu, India, in April 1996. He received his master's degree in High Voltage Engineering from College of Engineering, Anna University, Guindy, Chennai, Tamil Nadu, India, in February 1999, and Ph.D. degree in Electrical and Electronics Engineering department from Anna University, Chennai, Tamil Nadu, India, in 2011. His main areas of interest are electromagnetic field and high voltage engineering.

J. Lydia received the bachelor's degree in Electrical and Electronics Engineering from Easwari Engineering College, Chennai, India, in 2004. She received master's degree in Power Electronics and Drives from the Karunya Institute of Technology and Sciences, Deemed University, in 2006, and Ph.D. degree in Electrical Engineering from Anna University, Chennai, India, in 2024. She is currently working as an Assistant Professor in the Department of Electrical and Electronics Engineering, Easwari Engineering College. Her areas of interest are electromagnetic fields and high-voltage engineering. She is a member of MISTE.

S. Leones Sherwin Vimalraj is a Professor in the Department of Electronics and Communication Engineering, Panimalar Engineering College, Chennai, India. He completed his B.E. in Electronics and Communication Engineering from Karunya Institute of Technology, Bharathiar University, India, in 2001. He obtained his M.E. in Optical Communication Engineering (2004) from College of Engineering, Guindy, Anna University, and Ph.D. degree in Wireless Communication Engineering (2015) from Dr. MGR Educational and Research Institute, Deemed University, Chennai, India. His research areas include wireless communication, network engineering, computing and evolutionary algorithms. He is a member of IETE.